



Room 14-0551
77 Massachusetts Avenue
Cambridge, MA 02139
Ph: 617.253.5668 Fax: 617.253.1690
Email: docs@mit.edu
<http://libraries.mit.edu/docs>

DISCLAIMER OF QUALITY

Due to the condition of the original material, there are unavoidable flaws in this reproduction. We have made every effort possible to provide you with the best copy available. If you are dissatisfied with this product and find it unusable, please contact Document Services as soon as possible.

Thank you.

Some pages in the original document contain pictures, graphics, or text that is illegible.

NEAR-RECEIVER SCATTERING OF TELESEISMIC BODY WAVES
IN LAYERED CRUST-MANTLE MODELS HAVING IRREGULAR INTERFACES

by

Kenneth Lee Larner

Gp.E., Colorado School of Mines
(1960)

SUBMITTED IN PARTIAL FULFILLMENT
OF THE REQUIREMENTS FOR THE
DEGREE OF DOCTOR OF
PHILOSOPHY

at the

MASSACHUSETTS INSTITUTE OF TECHNOLOGY

February, 1970

Signature of Author.

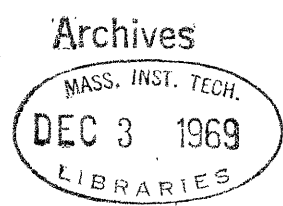
Department of Earth and Planetary Sciences
December 1, 1969

Certified by

10 *A* Thesis Supervisor

Accepted by.

Chairman, Departmental Committee
on Graduate Students



NEAR-RECEIVER SCATTERING OF TELESEISMIC BODY WAVES IN
LAYERED CRUST-MANTLE MODELS HAVING IRREGULAR INTERFACES

by

Kenneth Lee Larner

Submitted to

the Department of Earth and Planetary Sciences

on December 1, 1969

in partial fulfillment of the requirements for the
degree of Doctor of Philosophy

ABSTRACT

The scattering of teleseismic body waves in a laterally heterogeneous crust or upper mantle gives rise to wavelength-dependent, spatial variations in amplitude and time delay along the Earth's surface. Seismologists using body wave spectral amplitudes and $dt/d\Delta$ to study the structure of the Earth's interior find increasing need to understand the extent to which their data is contaminated by such scattering. This thesis describes a practical method for interpreting seismic observations on the surface of a layered medium having irregular-shape interfaces. The method may be used for studying the shape of the Moho discontinuity, for example, using the observed spectral amplitude and phase delay anomalies caused by the scattering of teleseismic body waves. The method is also useful for the engineering-seismological study of earthquake motions of soft superficial layers of laterally varying thickness. A further application can be made to the interpretation of amplitude and time delay anomalies in seismic refraction studies.

In the most general problem treated, the medium is multi-layered, having both plane interfaces and irregular interfaces (including possibly the free surface) that have arbitrary, deterministic shapes varying in one direction. That is, the shapes are characterized by a common strike direction. The incident plane body waves may arrive from depth at any azimuth relative to the strike direction. In the method, the scattered field is described as a superposition of plane waves, and application of the continuity equations at the irregular interfaces yields coupled integral

equations in the wave number spectral coefficients. The Haskell matrix method is used for treatment of continuity conditions at the plane interfaces. The equations are replaced by algebraic-sum equations over discrete wave numbers by making the interface shape periodic. They are then satisfied in the wave number domain by fast-Fourier transforming and truncating. Analytic continuation of the solutions to complex frequencies causes smoothing that reduces lateral interferences associated with the periodic interface shape and permits comparison of computed results with finite bandwidth observations. Increasing the imaginary part of frequency also inhibits layer reverberation effects while emphasizing early arrivals.

Analyses of the residuals in the interface stresses and displacements, performed for each computed solution, provides estimates of the errors attributable to approximations in the method. The relative root-mean-square residual errors are generally less than 5% and often less than 1%. Another error measure, based upon conservation of energy, is used in problems involving real frequency. The method requires no a priori assumption of small interface irregularities as in perturbation techniques, and we find that rather severe irregularities may be treated. The method is appropriate for wavelengths comparable to the dimensions of the irregularity. The accuracy is confirmed in comparisons with time domain solutions obtained using a finite difference technique and a laboratory refraction model study.

The method is applied to a variety of problems involving SH, SV, and P waves incident in models of 'soft basins', 'dented Moho', 'stepped Moho', variable surface topography, and localized intrusions. The results are compared with those derived from flat-layer theory and ray theory and suggest the limits to the ranges of applicability of those theories. In addition to vertical interference effects familiar in the flat-layer, we observe the effects of lateral interference as well as those of ray-geometry. Conversion, at the irregular interfaces, of teleseismic P-wave motion into SV and SH motion is observed as well as rotations in the apparent arrival azimuths.

The method is applied to a study of the depth and shape of the Moho under the Montana LASA. We find conclusive evidence that the Moho has an irregular shape with a linear trend $N64^{\circ}E \pm 6^{\circ}$. The computed depth to the center of the irregularity, 48 ± 5 km, is likely an upper estimate. The implied shape is step-like, with depth increasing toward the NW by 11 km over a horizontal distance of only 20 km. Our method should be useful for future investigation of such severe deep-seated variations.

Thesis Supervisor: Keiiti Aki

Title: Professor of Geophysics

This thesis is dedicated to the
memory of a gifted, young geophysicist
and friend-

Bijan Nourbehecht

ACKNOWLEDGEMENTS

It was my extremely good fortune to have Keiiti Aki as my advisor. He originally proposed the outlines of the problem and, throughout, maintained an enthusiastic interest both in the study and in my progress. It has been a pleasure being a student of a man whose outstanding scientific ability is rivaled by his human warmth.

I greatly appreciate the numerous discussions with David Boore. These sessions proved valuable at several critical stages in this work.

I join so many others in thanking Ralph Wiggins for the use of his computer subroutines and for his advice on computer usage. My thanks to Ralph for fruitful discussion of the geophysical problem as well.

I benefitted from the comments of Ted Madden, Stan Laster, and Roy Greenfield early in this study and those of Don Helmberger, Clint Frasier, and Jerry Ware at later stages. I value my association with each of these individuals as well as with Nafi Toksöz who provided friendly interest and guidance.

I wish to express my gratitude for the support received in the form of a Whitney Fellowship, National Science Foundation Fellowship, and M.I.T. graduate research assistantships.

Special thanks go to my parents Hy and Myrtle Larner for their steadfast encouragement over the years.

My wife, Sandra, assisted in the preparation of this manuscript. To this project, she applied the same efficiency and creativity that she

reserves for her large variety of artistic interests.

This research was supported partly by the National Science Foundation under Grant GA-4039, and partly by the Advanced Research Project Agency and was monitored by the Air Force Office of Scientific Research under contract AF 49(638)-1632.

ERRATA for
 NEAR-RECEIVER SCATTERING OF TELESEISMIC BODY WAVES IN
 LAYERED CRUST-MANTLE MODELS HAVING IRREGULAR INTERFACES
 by K. L. Larner

Note: Occasional corrections in the following list may already be incorporated into your copy of the thesis.

Page	Paragraph	Line	Errors and Corrections
iii	3	6	should read "... in the flat-layer theory, we ..."
11	1	4	"interfaces" should be "interface"
28	1	5	"Thompson" should be "Thomson"; this error occurs several times elsewhere.
28	3	9	misspelling: "dyadic"
39	3 lines after (2.43)		should read "... For $m=0$, we set $z_{m-1}=z_0=0$; and for $m=s+1$, we set $z_{m-1}=z_{s-1}$..."
42	2	3	"(2.52)" should be "(2.51)"
60	after (3.11)		"where $\xi_{\alpha_n} = +[k_{\alpha_n}^2 - \eta^2]^{1/2}$ is the length of the projection of the wavenumber vector onto the ..."
83	equation (4.6)		insert brackets in the numerator: $\sum_n \{ k_{\alpha_n}^2 \dots \dots \dots V_{\alpha_n}^d ^2 \}$
104	2	2	"difference" should be "differences"
110	1	5	replace "interface" by "displacement"
110	2	3	misspelling: "influencing"
135	2	6	should read "...relatively large differences in the localized residuals at the steps ..."
178	2	11	replace "digitized" by "digitizing"
182	2nd line from bottom		misspelling: "mixing"

ERRATA (continued)

Page	Paragraph	Line	Errors and Corrections
203	2	11	should read "... in the Moho at IASA persists ..."
208	3	2	"vector" should be "vectors"
213	equation after (A22)		delete the second equals sign
212	include in eqn (A18)		the following: $A_1 \delta(k-k_0) = [l_{44} \phi^* - l_{34} \psi^*] / \mathcal{L} \begin{pmatrix} 3 & 3 \\ 4 & 4 \end{pmatrix}$ $A_2 \delta(k-k_0) = [-l_{43} \phi^* + l_{33} \psi^*] / \mathcal{L} \begin{pmatrix} 3 & 3 \\ 4 & 4 \end{pmatrix}$ $A_3 \delta(k-k_0) = V^* / \rho_{22}$
215	4	4	should read "... $A_1 \delta(k-k_0) = \phi^*$, $A_2 \delta(k-k_0) = \psi^*$, $A_3 \delta(k-k_0) = V^* \dots$ "
221	1	5	" $V_0'(\kappa)$ " should be " $U_0'(\kappa)$ "
245	2	6	should read " $S_{ij}^{(m)}$ to be..."
249	equation (E16)		close denominator with] on the right
249	eqn following (E16)		close on right with }
263	line following (G16)		should be "... $T_0 = \dots$ "
267	2	5	should read "problem. Normalization is to the vertical component W for incident P waves and to the horizontal component U for incident SV waves."

TABLE OF CONTENTS

	Page
ABSTRACT.	ii
DEDICATION.	iv
ACKNOWLEDGEMENTS.	v
TABLE OF CONTENTS	vii
LIST OF FIGURES	xi
LIST OF TABLES.	xiv
Chapter	
I. INTRODUCTION.	1
1.1. Purpose and Scope	1
1.2. Outline of Method and Chapter Contents.	7
II. FORMULATIONS OF PROBLEMS.	10
2.1. Introduction.	10
2.2. SH-Wave Scattering Problems	12
2.2.1. Two half-spaces separated by an irregular interface	12
2.2.2. Layer of non-uniform thickness over a half-space: layer bounded by a plane free surface.	20
2.2.3. Layer of non-uniform thickness over a half-space: both the free surface and interface are irregular	22
2.3. Elastic-Wave Motion in a Layered Medium Having One Irregular Interface	25
2.3.1. Introduction.	25
2.3.2. Representation of the displacement and stress fields	28
2.3.3. Reduction to integral equations	36
2.3.4. Properties of the integral equations.	44
2.4. Elastic-Wave Motion in a Multi-Layered Half- Space Having One Irregular Interface.	47

Chapter	Page
2.5. Elastic-Wave Motion in a Multi-Layered Medium Having Two or More Irregular Interfaces	49
III. APPROXIMATE SOLUTION OF THE INTEGRAL EQUATIONS.	52
3.1. Introduction.	52
3.2. Method of Solution.	55
3.3. Some Features of the Solution	59
3.4. Smoothing by the Use of Complex Frequency	62
3.4.1. Comparison with finite bandwidth signals.	62
3.4.2. Reducing the effect of the periodic interface shape	63
3.4.3. Interpreting the complex frequency solutions	63
3.4.4. Implications in the use of complex source wave numbers k_0 and η_0	66
3.4.5. Reducing the effects of singularities	73
3.4.6. Practical use for complex frequency solutions	74
3.5. Normalization of the Solutions.	74
IV. ANALYSIS OF ERROR AND RESOLUTION.	77
4.1. Introduction.	77
4.2. Error Measures.	80
4.2.1. Relative root-mean-square error (RMSE).	80
4.2.2. Conservation of energy.	83
4.3. Examples of Errors.	85
4.3.1. Truncation error.	85
4.3.2. Inherent error.	94
4.4. Smoothing Effects of Complex Frequency.	98
4.5. Critical Parameters	107
4.6. Comparison with a Solution Obtained by a Finite Difference Technique	110
V. APPLICATIONS TO SEISMIC WAVE SCATTERING PROBLEMS.	117
5.1. Introduction and Summary.	117

Chapter	page
5.2. SH Wave Scattering Problems.	120
5.2.1. Two half-spaces separated by an irregular interface.	120
5.2.2. Irregular Moho problems.	125
5.2.3. Soft basin problems.	138
5.2.4. Mountains with roots	146
5.2.5. Love waves scattered from surface topography	146
5.3. P-SV Wave Scattering Problems.	152
5.3.1. Comparison with a laboratory refraction model study	152
5.3.2. Irregular Moho problems.	154
5.3.3. Spectral amplitude ratios.	160
5.4. Arbitrary-Azimuth Incidence Problems	166
5.5. Application to Montana LASA Crustal Structure.	177
5.5.1. Determination of strike direction.	177
5.5.2. Depth and shape of the Moho.	189
VI. CONCLUSION.	201
6.1. General Comments	201
6.2. Computational Time	202
6.3. Recommendations for Future Work.	203
 APPENDIXES	
A. RELATIONSHIPS BETWEEN UPGOING AND DOWNGOING WAVES.	206
A1. Review of Flat-Layer Theory.	206
A2. Sequence of Flat Layers With One Irregular Interface.	210
A3. Layered Half-Space Having One Irregular Interface.	216
A4. More Than One Irregular Interface in the Layer Sequence	218
B. SINGULARITIES OF THE INTEGRAL EQUATIONS	221
C. DETAILS IN THE DERIVATION OF INTEGRAL EQUATION (2.52)	225
D. REPRESENTATION THEOREMS FOR USE IN ERROR ESTIMATES.	234

APPENDIX	Page
E. CONSERVATION OF ENERGY.	243
F. TABLE OF ERRORS AND CRITICAL PARAMETERS	251
G. RAY THEORETICAL METHOD.	257
REFERENCES.	269
BIOGRAPHICAL NOTE	274

LIST OF ILLUSTRATIONS

Figure (abridged captions)	page
2.1 Problem configuration: two half-spaces	13
2.2 Scattering waves from secondary sources at the interface . . .	16
2.3 Problem configuration; layer over a half-space	21
2.4 Problem configuration: free surface and interface are irregular	23
2.5 Problem configuration: general elastic wave scattering	26
2.6 Source wave propagation vector	33
2.7 The dip angle and unit normal vector at interface s.	37
3.1a Top sheet of complex k-plane; ω real	70
3.1b Top sheet of complex k-plane; ω complex.	70
3.2 Locations of summation wave numbers k_n on complex k-plane. . .	72
4.1 Truncation errors for a soft basin problem	86
4.2 Wave number spectra.	90
4.3 Truncation errors for P-wave scattering at a dented Moho . . .	92
4.4 Irremovable residuals in a stepped Moho problem.	95
4.5 Smoothing of amplitude distribution by varying the imaginary component of frequency.	99
4.6 Removal of layering effects.	102
4.7 Influence of complex frequency in a P-wave scattering problem	105
4.8 Comparison of various methods: solution for a soft basin problem	112
4.9 Seismograms computed using the finite difference method. . . .	113
4.10 Exponential time windowed seismograms.	114
5.1 Effect of wavelength on SH wave scattering	121

Figure	page
5.2	Wave number spectra. 124
5.3	Free surface displacements for 10-km wavelength SH waves scattered at a depression in the Moho 126
5.4	Free surface displacements for 10-km wavelength SH waves scattered at a rise in the Moho 129
5.5	Free surface displacements for 20-km wavelength SH waves scattered at a depression in the Moho 130
5.6	Influence of interface shape and layer parameters on SH wave scattering. 132
5.7	SH wave scattering in stepped Moho problems. 134
5.8	Comparison of scattering from steep and gentle gradient step irregularities 136
5.9	Schematic diagram of wave diffraction from a step. 137
5.10	Response of a soft basin to plane SH waves: $D = \lambda_1/5$ 140
5.11	Response of a soft basin to plane SH waves: $D = \lambda_1/2$ 141
5.12	Response of a flat, soft basin to plane SH waves: $D = \lambda_1/4$, $\tau = 9.09$ sec 142
5.13	Response of a flat, soft basin to plane SH waves: $D = \lambda_1/4$, $\tau = 90.9$ sec 143
5.14	Response of a soft basin to long wavelength S waves. 145
5.15	Generation of Love waves by SH wave scattering at a valley . . 147
5.16	Love wave dispersion curves. 150
5.17	Wave number spectra for SH wave scattering at topographic irregularities. 151
5.18	Comparison with a laboratory refraction model study. 153
5.19	Effects of wavelength and decay time on P-wave scattering. . . 155
5.20	Effects of layer thickness and irregularity amplitude on P-wave scattering 156
5.21	Vertical motion due to vertically incident S waves 158
5.22	Comparison with ray theory and flat-layer theory 159
5.23	Spectral amplitude ratio vs. D_f from flat-layer theory 161

Figure	page
5.24	Spatial distributions of spectral amplitude ratios: gentle irregularities, $f=0.1$ cps 163
5.25	Spatial distributions of spectral amplitude ratios: gentle irregularities, $f=0.087$ cps 164
5.26	Spatial distributions of spectral amplitude ratios: steep irregularities. 165
5.27	Scattering of P, SV, and SH waves: $\Omega_0=90^\circ$ 167
5.28	Horizontal particle motion ellipses. 169
5.29	Apparent azimuths based upon wavefront directions. 171
5.30	Comparisons of solutions to arbitrary azimuth problems and to P-SV problems. 172
5.31	Scattering of P waves at grazing incidence along strike. . . . 174
5.32a	Three multi-layered crust models 175
5.32b	Free surface motion due to P-wave scattering in the multi-layered models. 176
5.33	Plan view of Montana LASA. 179
5.34	Trend measure vs. trial trend direction: 3 events. 184
5.35	Histograms for estimating Moho strike at Montana LASA. . . . 188
5.36	Examples of observed spectral amplitudes and time delays . . . 190
5.37	Smoothed spatial distributions of spectral amplitude for E. KAZAKH event 191
5.38	Scattering of P waves at a step in the Moho. 193
5.39	Theoretical surface displacement peak and trough positions vs. $\tan \theta_1$ 194
5.40	Observed surface displacement amplitude and phase peak positions vs. $\tan \tilde{\theta}_1$ 196
5.41	Single layer model for Montana LASA structure. 198
A1	Sequence of flat layers. 207
G1	Problem configuration: ray theoretical method. 258
G2	Schematic diagram showing a tube of rays 262

LIST OF TABLES

Table		page
3.1	Table of Values of the Matrix Size Number K for Different Scattering Problems	58
5.1	Layer and Interface Parameters for the Examples in Figure 5.6	131
5.2	Free Surface and Interface Shape Parameters for the Cases in Figures 5.16 and 5.17.	149
5.3	Earthquake Event Data.	180
5.4	Data Used in Determination of Trend Direction at Montana LASA.	185
5.5	Results of Trend Determination	187
5.6	Parameters for Single Layer Models of Montana LASA Structure	199
F1	Table of Errors and Critical Parameters.	253

CHAPTER I

INTRODUCTION

1.1. Purpose and Scope

This thesis is an exposition, with numerous applications to problems in seismology, of a practical method for obtaining solutions to problems involving the scattering of plane elastic waves in a class of laterally heterogeneous, layered media. The existence of significant lateral variations in the seismic properties of the Earth's crust is a well established fact, and increasing evidence makes it likely that small-scale variations (say, less than 50 km in width) exist as deep as the Moho and deeper into the upper mantle. Incident teleseismic body waves with essentially plane wavefronts over some small area will be scattered in the inhomogeneous crust, resulting in variations in the observed displacement amplitudes and time delays over the Earth's surface. These variations will be dependent upon the wavelength of the incident wave relative to the dimensions of the inhomogeneities.

The observed spectral variations are of interest for two general reasons. One is the possibility that they may be diagnostic of the scattering region, and thus be useful for studying subsurface structure. For example, in section 5.5 we use both spectral amplitude and phase delay observations at the Montana LASA to infer the depth and shape of the Moho. The second reason is the following. Many recent studies of the elastic and Q structure of the interior of the Earth employ observed spectral displacement amplitudes and $dT/d\Delta$ in theories that assume flat-layering

near the receivers. Anomalous amplitudes and time delays caused by scattering (including wave focusing and diffraction) can often contaminate the results of such studies. Therefore, it would be valuable to have theoretical solutions which could be used to estimate the effects of scattering from anticipated inhomogeneities.

The method described here provides such solutions for scattering in layered media having irregular-shaped interfaces. The technique, though its formulation is based upon an old idea described by Rayleigh (1907, 1945), is made feasible by the speed and convenience of the digital computer as well as by the availability of the fast-Fourier transform algorithm. The method is practical, thus far, only for interface shapes that vary in only one-dimension; that is, we allow crustal variations in only one lateral direction, normal to the strike. There is convincing evidence for such one-dimensional irregularities on various scales (Mikumo, 1965; Greenfield and Sheppard, 1969; our own investigation of the Montana LASA). Even were this not so, new aspects in our solutions over those found in the flat-layer theory or ray theory solutions provide advances toward our understanding of wave scattering in the more general case. The same is true of the relationship between irregular interface problems and lateral velocity-transition problems.

Our method is applicable to the so-called "ground motion" problem. The spectrum of seismic motion at the Earth's surface shows peaks and troughs due to constructive and destructive interferences within the surface layers. Earthquake seismologists are interested in this problem because they can utilize the shape of spectrum for studying the crustal layering. The engineering seismologists are concerned about this problem

because the ground motion can be amplified significantly at the resonance frequencies. The case of SH waves in horizontally uniform layers has been extensively studied by Kanai and his colleagues (Kanai, 1952; Kanai et al., 1959). Cases involving P and SV waves have been studied by Haskell (1960, 1962), Phinney (1964), and others, using the Thomson-Haskell method (Haskell, 1953). It is important to know how the resonance conditions are affected by the lateral variation of layer thickness. We shall show some results of the successful application of our method to the above problems.

The method also provides valid solutions even for grazing incidence (horizontal propagation) to the interfaces, and may provide a new tool for the interpretation of amplitudes and arrival times in refraction seismology.

In our method, we compute spectral (single frequency) amplitude and phase delay distributions in deterministic, forward-solution problems with the source wave and layered system given. Although it was not done here, the single frequency solutions could, of course, be used to Fourier synthesize transient time solutions. To aid in practically accomplishing such a Fourier synthesis and for other reasons to be described later, we allow the frequency ω to be complex. This use of complex frequency is equivalent to smoothing the solutions over a real frequency band and yields spectral amplitudes and phase delays that can be directly compared with spectral analyzed seismograms premultiplied by prescribed time windows.

Although the models are laterally heterogeneous in only one direction, we allow the source wave to be incident from any azimuthal direction relative to the strike of the trending structure. In such problems, P-, SV-, and SH-wave motions are coupled so that a transverse component of

motion can arise from the scattering of incident P or SV waves.

Our solutions may be considered as 'middle frequency' solutions in the sense that the wavelengths involved are comparable to the sizes of the interface anomalies. Although the accuracy declines as the wavelengths become small, the solutions are generally valid down to wavelengths that are sufficiently short to obtain adequate comparisons with geometrical ray theory. This middle frequency range extends in the other direction to wavelengths that are so long that the waves essentially no longer 'see' the interface roughness. Also, our solutions are near-field in that the observation points (receiver stations) generally are located within 10 to 20 wavelengths distance from the interface anomalies.

This thesis has four goals. The first is a detailed exposition of the theoretical formulation of the wave scattering problems and of their practical solution. The method is approximate both in the formulation of the problems and in their numerical solution; hence, the second goal is to indicate the range of validity of our method by presenting an estimate of the accuracy of the computed solution in each practical problem. The third goal is to present solutions to a variety of wave-scattering problems that are directly applicable to problems of current interest in seismology. Finally, we demonstrate an application of the method with the determination of Moho depth and shape at Montana LASA.

Following Rayleigh, we represent the scattered wave field as a linear superposition of plane waves where the coefficients are determined in such a way that the boundary conditions are approximately satisfied. There are several approximate ways to satisfy the boundary conditions.

Rayleigh used an iterative approximation, expanding the boundary condition in a power series in the amplitude of the corrugation. The same approximation has been applied to seismic problems by Abubakar (1962 a,b,c), Dunkin and Eringen (1962), Asano (1960, 1961, 1966), and Levy and Deresiewicz (1967). Meecham (1956) used a variational method in which the boundary condition is satisfied in a least-squares sense. The method presented here is closer to Meecham's, but takes advantage of the fast Fourier transform algorithm (Cooley and Tukey, 1965) and satisfies the boundary condition in the wave number domain.

The emphasis in our method is on its practical value for obtaining theoretical solutions in a form immediately useful for the study of problems in seismology. In the abovementioned investigations of seismic wave scattering, the interface shapes are taken to be sinusoidal (corrugated) and of small amplitude relative to the wavelengths of the corrugations and of the waves. Their solutions are presented as curves of the amplitudes of the primary, first scattered order, and possibly second scattered order plane reflected and transmitted waves as functions of the ratio of a wave wavelength to corrugation wavelength. Solutions in this form are not immediately useful for application to seismic wave scattering in layered media with irregular interfaces of arbitrary shape. Moreover, the requisite assumption that such solutions to sinusoidal boundary problems can be superposed to yield the solution to arbitrary-shaped boundary problems is valid only to the first order in the amplitudes of the irregularities.

Our method makes no a priori assumption concerning the sizes and shapes of the interface irregularities or the wavelengths involved. Of course, the accuracy of our solutions is stringently dependent upon the sizes of

such parameters; however, we can check the accuracy of the computed solutions using error measures based upon the residual discontinuities in stresses and displacements at the interfaces. We find that we can obtain useful solutions to problems involving rougher interface shapes than are allowed in the various perturbation techniques.

There are various other approaches to this type of wave-scattering problem. None are exact, as befitting wave diffraction problems in which the boundaries do not coincide with the constant coordinates of a coordinate system in which the wave equation is separable. Banaugh (1962) uses a representation theorem to formulate his solution. The integral equations formulated are exact; however, approximations used in their actual solution subject the solutions to truncation errors that are comparable to those that we encounter. This is particularly true for the application of Banaugh's method to scattering at irregular interfaces rather than at isolated obstacles (also, see Sharma, 1967). Other theoretical investigations of scattering of plane waves generally involve perturbation methods in which the interface shape has a very small amplitude anomaly relative to the wavelength (Gilbert and Knopoff, 1960; Herrera, 1964; and McIvor, 1969).

Two analog methods are the finite-difference method (Boore, 1969) and laboratory model studies (for example; Laster, et. al., 1967). These have the advantage that solutions are computed directly in the time domain. In both methods, the time duration is limited by the boundaries of the model (or grid network). Probably the most critical factor in the finite-difference method is the accuracy of the approximations for the interface conditions; in the laboratory model it is the nature of the interface bonding and the coupling of the transducers to the medium. In this thesis,

we present comparisons with solutions obtained by these methods.

Finally we mention the ray theoretical methods. The ray theory is a high frequency approximation which often yields useful solutions, particularly for time delay, to wave scattering at irregular interfaces. Mereu (1969) and Mechler and Rocard (1967) have applied the ray theory to seismic wave scattering at irregular interfaces. In our examples we demonstrate limitations in the use of simple ray theory.

The essential form of the method presented here was derived by Aki and Larner, (1970) in a study of SH wave scattering in a layer of nonuniform thickness over a half-space. The new contributions in this thesis include the extension to the general problem of scattering of any type of elastic wave (P, SV, or SH) incident at arbitrary azimuth relative to the strike of the irregular structure, the inclusion of an arbitrary number of additional plane layers, and the extension to cases involving irregular free surface topography. These extensions enlarge the variety of seismic problems to which the method can be applied. The techniques used to determine the trend of the Moho irregularity at Montana LASA are also new.

1.2. Outline of Method and Chapter Contents.

Our method for solving the elastic wave scattering problems is presented in Chapters II and III. Several problems are formulated in Chapter II in the following manner. The wave field in each layer is represented as a superposition of plane waves whose complex amplitudes are to be determined by satisfying boundary conditions at the interfaces and at infinity. The continuity requirements at plane interfaces are

used to reduce the number of unknown wave amplitudes to just the number of boundary conditions required at each irregular interface. By writing these boundary conditions explicitly, we obtain a set of coupled integral equations (one equation for each boundary condition) whose approximate solution yields the complex wave amplitudes.

The most general problem that we consider is the scattering of plane elastic waves (longitudinal or transverse) incident from depth at an arbitrary azimuth relative to the strike of the interface irregularities. However, as an aid to the reader, we introduce the technique by first considering three short scalar problems involving incident SH waves propagating in the plane normal to the strike of the interface irregularity. Each problem treated in Chapter II is taken to the point of writing the integral equations. Appendixes A, B, and C lend supporting discussions.

The method of approximating the solutions of the integral equations is presented in Chapter III. By assuming the interface shape to be periodic (with large period relative to the width of the isolated irregularities), we can replace the integral equations by infinite-sum equations over discrete wave numbers. These equations are Fourier transformed and truncated to a finite number of wave number terms. That same number of equations is retained. The resulting large system of simultaneous linear equations is then solved numerically. The method is applicable to the solutions of all the problems considered in Chapter II. Some implications inherent in our use of complex frequency smoothing are also discussed in Chapter III.

The error analysis in Chapter IV is crucial to the evaluation of the

effectiveness of the technique. Two measures of accuracy are defined (derivations are given in Appendixes D and E). Both are related to the residual displacements and stresses at the irregular interfaces. The numerical values of the error measures in every example presented in this thesis are listed in Table F1 of Appendix F. Several examples are presented in Chapter IV to demonstrate the dependence of interface residuals upon the truncation of the equations and upon the shape of the irregular interface. The trade-off between stability and resolution achieved through varying the imaginary part of frequency is also displayed in examples. Chapter IV concludes with a comparison of solutions obtained by our method and the method of finite differences. The excellent agreement provides a check on both methods and also confirms our understanding of the relationship between the complex frequency solutions and smoothed time-domain solutions.

Chapter V is the culmination of the thesis. In it, solutions to a number of problems of interest in seismology are presented. A summary of the examples discussed is given in section 5.1. Section 5.5 is an application to the study of the deep subsurface structure at Montana LASA. We find that the observed spectral displacement amplitudes, as well as time delays, are diagnostic of the trend direction of the Moho irregularity. The amplitudes yield estimates of depth; the time delays give the amplitude of the Moho irregularity; and a combination of the two data suggests the slope and location of the irregularity.

Chapter VI concludes the thesis with a short discussion of the computational time requirements and recommendations for future work.

CHAPTER II
FORMULATIONS OF PROBLEMS

2.1. Introduction.

In this chapter, we formulate the solutions to several related problems involving the scattering of plane elastic waves in layered media in which some interfaces have one-dimensionally irregular shapes. In each problem, the wave fields are represented as linear superpositions of plane waves. By imposing continuity conditions at the interfaces, we reduce the problems to the solutions of coupled integral equations in which the unknown functions are the complex amplitudes of waves leaving the interfaces. The approximate method for solving these equations is described in Chapter III.

In Section 2.2, three simple two-dimensional problems involving the scattering of SH waves are discussed. There, the wave fields are scalar, and all wave propagation is parallel to a given plane. These SH wave problems are special cases of the larger problems developed in the sections that follow and are designed to briefly introduce the essential features in the formulation of the integral equations. The first problem involves scattering at the irregular interface separating two half-spaces. Our formulation is that applied by Rayleigh (1907, 1945), Meecham (1956), and Heaps (1957) to the scattering of acoustic waves and by Abubakar (1962a, b, c) and Asano (1960, 1961, 1966) to the scattering of seismic waves. In the

second problem, one of the half-spaces is replaced by a layer bounded by a plane free surface. Here, the vanishing stress condition at the plane free surface is employed to reduce the number of unknown functions down to the number of boundary conditions at the irregular interfaces. The final SH wave scattering problem discussed also involves a layer over a half-space, but in this case both the interface and the free surface are irregular.

In Section 2.3, we consider the larger, more general problem of the scattering of plane P or S waves incident from an arbitrary azimuthal direction. The medium consists of a sequence of layers between two half-spaces where all, but one, of the interfaces are plane and parallel. That interface is roughly parallel to the others but has a one-dimensionally irregular shape. Because the incident waves may arrive from any direction, the P, SV, and SH wave motions are generally coupled, and the scattered waves do not propagate in directions parallel to the same plane. We use the flat-layer wave theory of Haskell (1953) to iteratively satisfy the continuity conditions at the plane boundaries and thereby reduce the number of unknown wave amplitudes in the problem.

In Section 2.4, a similar problem is treated, differing in that one of the half-spaces is removed; that is, the upper-most interface is free. This problem serves as a model for the scattering of teleseismic body waves incident from the mantle at arbitrary azimuths relative to the strike of, say, an irregular Moho discontinuity. This model is used, in Chapter V, for the computation of three-component displacement amplitude and phase delay anomalies along the free surface.

In the final section (2.5), we obtain the integral equations for problems where more than one of the interfaces are irregular. The extension to these cases is straightforward. However, the number of unknown complex wave amplitudes required to describe the wave fields increases with the number of irregular interfaces. Thus, significantly more computational effort is required to obtain comparable accuracy in the numerical solution of the integral equations.

2.2. SH Wave Scattering Problems.

2.2.1. Two half-spaces separated by an irregular interface. In all our problems, we shall use rectangular Cartesian coordinates (x,y,z) with the positive z -coordinate (depth) directed vertically downward and the x - and y - axes horizontal. Consider the medium, shown in Figure 2.1, consisting of two homogeneous, isotropic solid half-spaces joined by the irregular interface at depth $z = \xi(x)$. The medium is uniform in the y -direction; that is, the y -direction coincides with the strike or trend direction of the interface shape. The medium above the interface ($z < \xi$) has shear velocity β_1 and density ρ_1 and that below the interface, β_2 and ρ_2 . We wish to determine the motion anywhere in the medium in response to plane harmonic SH waves, polarized in the y -direction, that are incident from depth in the lower medium parallel to the x - z plane at the angle θ_0 from the z -axis. The problem is two-dimensional, and the solution is independent of y .

Let the displacements in the upper and lower media be $\hat{v}_1(x,z)$ and $\hat{v}_2(x,z)$, respectively. We represent the harmonic time dependence by the

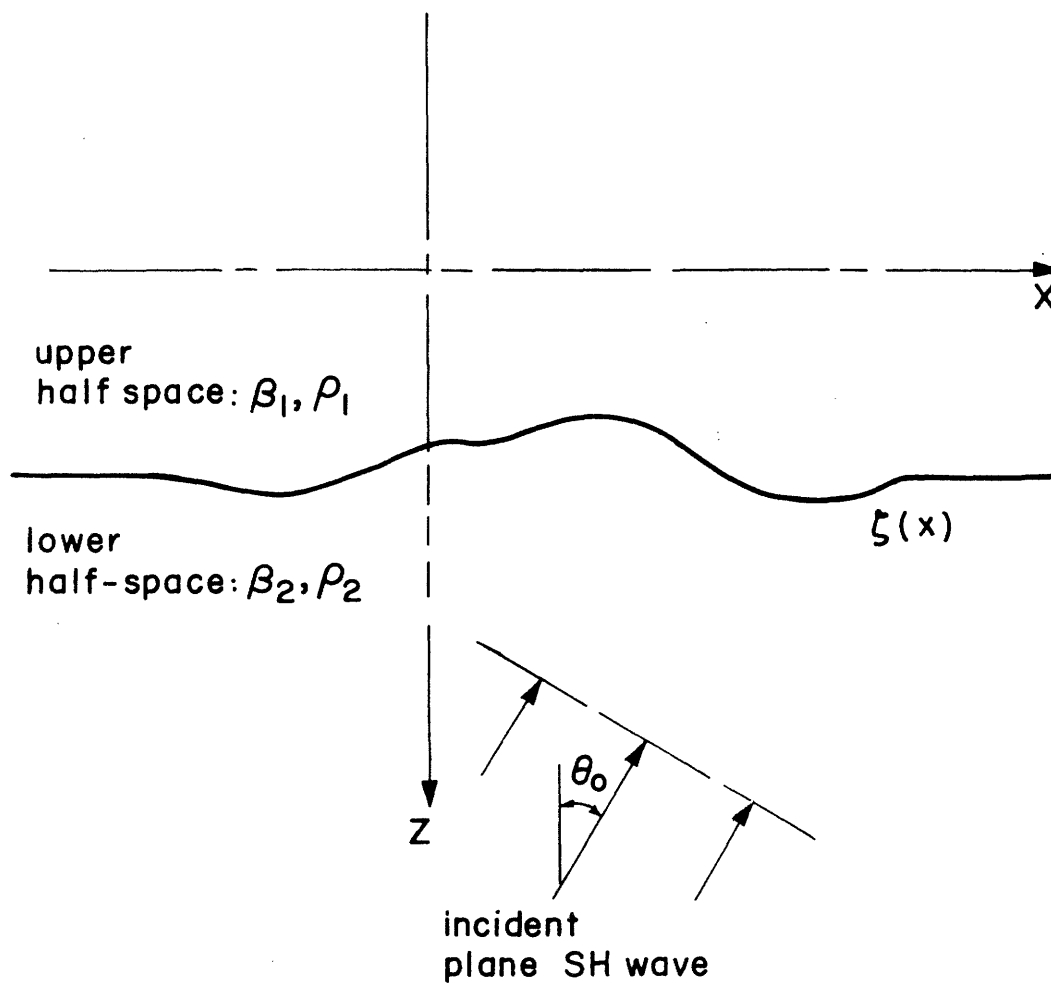


Figure 2.1. Problem configuration for plane SH wave scattering at the irregular interface separating two half-spaces.

complex exponential $e^{-i\omega t}$ where the radial frequency ω satisfies

$$0 \leq \arg(\omega) < \pi/2 \quad (2.1)$$

We suppress the common factor $e^{-i\omega t}$ in all that follows. The displacements satisfy the scalar Helmholtz equations

$$(\nabla^2 + \omega^2/\beta_j^2) \hat{V}_j = 0 \quad ; \quad j=1,2$$

so that they can be expressed as the following superpositions of plane waves

$$\hat{V}_1(x,z) = \int_{-\infty}^{\infty} V_1^u(k) e^{ikx - i\gamma_1' z} dk \quad (2.2)$$

$$\hat{V}_2(x,z) = e^{ik_0 x - i\gamma_0' z} + \int_{-\infty}^{\infty} V_2^d(k) e^{ikx + i\gamma_2' z} dk \quad (2.3)$$

Here, k_0 and γ_0' are the x- and z-components of the wave number of the incident waves, respectively, and

$$\gamma_0' = (\omega^2/\beta_2^2 - k_0^2)^{1/2} = (\omega/\beta_2) \cos \theta_0 \quad (2.4)$$

$$v_j' = (\omega^2/\beta_j^2 - k^2)^{1/2} \quad ; \quad j = 1, 2 \quad (2.5)$$

The coefficients v_1^u and v_2^d are the complex amplitudes of the plane waves that describe the scattered field and are to be determined by satisfying the boundary conditions at the interface. The superscripts "d" and "u" denote downgoing and upgoing waves, respectively, once the signs of the radicals v_0' , v_1' , and v_2' are fixed by appropriate definitions of the branch lines and the top sheet of complex k -plane. (see section 3.4.4)

In this thesis, the term upgoing waves denotes waves that not only propagate upward in a real sense, but also those inhomogeneous or evanescent waves (Brekhovskikh, 1960) that attenuate in the upward (decreasing z) direction. Likewise, downgoing waves are waves that either propagate downward or attenuate with increasing z . For example, for the case of real ω in this first problem, inhomogeneous scattered waves in the upper medium are associated with wave numbers such that $|k| > \omega/\beta_1$. These waves carry no energy away from the interface, and hence are sometimes called interface waves.

The description of the wave field given by (2.2) and (2.3) is the same as that used by Rayleigh in his study of the scattering of acoustic waves by a grating. Lippmann (1954) and Uretzky (1965) have questioned the validity of such a description of the wave field. In fact, (2.2) and (2.3) cannot completely represent the wave field for the following reason. The interface is the locus of secondary point sources of scattered waves, as shown in Figure 2.2. For $\zeta(x) < z < \zeta_{\max}$, where ζ_{\max} is the

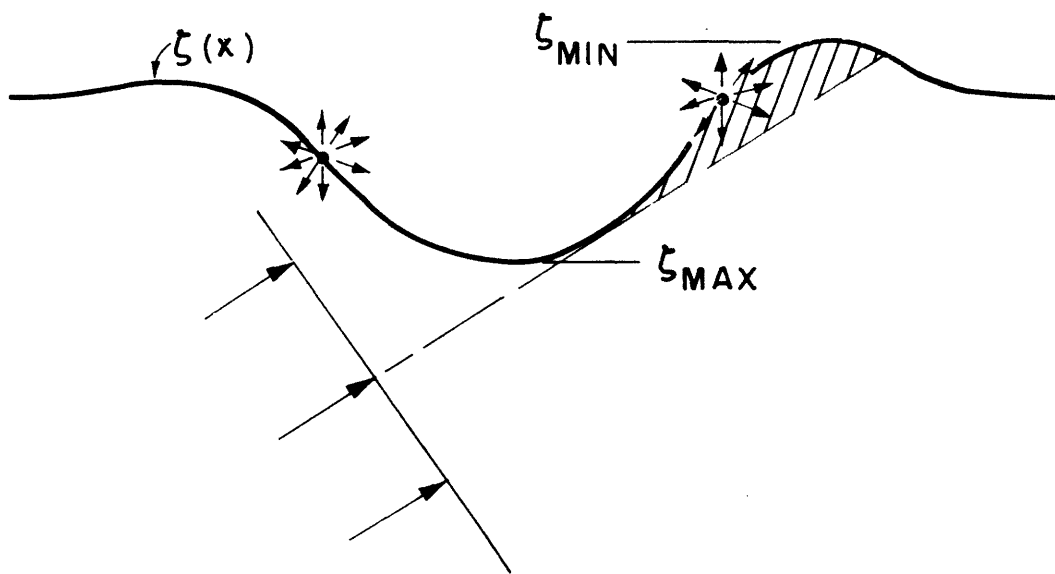


Figure 2.2. Schematic diagram illustrating scattered upgoing and downgoing waves throughout the interval $\zeta_{\text{min}} < z < \zeta_{\text{max}}$ from secondary sources at the irregular interface.

maximum of $\xi(x)$, the scattered field in the lower medium includes waves that are locally upgoing. However, the source wave is the only upgoing wave allowed in our expression (2.3) for the field in the lower medium. A similar difficulty arises with expression (2.2) for the field in the upper medium. The discrepancy is greatest in problems involving large interface slopes, particularly when the source wave length is smaller than the amplitude $(\xi_{\max} - \xi_{\min})$ of the interface irregularity.

Expressions (2.2) and (2.3) are therefore only approximate representations of the wave field and, consequently, the boundary conditions at the interface cannot be satisfied rigorously (otherwise the uniqueness theorem would be violated). However, in many problems these scattered upgoing waves near the interface in the lower medium and downgoing waves in the upper medium are negligibly small, and (2.2) and (2.3) are satisfactory for practical purposes. If so, small residuals or discontinuities left at the interfaces would generate even smaller errors in the motion computed for positions removed from the interface. Therefore, we assume that (2.2) and (2.3) are good approximations to the wave fields near the interface, and test the adequacy of this assumption by evaluating the residuals in the boundary conditions in each practical problem.

The formulation of every problem studied in this thesis is patterned on expressions (2.2) and (2.3); thus, in all cases, our solutions are approximate. Further implications associated with the inherent error in this Rayleigh formulation are considered in Chapter III.

For this first SH wave problem, the boundary conditions are the continuity of stress and displacement at the interface; these are

$$\left. \begin{aligned} \hat{V}_1 &= \hat{V}_2 \\ \mu_1 \frac{\partial \hat{V}_1}{\partial n} &= \mu_2 \frac{\partial \hat{V}_2}{\partial n} \end{aligned} \right\} \text{ at } z = \zeta(x) \quad (2.6)$$

where μ_1 is the rigidity of upper medium, μ_2 is that of the lower medium, and $\frac{\partial}{\partial n}$ represents the space derivative in the direction normal to the interface.

$$\frac{\partial}{\partial n} \equiv \underline{n} \cdot \text{grad} = n_x \frac{\partial}{\partial x} + n_z \frac{\partial}{\partial z} \quad (2.7)$$

$$\begin{aligned} n_x(x) &= -S(1+S^2)^{-1/2} \\ n_z(x) &= (1+S^2)^{-1/2} \\ S(x) &= \frac{d\zeta(x)}{dx} = \text{interface slope} \end{aligned} \quad (2.8)$$

Using (2.2), (2.3), (2.7), and (2.8) in equations (2.6), we get

$$\begin{aligned} \int_{-\infty}^{\infty} [v_1^u(k) f_{11}(k,x) + v_2^d(k) f_{12}(k,x)] e^{ikx} dk &= h_1(k_0, x) e^{ik_0 x} \\ \int_{-\infty}^{\infty} [v_1^u(k) f_{21}(k,x) + v_2^d(k) f_{22}(k,x)] e^{ikx} dk &= h_2(k_0, x) e^{ik_0 x} \end{aligned} \quad (2.9)$$

where the known coefficients are

$$\begin{aligned}
 f_{11}(k,x) &= e^{-i\nu_1' \zeta(x)} \\
 f_{12}(k,x) &= -e^{i\nu_2' \zeta(x)} \\
 f_{21}(k,x) &= \mu_1 [k s(x) + \nu_1'] e^{-i\nu_1' \zeta(x)} \\
 f_{22}(k,x) &= -\mu_2 [k s(x) - \nu_2'] e^{i\nu_2' \zeta(x)}
 \end{aligned} \tag{2.10}$$

and the source terms are

$$\begin{aligned}
 h_1(k_0,x) &= e^{-i\nu_0' \zeta(x)} \\
 h_2(k_0,x) &= \mu_2 [k_0 s(x) + \nu_0'] e^{-i\nu_0' \zeta(x)}
 \end{aligned} \tag{2.11}$$

By solving the integral equations (2.9) for $v_1^u(k)$ and $v_2^d(k)$, we can determine the wave field in any part of the medium. That is the task in Chapter III. Equations (2.9) are prototypes of the integral equations that will be obtained in subsequent problems in this thesis. The essential features are

- 1) there is one integral equation for each boundary condition,
- 2) there is one unknown function for each boundary condition, and
- 3) the coefficients $f_{ij}(k,x)$ and $h_j(k_0,x)$ are functions of x only through the x -dependence of the irregular boundary shape.

If the interface were plane, the integrals would reduce to Fourier integrals and the equations could be solved trivially. In that case, no wave number coupling would arise; that is, the scattered field would consist simply of plane waves characterized by the incident wave number k_0 . We note that, for this problem as well as for the next two SH wave motion problems, the coefficients $f_{ij}(k,x)$ are well behaved functions of k .

2.2.2. Layer of non-uniform thickness over a half-space: layer bounded by a plane free surface. Consider, now, SH wave scattering in a medium consisting of a layer over a half-space. As illustrated in Figure 2.3, the layer (medium 1) is bounded below by the irregular interface at $z = \zeta(x)$ and above by the plane free surface at $z=0$. We are interested in the motion along the free surface when an SH wave is incident from depth in medium 2 as in the previous problem. Equation (2.3) again approximately represents the solution in the half-space, but now upgoing and downgoing waves are required to approximately describe the wave field $\hat{v}_1(x,z)$ in the layer. We write

$$\hat{v}_1(x,z) = \int_{-\infty}^{\infty} [v_1^u(k) e^{ikx - i\nu_1'z} + v_1^d(k) e^{ikx + i\nu_1'z}] dk \quad (2.12)$$

The vertical component of wave number ν_1' is defined as before by (2.5), and the downgoing wave amplitude $v_1^d(k)$ is a new unknown in the problem. In addition to the interface conditions (2.6), we must satisfy the vanishing stress requirement at the free surface

$$\frac{\partial \hat{v}_1(x,0)}{\partial z} = 0 \quad (2.13)$$

Requirement (2.13) is satisfied when

$$v_1^d(k) = v_1^u(k) \quad (2.14)$$

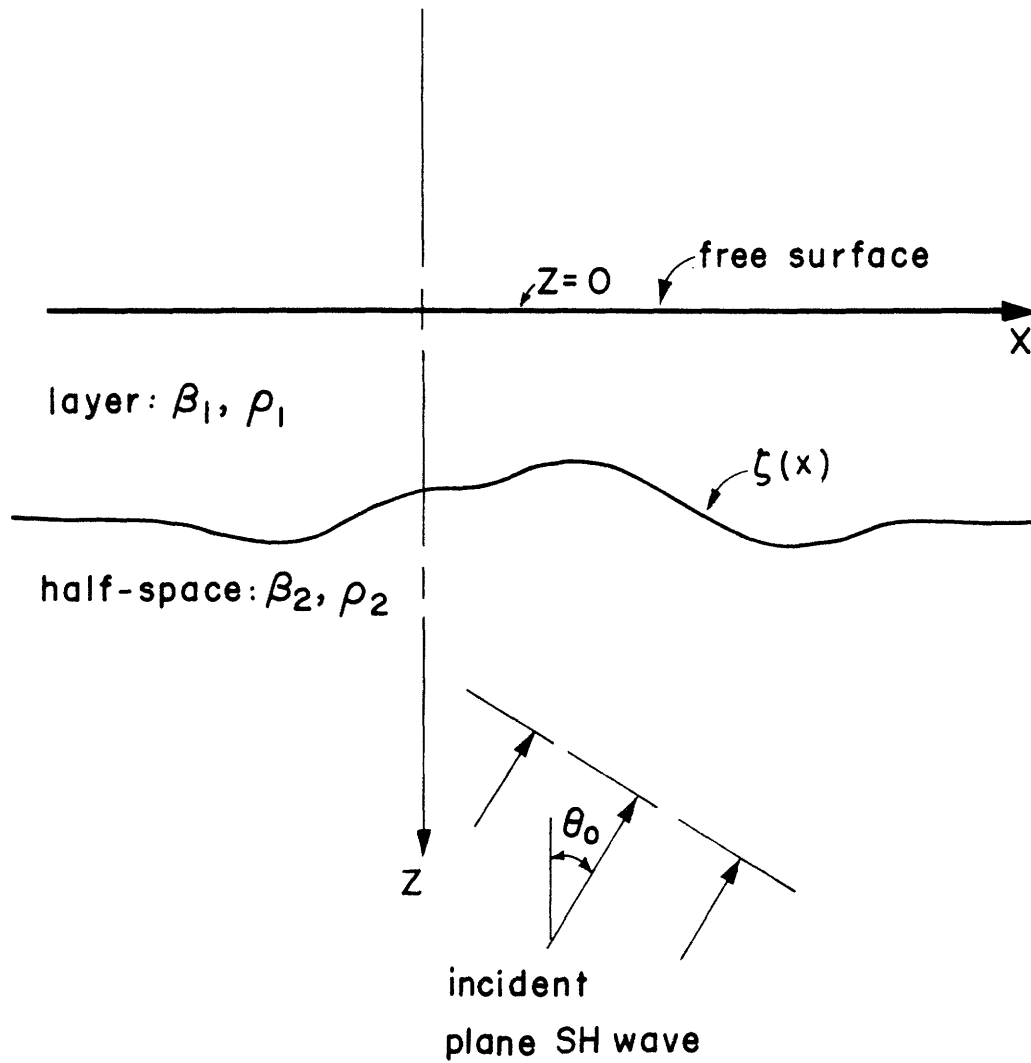


Figure 2.3. Problem configuration for plane SH wave scattering in a layer of nonuniform thickness over a half-space. The free surface is plane.

That is, no wavenumber coupling occurs at the plane free surface. Using (2.14), we eliminate the function $v_1^d(k)$ in (2.12), and write

$$\hat{v}_1(x, z) = 2 \int_{-\infty}^{\infty} v_1^u(k) \cos v_1' z e^{ikx} dk \quad (2.15)$$

As in the previous case, the wave fields are expressed in terms of the amplitudes $v_1^u(k)$ and $v_2^d(k)$ of waves leaving the irregular interface. Use of (2.3), (2.15), (2.7), and (2.8) in the interface continuity conditions (2.6) again yields the coupled integral equations (2.9) for the determination of $v_1^u(k)$ and $v_2^d(k)$. The only change from the previous case is that $f_{11}(k, x)$ and $f_{21}(k, x)$ in (2.10) are replaced by

$$\begin{aligned} f_{11}(k, x) &= 2 \cos v_1' \xi(x) \\ f_{21}(k, x) &= 2\mu_1 [k s(x) \cos v_1' \xi(x) - i v_1' \sin v_1' \xi(x)] \end{aligned} \quad (2.16)$$

The motion at the free surface is, by (2.15),

$$\hat{v}_1(x, 0) = \int_{-\infty}^{\infty} 2 v_1^u(k) e^{ikx} dk \quad (2.17)$$

which is just a Fourier synthesis over wave number.

2.2.3. Layer of non-uniform thickness over a half-space: both the free surface and interface are irregular. As shown in Figure 2.4, the configuration for this problem differs from that for the last one in that the free surface no longer is plane, but rather has the irregular shape given by $z = \xi_s(x)$. We wish to determine the response of the medium to an incoming SH wave as in the previous problems.

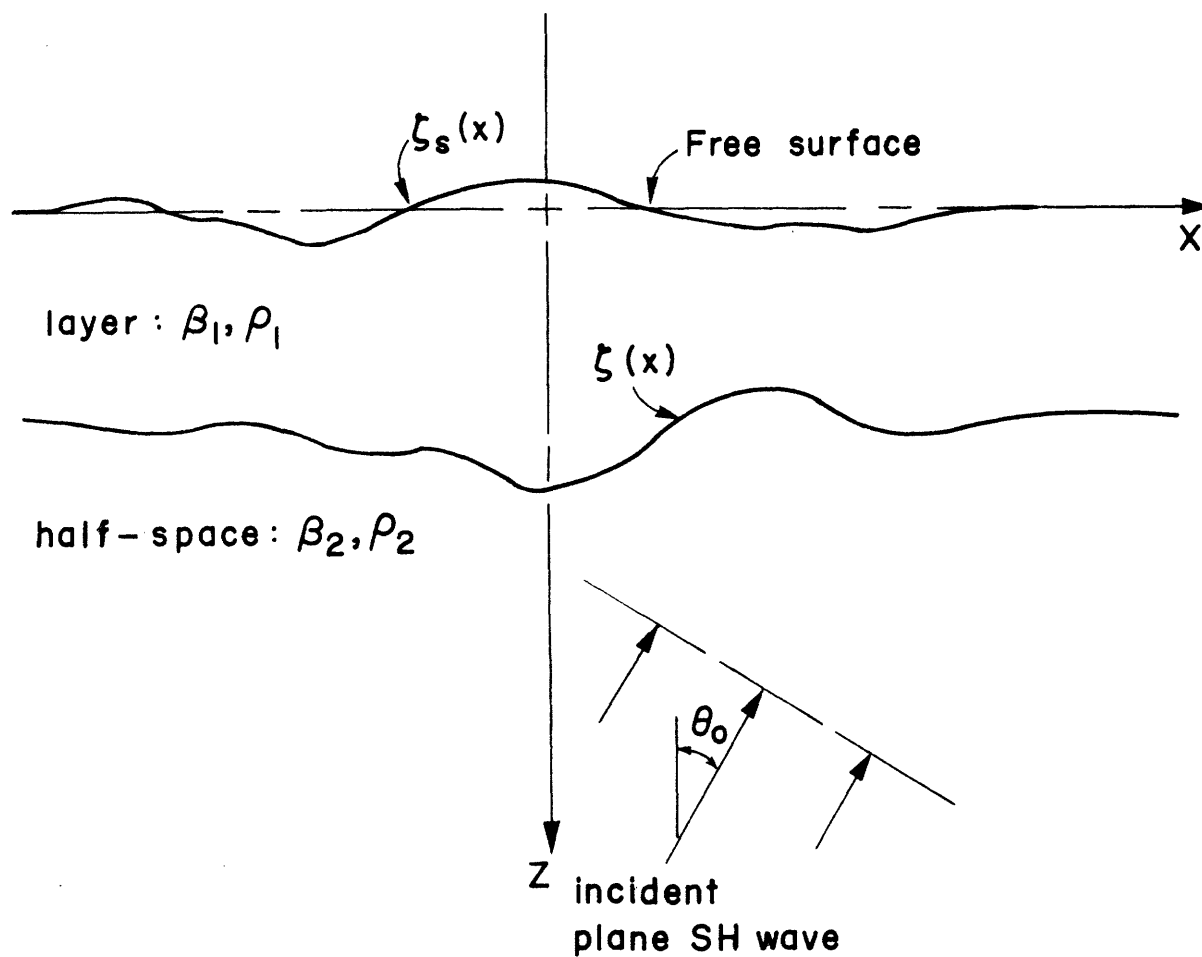


Figure 2.4. Problem configuration for plane SH wave scattering in a layer of nonuniform thickness over a half-space. Both the free surface and interface are irregular.

The approximate displacement fields in the layer and half-space are given by (2.12) and (2.3), respectively. The three wave amplitudes $v_1^d(k)$, $v_1^u(k)$, and $v_2^u(k)$ will be determined by solving three coupled integral equations. Two of the equations are provided by the interface continuity conditions (2.6) and the third arises from the vanishing stress condition at the free surface

$$\frac{\partial \hat{V}_1}{\partial n_s} = 0 \quad \text{at } z = \zeta_s(x)$$

where

$$n_s = n_{sx} \frac{\partial}{\partial x} + n_{sz} \frac{\partial}{\partial z}$$

$$n_{sx} = -S_s (1 + S_s)^{-1/2}$$

$$n_{sz} = (1 + S_s)^{-1/2}$$

and $s_s(x) = \frac{d\zeta_s(x)}{dx}$ is the slope of the free surface. Using (2.12) and (2.3) in the boundary conditions yields

$$\int_{-\infty}^{\infty} [v_1^u(k) f_{11}(k, x) + v_2^d(k) f_{12}(k, x) + v_1^d(k) f_{13}(k, x)] e^{ikx} dk = h_1(k_0, x) e^{ik_0 x}$$

$$\int_{-\infty}^{\infty} [v_1^u(k) f_{21}(k, x) + v_2^d(k) f_{22}(k, x) + v_1^d(k) f_{23}(k, x)] e^{ikx} dk = h_2(k_0, x) e^{ik_0 x} \quad (2.18)$$

$$\int_{-\infty}^{\infty} [v_1^u(k) f_{31}(k, x) + v_1^d(k) f_{33}(k, x)] e^{ikx} dk = 0$$

The functions $f_{1j}(k,x)$ and $h_j(k_0,x)$, $i, j=1,2$ are those given in (2.10) and (2.11) for the half-spaces problem. The new coefficients are

$$\begin{aligned} f_{13}(k,x) &= e^{i\gamma_1' \xi(x)} \\ f_{23}(k,x) &= \mu_1 [k s(x) - \gamma_1'] e^{i\gamma_1' \xi(x)} \\ f_{33}(k,x) &= [k s_s(x) - \gamma_1'] e^{i\gamma_1' \xi_s(x)} \\ f_{31}(k,x) &= [k s_s(x) + \gamma_1'] e^{-i\gamma_1' \xi_s(x)} \end{aligned} \quad (2.19)$$

Summarizing the results for these three SH wave problems, we found that the wave fields are expressible in terms of the complex amplitudes of waves that leave irregular interfaces and that these wave amplitudes are solutions to an equal number of coupled integral equations -- one for each boundary condition at each irregular boundary.

2.3. Elastic-Wave Motion in a Layered Medium Having One Irregular Interface.

2.3.1. Introduction. We now consider a larger, more general problem in elastic-wave scattering. As shown in Figure 2.5, the medium consists of $\tilde{n}+1$ homogeneous, isotropic solid layers. Layers \tilde{n} and 0 are half-spaces; the other layers either have uniform thicknesses and are joined at plane interfaces at constant depths $z=z_m$ or have thicknesses that vary in the x -direction only and are joined at the irregular interface $z=z_s(x)$. Each layer m is characterized by density ρ_m , longitudinal wave velocity α_m , and shear wave velocity β_m . The irregular interface s separates layers s above and $s+1$ below.

We wish to determine the displacement field response of the medium to plane P or S waves incident from depth ($z=\infty$) in the half-space \tilde{n} at the

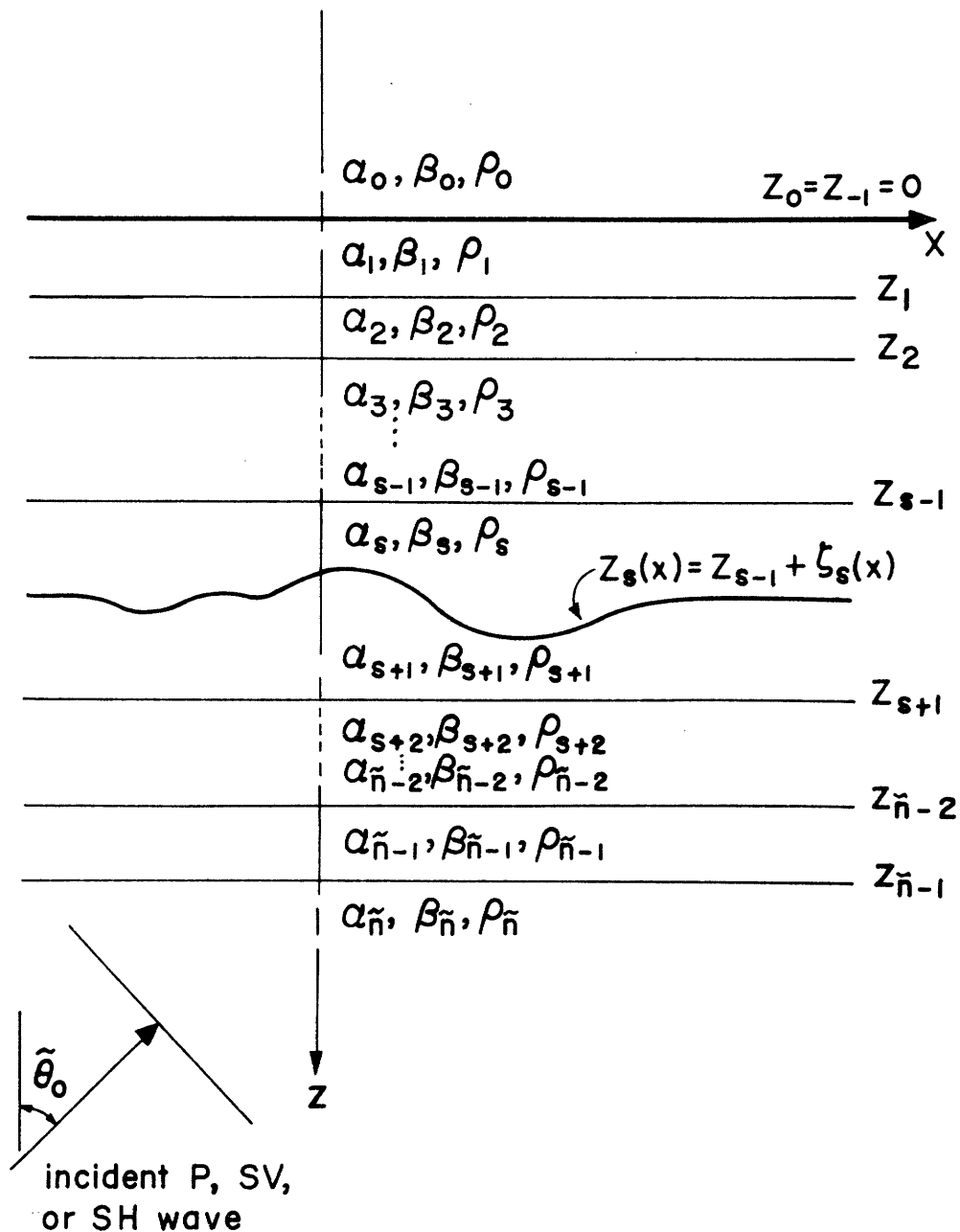


Figure 2.5. Problem configuration for plane elastic wave scattering in an $\tilde{n}+1$ layer medium having the single irregular interface s . $\tilde{\theta}_0$ is the angle between vertical and the projection of the source wave propagation vector onto the x - z plane.

angle θ_0 from vertical. In contrast to the SH-wave problems, now the source wave need not be propagating parallel to the x-z plane. That is, the source wave is incident at an arbitrary azimuthal angle relative to the strike of the interface shape.

This problem is more complicated than the previous problems for several reasons. The scattered field is now vector, consisting of coupled P, SV, and SH waves. Furthermore, the scattered waves are no longer confined to propagate parallel to the vertical plane containing the source wave propagation vector. The problem, therefore, is no longer strictly two-dimensional. However, the simplification that the irregular interface have the one-dimensional (washboard) shape allows us to develop the solution as though the problem were two-dimensional. That is, as before, the solution wave fields will be expressed as integrals over the x-component of wave number rather than as double integrals over both the x- and y-components of wavenumber.

The formulation of this problem proceeds analogously to the treatment of the SH wave problems. However, because of the greatly increased algebra accompanying the vector fields and increased number of interface continuity conditions, many details are relegated to the appendixes. We shall follow the Thomson—Haskell flat layer wave theory (Thomson, 1950; Haskell, 1953) to iteratively satisfy the continuity conditions at the plane boundaries. The solution for motion anywhere in the medium is thereby reduced to the determination of the complex amplitudes of the six waves leaving the irregular interface (P, SV, and SH waves upgoing in layer s and downgoing in layer $s+1$). This number equals the number of continuity requirements at the irregular interface, each of which provides an integral equation involving the six wave amplitudes.

After k-spectrum decomposing the wave fields (i.e., expressing the fields as superpositions of plane waves), we introduce what we call propagation coordinates. With these new coordinates as bases for expressing the spectrally decomposed motion, the solutions are in a form particularly amenable to reduction using the Thompson-Haskell technique.

The existence of plane boundaries in this problem makes the integral equations singular when the temporal frequency ω is real. The singularities are associated with trapped modes (such as Rayleigh waves, generalized Rayleigh waves, Love waves) in the plane layers. This singular behavior is considered in the approximate method of solution discussed in Chapter III.

2.3.2. Representation of the displacement and stress fields. As before, let the source wave have the simple harmonic time dependence $e^{-i\omega t}$ where the frequency ω may be complex as described in section 3.4. The Fourier transformed vector equation of motion for an isotropic elastic solid m is

$$-\rho_m \omega^2 \underline{\hat{U}}_m(\underline{r}, \omega) = (\lambda_m + 2\mu_m) \nabla(\nabla \cdot \underline{\hat{U}}_m) - \mu_m \nabla \times (\nabla \times \underline{\hat{U}}_m) \quad (2.20)$$

where $\underline{\hat{U}}_m = (\hat{u}_m, \hat{v}_m, \hat{w}_m)$ is the vector displacement with (x, y, z) components, λ_m and μ_m are the Lamé constants, and \underline{r} is the space position vector (single underbars denote vector quantities and column matrices, double underbars denote second order tensors and square matrices). Using dyadic notation (Nadeau, 1964) to economize on the use of subscripts, we write the stress tensor field $\underline{\hat{S}}_m$ in the isotropic elastic solid m in terms of the displacement field.

$$\hat{\underline{S}}_m(\underline{r}, \omega) = \lambda_m \underline{\underline{1}}_3 (\nabla \cdot \hat{\underline{U}}_m) + \mu_m (\nabla \hat{\underline{U}}_m + \hat{\underline{U}}_m \nabla) \quad (2.21)$$

where $\underline{\underline{1}}_3$ is the idemfactor or unity dyadic.

We shall represent the total displacement and stress fields, in each layer m , as superpositions of the respective fields arising from elementary plane waves. That is,

$$\hat{\underline{U}}_m(\underline{r}, \omega) = \int_{-\infty}^{\infty} \underline{U}_m(\underline{r}, \omega, k) dk \quad (2.22)$$

$$\hat{\underline{S}}_m(\underline{r}, \omega) = \int_{-\infty}^{\infty} \underline{S}_m(\underline{r}, \omega, k) dk \quad (2.23)$$

where the wave number k is the x -component of the propagation vectors associated with upgoing and downgoing P and S waves. The k -spectrum decomposed fields \underline{U}_m are derived from displacement potentials by means of the Helmholtz theorem

$$\underline{U}_m(\underline{r}, \omega, k) = \nabla \tilde{\phi}_m(\underline{r}, \omega, k) - \nabla \times (\underline{B}_m + \nabla \times \underline{C}_m) \quad (2.24)$$

where

$$\begin{aligned} \underline{B}_m(\underline{r}, \omega, k) &= (0, 0, \tilde{\chi}_m(\underline{r}, \omega, k)) \\ \underline{C}_m(\underline{r}, \omega, k) &= (0, 0, \tilde{\psi}_m(\underline{r}, \omega, k)) \end{aligned} \quad (2.25)$$

The scalar displacement potentials $\tilde{\Phi}_m$, $\tilde{\Psi}_m$, and $\tilde{\chi}_m$ satisfy the scalar wave equations

$$\begin{aligned} (\nabla^2 + k_{\alpha_m}^2) \tilde{\Phi}_m &= 0 \\ (\nabla^2 + k_{\beta_m}^2) \tilde{\Psi}_m &= 0 \\ (\nabla^2 + k_{\beta_m}^2) \tilde{\chi}_m &= 0 \end{aligned} \quad (2.26)$$

where the following notation is used

$$k_{\alpha_m} = \omega / \alpha_m ; \text{ longitudinal wave number}$$

$$k_{\beta_m} = \omega / \beta_m ; \text{ shear wave number}$$

The potentials $\tilde{\Phi}_m$, $\tilde{\Psi}_m$, and $\tilde{\chi}_m$ are k-spectrum decomposed quantities; that is, they are potentials for plane wave motion which may be written as

$$\begin{aligned} \tilde{\Phi}_m(\underline{r}, \omega, k) &= \phi_m(k, z) e^{ikx + i\eta_0 y} \\ \tilde{\Psi}_m(\underline{r}, \omega, k) &= \bar{\Psi}_m(k, z) e^{ikx + i\eta_0 y} \\ \tilde{\chi}_m(\underline{r}, \omega, k) &= \chi_m(k, z) e^{ikx + i\eta_0 y} \end{aligned} \quad (2.27)$$

where η_0 is the y-component of wave number associated with the source wave. Before proceeding, we must justify the spectral decomposition of the fields into waves having different x-components of wave number k but having just the single y-component of wave number η_0 .

The usual procedure in the solution of problems involving plane parallel boundaries (Harkrider, 1964) or vertically inhomogeneous media (Saito, 1968) is to first Fourier transform the problem on not only the time variable but

also the x and y coordinates. In those cases, for plane wave source problems, the boundary conditions at the interfaces could be satisfied for all values of x and y only if the x and y dependences of the fields in all layers were the same as that of the source wave. That is, the fields would consist of upgoing and downgoing waves having the same x and y components of wave number as those of the source wave. Moreover, the P-SV and the SH wave motions would be uncoupled.

In general, when one or more of the interfaces has an irregular shape, all types of wave motion (P, SV, and SH) are coupled. When the depth of the interface is an arbitrary function of both x and y, we must expect the scattered field to consist of waves that propagate in all directions. In that case, we would represent the fields as superpositions of waves having all x-components of wavenumber k and all y-components of wavenumber η . However, because the interface shapes that we consider are one-dimensional (independent of y), the boundary conditions can be satisfied for all y only if the scattered waves all have the same y component of wave number η_0 as that of the source wave. Essentially, we have Fourier transformed on the y dependence of the problems.

Because of the inherent error associated with the Rayleigh type formulation (section 2.2.1), the representations (2.22) and (2.23) as superpositions of plane waves cannot be complete near the irregular interface. For depths between the minimum and maximum depth of the irregular interface, (2.22) and (2.23) could be complete descriptions of the fields only if in (2.27) $\Phi_m(k, z)$, $\bar{\Psi}_m(k, z)$, and $\chi_m(k, z)$ had the form

$$a(z) e^{\pm i\gamma z}$$

where a is a non-constant function of z and ν is a vertical component of wave number. However, our plane wave representation imposes the restriction that a be constant, independent of z .

Consider, now, a source wave incoming from depth in the half-space \tilde{n} and having the form $e^{i(k_0 x + \eta_0 y - \nu_0 z)}$ where k_0 , η_0 , and ν_0 are the x , y , and z components of wave number, respectively. That is, the source propagation vector \mathcal{K}_c has (x, y, z) components given by

$$\begin{aligned} k_0 &= \mathcal{K}_c \sin \theta_0 \cos \Omega_0 = \mathcal{K}_0 \cos \Omega_0 \\ \eta_0 &= \mathcal{K}_c \sin \theta_0 \sin \Omega_0 = \mathcal{K}_0 \sin \Omega_0 \\ \nu_0^2 &= \mathcal{K}_c^2 - \mathcal{K}_0^2 \end{aligned} \quad (2.28)$$

where

$$\mathcal{K}_c = \begin{cases} k_{\alpha \tilde{n}} & \text{for P wave} \\ k_{\beta \tilde{n}} & \text{for S wave} \end{cases}$$

θ_0 is the angle of incidence; the acute angle between vertical and the direction of propagation,

Ω_0 is the azimuth angle, measured from the positive x -direction to the positive y -direction

$\mathcal{K}_0 = \mathcal{K}_c \sin \theta_0$ is the horizontal component of wave number.

These quantities are shown in Figure 2.6.

Since all the scattered waves propagate with the same y -component of phase velocity, then associated with each value k in (2.22) or (2.23) is a horizontal component of wavenumber \mathcal{K} and an azimuth angle Ω given by

$$\begin{aligned} \mathcal{K} &= (k^2 + \eta_0^2)^{1/2} \\ k &= \mathcal{K} \cos \Omega \end{aligned} \quad (2.29)$$

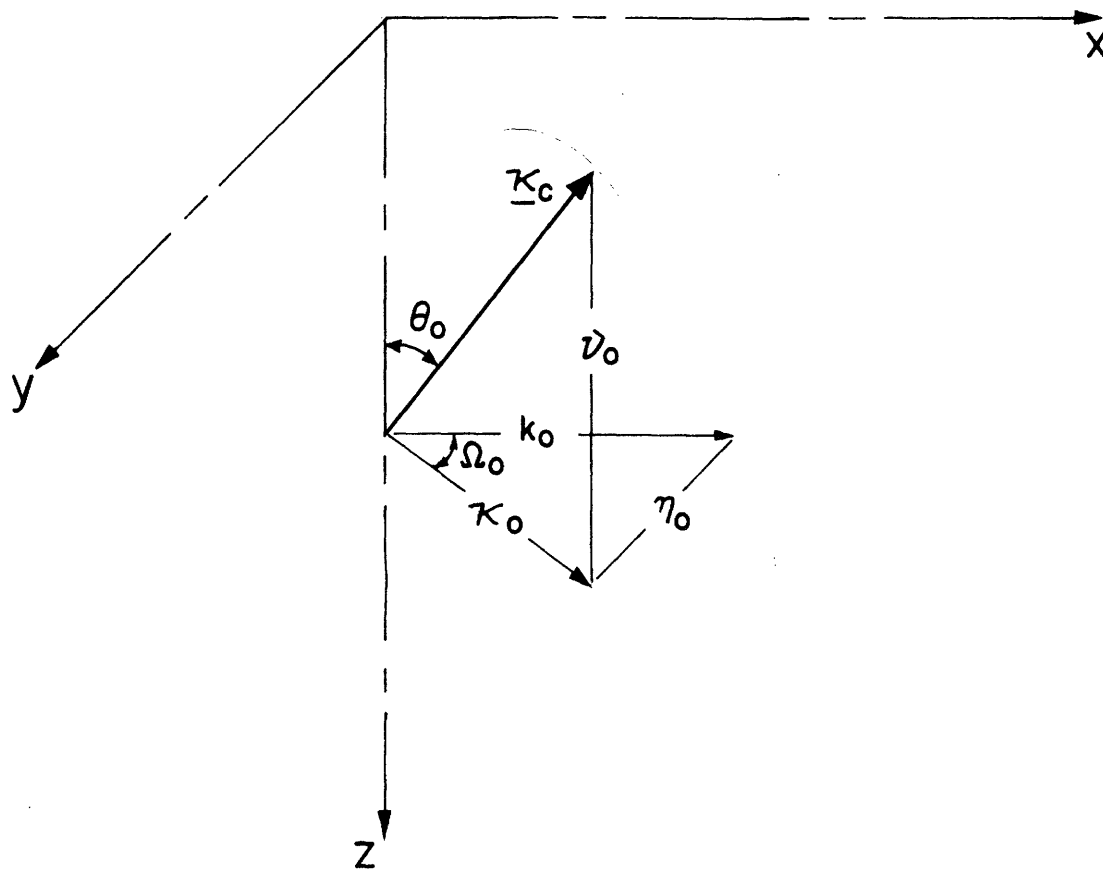


Figure 2.6. Schematic representation of the terms associated with the source wave propagation vector.

The angle Ω is the angle by which we must rotate the x-z plane about the z-axis to bring it into coincidence with the vertical plane that contains the propagation vectors associated with k . Let us call this plane the propagation plane, and define a new rectangular Cartesian coordinate system (x', y', z') with unit basis vectors \underline{e}'_x , \underline{e}'_y , and \underline{e}'_z ; where $\underline{e}'_z = \underline{e}_z$, \underline{e}'_x is parallel to the horizontal component of the propagation vector, and $\underline{e}'_y = \underline{e}'_z \times \underline{e}'_x$. The propagation plane, the propagation coordinates (x', y', z') , and the defining azimuth angle Ω are all functions of k .

Let primed vectors and tensors denote vectors and tensors whose elements are expressed in terms of propagation coordinate bases. For example, the space position vector is

$$\underline{r}' = \underline{\underline{R}}_k \cdot \underline{r} \quad (2.30)$$

where

$$\underline{r}' = \begin{pmatrix} x' \\ y' \\ z' \end{pmatrix} ; \quad \underline{r} = \begin{pmatrix} x \\ y \\ z \end{pmatrix}$$

and

$$\underline{\underline{R}}_k = \begin{pmatrix} \cos \Omega & \sin \Omega & 0 \\ -\sin \Omega & \cos \Omega & 0 \\ 0 & 0 & 1 \end{pmatrix} \quad (2.31)$$

is the rotation tensor (dyadic) for rotating the (x, y, z) standard coordinate system into a given propagation coordinate system.

In using the Thomson--Haskell technique to exactly satisfy the boundary conditions at the plane boundaries, it is advantageous to express the elements of the spectrally decomposed displacements \underline{U}_m and stresses \underline{S}_m in terms of the propagation coordinate bases (in the flat layer theory,

the P-SV and SH wave motions are uncoupled in the appropriate propagation plane). The new bases provide frameworks for convenient definitions of the wave amplitudes (equations (2.37)) used in our solutions.

Equations (2.22) and (2.23) become

$$\hat{\underline{U}}_m(\underline{r}, \omega) = \int_{-\infty}^{\infty} \underline{\underline{R}}_k^T \cdot \underline{U}'_m dk \quad (2.32)$$

$$\hat{\underline{S}}_m(\underline{r}, \omega) = \int_{-\infty}^{\infty} \underline{\underline{R}}_k^T \cdot \underline{S}'_m \cdot \underline{\underline{R}}_k dk \quad (2.33)$$

Here we have used the unitary property for the rotation dyadic, $\underline{\underline{R}}_k^T \cdot \underline{\underline{R}}_k = \underline{\underline{1}}_3$ where $\underline{\underline{R}}_k^T$ is the transpose of $\underline{\underline{R}}_k$.

The six continuity conditions at the interface are

$$\left. \begin{aligned} \hat{\underline{U}}_s(\underline{r}_s, \omega) &= \hat{\underline{U}}_{s+1}(\underline{r}_s, \omega) \\ \hat{\underline{T}}_s(\underline{r}_s, \omega) &= \hat{\underline{T}}_{s+1}(\underline{r}_s, \omega) \end{aligned} \right\} \begin{aligned} \text{at } z &= z_s(x) \\ &= z_{s-1} + \xi_s(x) \end{aligned} \quad (2.34)$$

where $\hat{\underline{T}}_s(\underline{r}_s, \omega)$ and $\hat{\underline{T}}_{s+1}(\underline{r}_s, \omega)$ are the stress vectors acting on the interface. They are given by

$$\hat{\underline{T}}_s(\underline{r}_s, \omega) = \hat{\underline{S}}_s(\underline{r}_s, \omega) \cdot \underline{n}_s = \int_{-\infty}^{\infty} \underline{\underline{R}}_k^T \cdot \underline{S}'_s \cdot \underline{\underline{R}}_k \cdot \underline{n}_s dk \quad (2.35)$$

$$\hat{\underline{T}}_{s+1}(\underline{r}_s, \omega) = \hat{\underline{S}}_{s+1}(\underline{r}_s, \omega) \cdot \underline{n}_s$$

where

$$\underline{n}_s = \begin{pmatrix} -\sin Y \\ 0 \\ \cos Y \end{pmatrix} \quad (2.36)$$

is the unit normal to the interface at $\underline{r}_s = (x, y, z_s(x))$, and Y is the dip angle at the irregular interface, i.e., $\tan Y = \frac{dz_s(x)}{dx}$. The configuration is shown in Figure 2.7.

2.3.3. Reduction to integral equations. We now develop the boundary condition integral equations by obtaining explicit expressions for \hat{u}_s , \hat{u}_{s+1} , \hat{T}_s , and \hat{T}_{s+1} at interface s . First note that the exponents in equations (2.27) may be written as

$$kx + \eta_0 y = \kappa (x \cos \Omega + y \sin \Omega) = \kappa x'$$

Thus, the wave potentials $\tilde{\Phi}_m$, $\tilde{\Psi}_m$, and $\tilde{\chi}_m$ are independent of the y' coordinate and, by (2.24) and (2.25), the components of displacement in the propagation coordinates are

$$\begin{aligned} u'_m(\underline{r}, \omega, k) &= \frac{\partial \tilde{\Phi}_m}{\partial x'} - \frac{\partial}{\partial z'} \left(\frac{\partial \tilde{\Psi}_m}{\partial x'} \right) = \frac{\partial \tilde{\Phi}_m}{\partial x'} - \frac{\partial \tilde{\Psi}_m}{\partial z'} \\ v'_m(\underline{r}, \omega, k) &= \frac{\partial \tilde{\chi}_m}{\partial x'} \\ w'_m(\underline{r}, \omega, k) &= \frac{\partial \tilde{\Phi}_m}{\partial z'} + \frac{\partial}{\partial x'} \left(\frac{\partial \tilde{\Psi}_m}{\partial x'} \right) = \frac{\partial \tilde{\Phi}_m}{\partial z'} + \frac{\partial \tilde{\Psi}_m}{\partial x'} \end{aligned} \quad (2.37)$$

where

$$\tilde{\Psi}_m = \frac{\partial \tilde{\chi}_m}{\partial x'}$$

By using the propagation coordinate system together with the particular form (2.24) of the Helmholtz theorem, we see that the u'_m and w'_m motions in the propagation plane are derivable from only two potentials, $\tilde{\Phi}_m$ and $\tilde{\Psi}_m$.

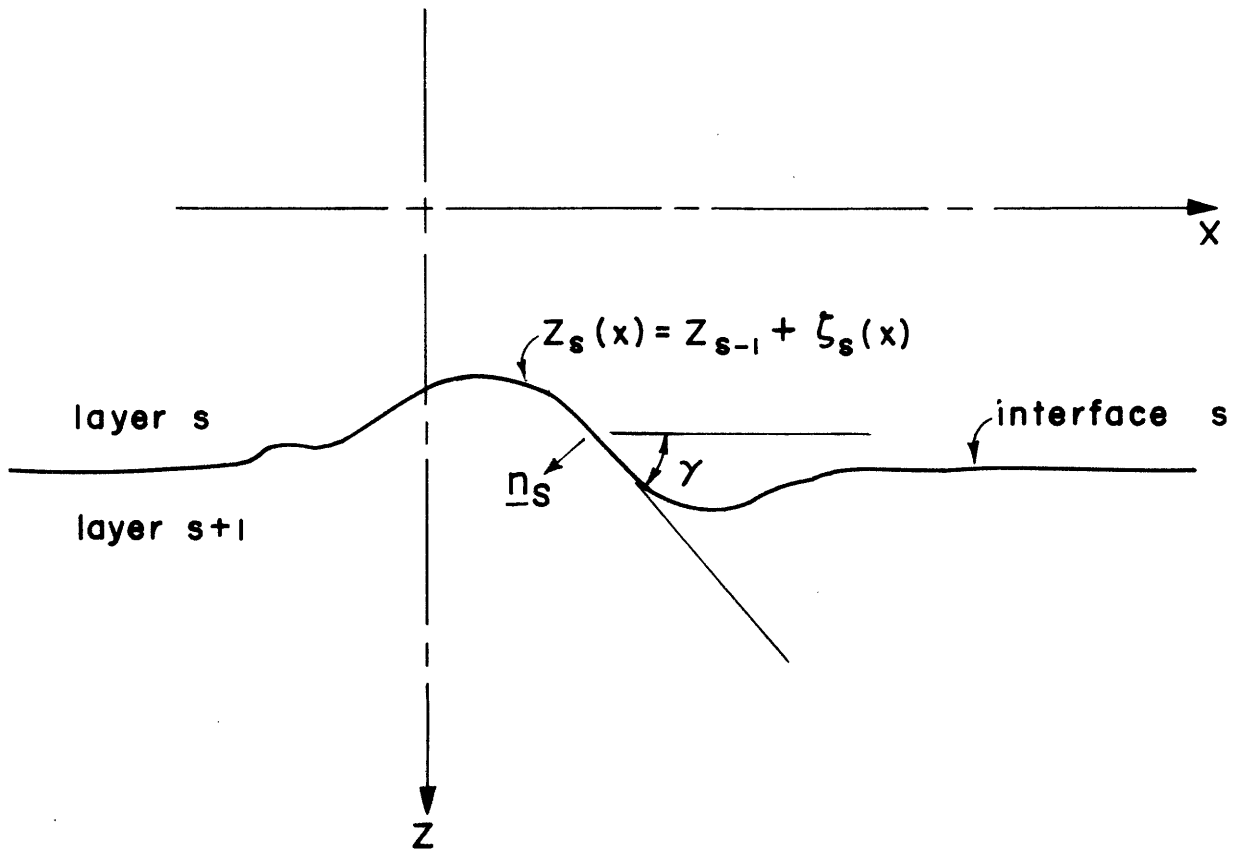


Figure 2.7. The dip angle $\gamma(x)$ and the unit normal vector \underline{n}_s at the irregular interface s.

the P and SV wave potentials respectively. The horizontal motion v'_m normal to the propagation plane (SH motion) is itself a solution of the scalar wave equation; that is,

$$(\nabla^2 + k_{\beta_m}^2) v'_m = 0 \quad (2.38)$$

We now introduce explicit forms for the plane wave expressions that we have assumed for the potentials. In each layer m , we let

$$\begin{aligned} \tilde{\Phi}_m(\underline{r}, \omega, k) &= [\phi_m^d(\kappa) e^{i\gamma_m(z-z_{m-1})} + \phi_m^u(\kappa) e^{-i\gamma_m(z-z_{m-1})}] e^{i(kx+\eta_0 y)} \\ \tilde{\Psi}_m(\underline{r}, \omega, k) &= [\psi_m^d(\kappa) e^{i\gamma'_m(z-z_{m-1})} + \psi_m^u(\kappa) e^{-i\gamma'_m(z-z_{m-1})}] e^{i(kx+\eta_0 y)} \\ \tilde{V}'_m(\underline{r}, \omega, k) &= [v_m^d(\kappa) e^{i\gamma'_m(z-z_{m-1})} + v_m^u(\kappa) e^{-i\gamma'_m(z-z_{m-1})}] e^{i(kx+\eta_0 y)} \end{aligned} \quad (2.39)$$

where γ_m and γ'_m are the vertical components of wave number, defined as

$$\begin{aligned} \gamma_m &= (k_{\alpha_m}^2 - \kappa^2)^{1/2} \\ \gamma'_m &= (k_{\beta_m}^2 - \kappa^2)^{1/2} \end{aligned} \quad m=0,1,\dots,n \quad (2.40)$$

The ambiguity in the definitions of the signs of the radicals is removed by choosing the top sheet of the complex k -plane appropriate to our choice of complex frequency

$$0 \leq \arg(\omega) < \pi/2$$

as discussed in section 3.4.4. By so defining γ_m and γ'_m , the coefficients $\phi_m^d(\kappa)$, $\psi_m^d(\kappa)$, and $v_m^d(\kappa)$ are the complex amplitudes of downgoing P, SV, and SH waves respectively; likewise, $\phi_m^u(\kappa)$, $\psi_m^u(\kappa)$, and $v_m^u(\kappa)$ are the complex amplitudes of upgoing waves. For the problems posed here,

$$\begin{aligned}
\phi_{\tilde{n}}^u(\kappa) &= \phi^* = \epsilon_p \delta(k-k_0) \\
\psi_{\tilde{n}}^u(\kappa) &= \psi^* = \epsilon_v \delta(k-k_0) \\
v_{\tilde{n}}^u(\kappa) &= v^* = \epsilon_h \delta(k-k_0)
\end{aligned}
\tag{2.41}$$

are given amplitudes of the plane source waves in the half-space \tilde{n} . (Stars denote source terms here). $\delta(x)$ is the Dirac delta function. Its use is justified here because the quantities (2.41) always appear within integrands in integrals such as (2.32) and (2.33). In (2.41).

$$\begin{aligned}
\text{for a P wave source:} & \quad \epsilon_p=1, & \epsilon_v = \epsilon_h=0 \\
\text{for an SV wave source:} & \quad \epsilon_v=1, & \epsilon_p = \epsilon_h=0 \\
\text{for an SH wave source:} & \quad \epsilon_h=1, & \epsilon_p = \epsilon_v=0
\end{aligned}
\tag{2.42}$$

Also, as no waves are incoming from $z=-\infty$ in the upper half-space, we require

$$\phi_o^d = \psi_o^d = v_o^d = 0
\tag{2.43}$$

In (2.39), the z_{m-1} may be any constants, but we choose them such that each z_{m-1} is the depth to the upper boundary of layer m for all layers with the exception of layer $s=1$ and half-space 0 (see Figure 2.5). For $m=0$, we set $z_{m-1}=z_{s-1}$. These choices are for convenience in the use of the flat-layer theory in Appendix A.

Using the potentials defined by (2.39) in (2.37), we can write the k -spectrum decomposed components of displacement and stress in the propagation coordinate bases. Henceforth, we suppress the common factor $e^{i(kx+\eta_0 y)}$ by supposing that all quantities are evaluated at $x=0$, $y=0$. The displacements are

$$\begin{aligned}
u'_m &= i\kappa e^{i\rho_m} \phi_m^d - i\gamma'_m e^{i\rho_m} \psi_m^d + i\kappa e^{-i\rho_m} \phi_m^u + i\gamma'_m e^{-i\rho_m} \psi_m^u \\
w'_m &= i\gamma'_m e^{i\rho_m} \phi_m^d + i\kappa e^{i\rho_m} \psi_m^d - i\gamma'_m e^{-i\rho_m} \phi_m^u + i\kappa e^{-i\rho_m} \psi_m^u \\
v'_m &= e^{i\rho_m} V_m^d + e^{-i\rho_m} V_m^u
\end{aligned} \tag{2.44}$$

where $p_m \equiv \gamma'_m(z-z_{m-1})$ and $q_m \equiv \gamma'_m(z-z_{m-1})$.

The components of stress acting on a plane $z=\text{constant}$ are

$$\begin{aligned}
S_{z\bar{z}}^{(m)}/\mu_m &= f_m e^{i\rho_m} \phi_m^d - 2\kappa\gamma'_m e^{i\rho_m} \psi_m^d + f_m e^{-i\rho_m} \phi_m^u + 2\kappa\gamma'_m e^{-i\rho_m} \psi_m^u \\
S_{x\bar{x}}^{(m)}/\mu_m &= -2\kappa\gamma'_m e^{i\rho_m} \phi_m^d - f_m e^{i\rho_m} \psi_m^d + 2\kappa\gamma'_m e^{-i\rho_m} \phi_m^u - f_m e^{-i\rho_m} \psi_m^u \\
S_{y\bar{y}}^{(m)}/\mu_m &= i\gamma'_m e^{i\rho_m} V_m^d - i\gamma'_m e^{-i\rho_m} V_m^u
\end{aligned} \tag{2.45}$$

where $f_m \equiv 2\kappa^2 - k_{\beta_m}^2$.

The three other independent components of stress are

$$\begin{aligned}
S_{x\bar{y}}^{(m)}/\mu_m &= (2k_{\alpha_m}^2 - k_{\beta_m}^2 - 2\kappa^2) e^{i\rho_m} \phi_m^d + 2\kappa\gamma'_m e^{i\rho_m} \psi_m^d \\
&\quad + (2k_{\alpha_m}^2 - k_{\beta_m}^2 - 2\kappa^2) e^{-i\rho_m} \phi_m^u - 2\kappa\gamma'_m e^{-i\rho_m} \psi_m^u \\
S_{x'y'}^{(m)}/\mu_m &= i\kappa e^{i\rho_m} V_m^d + i\kappa e^{-i\rho_m} V_m^u \\
S_{y\bar{y}}^{(m)}/\mu_m &= (2k_{\alpha_m}^2 - k_{\beta_m}^2) e^{i\rho_m} \phi_m^d + (2k_{\alpha_m}^2 - k_{\beta_m}^2) e^{-i\rho_m} \phi_m^u
\end{aligned} \tag{2.46}$$

We may write (2.44) and (2.45) as the two uncoupled matrix equations

$$\underline{M}_m(\kappa, z) = \underline{E}_m(\kappa, z) \underline{\mathcal{O}}_m(\kappa) \tag{2.47}$$

and

$$\underline{m}_m(\kappa, z) = \underline{E}_m(\kappa, z) \underline{d}_m(\kappa)$$

where \underline{M}_m is the motion-stress vector for P-SV motion and \underline{m}_m is the motion-stress vector for SH motion. That is,

$$\underline{M}_m(\kappa, z) = \begin{pmatrix} u'_m \\ w'_m \\ S_{z'z'}^{(m)} \\ S_{x'z'}^{(m)} \end{pmatrix} ; \quad \underline{m}_m(\kappa, z) = \begin{pmatrix} v'_m \\ S_{y'z'}^{(m)} \end{pmatrix} \quad (2.48)$$

\underline{D}_m and \underline{d}_m are wave amplitude vectors.

$$\underline{D}_m(\kappa) = \begin{pmatrix} \phi_m^d \\ \psi_m^d \\ \phi_m^u \\ \psi_m^u \end{pmatrix} ; \quad \underline{d}_m(\kappa) = \begin{pmatrix} v_m^d \\ v_m^u \end{pmatrix} \quad (2.49)$$

The 4×4 matrix \underline{E}_m and the 2×2 matrix \underline{e}_m are counterparts of the E_m matrices of Haskell(1953), differing in that he uses $e^{i\omega t}$ time dependence and defines his motion-stress and wave amplitude vectors differently. The elements of \underline{E}_m and \underline{e}_m may be written directly from (2.44) and (2.45) and are given, for reference, in Appendix A.

In Appendix A, we use the Thomson—Haskell theory to express the incoming waves at the irregular interface ($\phi_s^d, \psi_s^d, v_s^d, \phi_{s+1}^u, \psi_{s+1}^u$, and v_{s+1}^u) in terms of the outgoing wave amplitudes plus source terms. The procedure is analogous to our use of the vanishing stress condition at the plane free surface to eliminate the wave amplitude v_1^d in the SH wave problem discussed in section 2.2.2. The pertinent results from Appendix A (equations (A17) and (A26)) are repeated here

$$\begin{aligned}
\phi_{s+1}^u &= A_1 \delta(k-k_0) + B_1 \phi_{s+1}^d + C_2 \psi_{s+1}^d \\
\psi_{s+1}^u &= A_2 \delta(k-k_0) + C_1 \phi_{s+1}^d + B_2 \psi_{s+1}^d \\
V_{s+1}^u &= A_3 \delta(k-k_0) + B_3 V_{s+1}^d
\end{aligned} \tag{2.50}$$

and

$$\begin{aligned}
\phi_s^d &= \bar{B}_1 \phi_s^u + \bar{C}_2 \psi_s^u \\
\psi_s^d &= \bar{C}_1 \phi_s^u + \bar{B}_2 \psi_s^u \\
V_s^d &= \bar{B}_3 V_s^u
\end{aligned} \tag{2.51}$$

where all quantities in these equations are functions of \mathcal{K} (or k). The terms involving A_1 , A_2 , and A_3 are source terms effectively carried up from half-space \tilde{n} through layer $s+1$. The coefficients $A_1, A_2, \dots, \bar{C}_1, \bar{C}_2$ are given explicitly in Appendix A in terms of the elements of matrices that are products of layer matrices. For the multi-layered medium with one irregular interface, the appropriate expressions are (A18) and (A27) with ϕ^* , ψ^* , and V^* given by (2.41).

Now consider the displacement and stress fields in layers s and $s+1$ at the irregular interface. Details of what follows are given in Appendix C. Inserting (2.50) and (2.52) into (2.44), (2.45), and (2.46) enables us to write the components of $\underline{U}'_s(\underline{r}_s, \omega, k)$ and $\underline{S}'_s(\underline{r}_s, \omega, k)$ as linear combinations of ϕ_s^u , ψ_s^u , and V_s^u , and to write the components of $\underline{U}'_{s+1}(\underline{r}_s, \omega, k)$ and $\underline{S}'_{s+1}(\underline{r}_s, \omega, k)$ as linear combinations of ϕ_{s+1}^d , ψ_{s+1}^d , and V_{s+1}^d , plus the three source terms $A_j \delta(k - k_0)$, $j=1,2,3$. Applying the tensor transformations indicated in (2.32) and (2.33), we express the components of $\underline{U}_s(\underline{r}_s, \omega, k)$, $\underline{S}_s(\underline{r}_s, \omega, k)$, $\underline{U}_{s+1}(\underline{r}_s, \omega, k)$ and $\underline{S}_{s+1}(\underline{r}_s, \omega, k)$ (elements

given in the standard coordinate system basis) also as linear combinations of the waves leaving the interface plus the source terms. Finally, we postmultiply the stress tensors $\underline{S}_s(\underline{r}_s, \omega, k)$ and $\underline{S}_{s+1}(\underline{r}_s, \omega, k)$ by \underline{n}_s as indicated in (2.35).

Putting these expressions into integrals (2.32) and (2.35) and, in turn, using the integrals in boundary conditions (2.34), we obtain the following matrix integral equation

$$\int_{-\infty}^{\infty} \underline{F}(\kappa, x) \cdot \underline{C}_s(\kappa) e^{ikx} dk = \underline{N}(\kappa_0, x) e^{ik_0 x} \quad (2.52)$$

where \underline{F} is a 6x6 matrix whose elements $f_{ij}(\kappa, x)$ are written in equation (C18) of appendix C. $\underline{C}_s(\kappa)$ is a 6x1 matrix of the unknown wave amplitudes

$$\underline{C}_s(\kappa) = \begin{pmatrix} \phi_s^u \\ \phi_{s+1}^d \\ \psi_s^u \\ \psi_{s+1}^d \\ v_s^u \\ v_{s+1}^d \end{pmatrix} \quad (2.53)$$

and \underline{N} is a 6x1 matrix of source terms whose elements h_i , $i=1, \dots, 6$ are given (C17). The six equations implied by (2.52) express, respectively, continuity of the

x-component of the displacement vector,

z-component of the displacement vector,

z-component of the stress vector acting on interface s ,

x-component of the stress vector acting on interface s ,

y-component of the displacement vector, and

y-component of the stress vector acting on interface s .

In deriving (2.52), the source terms were brought to the right side after using the sifting property of the Dirac delta function.

Integral equation (2.52) is a generalized form of the integral equations (2.9) and (2.18) obtained in the SH wave motion examples. By solving (2.52) for $\underline{C}_s(\underline{\kappa})$, we can determine the wave field in any part of the medium as follows. Having determined the amplitudes of the waves leaving interface s , we first compute the amplitudes of the waves approaching interface s using (A17) and (A26). We can then use the wave amplitude vectors $\underline{\mathcal{L}}_s$, \underline{d}_s , $\underline{\mathcal{L}}_{s+1}$, and \underline{d}_{s+1} in the flat-layer theory (equations (A3) through (A8)) to determine the wave amplitudes and motion-stress vectors in any other layer p . Finally, the total displacement and stress fields are determined by the integrals (2.22) and (2.23).

2.3.4. Properties of the integral equations. The coefficient matrix $\underline{\mathcal{F}}(\underline{\kappa}, x)$ and source vector $\underline{H}(\underline{\kappa}_0, x)$ depend on x only through $\zeta_s(x)$ and $\frac{d\zeta_s}{dx}$, i.e., through the irregularity of the interface shape. If the interface were plane with $\zeta_s = \text{constant}$, then (2.52) could be solved trivially by first writing it as

$$\int_{-\infty}^{\infty} [\underline{\mathcal{F}}(\underline{\kappa}) \cdot \underline{C}_s(\underline{\kappa}) - \underline{H}(\underline{\kappa}_0) \delta(k - k_0)] e^{ikx} dk = 0$$

Since this equation must hold for any x , the quantity in brackets must vanish identically. The wave amplitude vector $\underline{C}_s(\underline{\kappa})$ would thus satisfy

$$\underline{\mathcal{F}}(\underline{\kappa}_0) \cdot \underline{C}_s(\underline{\kappa}_0) = \underline{H}(\underline{\kappa}_0) \delta(k - k_0)$$

$$\underline{C}_s(\underline{\kappa}) = 0 ; \quad \underline{\kappa} \neq \underline{\kappa}_0$$

and all waves would have the source horizontal wave number $\mathcal{K}_0 = (k_0^2 + \eta_0^2)^{1/2}$

In that case, for convenience, we might align the standard coordinate (x,y,z) axes with the propagation coordinate axes. Then $\Omega_0 = 0$; also

$Y = \tan^{-1} \left(\frac{d\mathcal{K}_0}{dx} \right) = 0$. According to (C18) the $\underline{\underline{J}}$ matrix would have the form

$$\underline{\underline{J}} = \begin{pmatrix} f_{11} & f_{12} & f_{13} & f_{14} & 0 & 0 \\ f_{21} & f_{22} & f_{23} & f_{24} & 0 & 0 \\ f_{31} & f_{32} & f_{33} & f_{34} & 0 & 0 \\ f_{41} & f_{42} & f_{43} & f_{44} & 0 & 0 \\ 0 & 0 & 0 & 0 & f_{55} & f_{56} \\ 0 & 0 & 0 & 0 & f_{65} & f_{66} \end{pmatrix} \quad (2.54)$$

Also, by (C17) and (A18), $\underline{\underline{H}}$ would be such that $h_i(\mathcal{K}_0)$, $i=1,2,3,4$ depend only on the P and SV source potentials ϕ^* and ψ^* , and $h_5(\mathcal{K}_0)$ and $h_6(\mathcal{K}_0)$ depend only on the SH source displacement v^* . Thus, the solution would reduce to the familiar result that, for a flat-layered medium, the P-SV wave motion and the SH wave motion are uncoupled. Of course, the solution would be exact in that case.

As a second special case, consider an irregular interface problem involving an incident plane wave propagating parallel to the x-z plane. The azimuth angle associated with the propagation vector of the incident wave is $\Omega_0 = 0$. In this case, the y-component of wave number is $\eta_0 = 0$ for all scattered waves; thus all waves propagate parallel to the x-z plane. Then $\mathcal{K} = k$ and in (C17) and (C18), we set $\Omega = \Omega_0 = 0$. The resulting $\underline{\underline{J}}$ matrix again has the form (2.54). The source vector is (see equation (C17))

$$\underline{H}(\mathcal{K}_0, x) = \begin{pmatrix} u'^{\star} \\ w'^{\star} \\ -S_{x'z'}^{\star} \sin Y + S_{z'z'}^{\star} \cos Y \\ -S_{x'y'}^{\star} \sin Y + S_{y'z'}^{\star} \cos Y \\ v'^{\star} \\ -S_{x'y'}^{\star} \sin Y + S_{y'z'}^{\star} \cos Y \end{pmatrix}$$

By (C7) and (A18), we see that again $h_i(\mathcal{K}_0, x)$, $i=1,2,3,4$ depend only on the P and SV source potentials, and $h_5(\mathcal{K}_0, x)$ and $h_6(\mathcal{K}_0, x)$ depend only on the SH source displacement. Thus, for problems involving plane source waves propagating normal to the strike of the irregular interface, the P-SV and SH wave problems can be considered separately. Many of the examples presented in Chapter V involve these more simple problems of wave propagation parallel to the x-z plane.

Finally, as discussed in Appendix B, if the medium contains plane boundaries, some elements $f_{ij}(\mathcal{K}, x)$ of matrix $\underline{F}(\mathcal{K}, x)$ in (2.52) can be singular for certain values of k on the top sheet of the k -plane. If the integration path in (2.52) intersects any of these special values, the integral equations become singular. For example, if the frequency ω were taken real, the integral equation would be singular because singularities (associated with trapped wave modes) of some $f_{ij}(\mathcal{K}, x)$ occur for real values of k . This situation did not arise in the SH wave examples of section 2.2 because no trapped SH modes exist in media having one or no plane boundaries. As discussed in Chapter III, the singularities that may arise are avoided by making the frequency complex.

2.4. Elastic-Wave Motion in a Multi-Layered Half-Space Having One Irregular Interface.

The medium differs from that considered in section 2.3 in that the half-space 0 is replaced by free space, i.e., the interface at $z=z_0$ is free. Also, for now, let the free surface be plane. This problem is a special case of the one considered in section 2.3. Once again, the problem will reduce to integral equation (2.52) in the unknown wave amplitudes. The difference is that the coefficients \bar{B}_1 , \bar{B}_2 , \bar{B}_3 , \bar{C}_1 , and \bar{C}_2 used in equations (2.51), relating the complex wave amplitudes above the interface, take new forms appropriate to this new problem. These coefficients are given by equation (A37) of Appendix A rather than by (A27) as before.

We devote some attention to this problem now because it serves as a mathematical model for the scattering of teleseismic body waves in the nonhomogeneous crust near a receiver station on the Earth's surface. Of interest are the amplitude and phase delay anomalies in the radial, transverse, and vertical displacements (\tilde{u}_0 , \tilde{v}_0 , \tilde{w}_0) along the Earth's surface. We assume that the station spread involved is sufficiently small so that the teleseismic wave is approximately plane and incoming at a single angle of incidence. The displacements are

$$\begin{aligned}\tilde{u}_0(r_0, \omega) &= \hat{u}_0 \cos \Omega_0 + \hat{v}_0 \sin \Omega_0 \\ \tilde{v}_0(r_0, \omega) &= -\hat{u}_0 \sin \Omega_0 + \hat{v}_0 \cos \Omega_0 \\ \tilde{w}_0(r_0, \omega) &= \hat{w}_0(r_0, \omega)\end{aligned}\tag{2.55}$$

where $(\hat{u}_0, \hat{v}_0, \hat{w}_0)$ are the (x, y, z) components of displacement at the free surface (the y -direction is parallel to the strike of the irregular interface) and Ω_0 is the azimuth angle given in (2.28). The (x, y, z) displacements are, by (2.32),

$$\begin{aligned}
\hat{u}_0(\underline{r}_0, \omega) &= \int_{-\infty}^{\infty} [u'_0 \cos \Omega - v'_0 \sin \Omega] dk \\
\hat{v}_0(\underline{r}_0, \omega) &= \int_{-\infty}^{\infty} [u'_0 \sin \Omega + v'_0 \cos \Omega] dk \\
\hat{w}_0(\underline{r}_0, \omega) &= \int_{-\infty}^{\infty} w'_0(\underline{r}_0, \omega, k) dk
\end{aligned} \tag{2.56}$$

where Ω is the azimuth angle associated with waves having the x-component of wave number k .

Equations (A34) and (A36) of Appendix A give the spectral displacements (u'_0, v'_0, w'_0) in terms of the wave amplitudes ϕ_s^u , ψ_s^u , and v_s^u , which are determined by solution of integral equation (2.52). That is (restoring the exponential factor $e^{i(kx + \eta_0 y)}$),

$$\begin{pmatrix} u'_0 \\ w'_0 \end{pmatrix} = \underline{\tilde{N}}_{21}^{-1} \begin{pmatrix} \phi_s^u \\ \psi_s^u \end{pmatrix} e^{i(kx + \eta_0 y)} \tag{A34}$$

$$v'_0 = (v_s^u / \tilde{q}_{21}) e^{i(kx + \eta_0 y)} \tag{A36}$$

Here $\underline{\tilde{N}}_{21}$ and \tilde{q}_{21} are matrix elements arising in equations (A30) through (A33).

Combining (A34), (A36), and (2.56) with (2.55) yields expressions for the radial, transverse, and vertical displacements at the free surface which are just Fourier syntheses over the wave number k . Thus, we can use the fast-Fourier transformation algorithm (Cooley and Tukey, 1965) to synthesize the motion at the plane free surface.

When the free surface is the irregular interface, the synthesized displacements are no longer expressible simply as Fourier transforms;

however, the boundary value problem to be solved is smaller than the previous ones. Now only three conditions - the vanishing of the three components of stress at the free surface - must be fulfilled at the irregular boundary. Correspondingly, there are three fewer unknown wave amplitudes in this problem. Application of the stress-free requirements $\hat{T}_i(r_0, \omega) = 0$ yields three coupled integral equations for the wave amplitudes ϕ_1^d , ψ_1^d , and v_1^d . These equations can be written as the single matrix integral equation (2.52) where now $\mathcal{J}(\kappa, x)$ is a 3×3 matrix, $\underline{C}_s(\kappa)$ is the 3×1 matrix

$$\underline{C}_s(\kappa) \begin{pmatrix} \phi_1^d \\ \psi_1^d \\ v_1^d \end{pmatrix}$$

and $\mathcal{H}(\kappa_0, x)$ is a 3×1 matrix.

2.5. Elastic-Wave Motion in a Multi-Layered Medium Having Two or More Irregular Interfaces.

Now consider elastic wave scattering in layered media in which more than one interface is irregular (the strike directions are all parallel to the y -direction). These are the most general of the class of problems that we treat. The procedure is a straightforward extension of the one presented in section 2.3. At each internal irregular interface s , we obtain six integral equations from the requirements of continuity of stress and displacement set forth in (2.34). If the free surface is also irregular, we obtain three additional integral equations from the stress-free requirement.

Using (2.44), (2.45), and (2.46), the k-spectrum decomposed displacements and stresses in each layer are first written as linear combinations of the complex amplitudes of the three upgoing and three downgoing waves. The continuity conditions at plane boundaries are implemented in Appendix A to reduce the number of unknown wave amplitudes to the number of waves leaving all the irregular interfaces (no wave amplitudes are eliminated between irregular interfaces with no intervening plane boundaries). The pertinent relations are given in (A38) through (A42). Each displacement and stress in a layer at an irregular interface s is thus written as a linear combination of the amplitudes of the three outgoing waves and the amplitudes of the three waves outgoing from the next irregular interface toward interface s .

The boundary condition integral equations can be written as the matrix integral equation (2.52). Now the matrices \underline{J} , \underline{C}_s , and \underline{H} have the sizes $K \times K$, $K \times 1$, and $K \times 1$ respectively. If the free surface is plane, then $K=6M$ where M is the number of internal irregular interfaces. If the free surface is also irregular, then $K=6M+3$.

The scattering problems involving multiple irregular interfaces differ from those involving one irregular interface only in that the number of coupled integral equations requiring solution is increased with each additional irregular interface. This increase is significant when we consider the practical solution of these equations in the next chapter. Many of the elements $f_{ij}(\mathcal{K}, x)$ in the \underline{J} matrix are zeros because not all the unknown wave amplitudes in the problem enter into each boundary condition. Also, the source vector \underline{H} has only six non-zero elements - one for each condition at the deepest irregular interface.

The class of wave scattering problems could be considerably enlarged by lifting the restriction that the irregular interface shapes be one-dimensional. Application of our technique would lead to multiple integral equations over both the x- and y-components of wave number. Their practical solution would be prohibitively expensive with present computer speeds and storage capacities. In principal, the integral representation method of Banaugh(1962) can be used for this more general problem but it also would be too costly to implement.

CHAPTER III

APPROXIMATE SOLUTION OF THE INTEGRAL EQUATIONS

3.1. Introduction

The integral equations (2.52) cannot be solved analytically because, owing to the inherent error in the Rayleigh-type formulation, the integral equations are not exact. This suggests that we attempt an approximate method of solution. In so doing, we must ask 'to what solution is ours an approximation?' It is readily conceivable that this 'approximate solution' is nothing like the true solution to the scattering problem. Mikhlin (1957) points out that one should know that an integral equation possesses an exact solution before approximate methods can be applied with confidence.

Nevertheless, an approximate method may be appropriate for two reasons. First, since the plane wave description of the fields is exact when the interfaces are plane, we intuitively expect that small irregularities in interface shape will yield small departures from the true solution. Second, after obtaining approximate solutions, in each practical case, we compute the displacements and stresses at either side of the irregular interfaces. Therefore we can directly measure the residuals or discontinuities left at the interfaces. If these residuals are small (according to some measure as described in the next chapter), we can use the uniqueness theorem to help judge the quality of our solution. Since ours are valid solutions to the equations of motion and satisfy the boundary conditions exactly at the plane interfaces and at

$z=\infty$, they depart from the true solutions only to the extent that the residuals at the irregular interfaces behave as small additional sources in the problems.

In his treatment of elastic wave scattering at an irregular interface, Abubakar (1962 a,b,c) used a perturbation method to solve integral equations like (2.52). By restricting the roughness $\zeta_{\max} - \zeta_{\min}$ (where ζ_{\max} is the maximum of $\zeta_s(x)$ and ζ_{\min} , the minimum) to be small relative to the wavelengths involved and by limiting the maximum slope $\left| \frac{d\zeta_s}{dx} \right|_{\max}$ of the interface to be small, he expanded the unknown wave amplitudes as power series in $\epsilon = k_m (\zeta_{\max} - \zeta_{\min}) \ll 1$, where the wave number k_m is the maximum of $|k|$ in (2.52). Inserting the zero order terms into the integral equations reduced them to sets of Fourier transform pairs which could be solved by inversion. The solution for the next order terms (terms in ϵ^1) proceeded by iteration using the zero order solution. The second and higher order solutions are extremely cumbersome for even the simple problem involving a wave incident normal to a sinusoidal interface.

Levy and Deresiewicz (1967) extended Abubakar's method to problems involving systems of (small roughness) corrugated layers by employing a modification of Thomson's (1950) flat-layer technique. When an interface has periodic shape, the scattered field consists of plane waves propagating in discrete directions (section 3.3) either side of the primary direction (the propagation direction if the interfaces were planes). Each scattered wave is labeled with a scatter 'order number' $n=0, \pm 1, \pm 2, \dots$. The perturbation method solutions of Abubakar and of Levy and Deresiewicz have the property that, for sinusoidal interfaces, the maximum scatter order N equals the order of the solution in the power series expansion in ϵ . Levy and

Deresiewicz applied their method to problems involving P-SV waves normally incident to systems of sinusoidal corrugated layers. They presented curves of the first scattered order amplitudes of reflected and transmitted waves as functions of the ratio of the corrugation wavelength to the wavelength of one of the elastic waves. The utility of such curves is predicated on the assumption that scattering from an arbitrary shaped interface can be represented as the linear superposition of solutions for sinusoidal interfaces. This assumption is valid just to the first order, appropriate for interfaces having small roughness.

Asano (1960,1962,1966) also used a perturbation method, expanding the solutions in power series in the slope of the interface shape, and presented similar wave amplitude curves for normal incidence problems involving half-spaces separated by a sinusoidal interface. Asano could compute second order amplitudes before his solutions became too cumbersome.

Asano essentially followed the method of Rayleigh (1907, 1945) by assuming the interface shape to be periodic. Thus, at the outset, his solution was represented as a discrete sum of plane waves. Meecham (1956) and Heaps (1957), in studies of scattering of acoustic waves at fixed and free surfaces, also followed the discrete wave Rayleigh formulation but neither one used a perturbation method in which the interface roughness was a priori assumed to be small. Heaps obtained scattered wave amplitudes for a problem involving a sinusoidal interface by solving a system of linear algebraic equations derived from satisfying the boundary condition in nearly a least-squares sense. Meecham did not require sinusoidal interfaces to obtain numerical solutions. Using a variational method in which the boundary condition was satisfied in a least-squares sense, he also obtained

wave amplitudes by solving a system of linear algebraic equations. Computational limitations fixed the maximum number of scatter orders in the solution to 10.

The method presented in section 3.2 is closest to that of Meecham. We make the boundary periodic so as to replace the integral equations by infinite-sum equations. After truncating the equations, we take advantage of the fast Fourier transform algorithm (Cooley and Tukey, 1965) and satisfy the boundary conditions in the wave number domain. Final determination of the wave amplitudes reduces to the solution of a large system of linear equations. Some features of these solutions are discussed in section 3.3.

Our use of complex frequency influences some important details in the method. In section 3.4 we discuss the ways in which the use of complex frequency not only enhances the numerical computability and stability of the solutions but also increases their flexibility and practical value. When frequency is complex, the source wave number must also be defined complex. Implications associated with such a definition of source wave number are considered in section 3.4.

The method for normalizing the solutions and the general format used in the presentation of the examples in later chapters are discussed in section 3.5. There, we also indicate how our complex frequency solutions are to be compared with actual seismograms.

3.2. Method of Solution.

In order to solve the matrix integral equation (2.52), we convert it

into an infinite-sum equation by assuming a periodicity in the interface depth $z_s(x) = z_{s-1} + \zeta_s(x)$; that is

$$\zeta_s(x+mL) = \zeta_s(x) \quad m = \pm 1, \pm 2, \dots \quad (3.1)$$

In the examples that we consider in this thesis, each interface is plane except possibly over a localized interval in the x-coordinate. If L is taken to be large as compared with the length of this interval, the effect of repeated irregularities at distances mL can be diminished by making the frequency complex. This is similar to the introduction of a small amount of attenuation in the medium. To the extent that we compute amplitude and phase delay anomalies at distances from the interface irregularity that are no larger than L, our solutions are near-field.

When $\zeta_s(x)$ is periodic, $\underline{\mathcal{F}}(\kappa, x)$ and $\underline{\mathcal{H}}(\kappa_0, x)$ in equation (2.52) are also periodic because they depend on x only through ζ_s and $\frac{d\zeta_s}{dx}$. Let us multiply (2.52) by e^{-ik_0x} . Then we have

$$\int_{-\infty}^{\infty} \underline{\mathcal{F}}(\kappa, x) \underline{C}_s(\kappa) e^{i\tilde{k}x} d\kappa = \underline{\mathcal{H}}(\kappa_0, x) \quad (3.2)$$

where $\tilde{k} = k - k_0$. Since the right hand side of (3.2) is periodic in x, the left hand side likewise must be. Since $\underline{\mathcal{F}}(\kappa, x)$ is also periodic, \tilde{k} can only take such real values that satisfy

$$e^{i\tilde{k}x} = e^{i\tilde{k}(x+L)} \quad (3.3)$$

$$\text{or } \tilde{k}_n L = 2\pi n \quad n = 0, \pm 1, \pm 2, \dots$$

Thus the integral equation (3.2) must be replaced by the infinite-sum matrix equation

$$\sum_{n=-\infty}^{\infty} \underline{\underline{J}}_n(x) \underline{C}_{s,n} e^{2\pi i n x/L} = \underline{H}(\kappa_0, x) \quad (3.4)$$

where

$$\underline{C}_{s,n} = \underline{C}_s(\kappa_n) \Delta k_n$$

$$\underline{\underline{J}}_n(x) = \underline{\underline{J}}(\kappa_n, x)$$

$$\kappa_n = (k_n^2 + \eta_0^2)^{1/2}$$

$$k_n = k_0 + 2\pi n/L$$

$$\Delta k_n = 2\pi/L$$

(Note: Any statement concerning matrix quantities above and in what follows applies directly to each element of the matrix. For example, the elements of $\underline{\underline{J}}_n(x)$ are $f_n^{(ij)}(x) = f_{ij}(\kappa_n, x)$ where $f_{ij}(\kappa_n, x)$ is the row i -column j element of $\underline{\underline{J}}(\kappa_n, x)$).

We now truncate the infinite-sum equation to obtain its finite-sum approximation

$$\sum_{n=-N_1}^{N_2} \underline{\underline{J}}_n(x) \underline{C}_{s,n} e^{i2\pi n x/L} = \underline{H}(\kappa_0, x) \quad (3.5)$$

The truncation numbers N_1 and N_2 are positive integers which, in general, are unequal. For convenience, let $N_1 + N_2$ be an even number. Instead of solving the above equation directly in x , we first take the Fourier transform of both sides by multiplying by $\frac{1}{L} e^{-2\pi i m x/L}$ and integrating over $0 \leq x \leq L$. Letting $m = -N, \dots, 0, \dots, N$, where $2N = N_1 + N_2$, gives us $2N+1$ simultaneous linear matrix equations

$$\sum_{n=-N_1}^{N_2} \underline{\underline{J}}_{mn} \underline{C}_{s,n} = \underline{\underline{H}}_m(\kappa_0) \quad (3.6)$$

$$m = -N, \dots, 0, \dots, +N$$

where

$$\underline{\underline{J}}_{mn} = \frac{1}{L} \int_0^L \underline{J}_n(x) e^{2\pi i(n-m)x/L} dx$$

$$\underline{\underline{H}}_m = \frac{1}{L} \int_0^L \underline{H}(\kappa_0, x) e^{-2\pi imx/L} dx \quad (3.7)$$

Recall that the sizes of the matrices in (3.6) depend upon the specific scattering problem under consideration. Say that the sizes are

$$\begin{aligned} \underline{\underline{J}}_{mn} &: K \times K \\ \underline{C}_{s,n} &: K \times 1 \\ \underline{\underline{H}}_m &: K \times 1 \end{aligned}$$

where values of K for the different problems are given in Table 3.1.

TABLE 3.1
Table of Values of the Matrix Size Number K
for Different Scattering Problems.

Number of Internal Irregular Interfaces	Shape of Free Surface	K		
		SH Problems	P-SV Problems	General Problems
M	plane	2M	4M	6M
M	irregular	2M+1	4M+2	6M+3

Equations (3.6) imply a system of $(2N+1)K$ simultaneous linear scalar equations. Solution of this large system determines the wave amplitudes $\underline{C}_{s,n}$ which can be used to synthesize the motion anywhere in the medium.

For example, in the SH problem of a layer over a half-space discussed in section 2.2.2, $K=2$ and $\underline{C}_{S,n} = \begin{pmatrix} V_{1,n}^u \\ V_{2,n}^d \end{pmatrix}$. The synthesized displacements are

$$\begin{aligned} \hat{V}_{1N}(x, z) &= 2 \sum_{n=-N_1}^{N_2} V_{1,n}^u \cos \gamma'_{1,n} z e^{ik_n x} & (0 \leq z \leq \zeta(x)) \\ \hat{V}_{2N}(x, z) &= e^{ik_0 x - i\gamma'_0 z} + \sum_{n=-N_1}^{N_2} V_{2,n}^d e^{ik_n x + i\gamma'_{2,n} z} & (z \geq \zeta(x)) \end{aligned} \quad (3.8)$$

where

$$\begin{aligned} \gamma'_{j,n} &= (k_{\beta_j}^2 - k_n^2)^{1/2} ; \quad j=1,2 \\ k_n &= k_0 + 2\pi n/L \end{aligned} \quad (3.9)$$

The subscripts N in the displacements \hat{V}_{jN} exhibit the fact that these solutions were obtained by truncating equations (3.4) to order $2N+1$.

At the free surface, (3.8) becomes

$$\hat{V}_{1N}(x, 0) = 2 \sum_{n=-N_1}^{N_2} V_{1,n}^u e^{ik_n x} \quad (3.10)$$

This is the discrete wave version of equation (2.17).

3.3 Some Features of the Solution.

The integers n in these expressions are the scatter order numbers referred to in section 3.1. Recall that the horizontal component of source wave number defines an angle of incidence θ_0 in the lower half-space \tilde{n} , i.e.,

$$\sin \theta_0 = \kappa_0 / k_{\alpha \tilde{n}}$$

where $k_{\alpha_{\tilde{n}}} = \omega/\alpha_{\tilde{n}}$ is the source wave number (for concreteness, we have let the source wave be a P wave). Similarly, let $\tilde{\Theta}_0$ be the angle between vertical and the projection of the source propagation vector onto the x-z plane. Then

$$\sin \tilde{\Theta}_0 = k_0 / \xi_{\alpha_{\tilde{n}}} \quad (3.11)$$

where $\xi_{\alpha_{\tilde{n}}} = (k_{\alpha_{\tilde{n}}}^2 - \eta_0^2)^{1/2}$ is the projection of wavenumber $k_{\alpha_{\tilde{n}}}$ onto the x-z plane. We may also define acute angles $\tilde{\Theta}_{\tilde{n},n}^P$, which we associate with the nth scattered order P waves in the half-space \tilde{n} , as

$$\sin \tilde{\Theta}_{\tilde{n},n}^P = k_n / \xi_{\alpha_{\tilde{n}}} \quad n = -N_1, \dots, 0, \dots, +N_2 \quad (3.12)$$

Putting (3.11) and (3.12) into (3.9) gives

$$\sin \tilde{\Theta}_{\tilde{n},n}^P = \sin \tilde{\Theta}_0 + n \lambda_{\alpha_{\tilde{n}}} / L \quad (3.13)$$

where $\lambda_{\alpha_{\tilde{n}}} = 2\pi / \xi_{\alpha_{\tilde{n}}}$ is the apparent wavelength, in the x-z plane, of the P waves in the half-space. Thus, the directions of the scattered waves differ from the incident wave direction such that $\sin \tilde{\Theta}_{\tilde{n},n}^P$ differs from $\sin \tilde{\Theta}_0$ by integer multiples of $\lambda_{\alpha_{\tilde{n}}} / L$. When n becomes sufficiently large, $|\sin \tilde{\Theta}_{\tilde{n},n}^P| > 1$, i.e., $\tilde{\Theta}_{\tilde{n},n}^P$ becomes complex. These scattered orders are the inhomogeneous or evanescent waves.

Heaps (1957) believed that the inhomogeneous orders need not be retained in solving the scattering problems. In some examples that we discuss in Chapter V, (particularly those involving non-normal incidence), these larger scatter orders are required in order to adequately fulfill the boundary conditions.

The angles $\tilde{\Theta}_{\tilde{n},n}^s$ associated with the n th scattered order S waves in the lower half-space satisfy

$$\sin \tilde{\Theta}_{\tilde{n},n}^s = (\lambda_{\beta_{\tilde{n}}} / \lambda_{\alpha_{\tilde{n}}}) \sin \tilde{\Theta}_{\tilde{n},n}^p$$

where $\lambda_{\beta_{\tilde{n}}}$ is the apparent S wavelength in the x - z plane in half-space \tilde{n} .

Similar expressions could be written for the angles associated with scattered waves in other layers. These interpretations of the scattered wave directions are altered when the frequency ω is complex (section 3.4.4). When ω is complex, the planes of constant phase may be oblique to those of constant amplitude for some scattered waves.

Truncating the equations to $2N+1$ terms can introduce additional errors into the approximate solutions. The examples presented in the error analysis chapter indicate that the accuracy of the solutions is more often limited by truncation error than by the inherent error in the Rayleigh-type formulation. The Gaussian elimination method (Isaacson and Keller, 1966) is used to solve system (3.6). Because of computer time and storage limitations, the largest system of equations that we solve involves $(2N+1)K=165$ equations. According to Table 3.1, the maximum number of scattered orders included in a given solution is governed by the nature of the problem. For example, for the SH problem with a single internal irregular interface, $N_{\max}=40$. For the general arbitrary azimuth problems with a single internal irregular interface, $N_{\max}=13$.

Note that, by (3.13), N_2 is the number of waves scattered forward of the primary wave direction and N_1 is the number scattered backward relative to the primary direction. We have not investigated the relative sizes of N_1 and N_2 that minimize errors at the interfaces, with $N_1+N_2=2N$ given. Our experience suggests that the number of scattered waves propagating in directions

either side of vertical should be comparable. The judgement criterion is that the amplitudes of waves scattered in the most forward and rearward directions (waves whose x-components of wavenumber are k_{N_2} and k_{-N_1} respectively) be small relative to those near the primary direction. For large incidence angles $\tilde{\theta}_0$, we generally have $N_1 > N_2$.

We find that the large number of equations generally inverts with good numerical accuracy. Exceptions occur in some real frequency cases when trapped modes cause the system matrix to be singular. Also, in exceptional cases, the inherent error can make the system of equations divergent.

The system coefficient matrix is basically independent of the source wave (as defined by wave type - P, SV, SH - and by the x-component of wave number k_0) except for the restriction that the scattered field wave numbers k_n differ from k_0 by multiples of $2\pi/L$. Therefore, we economize on computation time by treating several source wave problems during a single Gaussian elimination solution of system (3.6). A limitation on the simultaneous solution of several source vector problems is discussed in section 3.4.3.

3.4. Smoothing by the Use of Complex Frequency.

3.4.1. Comparison with finite bandwidth signals. The solutions obtained above are responses to incident waves having the time function $e^{-i\omega t}$. When ω is real, the solution corresponds to the steady-state case; that is, the response to sinusoidal oscillations lasting from the infinite past. In this case, the frequency spectrum is a discrete line. In practical problems, we are always dealing with a signal of finite duration

which has a continuous spectrum over a certain frequency band. We would need an infinite number of line spectra solutions if we were to synthesize such a transient signal. A simple and effective way of avoiding this problem is to make the frequency complex. The usefulness of such a procedure in seismogram synthesis was pointed out by Phinney (1965).

With the frequency complex, the incident waves have the non-stationary shape of an exponentially increasing oscillation in which amplitude increases by a factor e at every time interval $\tau = 1/\omega_I$. Here, ω_I is the imaginary part of ω and must be taken positive for the reasons explained later. The frequency spectrum for the complex ω case is no longer discrete but is continuous with a bandwidth proportional to ω_I . Therefore the solution corresponds to a smoothed one over that frequency band. By this procedure, we lose in frequency resolution but gain in stability and economize on computation time for application to transient waves.

3.4.2. Reducing the effect of the periodic interface shape. Consider the contributions of disturbances at various parts of the medium to the motion at an observation point at $t=0$. The contribution from a travel distance d must have originated at that source point at $t \leq -d/\alpha$, where α is the propagation velocity of the fastest waves. Because of the exponentially increasing oscillation in the complex frequency cases, if $d/\alpha \gg \tau$ the amplitudes at the source which caused the disturbance were negligibly small, and therefore the contributions from the disturbance may be neglected. For example, if we take τ smaller than L/α , the undesirable effect of the repeated interface shape can be diminished.

3.4.3. Interpreting the complex frequency solutions. In later chapters, our solutions are presented as amplitude and phase delay anomalies

usually along a free surface. Here, we discuss how these complex ω solutions are to be compared with seismological observations.

The Fourier transform of a transient time signal $f(t)$ is

$$F(\omega) = \frac{1}{(2\pi)^{1/2}} \int_{-\infty}^{\infty} f(t) e^{i\omega t} dt \quad (3.14)$$

Let ω be complex with

$$\omega = \omega_R + i\omega_I = \omega_R(1+i\epsilon) \quad (3.15)$$

where ω_R and ω_I (and hence $\epsilon(\omega_R)$) are real and positive. Putting (3.15) into (3.14) gives

$$F(\omega) = F_\epsilon(\omega_R) = \frac{1}{(2\pi)^{1/2}} \int_{-\infty}^{\infty} [f(t) e^{-\omega_I t}] e^{i\omega_R t} dt \quad (3.16)$$

If $f(t)$ is identically zero before $t=0$, then F is analytic in the upper half-plane (ω_I was chosen positive for this reason). By (3.16), the complex ω transform F of the signal $f(t)$ is functionally the same as the real frequency ω_R transform F_ϵ of the exponentially time windowed signal $f(t) e^{-\omega_I t}$.

Consider now a linear time system; i.e., a conventional black box problem. If $H(\omega)$ is the system response of the realizable linear system (the Fourier transform of the unit impulse response), then according to the convolution theorem

$$F(\omega) = H(\omega) X(\omega) \quad (3.17)$$

where F and X are the Fourier transforms of the output and input functions $f(t)$ and $x(t)$ respectively ($x(t)$ and $f(t)$ are zero for $t < 0$). Equation (3.17)

is valid for complex ω by continuation from the real axis into the upper half of the complex ω -plane. Therefore, for the black box problem in which complex $\omega = \omega_R + i\omega_I$ is used in the arguments of the input spectrum $X(\omega)$ and of the system response function $H(\omega)$, by (3.16) and (3.17) the output spectrum $F_{\epsilon}(\omega_R)$ is the real frequency Fourier transform of the black box output $f(t)$ premultiplied by the exponential time function $e^{-\omega_I t}$.

Our space-time wave scattering problems can be cast in the form (3.17). Suppose that transient solutions to the plane wave scattering problems were available. Let one such solution at space position \underline{r} (say, the transverse component of displacement at the free surface) be $f(t; \underline{r}; c_x, c_y)$, where c_x and c_y are the x- and y-components of phase velocity defining the propagation direction of the incident waves. This transient response is the time convolution of a source time function $s(t; \underline{r}_1; c_x, c_y)$ at an arbitrary reference position \underline{r}_1 in the lower half-space \tilde{n} , with the unit impulse response function $v(t; \underline{r}_1, \underline{r}; c_x, c_y)$, i.e., the response at position \underline{r} to a unit impulse plane source wave (direction characterized by c_x, c_y) at position \underline{r}_1 .

Let $S(\omega; \underline{r}_1; c_x, c_y)$ be the Fourier transform of $s(t; \underline{r}_1; c_x, c_y)$ and $V(\omega; \underline{r}_1, \underline{r}; c_x, c_y)$ be the Fourier transform of $v(t; \underline{r}_1, \underline{r}; c_x, c_y)$. As in (3.17), the Fourier transforms satisfy

$$F(\omega; \underline{r}; c_x, c_y) = S(\omega; \underline{r}_1; c_x, c_y) V(\omega; \underline{r}_1, \underline{r}; c_x, c_y)$$

which holds for real ω and, by continuation, for complex ω . Note that V is the equivalent of the crustal transfer function in flat-layer theory (Haskell, 1962; Phinney, 1964). The difference is that our transfer function is dependent upon the locations \underline{r}_1 and \underline{r} relative to the locations

of all interface irregularities. Let us remove the source spectrum by normalizing F by the solution F_f to a similar layered-medium problem in which irregularities in the interface shapes are removed. The normalized response is

$$F_N(\omega; \underline{r}; c_x, c_y) = \frac{F(\omega; \underline{r}; c_x, c_y)}{F_f(\omega; \underline{r}; c_x, c_y)} = \frac{V(\omega; \underline{r}, \underline{r}; c_x, c_y)}{V_f(\omega; \underline{r}, \underline{r}; c_x, c_y)} \quad (3.18)$$

where V_f is the crustal transfer function of the flat-layered medium. But this ratio is just what we would compute by applying our complex frequency method (with fixed, real c_x and c_y) and normalizing by the Haskell solution in which the frequency is also complex.

We thus interpret our complex frequency solutions as follows. Suppose that theoretical solutions to the scattering problems involving transient source waves were available in the form of theoretical seismograms at stations along the free surface. For a problem involving $\omega = \omega_R + i\omega_I$ our computed normalized amplitudes and phases at each station are equal to the spectral amplitudes and phases at ω_R obtained by multiplying each seismogram by $e^{-\omega_I t}$, Fourier transforming, and normalizing by the Fourier transform of a similarly windowed flat-layer solution. The corresponding method for comparing our normalized solutions with actual seismograms is discussed in section 3.5. In section 4.6, we present a comparison of our solution with a synthetic seismogram solution obtained by using a finite difference technique.

3.4.4. Implications in the use of complex source wave numbers k_o and η_o . When ω is real, the incident wave direction is unambiguously

determined by choosing real values of the x- and y-components of wave number k_0 and η_0 such that

$$\kappa_0^2 = k_0^2 + \eta_0^2 \leq \kappa_c^2 \quad (3.19)$$

where κ_c is $k_{\alpha_{\tilde{n}}}$ for P-type source waves and $k_{\beta_{\tilde{n}}}$ for S-type source waves. For concreteness, consider P-type sources. Then the source wave direction makes the angle θ_0 with vertical, where

$$\sin \theta_0 = \kappa_0 / k_{\alpha_{\tilde{n}}} = \kappa_0 \alpha_{\tilde{n}} / \omega \quad (3.20)$$

Similarly, the projection of the source wave vector onto the x-z plane makes the angle $\tilde{\theta}_0$ with vertical, where

$$\sin \tilde{\theta}_0 = k_0 \bar{\alpha}_{\tilde{n}} / \omega \quad (3.21)$$

and $\bar{\alpha}_{\tilde{n}} = \alpha_{\tilde{n}} [1 - (\eta_0 / k_{\alpha_{\tilde{n}}})^2]^{-1/2}$ is the apparent velocity in the x-z plane.

The continuation of solution such as (2.22) into the complex ω -plane requires that the source direction wave numbers be

$$\begin{aligned} k_0 &= \omega / c_x = (\omega_R / c_x) (1 + i\epsilon) \\ \eta_0 &= \omega / c_y = (\omega_R / c_y) (1 + i\epsilon) \end{aligned} \quad (3.22)$$

and hence

$$\kappa_0 = \omega / c = (\omega_R / c) (1 + i\epsilon)$$

where c is the horizontal component of phase velocity of the source wave. So long as c_x , c_y , and c are real, the source direction given by (3.20) remains unambiguously determined as required in (3.18). Suppose, on the contrary,

that k_0 and η_0 had been chosen real with ω complex. Then $\sin \theta_0$ and $\sin \tilde{\theta}_0$ would be complex, i.e., θ_0 and $\tilde{\theta}_0$ would be complex. Just as we interpret complex frequency to mean smoothing over a frequency bandwidth proportional to ω_I , so do we interpret complex θ_0 as implying smoothing over direction of incidence proportional to the imaginary part of θ_0 . Such a smoothing over direction is unacceptable since we wish to compare our solutions with actual seismograms which are responses to waves having reasonably well defined source directions (we rule out multiple sources here, and note that the ambiguity in θ_0 caused by complex ω can be as large as the source angle itself when $\text{Re } \theta_0 > 50^\circ$ or 60°).

According to (3.22), when c is real the source wave number vector is

$$\underline{k}_c = \underline{k}_{cR} (1 + i\epsilon)$$

That is, the propagation direction remains the same as that for real frequency and is normal to both planes of constant amplitude and of constant phase.

The periodicity argument surrounding equation (3.2) leads to the restriction that $\tilde{k} = k - k_0$ take only discrete real values given by (3.3). Thus the wave numbers k_n in the infinite-sum equation (3.4) must all have imaginary parts equal to the imaginary part of k_0 . In the complex k -plane, this means that, when a plane source wave is given in terms of complex ω , k_0 , and η_0 , periodicity imposes the requirement that the summation in (3.4) be over discrete complex values of k_n that are equi-spaced along a line through k_0 parallel to the real k -axis.

Let us consider the complex k -plane in more detail, first discussing

the branch point locations and remarking on the choice of signs of the vertical components of wave number (equation (2.40)). At first look there appears to be pairs of branch points at $k=\pm \xi_{\alpha_m} = \pm [(\omega/\alpha_m)^2 - \eta_0^2]^{1/2}$ and at $k=\pm \xi_{\beta_m}$ associated with each layer in the medium. However, the effects of the plane layers enter into our solutions only through the layer matrices \underline{A}_m and \underline{a}_m , defined by (A6) and (A7) in Appendix A. Since the elements of \underline{A}_m and \underline{a}_m are all even functions of ν_m and ν'_m , we need not worry about the signs of ν_m and ν'_m for the plane layers. Examination of the coefficients $f_{ij}(\mathcal{K}, x)$ used in integral equation (2.52) (see equations (C18), (C3.1), (C3.2), (C5.1), (C5.2)) reveals that they are neither even nor odd functions of $\nu_s, \nu'_s, \nu_{s+1}, \nu'_{s+1}$ where the subscript s refers to any irregular interface. Neither are they even or odd functions of $\nu_{\tilde{n}}, \nu'_{\tilde{n}}, \nu_0, \nu'_0$ for the half-spaces \tilde{n} and 0. Thus, branch points are located only at the P and S wave numbers in layers bounded by irregular interfaces and in the half-space.

Figure 3.1a shows the first quadrant of the top sheet of the complex k -plane for real positive ω for some layered half-space problem involving a single irregular interface. The branch points lie on the real k -axis and the region of poles (the singularities discussed in Appendix B) extends along the real axis from $k=\pm \xi_{\alpha_{\tilde{n}}}$ to just beyond $k=\pm [(\omega/\beta_{\tilde{m},\tilde{n}})^2 - \eta_0^2]^{1/2}$ where β_{\min} is the slowest S wave speed (Jardetsky, 1953). The top sheet (Lapwood, 1949) is determined by extending the branch lines $\text{Im}(\nu_m)=0$ and $\text{Im}(\nu'_m)=0$ along the real axis from the branch points to the origin and thence along the imaginary axis to $k=i\infty$, and by choosing $\text{Im}(\nu_m)$ and $\text{Im}(\nu'_m)$ positive where $m=\tilde{n}, s, s+1$. $\text{Re}(\nu_m)$ and $\text{Re}(\nu'_m)$ are positive on the top sheet along the real axis (the integration

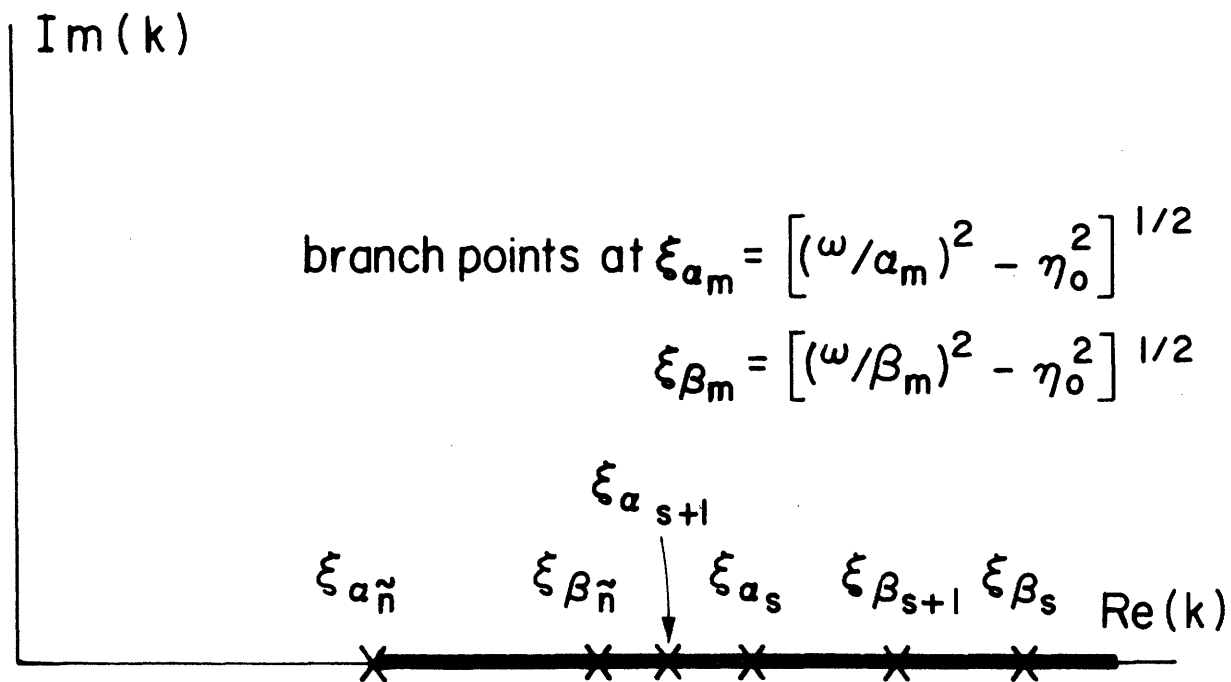


Figure 3.1a. Branch points and pole region on the top sheet of the complex k -plane for the real ω case. Crosses are branch points and heavy bar denotes the pole region.

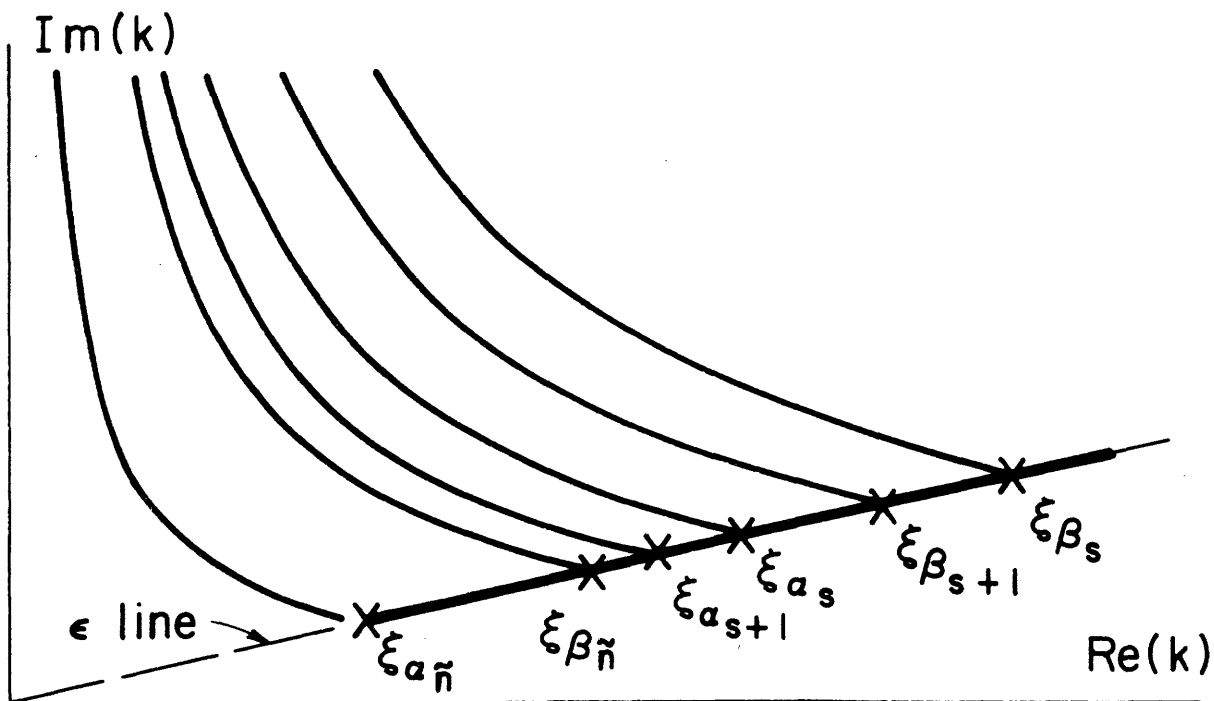


Figure 3.1b. Branch points, branch lines, and pole region on the top sheet of the complex k -plane for the case $\omega = \omega_R(1+i\epsilon)$. Crosses are branch points and the heavy bar denotes the pole region.

path) just below the branch lines when ω is given a small positive imaginary part.

Figure 3.1b shows the top sheet of the complex k -plane for the case $\omega = \omega_R (1 + i \epsilon)$. The branch points and poles are displaced into the first quadrant along the straight line having the slope ϵ (denoted here as the ϵ line). The branch lines become hyperbolas (Erekhovskikh, 1960) and $\text{Im}(\nu_m) > 0$, $\text{Im}(\nu'_m) > 0$ still define the top sheet. It is easy to show that, when ω_R and ϵ are positive, $\text{Re}(\nu_m)$ and $\text{Re}(\nu'_m)$ are positive below the respective hyperbolas and are negative above.

Figure 3.2 is an enlargement of the region of the complex k -plane between the origin and the branch point at $k = \xi_{\alpha_{\tilde{n}}}$. By (3.32), the incident wave angle $\tilde{\Theta}_0$ is unambiguously determined when k_0 lies along the ϵ line. The ratio $|k|/|\xi_{\alpha_{\tilde{n}}}|$ of distances from the origin is $\sin \tilde{\Theta}_0$. The summation wave numbers k_n are constrained to be equi-spaced along the horizontal line through k_0 . In the limit that the periodicity distance L in interface shape becomes infinite, the wave number spacing $2\pi/L \rightarrow 0$ and the summation reduces to an integration along the line $\text{Im}(k) = \text{Im}(k_0)$.

We can use the vertical distance of a given wave number from the ϵ line as a measure of the ambiguity in propagation direction. Thus, whenever ω is complex, the computed wave amplitudes $\underline{C}_{s,n}$ are associated with waves whose propagation directions are uncertain to varying extents. For these waves, planes of constant phase are oblique to the wave fronts. In fact, for k_n to the right of the dashed hyperbola in Figure 3.2, $\text{Re}(\nu_{\tilde{n}}) < 0$, so that those waves in half-space \tilde{n} attenuate downward toward

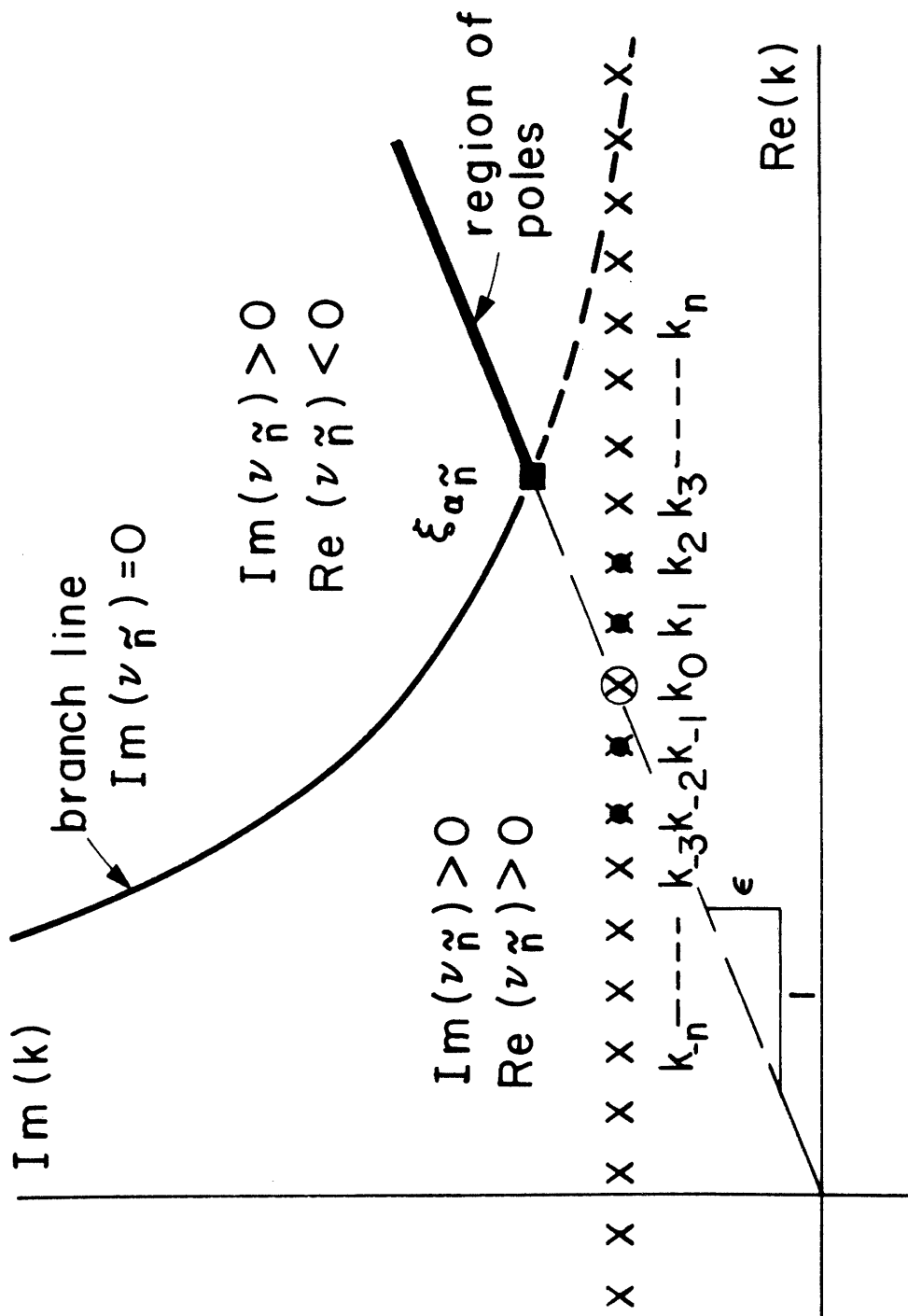


Figure 3.2. Locations of summation wave numbers k_n for the case $\omega = \omega_R(1+i\epsilon)$. The solid square is the branch point, the open circle is the principal source wave number, the solid circles are additional source wave numbers, and the crosses are the locations k_n .

$z = \infty$ but seem to propagate upward. Thus, it is difficult to attach simple physical meaning to the waves that contribute to our frequency smoothed solutions. When frequency is complex, our term downgoing waves actually refers to waves that attenuate in the direction of increasing z regardless of whether they are propagating upward or downward. Similarly, upgoing waves are waves that attenuate with decreasing z .

In the actual solution of the system of equations (3.6), we use several sources during a single Gaussian elimination (section 3.3). The circles in Figure 3.2 represent five such source wave numbers. The principal source (open circle) lies on the ϵ line. The additional sources (solid circles) must coincide with some k_n associated with k_0 and thus cannot lie on the ϵ line. Thus, in order to simultaneously solve several complex ω source problems, we must tolerate uncertainty in some of the source wave directions. So long as the source wave numbers do not depart much from k_0 , the problem is not a serious concern for us.

3.4.5. Reducing the effects of singularities. When ω is real, the integration (or summation) path is along the real k -axis on which lie the singularities associated with the trapped modes (Figure 3.1a). The linear system (3.6) cannot be inverted accurately unless special techniques are employed. We avoid these singularities by making ω complex. The poles are displaced into the first quadrant along the ϵ line (Figures 3.1b and 3.2) above the summation path. This shift results in a gain in the stability of our solutions (there are no other roots on the top sheet). We have mentioned only the singularities on the top sheet. Some poles on the lower sheet may lie near the branch lines and thus also limit the accuracy in

the case of real ω . These poles give rise to the leaking modes investigated by Gilbert (1964). When ω is complex, these poles are also displaced away from the integration path.

3.4.6. Practical use for complex frequency solutions. The use of complex frequency has practical value as well as computational value for our solutions. Premultiplying the seismograms by the exponential time window $e^{-\omega_I t}$ suppresses the later time motion. With ω_I sufficiently large, our solutions essentially represent first arrival motion and might then be compared with peak-to-trough amplitudes (after windowing) of the first motion on seismograms. Therefore, by varying ω_I in our technique, we can isolate the effects of wave focusing by the irregular interfaces from interference effects associated with multiple arrivals (including both vertical and lateral reverberations). Thus, in Chapter V, some of the solutions are compared with Haskell flat-layer theoretical solutions and others with single path ray theoretical solutions.

3.5 Normalization of the Solutions.

Here, we describe the basic format used in the presentation of the computed amplitudes and phase delays in later chapters. In the problems considered, the interface is irregular over some finite x -interval within the principal interval $0 \leq x \leq L$. In each case, the complex displacements at the free surface are normalized by dividing by the flat layer solution that would be obtained for a problem in which the interface irregularities were removed. For example, in the SH case of a layer over a half-space, we divide the solution (3.10) by the flat layer solution

$$\hat{V}_f(x, 0) = |V_f| e^{i\phi_f + ik_0 x}$$

The normalized solution is then

$$\hat{V}_{IN} / \hat{V}_f = 2 \sum_{n=-N_1}^{N_2} (|V_{i,n}^u| / |V_f|) e^{i(\phi_{i,n}^u - \phi_f) + i(k_n - k_0)x} \quad (3.23)$$

where $|V_{i,n}^u|$ and $\phi_{i,n}^u$ are the amplitude and phase of $V_{i,n}^u$. Away from the anomalies, the normalized amplitude approaches unity and the phase delay approaches zero. For the general, arbitrary azimuth problems, the solutions are likewise normalized by the corresponding Haskell solution (in which complex k_0 , η_0 , and ω are used). In so doing, the $e^{i(\eta_0 y + k_0 x)}$ factor is removed.

To compare these normalized solutions with actual seismograms along, say, a plane free surface, we first apply station time delays, i.e., we time shift the seismograms such that

$$t = t' - \frac{x - x_0}{c_x} - \frac{y - y_0}{c_y}$$

where t' is the real time; t is the new time variable at the station located at $(x, y, 0)$; $(x_0, y_0, 0)$ are Cartesian coordinates of some reference station; and c_x and c_y are the x- and y-components of phase velocity of the source wave. In practice, c_x and c_y would be estimated from mean travel-time delays across the seismometer array. Our solutions should then be compared with the Fourier transforms of the seismograms premultiplied by the time window $e^{-\omega_1 t}$.

The stresses and displacements at irregular interfaces are also normalized to the Haskell solution displacements at the free surface. The

stresses are first converted to equivalent units of displacement for comparison of the relative effects of the interface residuals in displacement and those in stress on the errors in motion at the free surface (section 4.2 and Appendix D).

The general format for the presentation of results is to display the medium configuration, layer parameters, and source directions at the bottoms of the figures, and to show the normalized amplitudes and phase delays directly above. The same horizontal scale for x-coordinate position is used in both portions of the figures. In all the examples, distances and velocities are given explicitly in units of km and km/sec respectively, and the problem scales are appropriate for simplified crust-mantle problems. The use of explicit dimensional units is simply for convenience; of course, the solutions are unchanged when all lengths are scaled equally. The interface periodicity distance in most cases shown is $L=256$ km.

CHAPTER IV
ANALYSIS OF ERRORS AND RESOLUTION

4.1. Introduction.

Several factors render our method approximate. The principal ones are the inherent error in the plane wave description of the wave fields and the truncation error in approximating the infinite-sum equations (3.4) by the finite-sum equations (3.5). The periodicity in interface shape can cause unwanted effects. Also, the solutions are subject to inaccuracy introduced during the numerical computations. It is imperative, therefore, that we devise some means for checking the accuracy of our method.

No exact solutions are available for comparison with the solutions computed using our technique. We must be content with estimating the accuracy by using internal measures of error based upon the computed solutions or by comparing our solutions with those obtained by using other approximate methods. In section 4.6, such a comparison is made with a solution obtained by the finite difference technique of Boore (1969). At present, there appears to be no sufficiently accurate two-dimensional laboratory model studies as standards for comparison (although in Chapter V we present a comparison with results of a model study by Laster, et.al. (1967)).

In section 4.2, we discuss two measures of the errors in our solutions. The first is a relative root-mean-square error (RMSE) based upon the

weighted residuals in computed stress and displacement at the irregular interfaces. In Appendix D, the Kirchhoff integral solution to the Helmholtz equation is used as a guide in estimating the errors, at positions removed from the irregular interfaces, that are attributable to the residuals at the interfaces. The argument is inhibited by the fact that the computed residuals are not the same as the actual errors at the interfaces and thus cannot be used in a representation theorem to actually compute the errors elsewhere. What we do get from the argument, at least in SH wave problems, is a conversion factor that enables us to write the interface stresses in units of 'equivalent displacement' so that errors attributable to the stress and displacement residuals can be compared.

It is more difficult to devise a single measure of the errors for the general elastic wave problems involving arbitrary incident azimuths. Now there are six-component residuals at each irregular interface, and these residuals have different relative effects upon the errors in each of the three components of displacement, say, at the free surface. The representation theorem has a quite complicated vector form in this case. We choose a single 'reasonable' conversion factor for again writing the interface stresses in units of equivalent displacement in order to obtain a single RMSE based upon the six weighted residuals.

The second measure of accuracy follows from the law of conservation of energy. This check, available to us only in cases involving real frequency ω , is derived in Appendix E. It has the advantages that it is easy to compute and that it provides a single measure of error even for the most general arbitrary azimuth problems. In Appendix E, we find that this measure is equivalent to a particular weighting of all the residuals at the

irregular interfaces. Although it is a comparatively insensitive measure of accuracy, the conservation of energy criterion provides the valuable service of confirming that the equations of motion are written correctly in programming for the computer.

In section 4.3, we examine representative examples of the residuals and errors encountered in our solutions. Figures displaying the displacements and stresses along the irregular interfaces provide the most meaningful displays of the errors in the method. However, they are too cumbersome to use for each example presented in this thesis. Instead, we note the RMSE corresponding to the examples shown in section 4.3, and thenceforth use only the errors listed in Table F1 of Appendix F as measures of the accuracy for the examples treated in Chapter V.

The influence of complex frequency on the character of the solutions is discussed in section 4.4. With increasing imaginary part of ω , the loss in resolution for the study of layering effects is compensated by a gain in stability associated with reducing periodicity effects and with reducing the oscillations caused by truncating the wave number spectrum.

The RMSE and conservation of energy error are listed in Table F1 of Appendix F for each example presented in this paper. Also listed in the table are the dimensionless parameters that we judge to be important factors in determining the sizes of the errors. The configurations, types, and sizes of the problems that we have investigated are so diverse that no systematic study was made to predict the size of error expected in a given problem. Rather, in section 4.5, we indicate which problem-parameters seem critical and how the errors generally behave with changes in these parameters. Based upon evaluation of errors in our solutions, we conclude

that for most of our examples the accuracy is limited primarily by the truncation error, and the RMSE is often a conservative measure of the errors for the displacement at the free surface.

The problem solved in section 4.6 by our method and by the finite difference method is that of the response of a low rigidity two-dimensional basin to vertically incident SH waves. The excellent agreement in both the amplitude and phase delay anomalies not only provides a comparative check on the accuracies of the two techniques but also displays the relationship between our complex frequency solutions and transient seismogram solutions.

4.2. Error Measures.

4.2.1. Relative root-mean square error (RMSE). As part of the computer output in each practical case, we plot the stresses and displacements along the irregular interfaces. Visual study of the residual discontinuities provides our best means for qualitatively judging the accuracy. To conserve space, we present only a few representative examples in section 4.3. For the remainder of the problems discussed (those in Chapter V), we use error measures that are conveniently expressed as single numbers which summarize the effects of the residuals in each case.

We define a relative root-mean-square error (RMSE) as a mean value of all the residuals along irregular interfaces divided by a mean value for the fields along the interfaces. In even the simplest problem of SH wave scattering in a layer over a half-space, we must contend with two kinds of residuals - those in stress and those in displacement - at the irregular interface. For the arbitrary azimuth problems there are six kinds of

residuals at each internal irregular interface. We must therefore select some rational scheme for weighting the RMSE associated with each type of residual and thence weighting the effects of residuals at each irregular interface. The most conservative approach would be to compute the RMSE for each component of stress and displacement at each interface and choose the largest as the overall measure.

Our experience indicates that such a measure is too pessimistic and of little practical value. Rather we compute, for a RMSE error at each irregular interface, an average of the six RMSE weighted according to the mean value of the corresponding fields at the interface. The final measure of error is then, for convenience, the largest of the interface RMS errors. That is, at interface m the interface error $(RMSE)_m$ is

$$(RMSE)_m = \frac{\sum_{i=1}^6 \langle u_{mi} \rangle (RMSE)_{mi}}{\sum_{i=1}^6 \langle u_{mi} \rangle} \quad (4.1)$$

In (4.1), the subscripts $i=1,2,3$ refer to the (x,y,z) components of displacement and $i=4,5,6$ refer to the (x,y,z) components of stress along the interface; $\langle u_{mi} \rangle$ is the root-mean-square value of 'equivalent displacement' i at the interface m (the term 'equivalent displacement' implies actual displacement for $i=1,2,3$, and stress measured in equivalent units of displacement for $i=4,5,6$ as described below);

$$\langle u_{mi} \rangle^2 = \sum_{j=1}^J |u_{mij}^A| |u_{mij}^B| \quad (4.2)$$

where u_{mij} is the equivalent displacement i at position j along interface m and superscripts A and B denote values just above and below the interface, respectively. The positions j along the interface are equi-spaced in the

x-coordinate. We take $J=128$ in most cases. Also in (4.1),

$$(RMSE)_{mi}^2 = \frac{\sum_{j=1}^J [|u_{mij}^A| - |u_{mij}^B|]^2}{\langle u_{mij} \rangle^2} \quad (4.3)$$

is the RMSE in equivalent displacement i at interface m . Combining (4.2) and (4.3) in (4.1) gives

$$(RMSE)_m = \frac{\sum_{i=1}^6 \left\{ \sum_{j=1}^J [|u_{mij}^A| - |u_{mij}^B|]^2 \right\}^{1/2}}{\sum_{i=1}^6 \langle u_{mi} \rangle} \quad (4.4)$$

Finally, our practical measure of error for problems involving M irregular interfaces is

$$RMSE = \max_{m=1, M} \{ (RMSE)_m \} \quad (4.5)$$

The conversion factor by which stresses are multiplied to obtain their equivalent values in units of displacement is $1/\rho, \beta, \omega$ for SH wave problems and $1/\rho, (\alpha, \beta)^{1/2} \omega$ for the general wave scattering problems (the subscripts 1 denote parameters for the uppermost layer). These choices are expedient, but reasonable according to the representation theorem arguments in Appendix D.

We do not compute a relative error measure based upon phase residuals. Those residuals are relatively smaller than the amplitude residuals so we let the RMSE based upon amplitudes suffice as the single measure of accuracy.

Of course, no single number can adequately summarize the extent to which interface conditions are not fulfilled. In particular, the RMSE tell nothing of the distribution of residuals along the interfaces and the resulting distribution of errors in displacements along the free surface.

However, comparison of the errors listed in Table F1 of Appendix F with the residuals and errors shown in the figures in section 4.3 provides a representative basis for interpreting the RMSE in problems discussed in the next chapter.

4.2.2. Conservation of energy. For any of the scattering problems considered, the exact solution anywhere in the lower half-space \tilde{n} below the deepest point of interface $\tilde{n}-1$ can be written as a superposition of the upgoing source wave and downgoing scattered waves just as in our approximate solutions. The difference is that the computed wave amplitudes only approximate those of the true solution. Similarly, above the uppermost point of interface 0 in the upper half-space 0, the exact solution is a superposition of upgoing scattered waves.

The true solutions satisfy the following conservation of energy requirement. For problems involving real ω the time averaged net flux of scattered wave energy across a plane at large (constant) depth in half-space \tilde{n} equals that across a plane at large height (constant negative z) in half-space 0. For cases in which interface 0 is a free surface, all the energy must be reflected back toward $z=+\infty$. We shall consider only these latter cases here. In Appendix E, we find that the complex wave amplitudes determined in our solutions must satisfy

$$\frac{\sum_n k_{\beta_n}^2 [\gamma_{\tilde{n},n} |\phi_{\tilde{n},n}^d|^2 + \gamma'_{\tilde{n},n} |\psi_{\tilde{n},n}^d|^2] + \gamma'_{\tilde{n},n} |V_{\tilde{n},n}^d|^2}{k_{\beta_n}^2 [\gamma_0 |\phi^*|^2 + \gamma'_0 |\psi^*|^2] + \gamma'_0 |V^*|^2} = 1 + \delta \quad (4.6)$$

where

$$\gamma_{\tilde{n},n} = [(\omega/\alpha_n)^2 - \kappa_n^2]^{1/2}$$

$$\gamma'_{\tilde{n},n} = [(\omega/\beta_n)^2 - \kappa_n^2]^{1/2}$$

are vertical components of wave number for the n th scattered order down-going waves in half-space \tilde{n} ; $\phi_{\tilde{n},n}^d$, $\psi_{\tilde{n},n}^d$, and $V_{\tilde{n},n}^d$ are the complex amplitudes of the P, SV, and SH waves; and ϕ^* , ψ^* , and V^* are the source wave amplitudes (equation (2.42)), only one of which is nonzero in a given problem. The summation is over the regular plane wave orders only (ω is real here), as explained in Appendix E. In (4.6), δ is a small error term which measures the departure of our solutions from satisfying the conservation of energy flux requirement.

This error is attributable to corresponding departures of the amplitudes $\phi_{\tilde{n},n}^d$, $\psi_{\tilde{n},n}^d$, and $V_{\tilde{n},n}^d$ from the values appropriate to the exact solutions. In Appendix E we demonstrate that δ can be interpreted as a weighted integral of the residuals at the irregular interfaces. A simple interpretation of our computed solutions is that they are the exact solutions to problems involving artificial sources associated with the residuals at the irregular interfaces. These act as sources and sinks of energy resulting in a non-zero time averaged net flux of energy across the planes deep in half-space \tilde{n} .

The error δ is more easily and accurately evaluated, by means of the summation over scattered wave orders on the left side of (4.6), than is the RMSE. However, this error is not a sensitive one for several reasons. First, the phases of the residuals generally oscillate along the interfaces, tending to cancel upon integration and thereby produce small values of δ . Second, this error measure does not have preferential weighting of the larger residuals (localized errors) as does the RMSE criterion. Last, the conservation of energy criterion provides a measure of the error in the solution for half-space \tilde{n} only and states nothing about the solution in the

layers.

The δ errors are listed in Table F1 for all problems involving real frequency. We cannot use this conservation of energy criterion in problems involving complex ω because time averaged energy flux is not conserved when the source time function is non-stationary. Note the very small values of δ in Table F1 for the problems studied. These are much smaller than Meecham (1956) and Heaps (1957) found in scalar problems involving acoustic wave scattering at rigid and free grating boundaries. Our solutions are comparatively more accurate because they were represented in terms of larger numbers of scattered wave orders.

4.3. Examples of Errors.

4.3.1. Truncation error. In Figure 4.1, are compared two solutions to a single scattering problem obtained using different truncation numbers N , where $2N+1$ is the number of scattered wave orders. The problem configuration is shown at the bottom of the figure. An SH wave (particle motion normal to the plane of the figure) of wavelength 50 km is incident vertically upon a two-dimensional basin 5 km deep by 50 km wide. The interface between the low-rigidity basin and the half-space has the shape of a single cycle cosine for $|x-x_0| \leq W/2$ and is flat outside this interval. That is

$$\zeta(x) = \begin{cases} D + \frac{c}{2} \left[1 - \cos \frac{2\pi(x-x_0-W/2)}{W} \right] ; & |x-x_0| \leq W/2 \\ D & ; |x-x_0| > W/2 \end{cases} \quad (4.7)$$

where D is the thickness of the layer in the flat portion away from the interface shape irregularity, c is the amplitude of the irregularity, W is

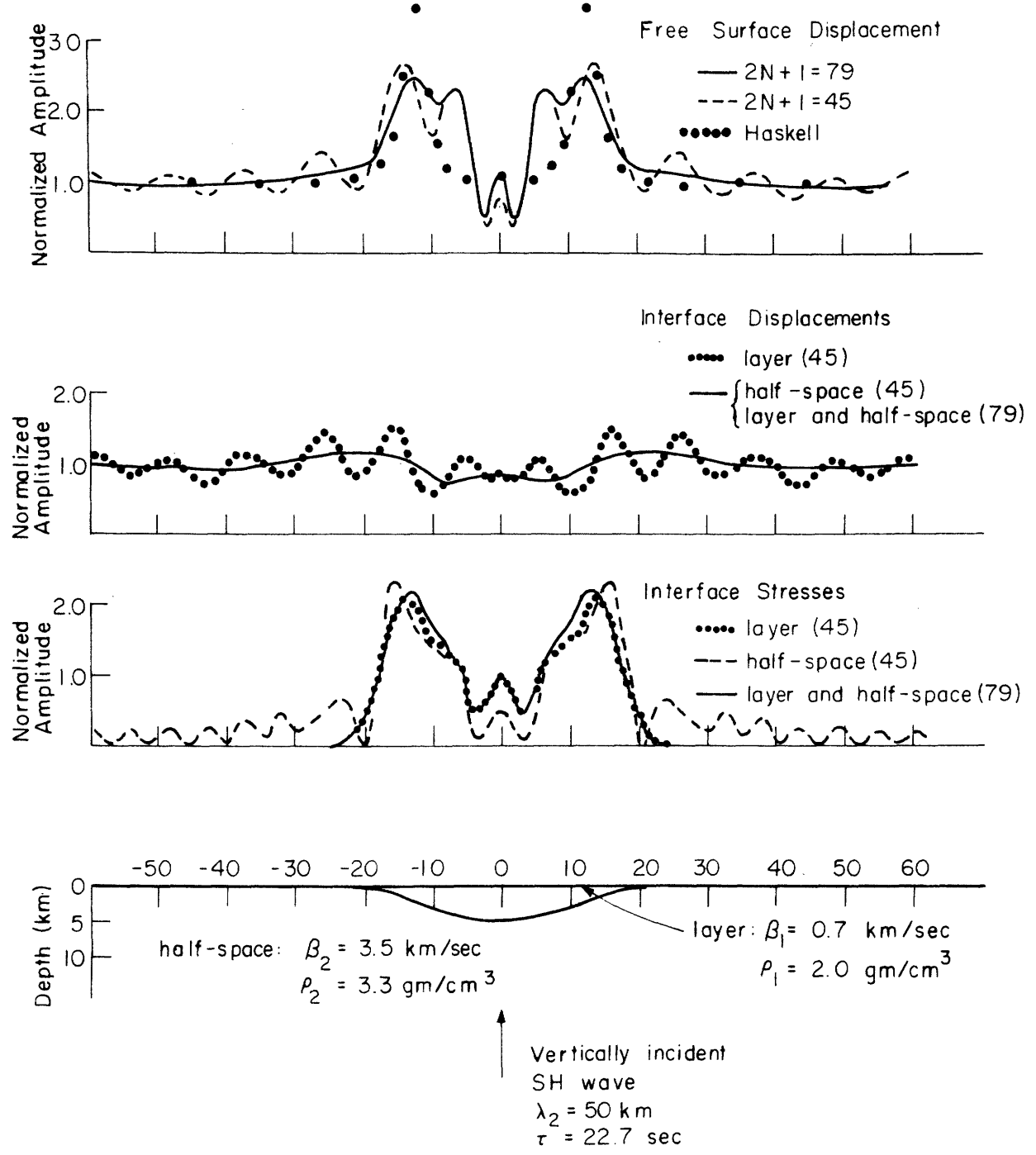


Figure 4.1. Spatial distributions of the normalized amplitude of free surface displacement, interface displacement, and interface stress displaying truncation errors for a soft basin problem. N is the truncation index. The Haskell solution is for motion at the surface of a flat layer having the local thickness beneath the observation position.

the width of the irregularity, and x_0 is the x-coordinate of the center of the anomaly (this shape repeats with periodicity $L=256$ km in the x-direction). In this problem $D=0.01$ km, $c=5.0$ km, $W=50$ km, and $x_0=0$. The simple analytic expression (4.7) for interface shape is used in many of the examples discussed later. It was chosen for convenience, and lends meaning to the width W and amplitude c for problems involving varying sizes of interface anomaly. In our method, the interface shapes can be quite arbitrary and could just as well be described numerically.

The solutions shown in Figure 4.1 were obtained using $2N+1=45$ and 79 scattered wave orders respectively. Spatial distributions of the amplitudes of displacement and stress at the interface are plotted in the middle of the figure. The displacement amplitudes were normalized by dividing by the amplitude of the free surface displacement obtained for the companion problem of a 0.01 km thick flat layer (with the irregularity removed) over a half-space. The stress amplitudes were normalized likewise after first multiplying by $1/\rho, \beta, \omega$ to obtain equivalent displacement amplitudes. When 45 coefficients are used to describe the scattered wave field, the interface displacements in the layer (dotted curve) oscillate about those in the half-space (solid line). When 79 coefficients are used, the interface displacements in both media are given by the same solid line. Thus, when an insufficient number (45) of scattered wave orders are used to represent the solution, the displacements in the half-space are well approximated whereas those in the layer are not. The reverse is true for the stresses at the interface.

This behavior is peculiar to the particular medium configuration and wavelengths in this problem. Since the stress-free requirement is

satisfied identically at the free surface, and the irregular interface is close to the free surface (particularly in the flat portion), the stresses must nearly vanish throughout the layer over the flat portion. Thus, when we approximately match boundary conditions, the stresses in the layer are somewhat predetermined. Since no similar requirement was imposed on displacements in the layer, the layer displacements are less well determined than are the layer stresses.

The RMSE in displacement residuals are 12% and 0.2%, and the RMSE in stress residuals are 42% and 1.9% for the 45 and 79 coefficient solutions respectively. Most of the contribution to the stress RMSE is from the flat portion of the interface where the mean stress nearly vanishes. Obviously, since the RMSE are small when 79 coefficients are used, the inherent error is insignificant in this problem and the free surface displacements are accurately computed.

The curves at the top of Figure 4.1 are the two solutions for amplitude of free surface displacement (normalized in the manner already described). The spatial distribution obtained using only 45 coefficients has the large-scale characteristics of the more accurate solution but oscillates about it. As we shall see later, these oscillations are caused by the abrupt truncation of the wave number spectrum. These errors are comparable in size to the displacement residuals at the interface, but are relatively insensitive to the large stress residuals over the flat portion of the interface. As is suggested in the discussion of equation (D6) in Appendix D, errors in the free surface displacement are more strongly governed by displacement residuals than by stress residuals when the layer thickness is small. In another example (Figure 4.3) where the layer thickness is greater, the errors are

dependent upon both residuals but decay with increasing distance from the irregular interface.

The dots at the top of Figure 4.1 are normalized amplitudes of displacement at the free surface computed using the local Thompson-Haskell approximation assuming that the layer has uniform thickness equal to the local thickness. Further comparisons with the flat-layer theory are described in Chapter V.

It is instructive to study the (x-component) wave number spectrum for this example. Figure 4.2 is such a plot of the scattered wave amplitudes $|v_{1,n}^u|$ versus the scatter order n (see equation (3.10)). The amplitude scale is in decibels below the amplitude of the primary ($n=0$) wave. For this case of vertical incidence, the wave amplitudes are even functions of n and we show only those for positive n . The wave amplitudes in the 45 and 79 coefficient solutions have similar dependence upon n . This suggests that the wave amplitudes are computed with some degree of finality and that the residuals and errors in Figure 4.1 are caused primarily by the abrupt truncation of the wave number spectrum. Indeed, the oscillation wavelength of approximately $11\frac{1}{2}$ km in the free surface displacement distribution can be ascribed to the interference of waves having the cutoff wave number $N=22$ with the primary wave. Such truncation errors are easily detected in our solutions.

The wave number spectrum displays other interesting features. Although the primary wave dominates the spectrum (because the layer is flat over much of the interval $0 \leq x \leq L$), the amplitudes decay slowly with increasing $|n|$ until $|n| \approx 25$ and even increase between $|n|=11$ and $|n|=18$. This wave number coupling is not insignificant. Such wave number coupling is partly

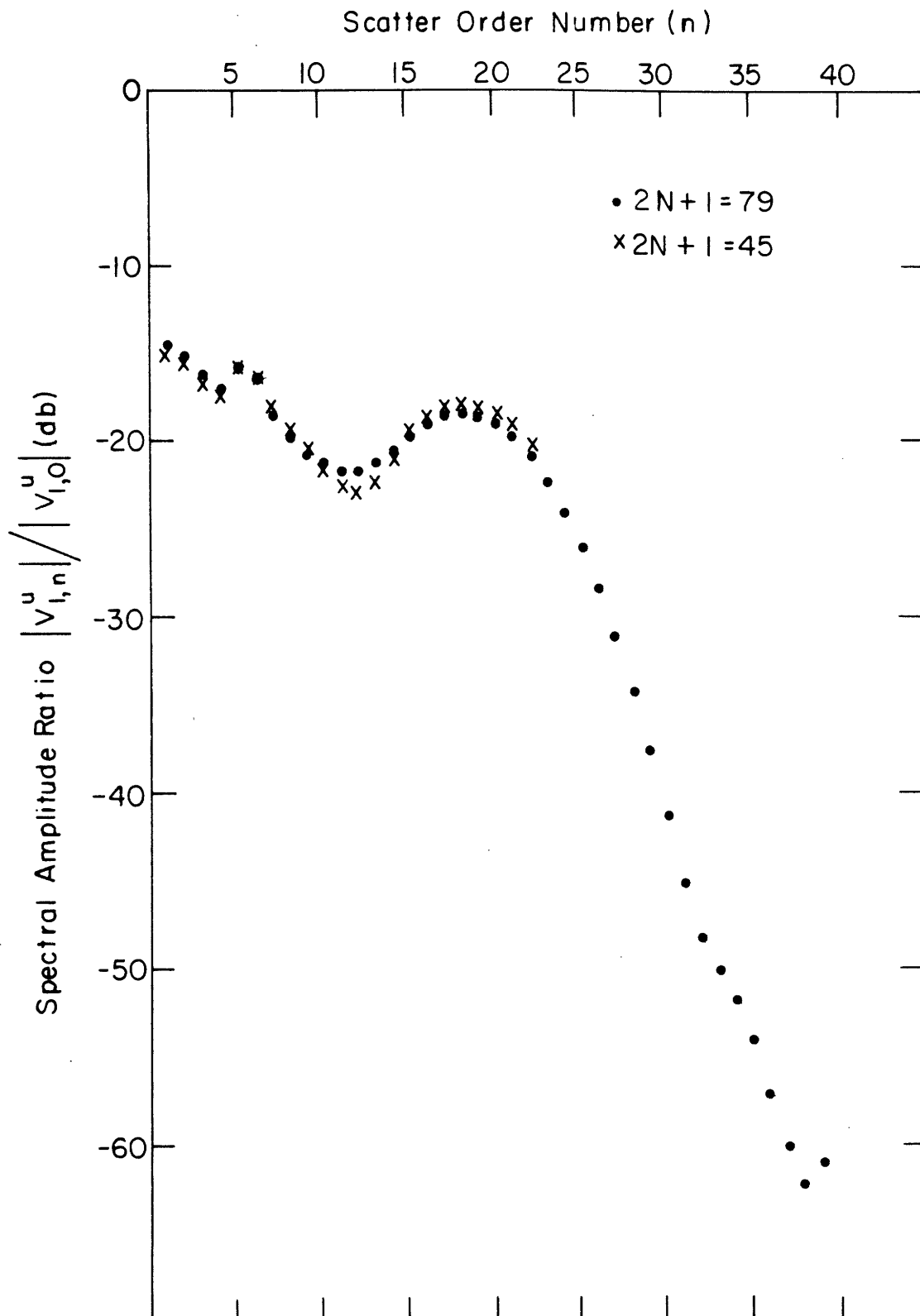


Figure 4.2. Wave number spectra for the two examples in Figure 4.1. $|v_{l,n}^u|$ is the amplitude of the nth order upgoing scatter wave at the free surface.

a manifestation of wave diffraction, but in this problem is predominantly caused by multiple reflections within the layer. The amplitudes decay rapidly beyond $|n| \approx 25$ because this value corresponds approximately to the wave number ω/β , of S waves in the layer (we say 'approximately' because frequency is complex in this example). In fact, we find that the truncation errors in this problem are measurably reduced when we use $2N+1=53$ scattered wave orders to describe the solution. The jump in the wave number spectrum at $n=5$ occurs for scattered waves that are nearly grazing (propagating nearly horizontally) in the half-space. Further examples of wave number coupling are discussed in Chapter V.

The observations made for this SH wave problem apply to comparable problems involving P-SV motion and problems involving arbitrary azimuth incidence. Let us now consider another example of a single layer over a half-space, but now the layer thickness is larger relative to the wavelengths in the problem. Figure 4.3 shows two solutions to the scattering of vertically incident P waves in a layer over a half-space. The medium parameters are apropos of a simple model of the crust and upper mantle. The layer thickness is given by (4.7) with $D=30$ km, $c=5$ km, $W=40$ km, and $x_0=0$. The P-wave wavelength in the half-space is 20 km (15 km in the layer) corresponding to a frequency $f=0.4$ cps. The decay time associated with this complex frequency solution is 9.95 sec. Since the one-way travel time for P waves propagating vertically through the layer is 5 sec, the solutions at the free surface have only small contributions from multiple reverberations within the layer.

Solutions were computed using $2N+1=17$ and 41 scatter orders. Continuity of the normal component of stress at the interface is well satisfied for the

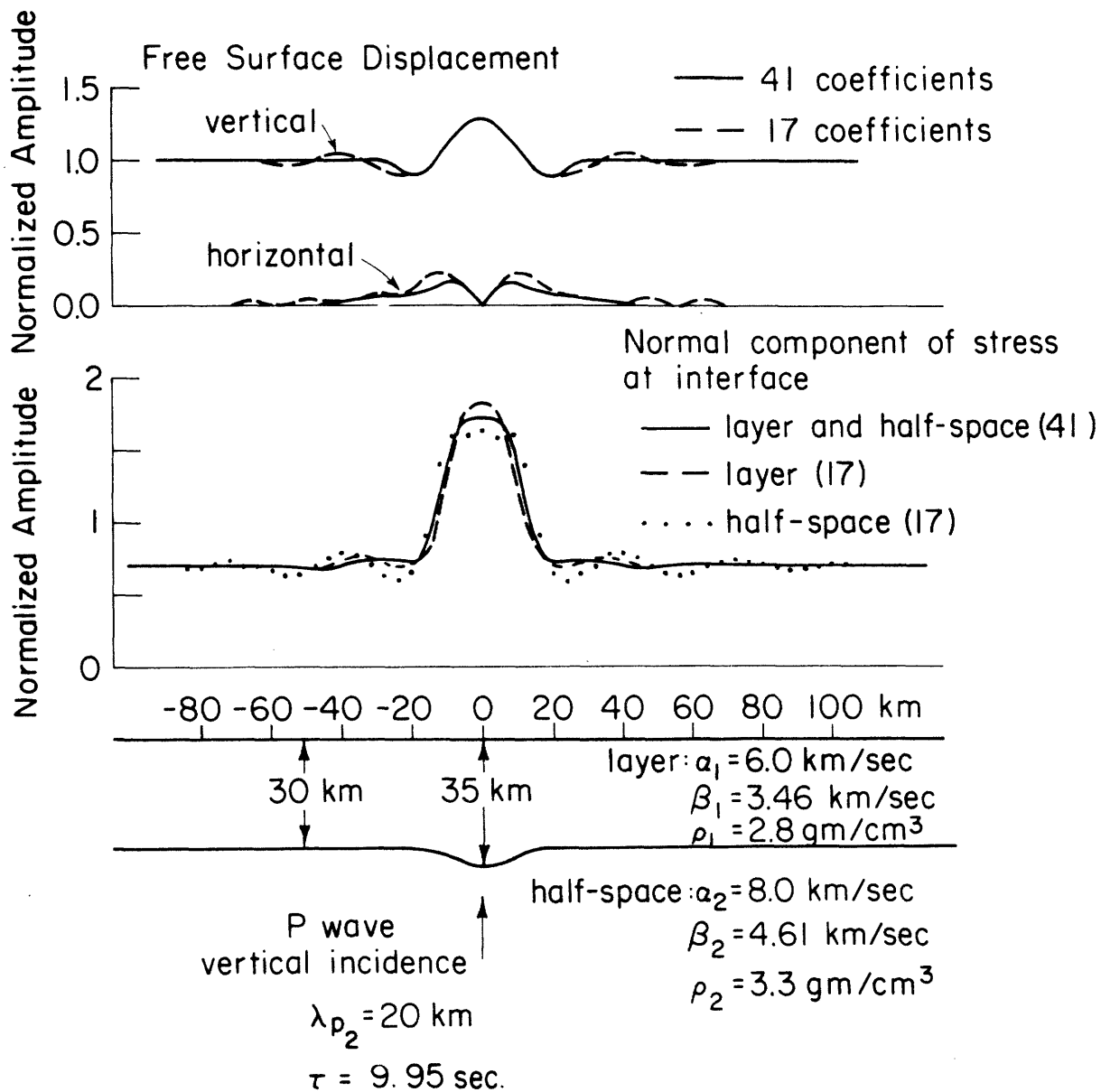


Figure 4.3. Spatial distributions of normalized amplitude of the two components of surface displacement and the normal component of stress at the interface, displaying truncation errors for a problem involving P-wave scattering at a dented Moho. Normalization is with respect to the vertical component of displacement at the free surface for the 30-km thick flat layer problem.

41 coefficient solution, whereas the interface residuals are large and oscillatory for the 17 coefficient solution. The residuals are largest near the interface anomaly but are well distributed along the interface. Comparable size residuals are observed for the normal component of displacement and the tangential components of stress and displacement (not shown here). We have shown only amplitude residuals in Figures 4.1 and 4.3. The phase residuals have similar behavior but are relatively smaller.

The normalized amplitudes of the horizontal and vertical displacements at the free surface are shown at the top of the figure. (The normalization of all the distributions shown is with respect to the amplitude of the vertical component of displacement in the corresponding flat-layer problem). The displacement at the free surface computed using only 17 coefficients is better than would be inferred from the sizes of the interface residuals. Note that the errors are larger for the horizontal component of motion. This is because SV waves dominate the horizontal motion while the longer P waves dominate the vertical motion. Truncation of the wave number spectrum is generally more deleterious to the shorter wave contributions to the solutions because those scattered waves span a narrower range about the primary wave direction than do the longer wavelength scattered waves.

The errors in the layer decay with increasing distance from the interface because the residuals are attributable primarily to the higher order wave number terms which attenuate away from the interface due to our smoothing with complex frequency. Thus, the RMSE can be a conservative estimate of the accuracy of the motion at the free surface. In cases that involve real ω , however, the errors at the free surface need not be smaller than those at the irregular interface.

It is of great practical importance to know that we can often obtain good solutions at the free surface while tolerating sizeable residuals at the interface, because of the significant savings in computation time for problems involving fewer scatter orders.

4.3.2. Inherent error. In some problems, we encounter relatively large interface residuals that cannot be reduced by increasing the number of scattered wave orders. In fact these residual errors may increase as more scatter orders are included. This type of error may be the intrinsic error in our Rayleigh-type formulation of the solutions as superpositions of plane waves. Uretzky (1965) suggests that the intrinsic error is manifested by asymptotic or semi-convergent behavior of the series representation in equations like (3.8). That is, as N increases from small values, the series approximation first approaches toward then diverges from the true solution. This is the behavior exhibited in the example shown in Figure 4.4.

In this problem, a 10 km wavelength SH wave (particle motion in the y -direction) is incident at $\theta_0 = 40^\circ$ from vertical upon a layer 25 km thick with a severe irregularity (step) at which the thickness varies 5 km. The shape of the step is a cosine for a half-cycle cosine (with wavelength 8 km) connected to half-wavelength cosines on both sides. The frequency is again 0.4 cps, and $\tau = 3.98$ sec as compared with $t_u = 8.33$ sec, the one-way travel time vertically through the layer. Therefore, the observed motion at the free surface is essentially devoid of contributions from multiple reflections.

The stresses at the interface (solid curves for the layer and dashed curves for the half-space) are displayed in the middle of the figure for

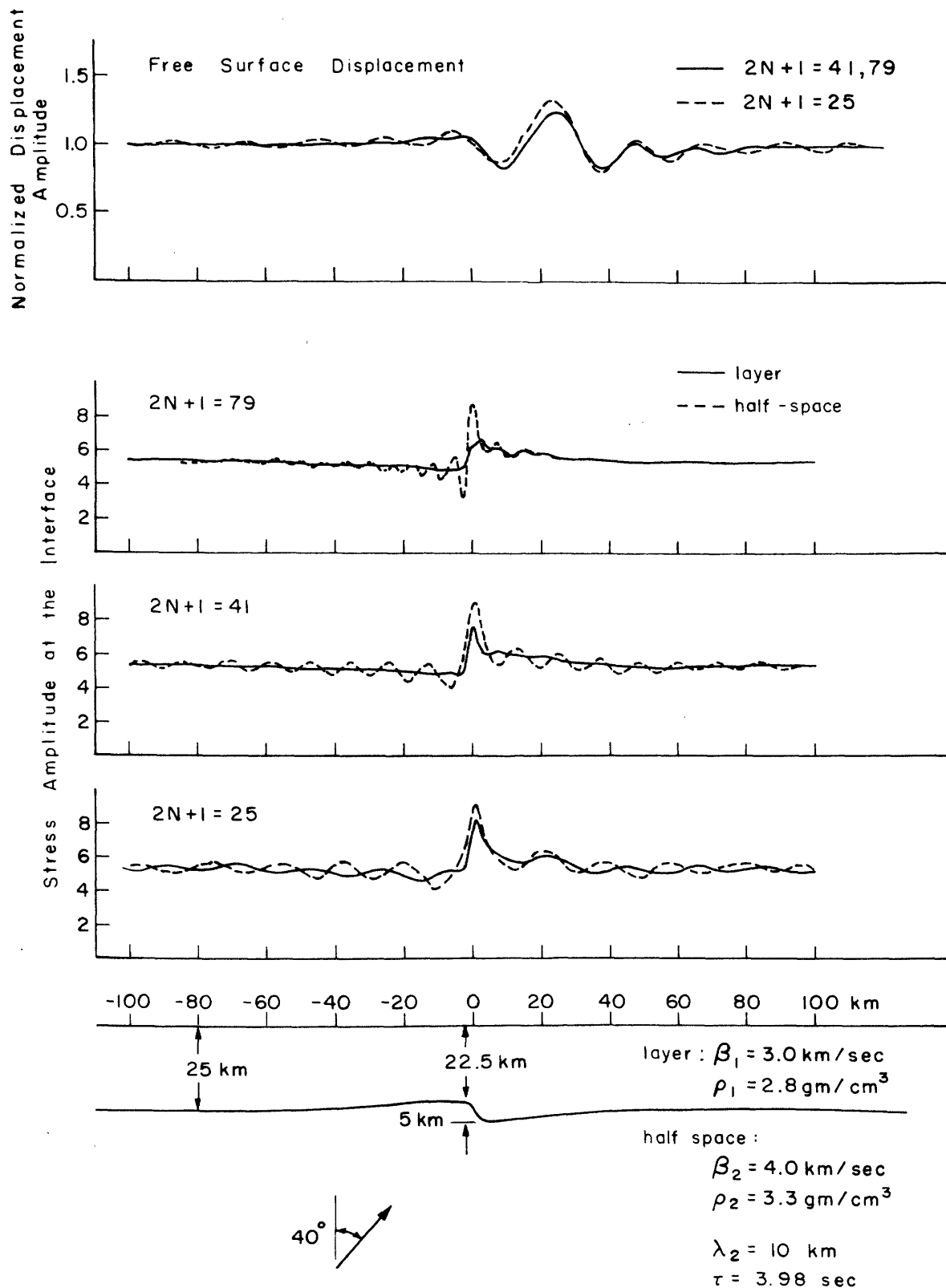


Figure 4.4. Examples of the irremovable residuals in stress at the interface for the problem of SH wave scattering at a step-shaped irregularity in the Moho. N is the truncation index.

three solutions obtained using $2N+1=25$, 41, and 79 coefficients. These normalized quantities are larger than the displacements at the free surface because they are viewed at the present time $t=0$ whereas the motion at the free surface is the response to interface motion in the past when the exponentially increasing source time function was smaller. The RMSE in stress residuals for these solutions are 0.0607, 0.0600, and 0.0640 as $2N+1$ increases through the three values. Another solution (not shown) obtained with $2N+1=61$ gave an RMSE in stress residuals of 0.0612. The sizes of these RMSE do not reflect the large residuals localized at the step although they are determined predominantly by them. In the 25 coefficient case, the truncation error is manifested as an oscillation of stresses in both media. As N increases, the oscillations in the layer diminish as does the stress RMSE slightly. However, as N increases further, the stress RMSE increases while the spatial oscillations in the half-space become more rapid and the oscillation amplitudes become larger and more concentrated near the step.

The number of coefficients beyond which the displacement residuals become divergent is generally different from that beyond which the stress residuals diverge. In the 25, 41, 61, and 79-coefficient solutions, the RMSE displacement residuals are 0.0816, 0.0480, 0.0196, and 0.0145 respectively. We have observed other solutions where the RMSE diverges more dramatically with increasing N . Those cases involve comparably steep interface slopes with larger interface shape amplitudes c relative to wavelength and invariably the RMSE are much larger than those shown here. The same oscillatory behavior of the interface stresses in the source wave medium is observed in those cases. Interestingly, however, the solutions in the layer remain stable as N increases. The free surface displacements

in Figure 4.4 typify this behavior. Although the localized stress residuals change significantly between the 41- and 79- coefficient solutions, the free surface displacement distributions are indistinguishable. Even the 25-coefficient solution for free surface motion is better than the interface stresses imply. One possible explanation is that the surface motion is controlled predominantly by interface displacements (rather than by stresses) whose residuals are well distributed along the interface. Another is that the stresses at the interface exhibit the behavior of the Gibb's phenomenon in which case, as N increases, the errors tend toward an irremovable limit but are so localized as to be ineffective sources for displacements removed from the interface. In any case, these solutions do not diverge radically as N increases to the maximum value allowed.

The question of the validity of the solutions for free surface motion in these cases is important because the stepped interface problems might be useful models for crustal layers offset by steeply dipping faults. An adequate check of the validity of the solutions must await independent solutions obtained by other techniques.

The examples considered in Figures 4.1, 4.3, and 4.4 are representative of the types of errors encountered in the problems to be discussed below. By far, most of the solutions that we obtain are limited by truncation errors; that is, errors that decrease with increasing values of N . The fact that our solutions suffer from an error inherent in the formulation is not of serious concern in most of the layer configurations that interest us. Most surprisingly, we even find that the existence of shadow zones in our problems does not imply large inherent errors. The residual errors are found not to depend systematically upon the angle of incidence. The

solutions appear to be valid even to grazing incidence ($\theta_0 = \pi/2$).

4.4. Smoothing Effects of Complex Frequency.

The use of complex frequency enhances the accuracy of the solutions in several ways. The most obvious example is when its use displaces the poles associated with trapped modes in plane layered media away from the summation path in the k-plane. No examples are given here since the errors resulting from the Gaussian elimination solution of equations having a nearly singular coefficient matrix are large and quite evident. For problems that are nonsingular for real ω , the RMSE are reduced somewhat by making ω complex while the errors away from the interface can be reduced significantly. The residuals at the irregular interface may be considered as sources of error fields. We have seen that the largest contributions to truncation errors are from the higher order scattered waves. With ω complex, the amplitudes of the scattered waves decrease with distance from the irregular interface, with the rate of decrease being greatest for the higher order (larger x-component of wavenumber) waves. Thus, introduction of complex ω results in smaller errors at the free surface.

Figure 4.5 demonstrates the stabilizing and smoothing of the computed free surface displacements effected by the use of complex frequency. This is an SH wave motion problem involving a half-space overlain by a layer $6\frac{1}{4}$ wavelengths thick with a 5 km by 50 km depression in the interface (equation (4.7) with $x_0=125$ km). A 10 km wavelength (in the half-space) wave is incident vertically. Normalized displacement amplitudes are shown for the three cases $\xi = \omega_I/\omega_R = 0, 0.01, \text{ and } 0.1$ (corresponding to $T = 1/\omega_I = \infty, 39.8, \text{ and } 3.98$ sec respectively). The amplitude scale applies

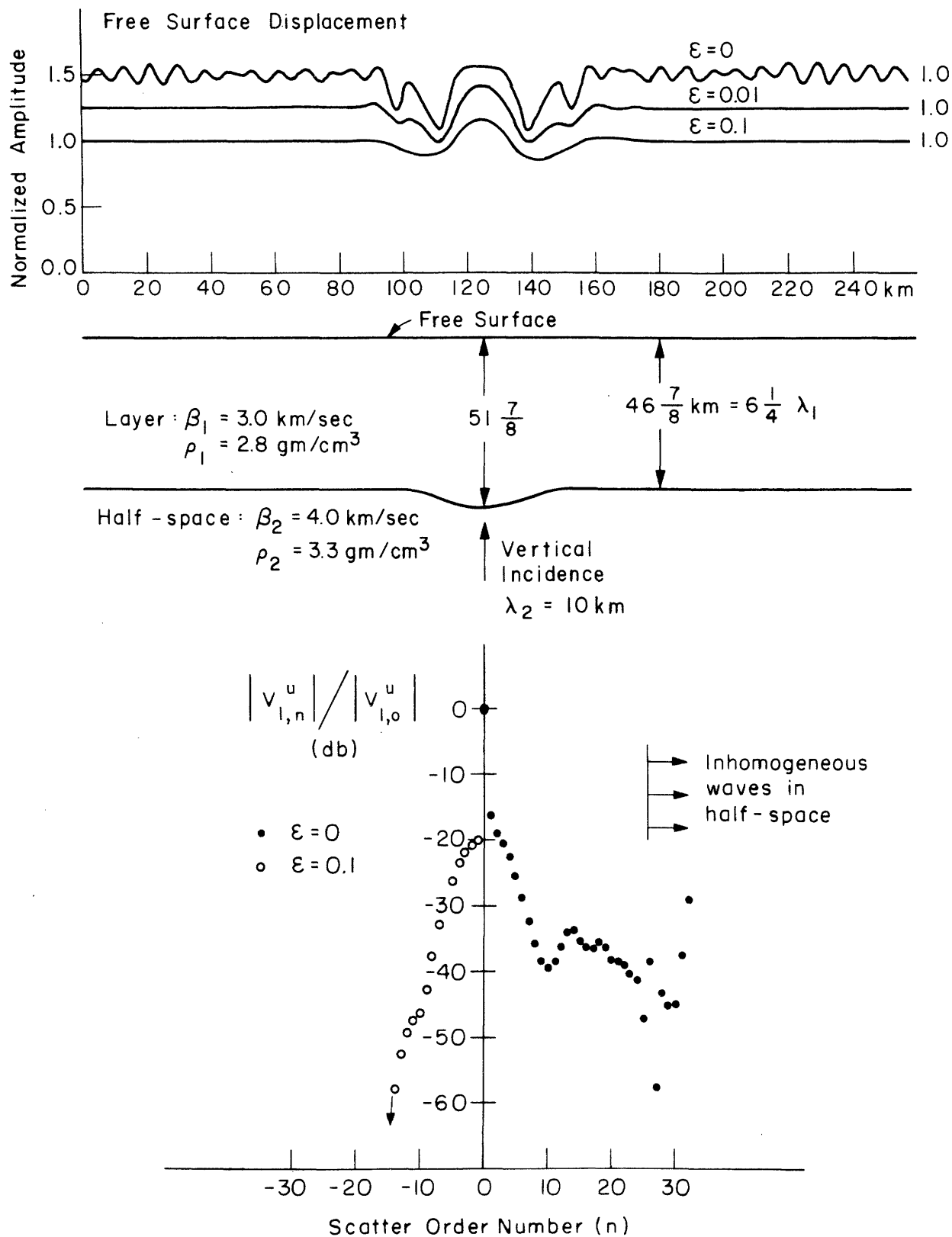


Figure 4.5. (Upper portion). Demonstration of the smoothing of the spatial distribution of amplitude at the free surface effected by varying the imaginary part of frequency: case of SH waves scattered at a dented Moho. ε is the ratio of the imaginary to real parts of frequency.
(Lower portion). Wave number spectra for two of the cases.

to the $\xi=0.1$ curves; the other curves are displaced upward. The use of complex frequency damps the oscillations along the limbs of the $\xi=0$ distribution. Those oscillations have 8-km wavelength, characteristic of the cutoff wavenumber ($N=32$ in these examples), and are thus caused by the sharp cutoff of the wave number spectrum. The larger inner two or three side lobes in the top curve are actual lateral wave interference effects. Increasing ω_I smooths out these side lobes.

In the case of real frequency, according to flat-layer wave theory, the layer vibrates in a resonance condition where the thickness is $6\frac{1}{4}$ wavelengths (see the discussion of the soft basin cases in Chapter V). The dips in the $\xi=0$ distribution either side of the flat portion over the center are explained in terms of anti-resonance in the flat-layer theory rather than by ray theory defocusing with focusing over the center. When the frequency becomes complex, these vertical interference effects deteriorate with the results that the main side lobes are less deep and the amplitude at the center of the anomaly is increased. The introduction of complex frequency alters the surface displacement distribution from one that is dominated by single frequency interference effects to one dominated by wave focusing effects.

The wave number spectra for the $\xi=0$ and $\xi=0.1$ cases, shown at the bottom of Figure 4.5, support some of the comments above. $|V_{1,n}^u|$ is the amplitude of waves upgoing in the layer with horizontal wave number $k_n=2\pi n/L$. For normal incidence the spectra are symmetric about $n=0$; thus the $\xi=0$ amplitudes are plotted only to the right, and the $\xi=0.1$ amplitudes only to the left of the $n=0$ line. For $\xi=0$, the amplitudes do not decay sufficiently rapidly out to the cutoff wavenumber, thus causing

the 8-km oscillations already mentioned. This significant wave number coupling is caused by multiple reverberations within the layer rather than by diffraction, as we shall see below. Waves scattered by the other interface depressions spaced $L=256$ km apart are propagating in both directions across the basic interval $0 \leq x < L$ thus causing the large amplitudes in the high scatter order terms. When ω is complex, the waves propagating in the higher wave number directions are so attenuated that the scattered waves from repeated depressions are insensible within the interval $0 \leq x < L$. In that case, the amplitude anomaly, albeit a smoothed one, is localized. The fact that in the $\xi=0.1$ case the wave amplitudes are very small for $|n| > 13$ does not imply that those waves are not required to adequately match conditions at the interface. The values $|V_{i,n}^u|$ are the actual amplitudes at the free surface. At the interface, the actual amplitudes are

$$|V_{i,n}^u| [\cos^2 \operatorname{Re}(\gamma'_{i,n}) \zeta \cosh^2 \operatorname{Im}(\gamma'_{i,n}) \zeta + \sin^2 \operatorname{Re}(\gamma'_{i,n}) \zeta \sinh^2 \operatorname{Im}(\gamma'_{i,n}) \zeta]^{1/2}$$

and it is readily demonstrated that the imaginary part of the vertical component of wave number $\operatorname{Im}(\gamma'_{i,n})$ increases with $|n|$. Thus the actual amplitudes of the higher order waves are not necessarily small at the interface.

The effectiveness of using complex ω to inhibit the influence of layering in our solutions is demonstrated in Figure 4.6. The interface shape, medium parameters, and wavelength are unchanged from those in the previous example. Here, we compare the displacement and time delay distributions along the $z=0$ plane for three cases. In each case, 10-km wavelength SH waves are incident at $\Theta_0 = 55^\circ$ from vertical in the lower half-space (medium 2). In two of the cases, the upper medium is a half-

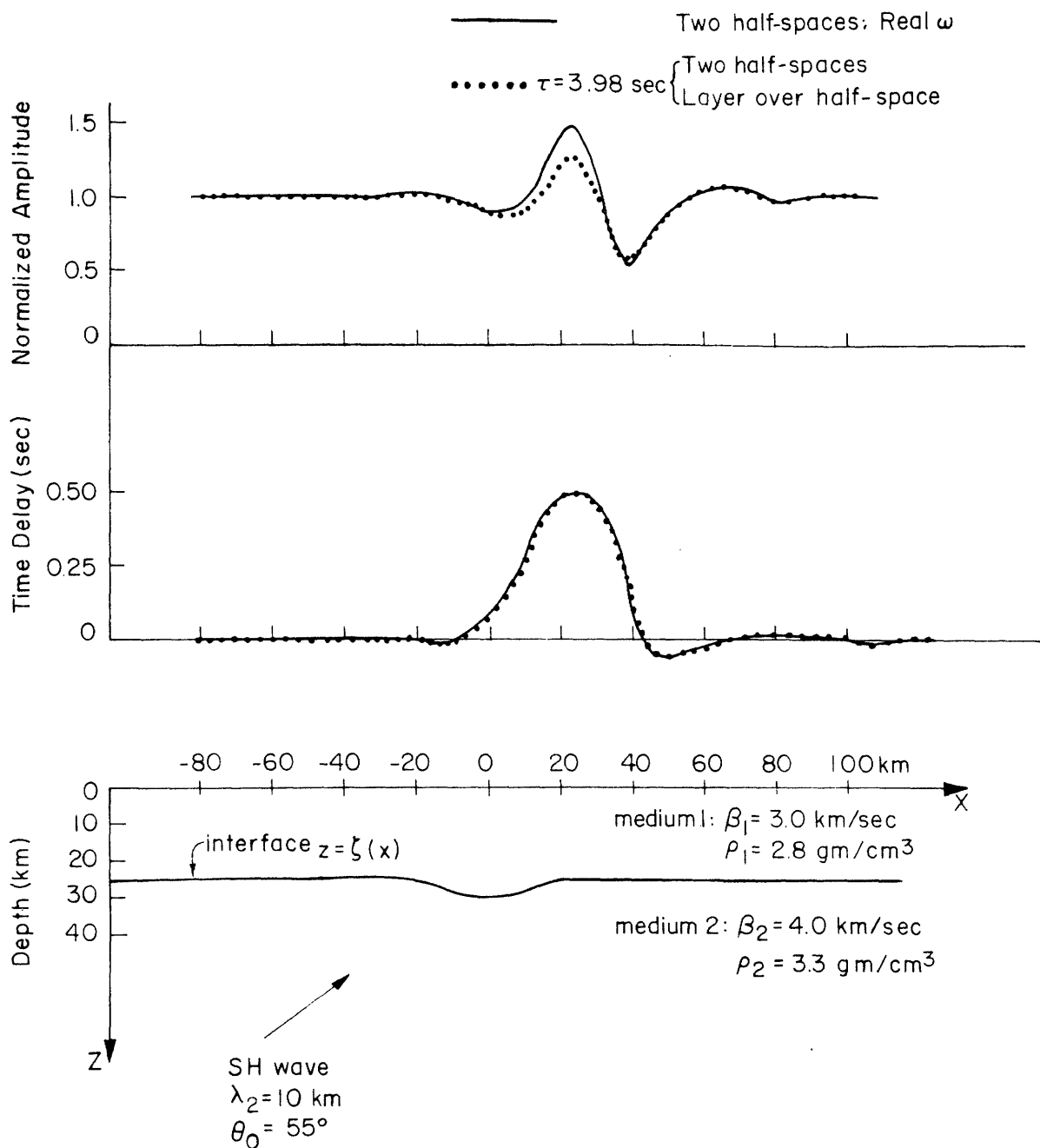


Figure 4.6. Spatial distributions of normalized amplitude and time delay for displacement along the plane $z=0$ for three problems, demonstrating the removal of layering effects when the decay time $1/\omega_I$ is short compared travel time through the layer. Time delay is relative to that for the corresponding plane interface problem.

space so that no layers are available in which multiple reflections can arise. These cases involve, respectively, real frequency ($\tau = \infty$) and complex frequency ($\tau = 3.98$ sec). The amplitudes and times are normalized to the solutions obtained for the corresponding problems involving half-spaces separated by a plane interface. In the third case, medium 1 is a layer and the plane $z=0$ is a free surface. In all cases, the depth to the flat portion of the interface is 25 km. Not shown in the figure are the amplitude and time delay distributions for a fourth case - that of real frequency waves where medium 1 is a surface layer. Those distributions display large oscillations (normalized amplitude varies from 0 to more than 4), for all values of x , that are caused by the interference between primary waves and the waves having the cutoff wave number. Although the RMSE (Table F1) are larger than those in the three more stable solutions shown in the figure, they are still small. In other words, to the accuracy indicated by the RMSE, those oscillatory amplitudes and phases time delays are the correct solutions to the problems involving periodic interface shape. When the layer is replaced by a half-space (also with ω real), the amplitude and time delay distributions become stable; that is, these distributions become flat and normalize to unity and zero, respectively, away from the anomalies. We conclude that the anomalies pictured are truly localized phenomena attributable to scattering from the single interface depression shown. Thus in the absence of layering, the periodic nature of the interface introduces no artificialities relative to the desired solution for scattering from an isolated anomaly. If the observation plane were removed further from the interface such that $D \gg L$, then the displacement anomalies from nearby irregularities would overlap. When $D \gg L$, the interface appears to an observer at $z=0$ to be a grating. Therefore,

only the near-field portions ($D \ll L$) of our solutions are meaningful as solutions to scattering from isolated interface irregularities. In practice, this means that the interface irregularities are generally less than 10 or 20 wavelengths distant from the receiver stations. We might remark that the study of scattering from isolated irregularities is but one use for our method. The interference between waves scattered from nearby irregularities is not without interest. By varying the imaginary part of frequency we can, in effect, control the number of repeated interface irregularities involved in a given problem.

Consider now the complex ω solutions shown in Figure 4.6. When $\tau = 3.98$ sec, the difference between the solutions at $z=0$ to the layer problem and to the half-space problem are too small to indicate in the figure. Evidently, the effects of all multiples within the layer are removed from the solution when $\omega_i = 1/\tau$ is this large. Thus the amplitude and time delay anomalies are appropriate to the first arrivals and might be compared with seismogram peak-to-trough amplitudes and first motion arrival times. In fact, the time delay distributions for the complex cases are indistinguishable from that for the real ω case shown. Even the reduction in peak amplitude at $x=23$ km is explained simply in terms of the diminution of a peak-to-trough amplitude caused by multiplying a transient solution by the exponential window $e^{-t/3.98}$. The arrival at $x=23$ km is delayed by 0.493 sec so that the window should reduce the amplitude by the factor $e^{-0.493/3.98} = 0.88$. The reduction observed in Figure 4.6 is 0.86.

The final example of the influence of complex frequency is shown in Figure 4.7. A 20-km wavelength P wave is vertically incident in a layer

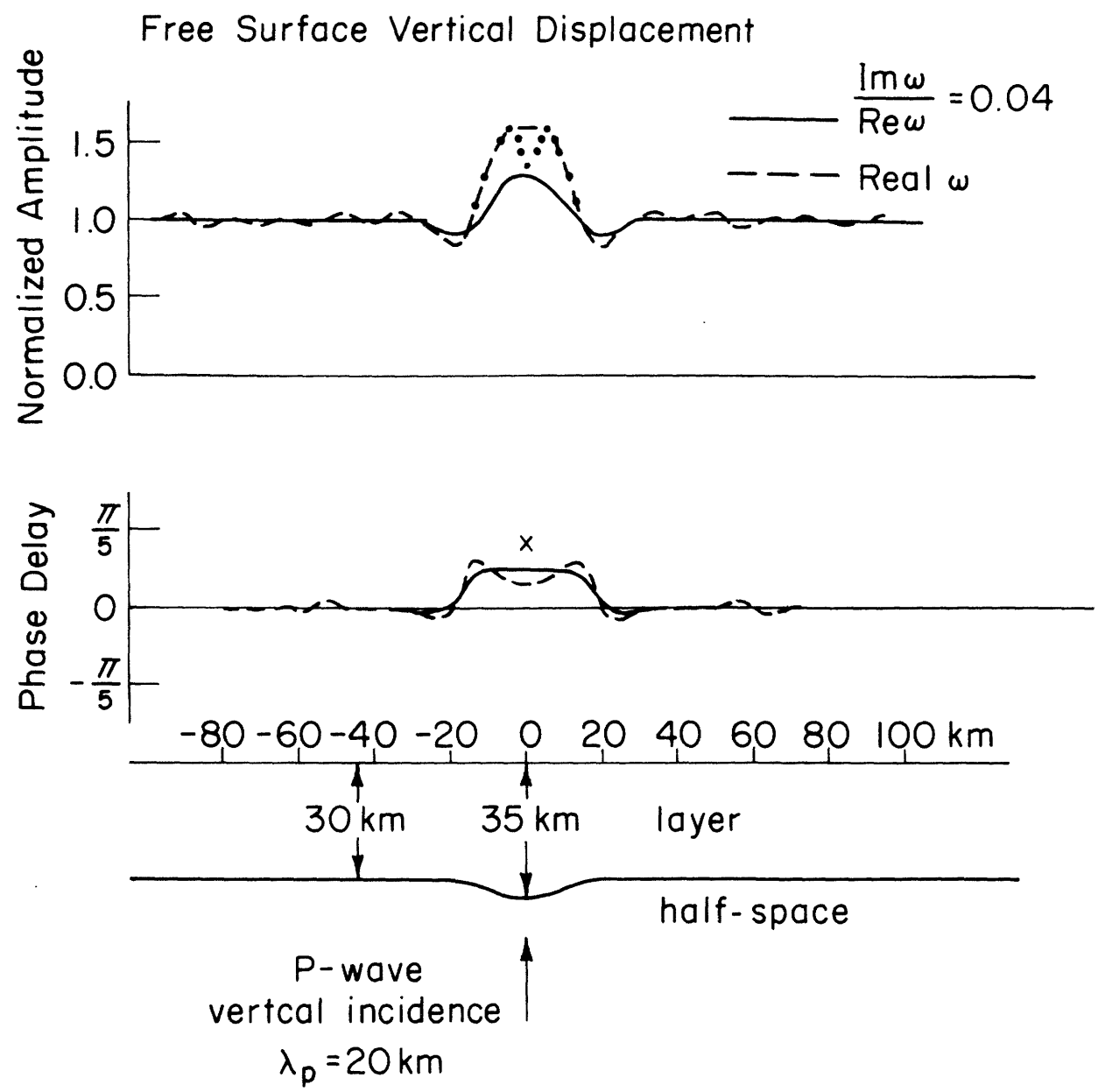


Figure 4.7. Spatial distributions of normalized amplitude and phase delay for vertical displacement at the free surface demonstrating the influence of complex frequency in the problem of the scattering of P waves at a depression in the Moho.

over half-space problem. The interface shape is the cosine depression (equation (4.7)) with $D=30$ km, $c=5$ km, $W=40$ km, and $x_0=0$. The vertical component of displacement is shown for cases involving $\epsilon=0$ and $\epsilon=0.04$ (corresponding to $\tau = \infty$ and 9.95 sec). As in the SH wave example, introduction of ω_I reduces the oscillations away from the anomalies and reduces the variation in the amplitude anomaly. The dots are amplitudes predicted using the local Thompson-Haskell flat-layer approximation (with real ω) that the layer is flat, having the local thickness directly beneath the observation point. Our real ω solution is surprisingly like that of the flat-layer approximation considering the ample opportunity for multiples to be deflected from the vertical propagation directions required in the flat-layer theory. Our solution does not follow the flat-layer solution directly over the irregularity because of the extreme sensitivity of the narrow dip in the flat-layer solution to strictly vertically propagating wave interference. The X in the phase delay plot is the phase delay predicted by considering the one way travel time delay for a ray passing through the center of the depression (this phase delay is nearly the same as that determined using the local Thompson-Haskell approximation). Neither of the two phase delays computed by our method is as large as that predicted by the ray theory. This discrepancy is found to be wavelength dependent; i.e., the solutions exhibit phase dispersion. The flat, plateau-like anomaly in the complex ω case is characteristic of the phase delay anomalies that we observe when wavelength is comparable to the width of the irregularity. The oscillation in the real ω phase delay anomaly is explained as a result of interference of scattered waves propagating in oblique directions.

4.5. Critical Parameters.

The sizes of the truncation errors and inherent errors encountered depend upon several critical dimensionless quantities. Because such a large number of problem parameters are involved and computational costs inhibited systematic evaluation of their effects, a discussion of the influence of the parameters must be qualitative. Suppose that a general problem configuration (i.e., number of layers, medium parameters, layer thicknesses) and the number of scattered wave orders ($2N+1$) are fixed. Also suppose that the shape, but not maximum amplitude or width, of the irregular interface is fixed.

The most critical parameters are c/λ and S_M , where $c = \zeta_{\max} - \zeta_{\min}$ is the amplitude of the interface irregularity, λ is the shortest wavelength in the problem, and $S_M = \left| \frac{d\zeta}{dx} \right|_{\max}$ is the maximum gradient of an irregular interface. The accuracy generally declines as either c/λ or S_M increases, doing so quite rapidly when the two parameters increase simultaneously. At interfaces having large slopes S_M , waves are scattered over a wide fan of directions and thus a large number of coefficients N would seem to be required to describe the scattered field. At the same time, however, the inherent error associated with the incomplete description of the wave field increases as N increases. The result is that the minimum attainable error in our asymptotic solutions increases with S_M .

The behavior of the errors with c/λ is complicated by another dimensionless parameter L/λ , where L is the interface periodicity length. Suppose, for example, we wished to study the dependence of our solutions upon the ratio c/λ while keeping N and L fixed. The ratio could be increased either by decreasing λ or by increasing all the scaled dimensions

in the problem. By decreasing λ , the truncation error will increase because the fan of scattered wave directions is narrowed (equation (3.13)). On the other hand, by increasing all the scaled dimensions of the problem (keeping L fixed), the periodic interfaces irregularities are made relatively closer to one another, thus changing some detail in the problem. We find that, when the residual errors are small (say less than 3%) and appear to be limited by truncation, the accuracy can be improved by increasing C and other problem dimensions while keeping λ and L fixed. However, when the errors are larger (as in the 'stepped' Moho problems considered later) and limited by the inherent error, we find that the accuracy declines as C increases. These observations are similar to those by Rayleigh (1945). In his solution for the scattering of acoustic waves from a corrugated interface, he found that when the maximum slope is very small, the solutions converge for any ratio C/λ although the rate of convergence is slower for shorter λ relative to the corrugation wavelength.

We use 256 values to describe the interface stress and displacement functions during the fast Fourier transformation of equations (3.5).

Aliasing in the wave number domain can arise if the interface shape is so rough or the anomalous zone so narrow relative to L that these continuous functions at the interface are not adequately sampled. Such aliasing errors are not considered severe in our problems because the rapid variations in interface depth are not 'seen' well by the longer wavelength problems generally treated in our method.

The fact that the accuracy of the method declines when S_M increases beyond unity does not impose a severe limitation on the practical value of the method for treating a wide variety of interface shapes of geophysical

interest. The method is best for middle frequencies; that is, for problems involving wavelengths comparable to the sizes of the interface irregularities. We will show that solutions are valid for wavelengths sufficiently short for useful comparison with the high frequency geometric ray theory approximations and sufficiently long so that the interfaces anomalies are practically unnoticed by the incident waves.

Most surprisingly, the accuracy is nearly independent of the source direction angle θ_0 , from normal incidence ($\theta_0=0$) through grazing incidence ($\theta_0=\pi/2$). Thus, we find no evidence that the presence of a shadow zone inhibits the accuracy of the solutions. Meehan (1956) found that the accuracy in his solutions actually increased with increasing θ_0 . We see no such systematic tendency in our solutions. An exception arises when an insufficient number N of coefficients is used in our solutions and the resulting truncation errors are large. In those cases, the accuracy declines as θ_0 increases. It is generally desirable that the summation wave numbers k_n (equation (3.4)) at least span the range $(-2\pi/\lambda, 2\pi/\lambda)$ where λ is the shortest wavelength (wavelength associated with the slowest waves) in the problem. Thus, when waves are incoming at near grazing from the left (negative x direction) a large number of coefficients may be required to describe waves scattered backward toward the negative x direction. Heaps (1957) suggested that scattered inhomogeneous waves need not be included to obtain accurate solutions. We find that, in many problems, particularly those involving large angles of incidence, accuracy requires the use of inhomogeneous scattered wave orders, notably those of the faster traveling P waves.

We did not investigate systematically the extent to which the sizes of

velocity and density contrasts at interfaces affect the accuracy. The influence of the density contrast is probably small. The example in Figure 5.6 indicates that RMSE increases with velocity contrast. We have seen in Figure 4.1 that the layer thickness can influence the nature of the stress and interface residuals, but in most cases we judge this affect also to be small.

In Table F1 listing the errors for all the examples discussed, we also list the parameters c/λ , S_M , and L/W judged to be critical factors influencing accuracy. W is the width of a single cosine when the interface shape is given by (4.7). In other problems such as the stepped Moho problems, W is the width of the cosine that describes just the steepest portion of the interface.

4.6. Comparison with a Solution Obtained by a Finite Difference Technique.

Recently, D. Boore has applied an independent approximate method - that of finite differences - to a variety of elastic wave scattering problems involving curved interfaces (Boore, 1969). In his method, the differential equations of motion and boundary conditions are replaced by finite difference analogs with motion defined only at discrete positions in a basically regular grid network in space and time. The resulting set of recursive equations is solved for the displacement at each grid point as a function of time once the motion is specified everywhere at two consecutive time steps. The finite difference method has the distinct advantage that it can treat transient motion problems. However, computer time and storage limitations impose practical restrictions upon the maximum size of the grid network and duration of time over which the transient solution can be observed.

To provide a comparative check of the accuracies in our techniques, Boore and this author applied our respective methods to the solution of a given wave scattering problem. The problem configuration is illustrated at the bottom of Figure 4.8. A plane SH wave is vertically incident upon low-rigidity basin. The medium parameters are the same as those in the example in Figure 4.1 and the interface depth is given by (4.7) with $D=1$ km, $c=5$ km, $W=50$ km and $x_0=0$. Since the solution is symmetric about the line $x=0$ (vertical line through the center of the depression), only the right half of the basin is shown in the figure. The source plane wave used in Boore's solution is a transient Ricker wavelet (Ricker, 1945) having a dominant wavelength of 64 km in the lower medium (the dominant period is 18.3 sec).

Figure 4.9 shows the computed seismograms at various positions x along the free surface. The reference trace is the response of a flat layer 1 km thick (corresponding to positions at large distances from the basin). Likewise, the dashed curve is the solution to a problem involving a 6 km thick flat layer. We shall return to a discussion of these seismograms shortly. According to the prescription given in section 3.4.3, to compare the seismogram solutions with our complex frequency solutions, the seismograms are first multiplied by the exponential window $e^{-\omega_I t}$ where ω_I is the imaginary part of frequency. The windowed signals are then Fourier transformed and the spectral solutions normalized by a similarly determined spectral solution for the 1-km flat layer problem. In the solution obtained using our method, the period is 17.1 sec and window decay time $\tau=1/\omega_I=13.32$ sec. Figure 4.10 shows the suite of seismograms in Figure 4.9 after multiplying by $e^{-t/13.32}$ (note that the amplitude scale is increased in Figure 4.10).

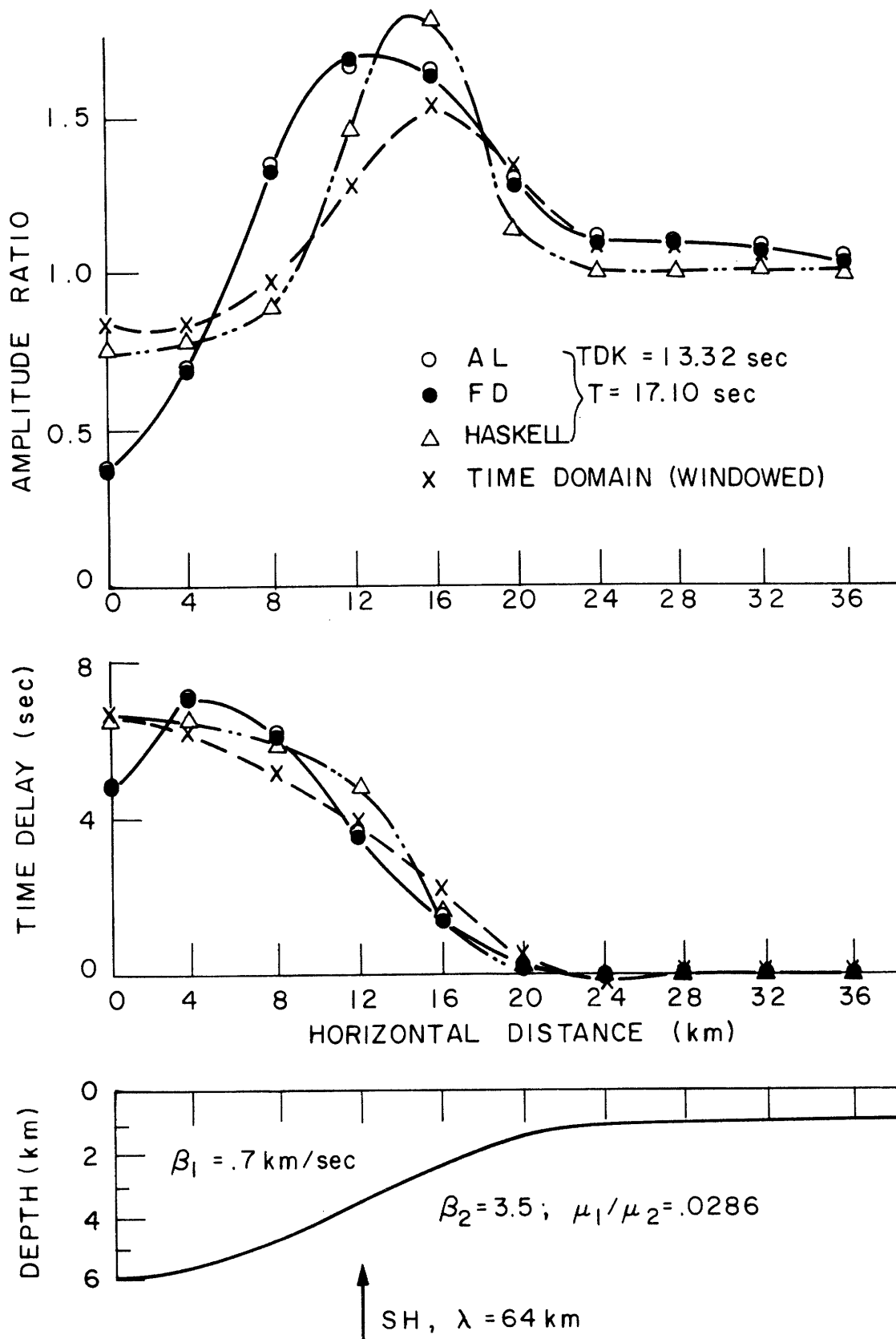


Figure 4.8. Comparison of normalized displacement amplitudes and time delays at the surface of a soft basin computed using four different methods. AL is our method; FD is the finite difference technique; and Haskell is the local thickness, flat layer approximation; all for $\tau = 13.32 \text{ sec}$ and period $T = 17.1 \text{ sec}$.

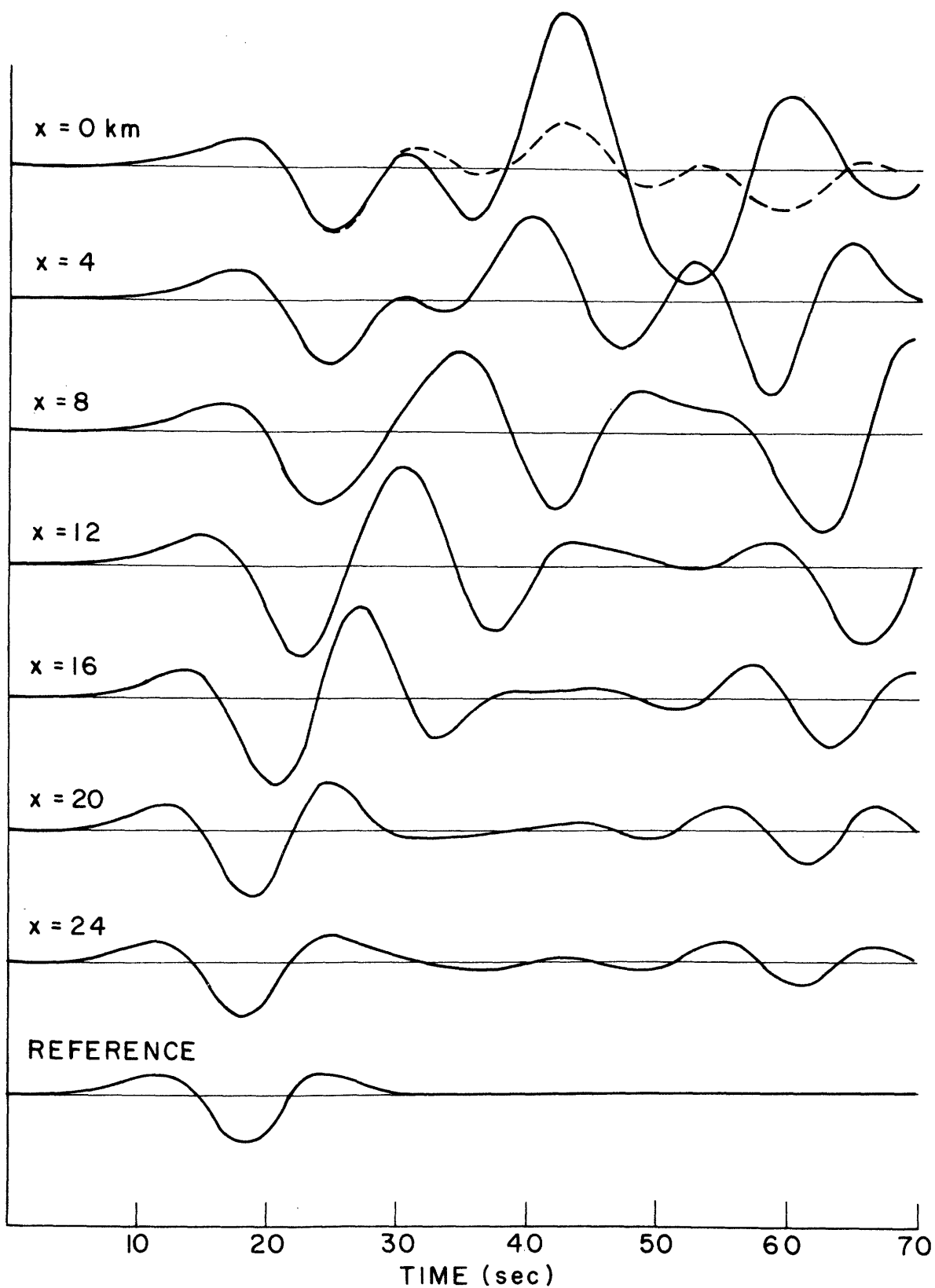


Figure 4.9. Finite difference-computed seismograms at positions along the free surface for the soft basin problem in Figure 4.8. x is the horizontal distance from the center of the basin. The dashed curve is the solution for the motion at the surface of a 6-km thick flat layer.

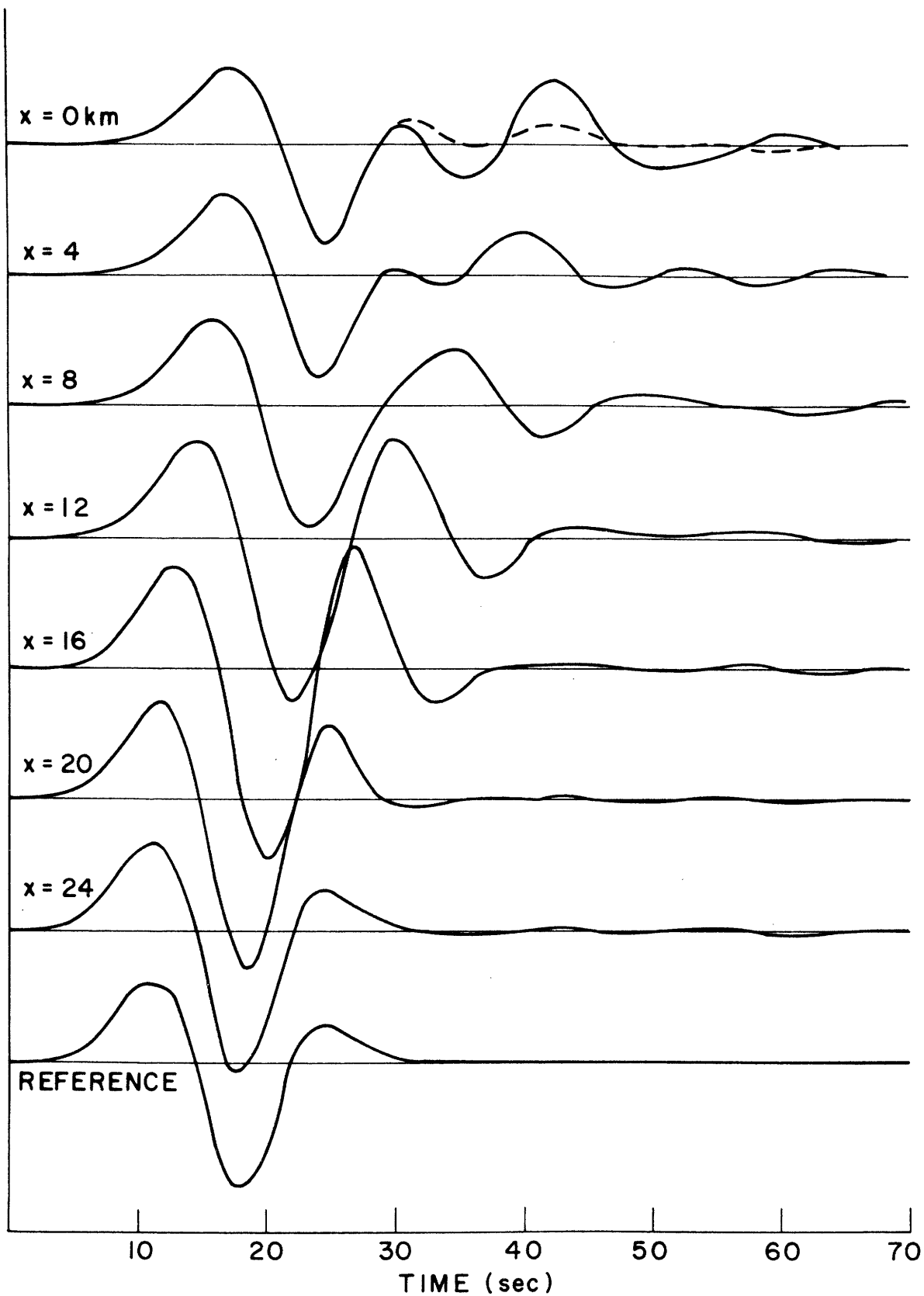


Figure 4.10. Results of multiplying the synthetic seismograms in Figure 4.9 by the exponential window with decay time $\tau = 13.32$ sec.

The normalized amplitude and time delay distributions obtained by the two methods are compared in Figure 4.8. In the figure, FD denotes the finite difference solution obtained in the above manner, and AL (for Aki-Larner) denotes our solution. The agreement for both amplitude and time delay is excellent, testifying to the accuracies of the independent methods. The two solutions also agree when a different value of ω_I is used thus confirming the interpretation of frequency smoothing as being equivalent to exponential time windowing the transient solution prior to Fourier analyzing. The solution labeled 'Haskell' is the local Thompson-Haskell approximation (with complex ω) for a flat layer having the local thickness beneath the observation point. The peak at $x=15$ km and trough at $x=0$ km correspond to conditions of resonance (thickness equal a quarter wavelength) and anti-resonance (thickness equal to a half wavelength) respectively for the 17.1 sec period. The departure of our solution from the Haskell solution is attributable to the interference of laterally propagating waves. This is seen best in Figure 4.10. The finite difference and flat layer solutions at $x=0$ compare well for the initial large peak and trough but disagree at later time. The excellent agreement for early time rules out ordinary wave focusing as a significant factor in this problem.

The comparison of the time domain and frequency domain solutions points out a pitfall in interpreting small spectral amplitude as implying small motion in time. At $x=0$, our computed spectral amplitude at 17.1 sec is smaller than the Haskell prediction while the peak seismogram motion is enhanced over that in the flat layer solution by the interference of laterally propagating waves. In general, we can use frequency domain solutions to make simple deductions about the time domain only for problems that do not involve later arriving reverberations. The time domain solutions

(x's) shown in Figure 4.8 are normalized amplitudes and time delays of the first large trough in the exponentially windowed seismograms in Figure 4.10, relative to those quantities in the reference trace. The agreement with the solutions obtained by the other methods is good only for $x > 20$ km. But, as seen in Figure 4.10, only in the seismograms at positions $x > 20$ km is motion dominated by the single Ricker wavelet arrival. For $x < 20$ km the seismograms are complicated by later arrivals.

Further discussion of this example is given in the paper by Boore, Larner, and Aki.

CHAPTER V

APPLICATIONS TO SEISMIC WAVE SCATTERING PROBLEMS

5.1. Introduction and Summary.

In this chapter, the method will be applied to a variety of wave scattering problems and the solutions discussed in terms of problems of interest in seismology. The primary intents are to demonstrate the various wave phenomena and to suggest the range of practical applications to seismology. Also, examples are selected to provide comparisons with solutions obtained by the computationally more rapid ray theoretical and flat-layer wave theoretical methods. Such comparisons can help to delimit the ranges of problem configurations to which those methods can be applied with confidence.

For convenience, the examples are divided into three groups - SH, P-SV, and arbitrary azimuth incidence problems - in order of increasing complexity in the presentation of results. Because we can obtain accurate solutions at smaller cost in the SH wave motion problems, most of the examples of wave focusing and interference effects involve SH motion. The first examples demonstrate effects of source wavelength relative to the dimensions of the interface anomaly, interface shape, incidence angle, and velocity contrast. Using a single layer over a half-space as a model for the crust and upper mantle, we compute displacement amplitude and phase delay anomalies along the free surface caused by scattering from various shapes of Moho irregularity such as depressions, rises, and step-like variations. Several examples of the seismological engineering problem of resonance in a sedimentary basin are discussed next. The problem, critical to questions of earthquake risk,

has generally been treated using flat-layer theory. Our results indicate that interference between laterally scattered waves in two-dimensional basins (and, by inference, in three-dimensional basins) can further enhance the resonant motion by a factor of 2 or more.

In this study, the only examples in which the free surface is irregular involve SH wave motion. We find that, in the crust-mantle models, the motion at the free surface is not significantly different from that when the surface is plane. This result suggests that the large motions often observed on mountains (D. James, personal communication) is attributable more to inhomogeneities beneath the mountains, such as mountain roots, than to the variable topography. The scattering of teleseismic SH waves into Love wave modes by surface topographic features is observed in solutions involving real frequency. We find that a) valleys are more efficient sources of scattered Love waves than are hills, b) surface features are more efficient sources than are irregularities in internal interfaces, and c) the higher order modes are more strongly excited than the lower.

The first example involving incident P waves is a comparison of vertical displacement amplitude and time delay anomalies for grazing incidence ($\theta_0 = \pi/2$) with the results from a laboratory model study of refraction in a layer over a half-space by Laster, Backus, and Schell (1967). The good comparison indicates that our method may be a useful interpretive tool in refraction seismology. The next examples demonstrate effects of wavelength, interface shape, and layer thickness in the scattering of P waves. In a problem involving vertically incident S waves (particle motion in the x-z plane), we find that a significant vertical component of motion can result above the interface anomaly. Phinney (1964) has shown that the spectral

ratio $V(f)/H(f)$ of vertical to horizontal displacement amplitude can be diagnostic of crustal structure on the assumption of uniform, flat layering. The technique has had only modest success most likely because of departures from flat layering in the crust (Ellis and Basham, 1968). By means of examples, we demonstrate how the successful implementation of the Phinney technique can be impaired by departures from flat layering.

The examples in the following section demonstrate the three components of motion resulting from interacting P, SV, and SH waves in the arbitrary azimuth incidence problems. Such interactions cause deviations of the apparent azimuth from the true arrival azimuth. Also, we find that the apparent azimuth as inferred by wavefront direction can be different from that inferred by resolving the horizontal components of motion. A further observation is that the amplitude variation for the vertical component of motion when projected onto the x-z plane (normal to the strike) is dependent primarily on the x-component of apparent velocity and is relatively insensitive to the azimuthal direction of the source wave. Cases involving waves incident at an azimuth parallel to the strike ($\alpha_0 = 90^\circ$) are exceptions. There, the spatial variations in amplitude can be quite sensitive to the incidence angle Θ_0 . The section concludes with a comparison of three cases involving multi-layered crust. We find, somewhat surprisingly, that details of layering can influence both the amplitude and phase delay anomalies caused by an irregular Moho even when the crustal layering is flat.

The final section in this chapter is an application to the study of crustal structure under the Montana Large Aperture Seismic Array (LASA). There, we first investigate the two-dimensional spatial distribution of spectral amplitudes and phases across the array to determine whether the

assumption of one-dimensional (trending) layering irregularities is valid. The evidence supports the assumption, and the estimated strike direction is $N64^{\circ} E \pm 6^{\circ}$. The spectral amplitude and phase delays for teleseismic arrivals from earthquakes at the various azimuths are plotted as a function of the x-coordinate positions (the x-direction is normal to the strike). Comparisons of these observations with solutions obtained by our method enables us to check the Greenfield and Sheppard (1969) model for crustal structure. Using their values for P-wave velocities and testing only a single layer model, we find that the crustal thickness is 48 ± 5 km as compared with 64 km in their model. The strike direction and amplitude of the Moho depth variation is comparable to that found by Greenfield and Sheppard.

5.2. SH Wave Scattering Problems.

5.2.1. Two half-spaces separated by an irregular interface. It is desirable to isolate the effects of wave focusing and interference caused by scattering at a single irregular interface from the interference effects attributable to multiple reflections in a layered system. Layering effects are absent in the example shown in Figure 5.1. The problem involves the scattering of steady-state SH waves at the irregular interface separating two-half-spaces. The waves are incident from depth in the lower half-space at $\theta_0 = 55^{\circ}$ from vertical, and the interface shape is plane with a single cycle cosine dent as given by (4.7) with $D=25$ km, $c=5$ km, $W=50$ km, and $x_0=0$. The configuration is the same as that shown in Figure 4.6.

Here, we are interested in the effects of wavelength relative to the size of the interface anomaly. In the figure are plotted the computed displacement and phase time delay anomalies along the plane $z=0$ in the upper

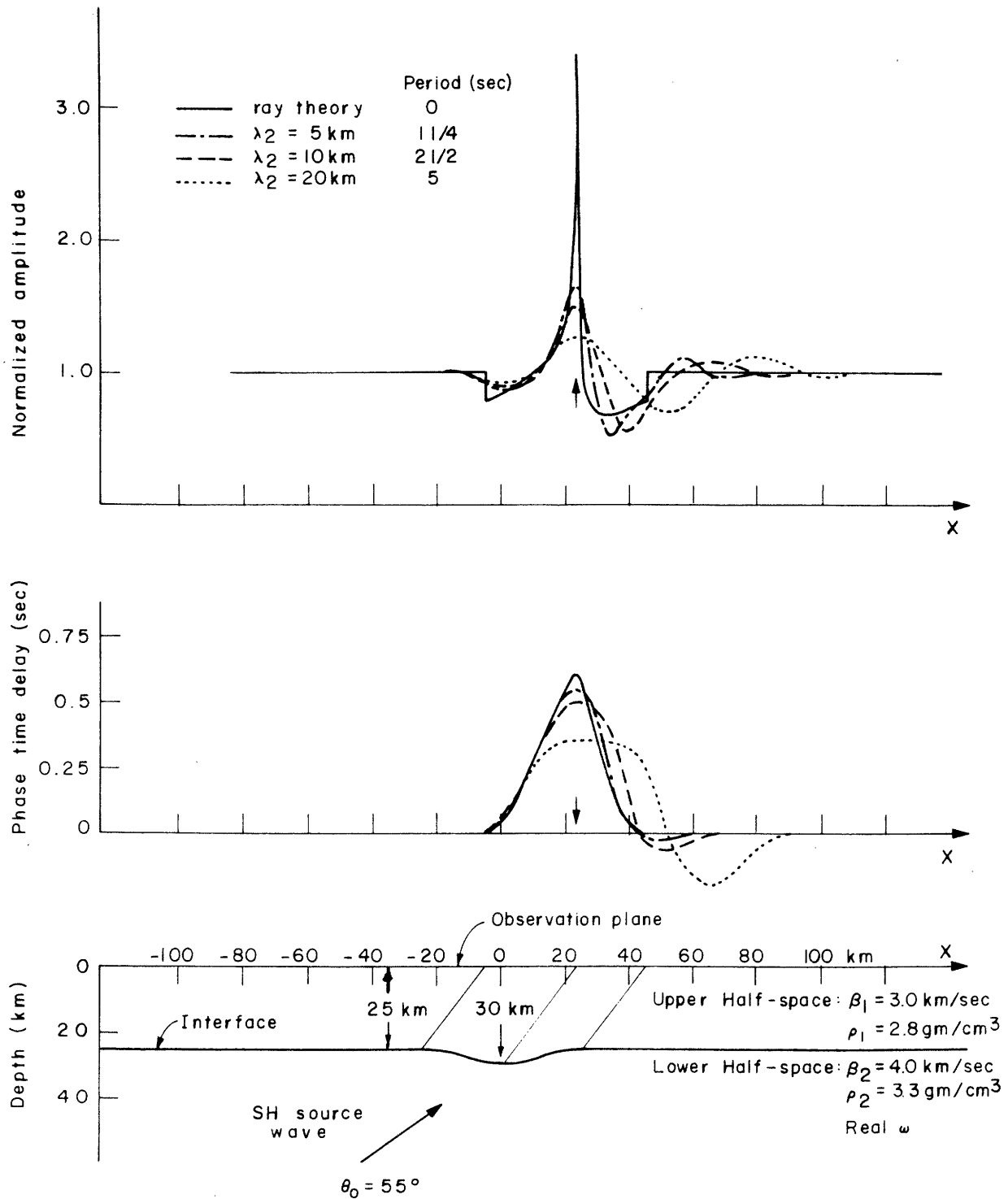


Figure 5.1. Effect of wavelength on SH wave scattering at a dented interface joining two half-spaces. Spatial distributions of displacement amplitude and time delay along a plane in the upper half-space. The ray theory solution was computed using the method described Appendix G. The arrows at $x=23 \text{ km}$ indicate the intersection of the geometric ray path through the trough of the dent with the observation plane.

half-space for incident waves having wavelengths 5, 10, and 20 km. The ray theoretical solution involves a Snell's law ray tracing procedure, and displacement amplitudes are computed using transmission coefficients for plane waves at plane interfaces with the assumption that energy flow is constant along tubes bounded by given rays. The ray theoretical solution displays artificial features that will not be observed in the case of real wave scattering. The vertical discontinuities in amplitude at $x=-5$ km and $x=45$ km arise from the sensitivity of the ray theoretical solution to the second derivative of interface shape which jumps from zero to its maximum absolute value at $x=25$ km. The large amplitude near $x=23$ km is caused by the proximity of the focal region. The ray theory predicts infinities in amplitude at a focal point and along caustics. Therefore it predicts infinities whenever the focal point or region lies between the irregular interface and the observation plane.

The ray theory predicts time delays well in the 5-km wavelength case. As wavelength increases, the peak time delay diminishes. When the wavelength is comparable to the width of the interface anomaly, ray theoretical interpretations of the phase delays yield underestimates of the amplitude of the irregularity. As we shall see, this phase dispersion is encountered in P-wave scattering solutions whenever the wavelength and the dimensions of the irregularity are comparable. One might question whether the negative time delays in the longer wavelength solutions in Figure 5.1 are in violation of causality. However, these are phase time delays and on close examination we find that for most values of x , the group time delays are positive. An exception may arise in the vicinity of $x=45-50$ km. But even there, a negative group time delay may not violate causality. Causality requires only that the real and imaginary parts of the crustal transfer function be

Hilbert transform pairs (Papoulis, 1962), hence the minimum phase delay is determined by the amplitude at all frequencies. As seen in Figure 5.1, the amplitudes vary with frequency and could thus be causally related to phase.

The ray-theoretical amplitudes are more sensitive than phases to the interface shape and its derivatives, and to the incidence angle. Hence, the ray-theoretical amplitudes do not fit our 5-km wavelength solution as well as do the phases. The peak amplitudes for all wavelengths occur at the position predicted for peak amplitude in the ray theory and, coincidentally, at the projection onto the surface, of the trough of the interface depression, along the geometric ray path. As wavelength increases, the anomalies broaden and have smaller variation. In the long wavelength limit, the anomaly disappears, i.e. the long waves no longer see the interface depression. Whereas the migration of position of the main peak with Θ_0 can indicate the depth of the irregular interface (if the medium velocities are known), the migrations of the side lobes would lead to errors in depth computed according to the ray-theoretical interpretation.

The wave diffraction that produces these wavelength-dependent effects is observed in the wave number spectra shown in Figure 5.2. These are the absolute values of the complex amplitudes of scattered waves in the upper half-space plotted against the ratio of x-component wave number k_n to k_{β_2} . The amplitudes are plotted in decibels below the primary wave amplitude at $k_0/k_{\beta_2} = \sin \Theta_0$. As wavelength increases, the amplitudes of the lower scatter order waves diminish, but coupling with the higher scatter orders increases. In the figure, the region denoted by 'R' is the wave number interval over which we expect scattered waves according to the ray theory.

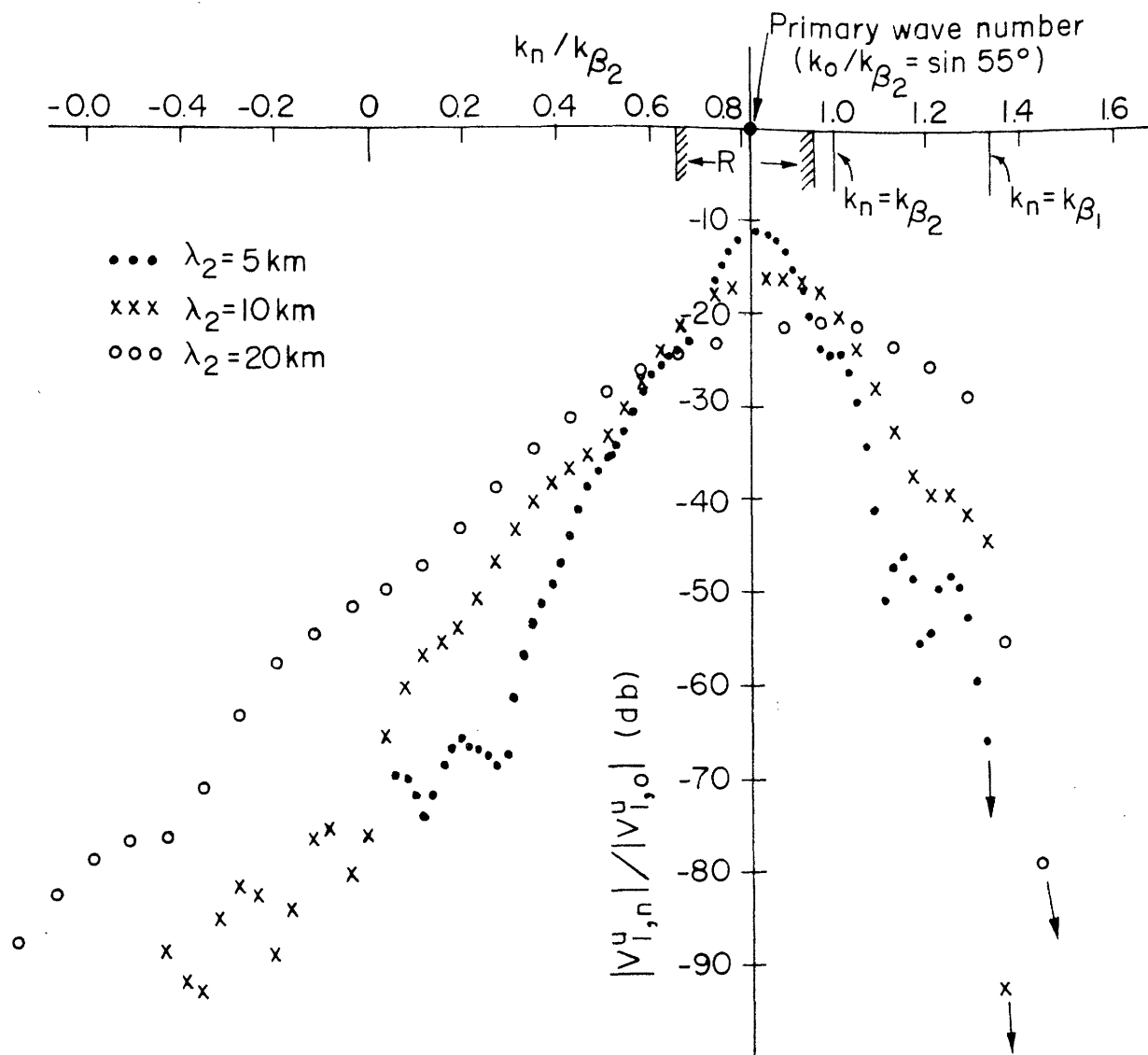


Figure 5.2. Wave number spectra for the three solutions shown in Figure 5.1 demonstrating the dependence of wave number coupling upon wavelength.

Coupling with wave numbers outside this interval is interpreted as wave diffraction. Values of k_n such that $|k_n|/k_{\beta_2} > 1$ correspond to inhomogeneous waves in the lower half-space. The large amplitudes of these waves indicate that they are required to match the interface conditions. The wave numbers such that $|k_n|/k_{\beta_1} > 1$ pertain to inhomogeneous waves whose amplitudes decay with increasing distance from the interface in the upper half-space. That the amplitudes of these inhomogeneous waves are very small implies that these waves are insensible at the observation plane $z=0$. However, they still may be required to match conditions at the interface.

5.2.2. Irregular Moho problems. In this section we consider examples of the spatial variations in amplitude and phase delay observed at the plane free surface of a layer over a half-space. The medium parameters are suitable for a simplified crust-mantle model. In the next few examples, the nominal thickness of the layer (the thickness where it is uniform) is 25 km, and the imaginary part of frequency ω_I is sufficiently large so that the exponential window is down to e^{-1} in 3.98 sec. This decay time is short compared with the travel time through the layer (10 sec for one way vertical path); therefore, the effects of multiples are nearly absent in these examples, and the anomalies might be compared with peak-to-trough amplitude and time delay anomalies in first arrivals. These SH wave examples exhibit features similar to the more interesting P-SV wave examples presented later.

In the examples shown in Figure 5.3, the interface has the same one cycle of a cosine shape as that in Figure 5.1 ($W=50$ km, $c=5$ km, $x_0=125$ km). Normalized displacements at the free surface caused by 10-km wavelength SH

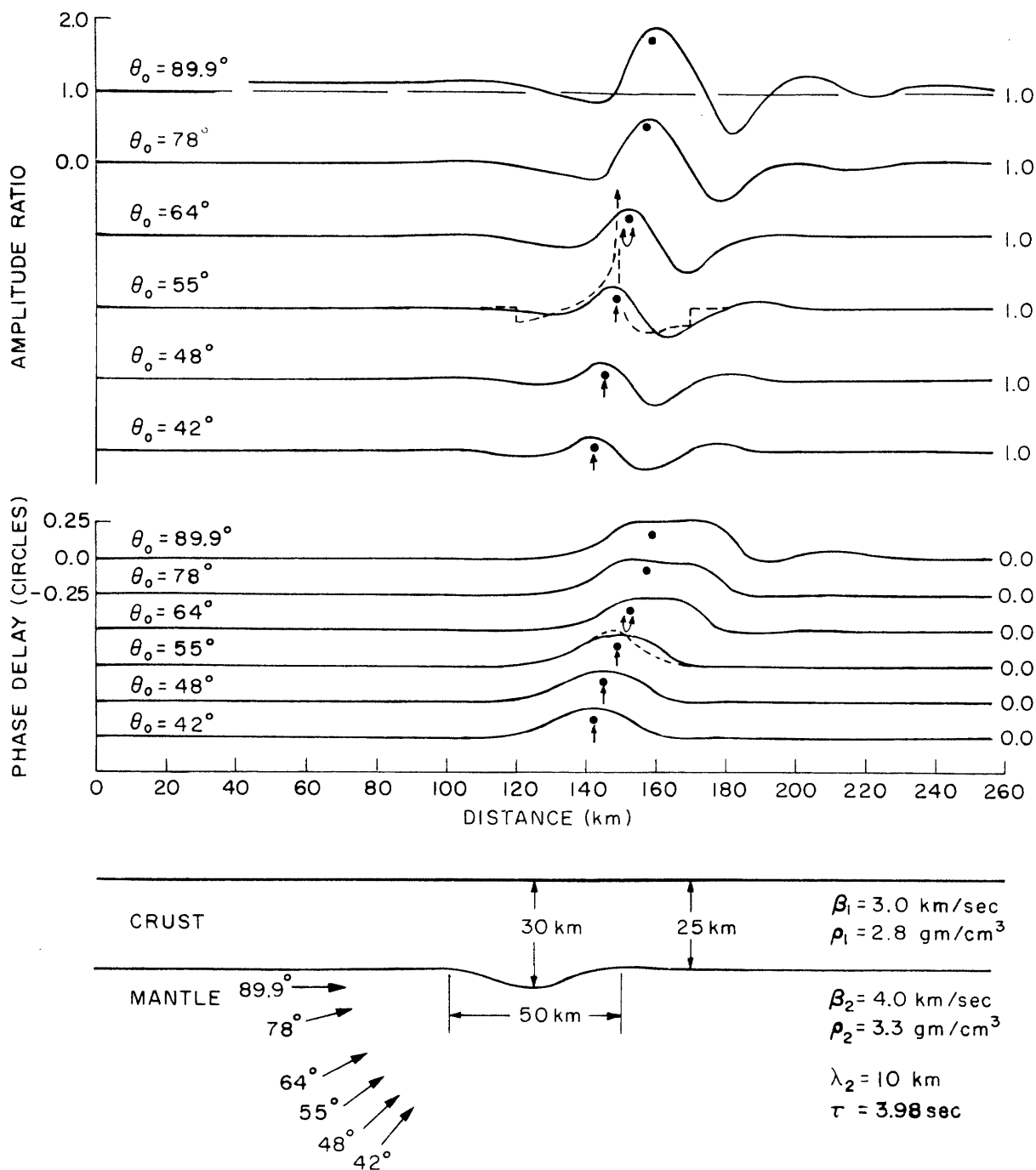


Figure 5.3. Normalized displacement amplitude and phase delay distributions along the free surface for 10-km wavelength SH waves scattered at a depression in the Moho. The scales are shown for the $\theta_0 = 89.9^\circ$ curves, and the other curves are displaced downwards. The dashed curves are ray theoretical solutions, the arrows indicate the locations of peak amplitude and phase delay according to the ray theory, and the dots are projected positions of the Moho trough along the geometric ray paths.

plane waves, incident at six different angles θ_0 from vertical, are plotted. The double arrows for the $\theta_0=64^\circ$ curves denote the intersection of caustics with the free surface. No ray theory arrows are shown for the $\theta_0=78^\circ$ and 89.9° cases because the ray theory solutions have shadow zone gaps. The RMS errors (Table F1) are small even for the $\theta_0=89.9^\circ$ case; therefore, the presence of shadow zones seems to introduce no special difficulty in our problems. Note that the amplitude variations and the breadths of the phase delay anomalies increase with increasing incidence angle and that the shapes of the anomalies are consistent with one another while θ_0 changes.

The dashed curves for the $\theta_0=55^\circ$ case are the same ray theoretical amplitudes and phase delay anomalies shown in Figure 5.1. Our solutions are reasonable, smoothed versions of the ray theoretical solutions. The x-coordinate locations of the dots coincide with those of the peak amplitudes in our solutions even for the case of grazing incidence. These consistent suites of curves and the small RMSE suggest that the solutions are valid even to grazing incidence.

The amplitude curve for the 89.9° case does not normalize to unity away from the anomaly as do those in the other cases because the grazing waves have seen repeated depressions rather than the uniform 25-km thick layer. Nevertheless, the anomalies for the case of grazing incidence should be of value in interpreting amplitudes and time delays in seismic refraction profiles. This will become apparent in the comparison with the laboratory model study discussed in section 5.3.1. However, we can point out here one difference between our horizontally propagating (in the half-space) source wave problems and those involving actual head waves. The head waves are

diffraction phenomenon arising from the interaction of curved wavefront waves with an interface. They seem to propagate along the interface and would be delayed upon encountering the interface depression. Therefore the phase delay curves would not return to zero delay to the right of the anomalies as in our cases. Ours return to zero because the waves at the interface are continually fed from below by our imposed plane source waves.

The next example is the case of scattering at a local rise in the Moho as shown in Figure 5.4. The residual errors (Table F1) are again small even for grazing incidence. Although the $\Theta_0 = 55^\circ$ curve compares well with the ray-theoretical solution except at the artificial discontinuities, the amplitude variations are more broad and less simple than in the previous cases. Moreover, they have no prominent features coinciding with either the dots or arrows (see figure caption for their meanings). Thus it would be more difficult to determine layer thickness from the migration with Θ_0 of features in the amplitude anomaly than in the case of a depression in the Moho. The phase delays compare well with the ray-theoretical prediction. However, they also exhibit dispersion with increasing wavelength.

The amplitude and phase delay anomalies shown in Figure 5.5 pertain to scattering for the same interface shape configuration as that in Figure 5.3, the difference being that the source wavelength is now 20 km. The solid curves for the four angles Θ_0 were obtained during a single Gaussian elimination solution as described in Chapter III. As was mentioned there, only one source direction could be defined unambiguously (source wave number on the ϵ line in Figure 3.2 when ω is complex). Thus, with $\Theta_0 = 58^\circ$ unambiguously, the source wave numbers for the $\Theta_0 = 43^\circ$ and 32° cases lie

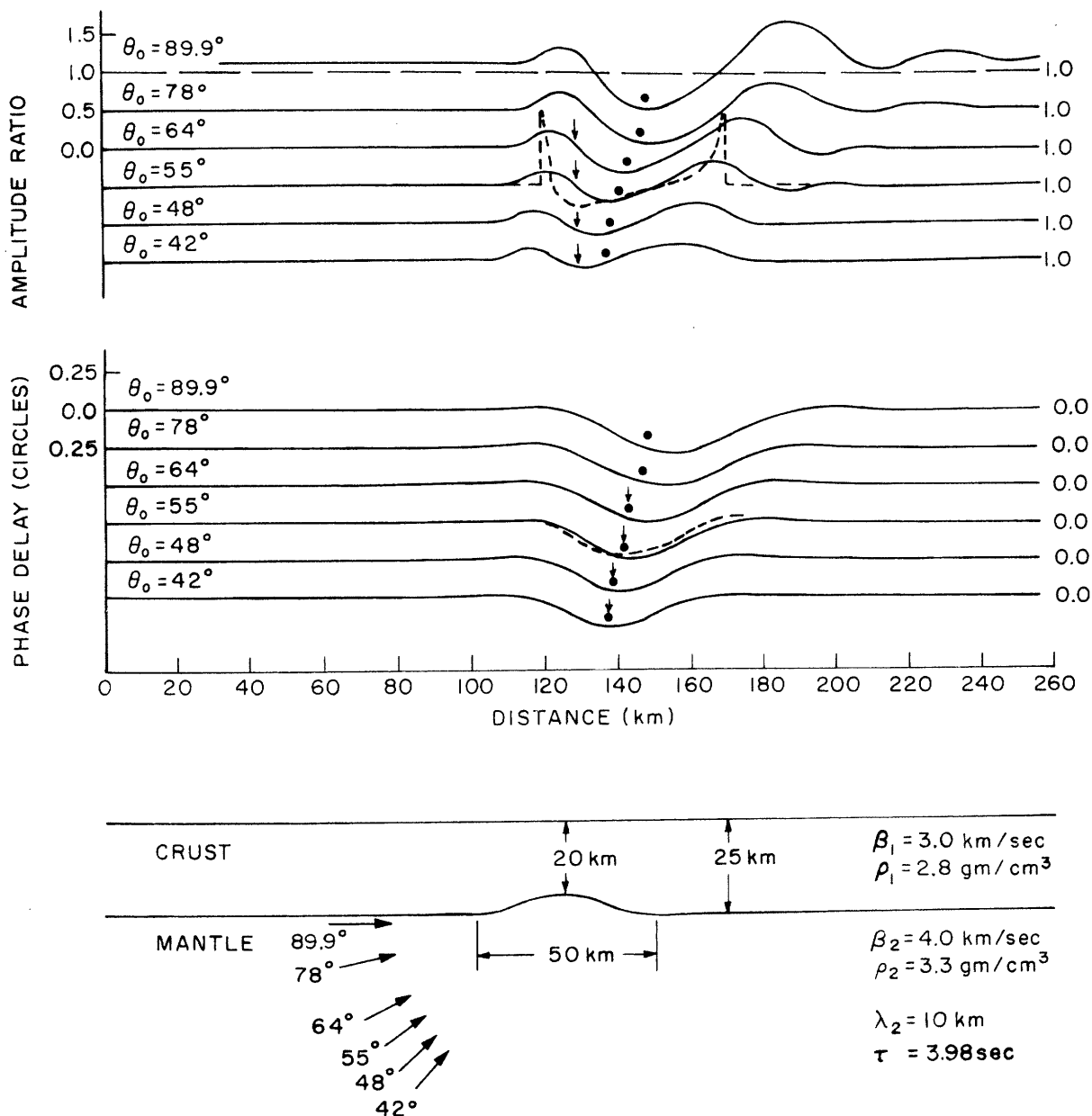


Figure 5.4. Normalized displacement amplitude and phase delay distributions for 10-km wavelength SH waves scattered at a rise in the Moho. The scales are shown for the $\theta_0 = 89.9^\circ$ curve, and the other curves are displaced downward. The dashed curves are ray theoretical solutions, the arrows indicate the locations of amplitude minima and phase advance maxima according to the ray theory, and the dots are projected positions of the Moho crest along the geometric ray paths.

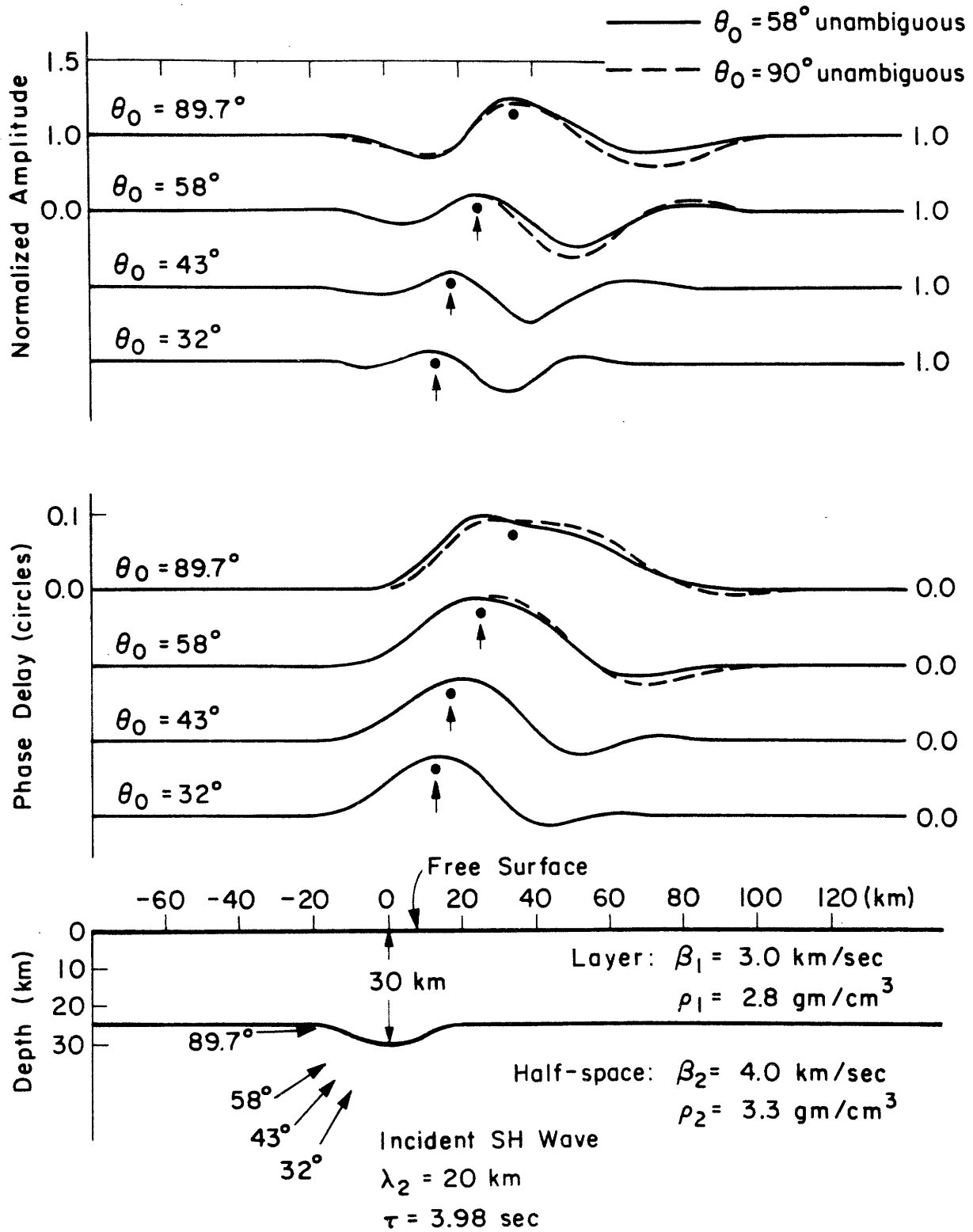


Figure 5.5. Normalized displacement amplitude and phase delay distributions along the free surface for 20-km wavelength SH waves scattered at a depression in the Moho. The scales are shown for the $\theta_0 = 89.7^\circ$ curves, and the other curves are displaced downward. The dots and arrows have the meanings stated in Figure 5.3.

TABLE 5.1

Layer and Interface Parameters for the Examples in Figure 5.6

Case	β_1 (km/sec)	c (km)	W (km)	D (km)
a	3.0	5	50	25
b	3.0	10	100	25
c	3.0	10	100	50
d	3.5	10	50	25
e	3.0	10	50	25

$$\beta_2 = 4.0 \text{ km/sec}$$

$$\rho_1 = 2.8 \text{ gm/cm}^3$$

$$\rho_2 = 3.3 \text{ gm/cm}^3$$

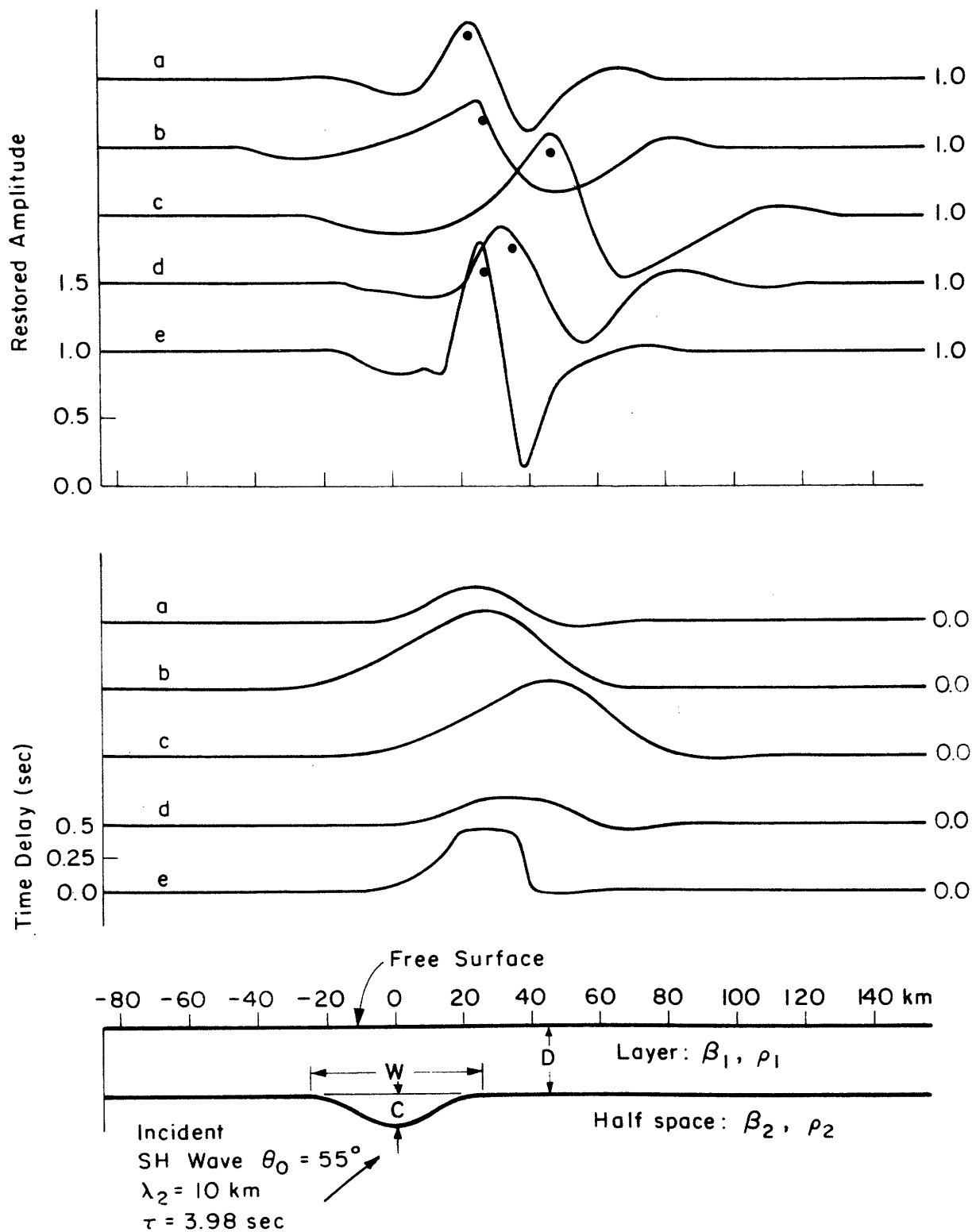


Figure 5.6. Effect of interface shape parameters and layer parameters on free surface displacement amplitude and phase delay anomalies for SH waves scattered at a depression in the Moho. The parameters for the five cases are listed in Table 5.1. The scales are shown for the case e curves and the other curves are displaced upward. The dots are projected positions of the Moho trough along the geometric ray paths.

above the ϵ line and that for $\Theta_0 = 89.7^\circ$ lies below. The ambiguity influences the shapes of the amplitude anomalies but not the peak positions. The dashed curves were computed for $\Theta_0 = 89.7^\circ$ unambiguously given. This example suggests practical limitations on attempts to obtain solutions to several source problems simultaneously when ω_I is large.

The five examples shown in Figure 5.6 display the effects of varying the interface shape parameters and medium parameters. In all cases, a 10-km wave is incident at $\Theta_0 = 55^\circ$ and the decay time is $\tau = 3.98$ sec. The interface depth is given by (4.7) with $x_0 = 0$ and W , c , and D given in Table 5.1. The term 'restored amplitudes' means normalized amplitudes, determined in the usual manner, multiplied by $e^{\Delta t/\tau}$ where Δt is the observed time delay. We have seen (Figure 4.6) that with the small value $\tau = 3.98$ sec, the solutions should be compared with early arrival amplitudes in the time domain. By restoring the factor $e^{\Delta t/\tau}$ in our complex-frequency solutions, we may then make direct comparisons with early motion in unwrapped time domain solutions. We do this in the comparison with the laboratory refraction model study in section 5.3.1. The comparison between cases d and e demonstrates the influence of velocity contrast. The RMSE (Table F1) are largest for case e; however, study of the interface residuals (not shown here) reveals that the errors are larger in the half-space and are probably quite small (less than 3%) in the layer.

The next examples involve 'stepped' Moho shapes, i.e. interfaces with gentle gradients except over a small interval where the gradient is steep. In Figure 5.7, the step height is 5 km, and the shape is a cosine for a half cycle (with wavelength 8 km) connected to half-wavelength cosines (wavelength 120 km) on both sides. The configuration may model the inter-

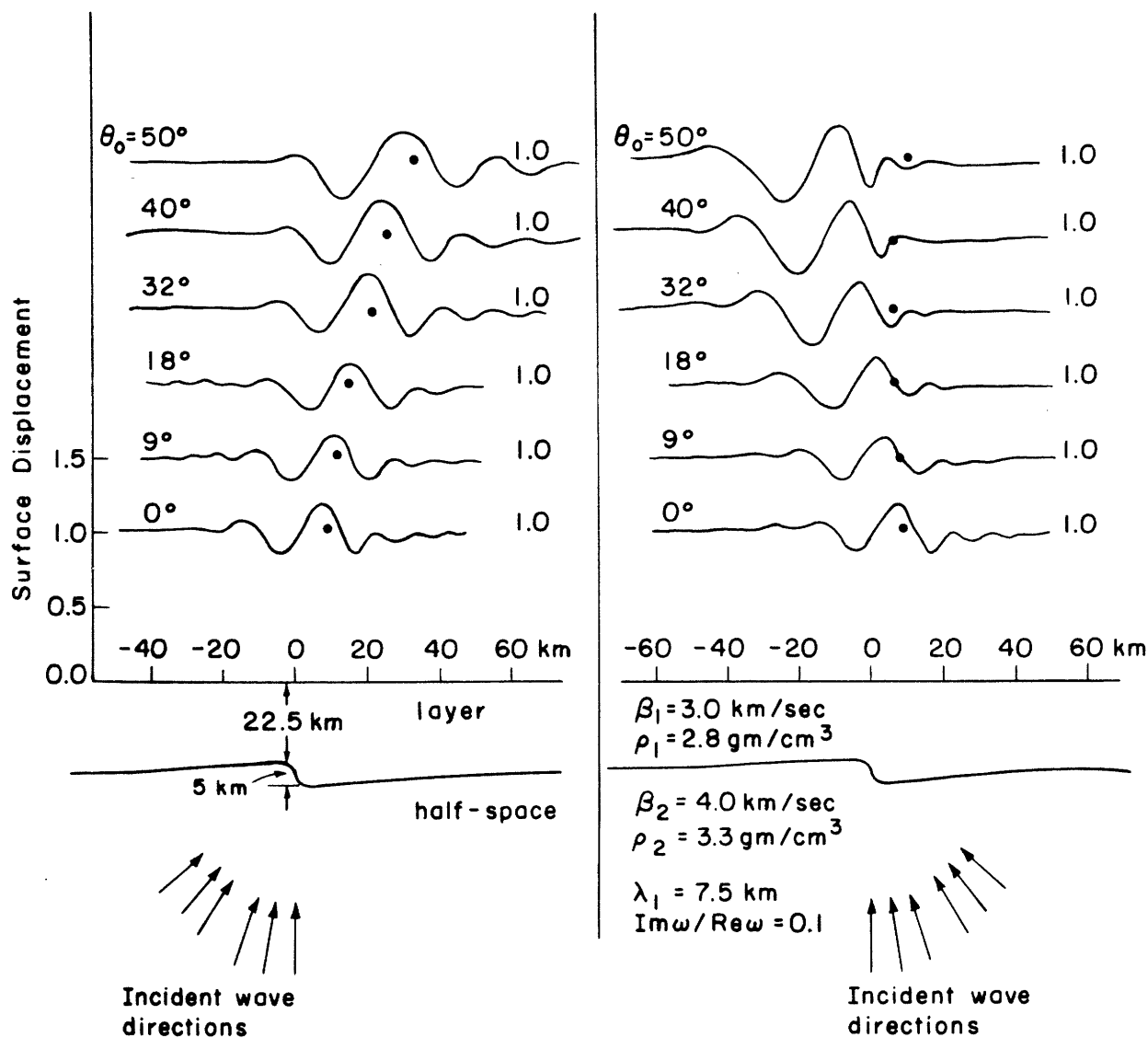


Figure 5.7. Spatial distributions of the normalized amplitude of SH displacement at the free surface above a step-shaped irregularity in the Moho. The scale is shown for the $\theta_0 = 0^\circ$ curve. The dots are projected positions of the center of the step along the geometric ray paths. λ_1 is the wavelength in the layer. The decay time $\tau = 3.98 \text{ sec}$.

section of a dip slip normal fault with the Moho. The medium parameters and nominal layer thickness are unchanged from those in the previous examples. The incident waves have 10-km wavelength and $1/\omega_I = 3.98$ sec. When waves are incident from the side of thinner crust to that of thicker crust, there is general agreement between the ray geometrically projected points of the center of the step and the maximum amplitudes calculated by our method. The RMS errors are not strongly dependent upon the incidence angle; however, the stress residuals for all values of Θ_0 are relatively large just at the step as shown previously in Figure 4.4. The validity of these amplitude anomalies must be evaluated in this light. The examples in the next two figures may provide further insight into the meaning of these solutions.

In Figure 5.8 we consider SH wave scattering in two stepped-Moho problems. In each case, the crust thickness varies as half cycles of a cosine from 25 km to 30 km over short intervals in x . In one case the x interval is 2 km (steep gradient) and in the other, the x interval is 8 km. The large-scale features in both the amplitude and time delay anomalies are comparable in the two cases despite the relatively large interface residuals localized at the steps. Of particular interest is the 33-km distance (from $x = -35$ km to $x = -2$ km) required for the time delays to attain their maximum values, independent of the gradients of the steps. The most evident differences between the two cases are the larger oscillations between $x = 30$ km and 60 km in the steep-gradient solutions. These oscillations are caused by the interference of the primary scattered waves and somewhat circular waves emanating from the step at $x = 50$ km, as depicted in Figure 5.9a. Figure 5.9b shows the theoretical amplitude and phase delays for two interfering plane waves having the amplitude ratio 0.25. The wave-

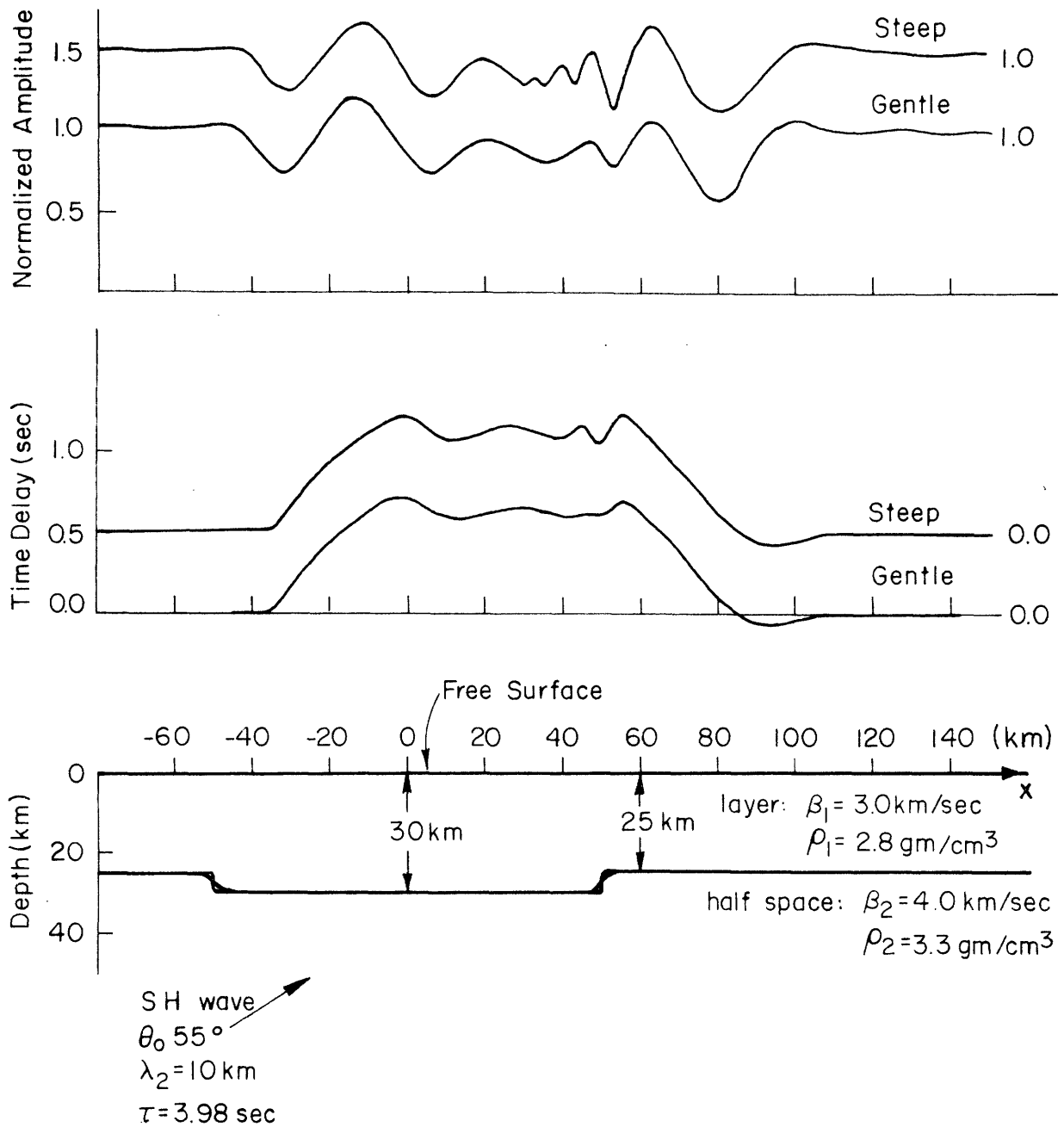


Figure 5.8. Spatial distributions of displacement at the free surface for SH-wave scattering at steep and gentle gradient steps in the Moho. The medium configurations for the two problems are superposed in the figure. The maximum gradients are 3.9 and 1.0. The common scales are shown for the gentle gradient curves.

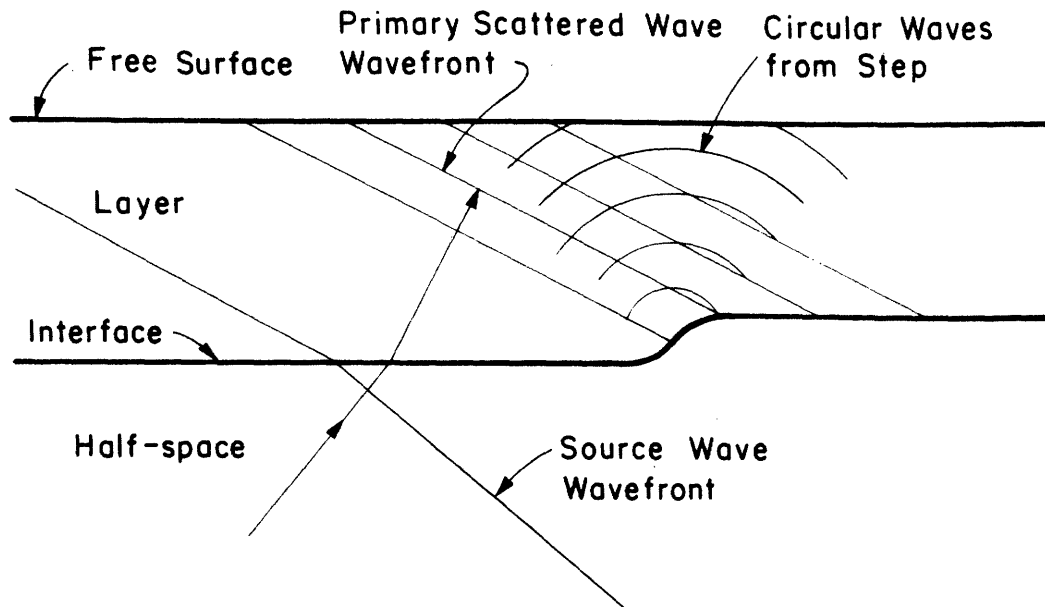


Figure 5.9a. Schematic diagram showing interference between primary scattered waves and waves diffracted from a step-shaped interface irregularity.

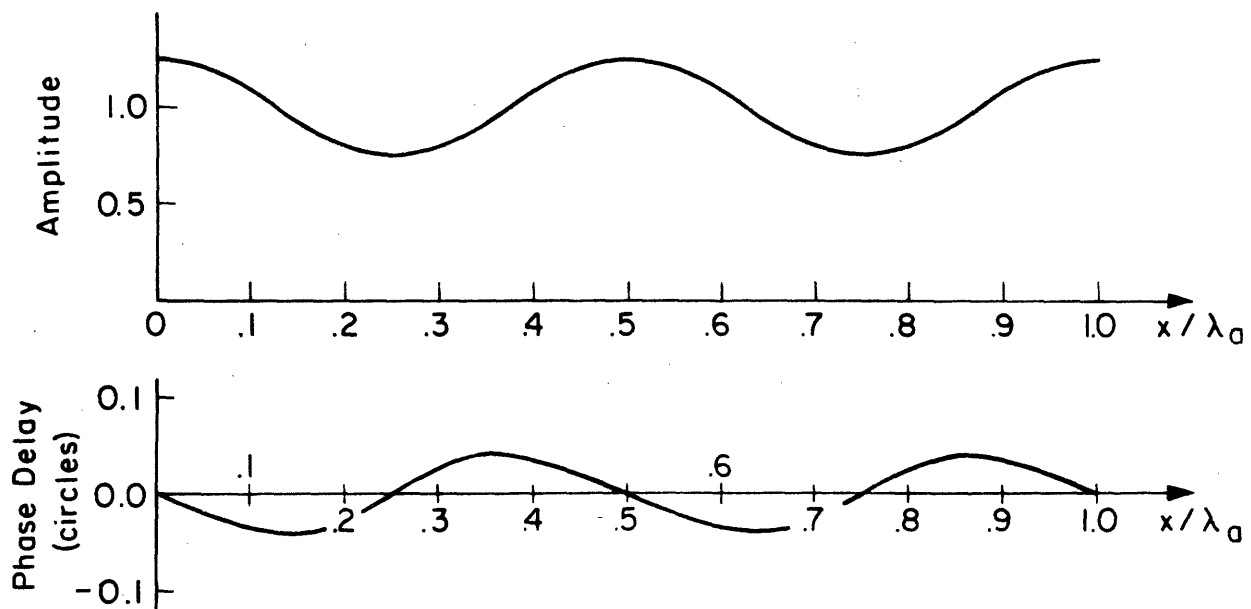


Figure 5.9b. Spatial distributions of amplitude and phase delay arising from two interfering plane waves. The wavelength $\lambda_0 = 4\pi / (k_A - k_B)$ where k_A and k_B are the x-components of wave number for the plane waves. The ratio of plane wave amplitudes is 0.25.

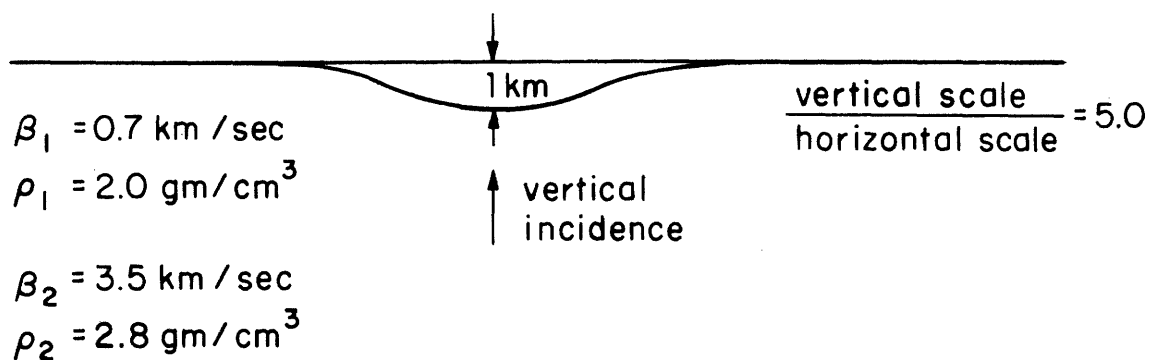
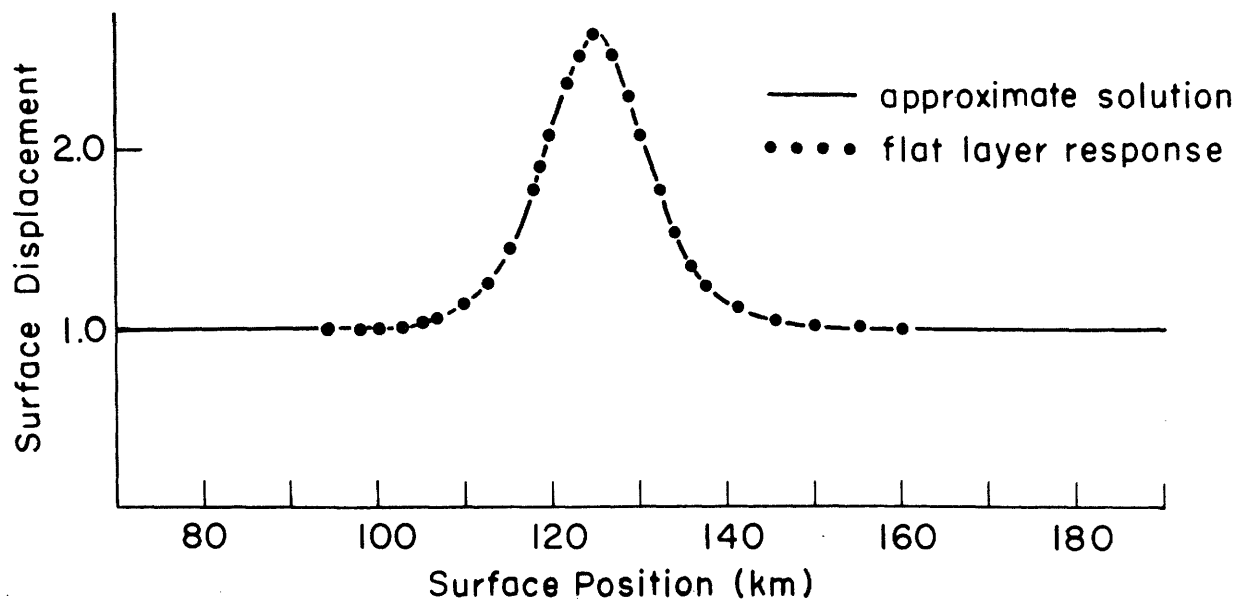
length of the oscillations ($\lambda_g/2$) is inversely proportional to the difference in the x-components of wave number for the two plane waves. This explains the decreasing peak-to-peak distance in the amplitude oscillations as x decreases from 60 km to 30 km in Figure 5.8.

Note, in Figure 5.9b, that the oscillations in phase delay cover only a small part of a circle. Similarly, the time delay curves in Figure 5.8 display only small oscillations. Such wave interference effects offer a partial explanation of the larger scatter in observed amplitudes than in arrival times (see the discussion of the Montana LASA data in section 5.5). Unfortunately, the interpretation of the curves in Figure 5.8 as wave interference does not determine whether the circular waves from the step represent actual diffraction effects or artificial effects caused by localized errors in our solutions.

5.2.3. Soft basin problems. It is well recognized in earthquake engineering that the ground surface motion of low-rigidity strata can be considerably enhanced at selected frequencies over the motion if the bedrock were exposed. The problem is usually discussed in terms of flat layer theory (Kanai, 1952; Kanai, et. al., 1959) assuming horizontally uniform flat sedimentary layers. For the case of SH waves vertically incident to a single layer over a half-space, the theory predicts enhancement by a factor $\rho_2 \beta_2 / \rho_1 \beta_1$ at frequencies such that $D/\lambda_1 = \left(\frac{2n+1}{4}\right)\pi$, where D is the layer thickness, λ_1 is the S wavelength in the layer, and n is a positive integer. In the next five figures we use our method to test the validity of the flat-layer theory when the soft basin is confined two-dimensionally.

In Figure 5.10, the basin shape is the single cycle cosine, equation (4.7), with $c=1$ km, $W=50$ km, $D=0.01$ km, and $x_0=125$ km. The SH-wave motion is polarized normal to the plane of the figure, and frequency is complex with decay time $\tau=9.39$ sec. The flat-layer approximation compares excellently with our solution (the solid line). The problem shown in Figure 5.11 differs in that the basin dimensions are doubled and frequency is such that the maximum depth is $(1/2)\lambda_1$ (anti-resonance) with decay time equal to 9.09 sec. Again the flat-layer approximation is very good. The oscillations in our solution are laterally propagating, wave interference effects. The waves that contribute primarily to this interference have wave numbers in the Love wave region of the wave number spectrum. This region is defined by wave numbers $|k_n| > |\omega/\beta_2|$. Pure Love waves do not exist here both because the basin depth is variable and because frequency is complex. Of course, the basin dimensions in this problem can be scaled to those in Figure 5.10 with frequency and decay time scaled accordingly. The flat-layer solution does not attain the peak $\rho_2 \beta_2 / \rho_1 \beta_1 = 7.0$ because complex frequency is used there also.

The basin shape in Figures 5.12 and 5.13 is flat, bounded by cosine shaped sides having a half-wavelength of 10 km. The solutions differ in that $\tau=9.09$ sec in Figure 5.12 and 90.9 sec in Figure 5.13. The large peaks in the wave number spectrum in Figure 5.13 account for the large oscillations in the surface displacement. These represent the interference between the vertically incident wave and pseudo-Love waves that are generated at the sides and trapped within the basin. The small, nearly constant displacements away from the basin indicate that the anomaly over the basin is not influenced by repeated basins every 256 km.



$\text{Im}\omega / \text{Re}\omega = 0.1$
 $c / \lambda_1 = 1/5$

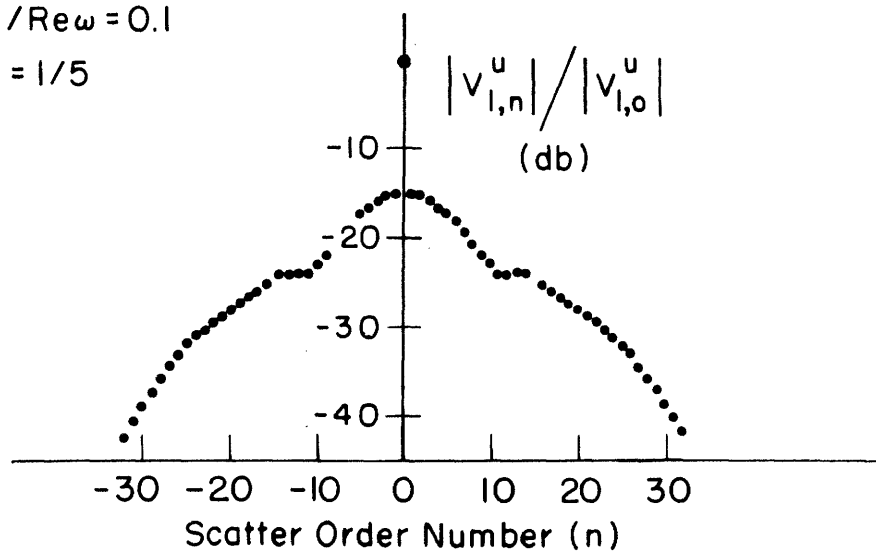


Figure 5.10. (Upper portion). Normalized amplitude of displacement response along the free surface of a soft basin to teleseismic SH waves: maximum depth is $1/5$ wavelength in the layer. The flat-layer response is the local Haskell approximation using layer thickness equal to that directly beneath the observation position.

(Lower portion). Wave number spectrum.

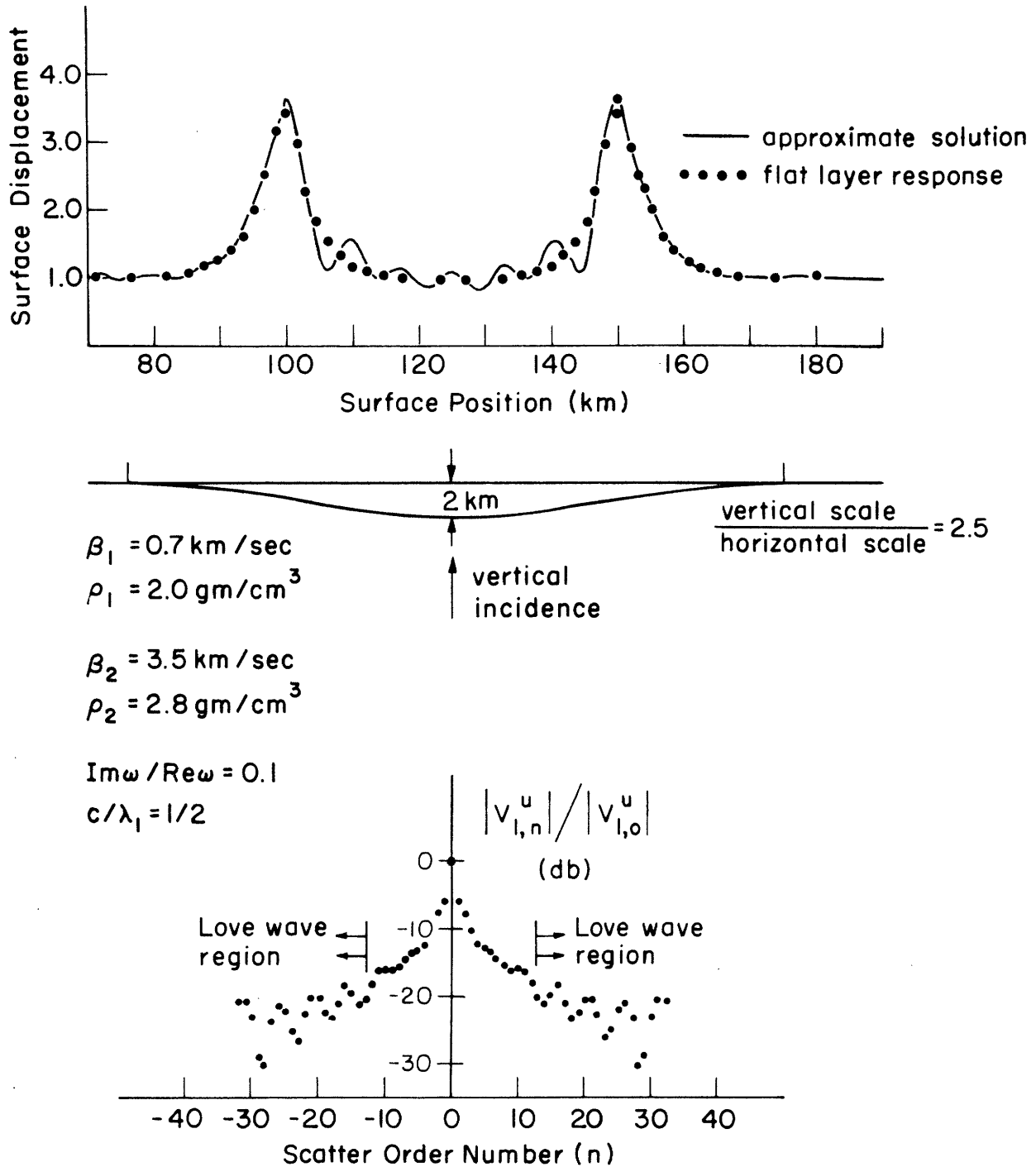


Figure 5.11. (Upper portion). Normalized amplitude of displacement response along the free surface of a soft basin to teleseismic SH waves: maximum depth is $1/2$ wavelength in the layer. The flat-layer response is the local Haskell approximation.

(Lower portion). Wave number spectrum.

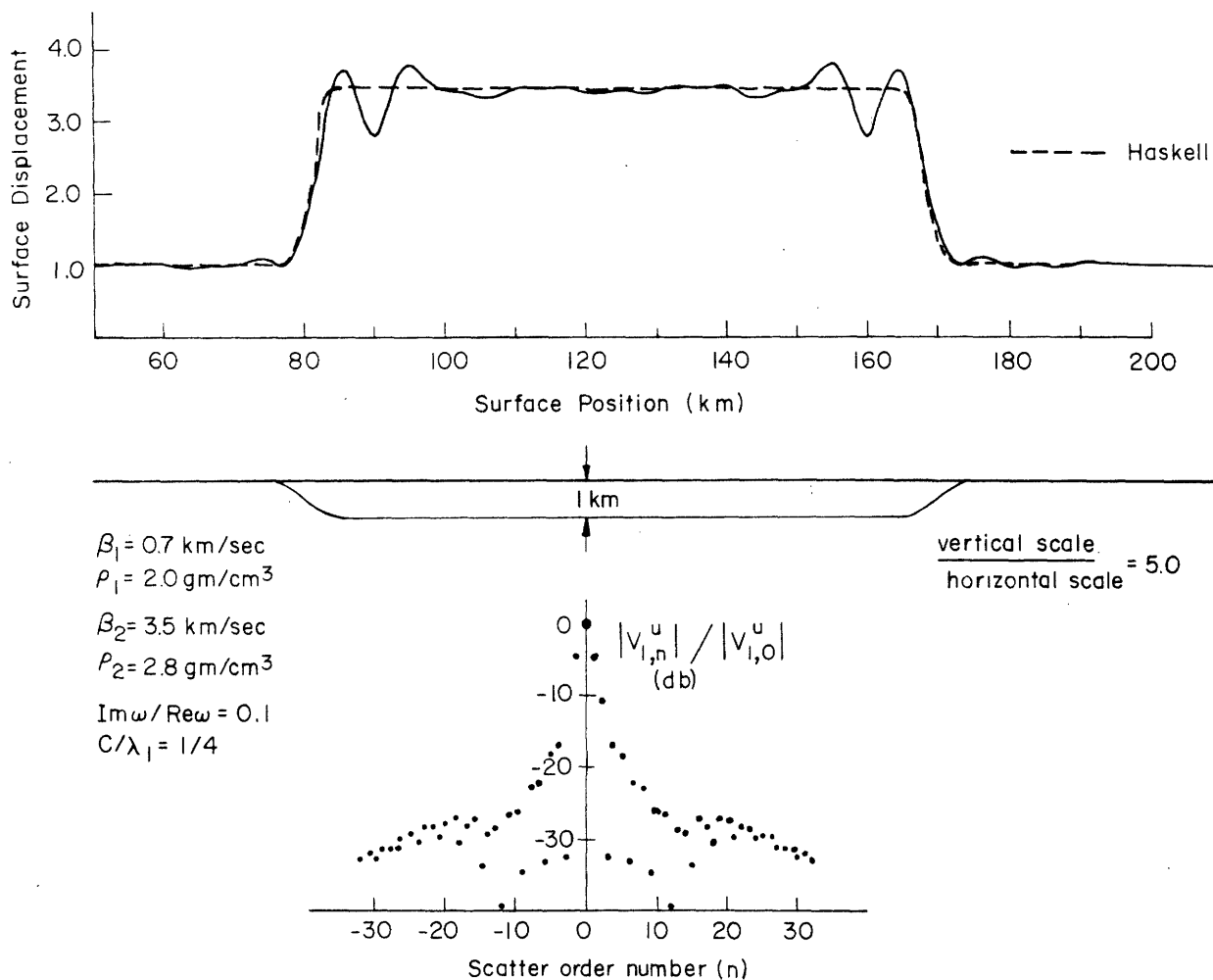


Figure 5.12. (Upper portion). Normalized amplitude of displacement response along the free surface of a flat, soft basin to vertically incident teleseismic SH waves: depth is $1/4$ wavelength (resonance). The exponential window decay time is $\tau = 9.09$ sec. Haskell denotes the local Haskell approximation.

(Lower portion). Wave number spectrum.

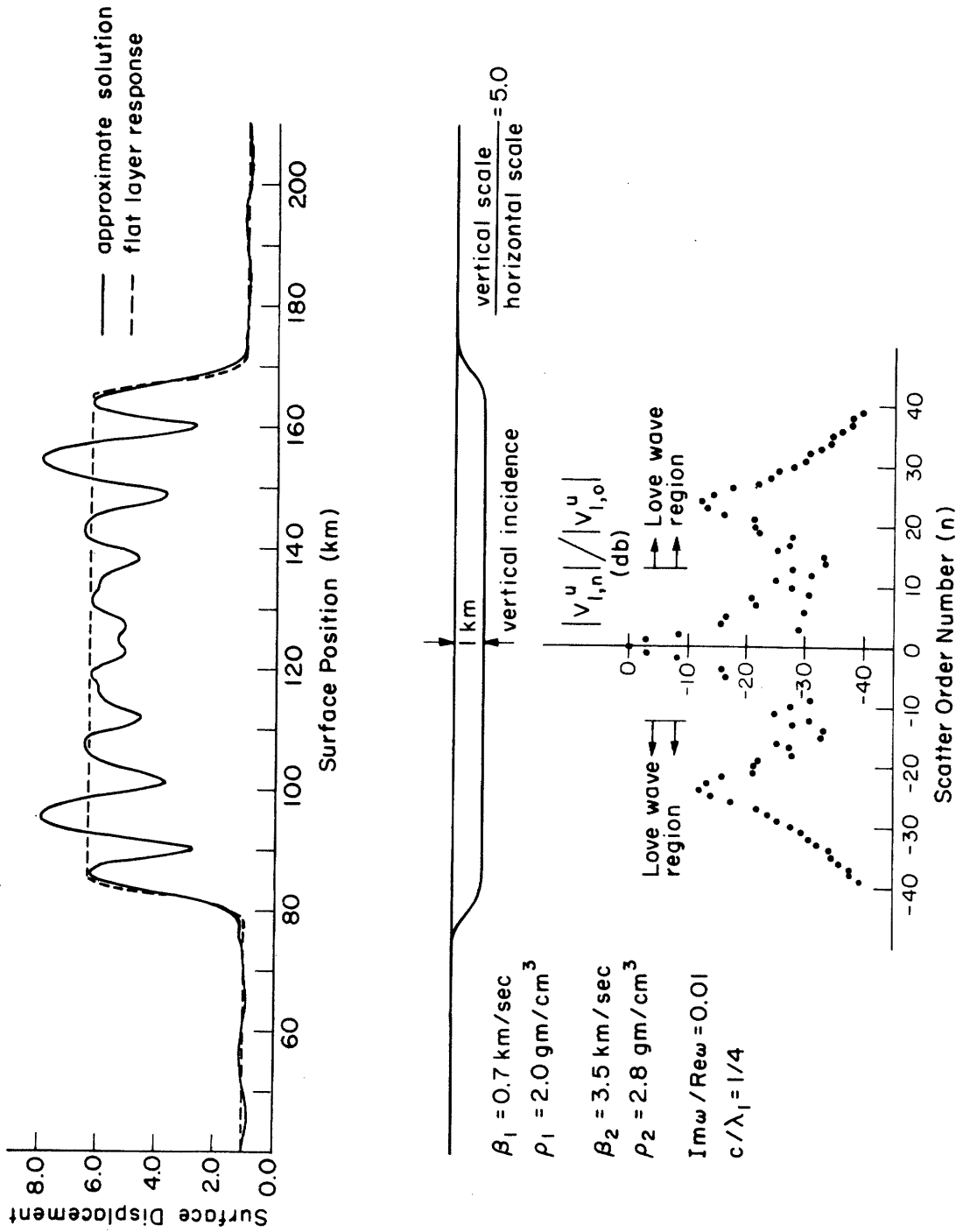


Figure 5.13. (Upper portion). Normalized amplitude of displacement response along the free surface of a flat, soft basin to teleseismic SH waves: depth is $1/4$ wavelength (resonance). The exponential window decay time is $\tau = 90.9$ sec. The flat layer response is the local Haskell approximation. (Lower portion). Wave number spectrum

Recognizing that wave attenuation can be large in the soft layers, seismologists often introduce damping into their flat-layer solutions. The result is a diminished resonant motion. It is readily shown (Brekhovskikh, 1960; Ewing, Jardetsky, and Press, 1957) that our complex frequency solutions are just special cases of solutions involving real frequency but with attenuation in the medium. Thus, Figures 5.12 and 5.13 demonstrate that attenuation in the sedimentary layers reduces not only the large flat-layer theory resonant motion but also the large oscillations that might result from laterally propagating waves trapped in basins.

In the comparison with the finite-difference solution (section 4.6), we found that the spectral amplitudes resulting from wave interference were not good indicators of peak motion in the time-domain solutions. However, large spatial oscillations in the spectral amplitudes are indicative that peak time domain solutions can be considerably enhanced. We thus expect to find large peak motions in the vicinity of rapid changes in thickness of the sedimentary layer. There was striking evidence for this effect based upon earthquake damage in Skopje, Yugoslavia (Poceski, 1969).

The final soft-basin example involves the response to waves whose length is comparable to the width of the basin. Many cases are shown in Figure 5.14. First note that the response to SH_y motion is not sensitive to the incident wave direction. For these long waves (100 km in the half-space) the motion of the basin apparently is determined by the vibration of the basement independent of Θ_0 . The large departure from the flat-layer solution when $\Theta_0 = 51^\circ$ implies that relatively more energy is trapped in the basin as Θ_0 increases. The response to waves with particle motion

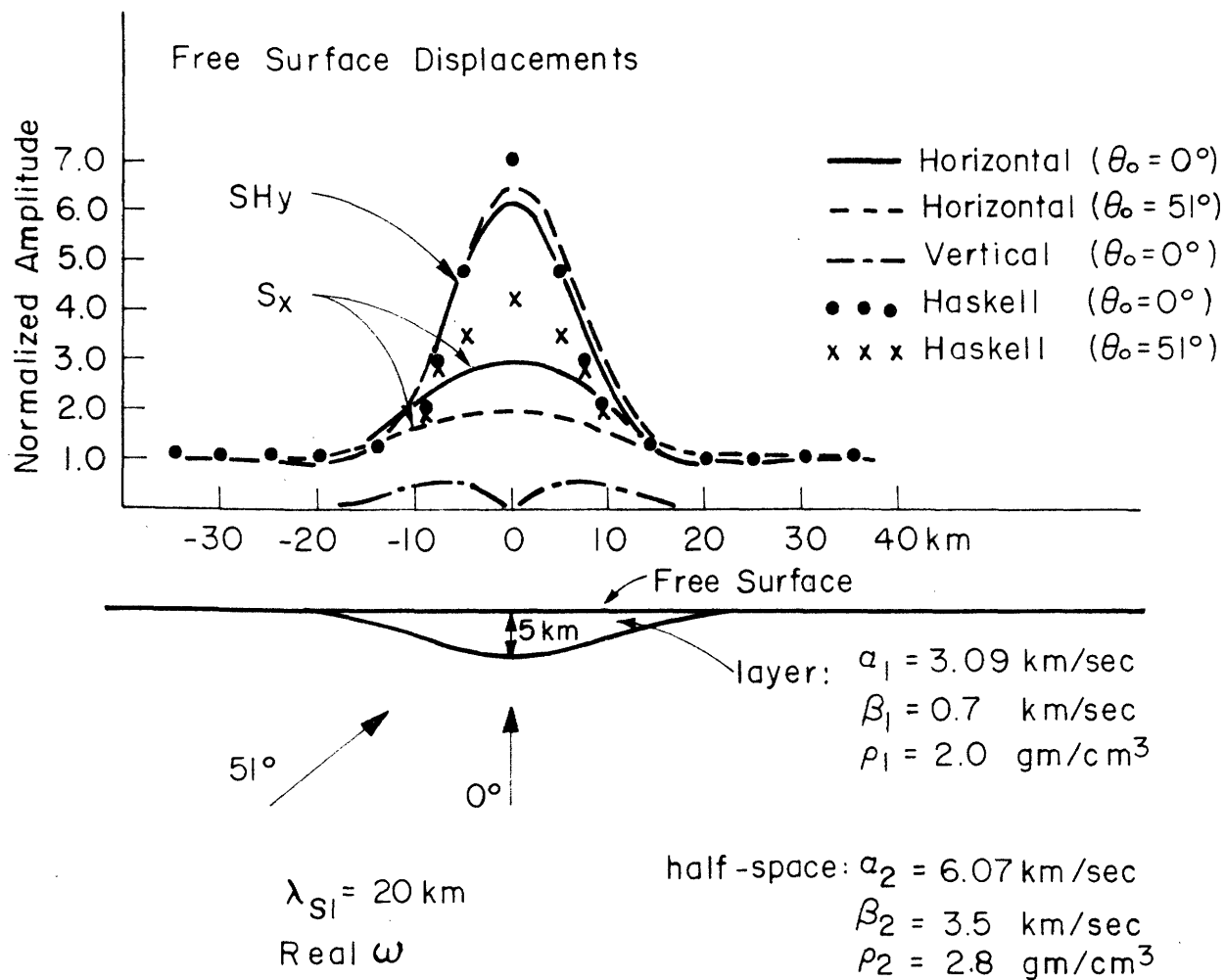


Figure 5.14. Response of a soft basin to long wavelength S waves: maximum depth is $1/4$ wavelength (resonance). SH_y denotes waves with particle motion normal to the plane of the figure. S_x denotes waves with particle motion in the plane of the figure. The flat-layer response is the local Haskell approximation.

in the plane of the figure is much reduced from the Haskell solution for both directions of incidence.

5.2.4. Mountains with roots. We have investigated problems involving SH-wave scattering in layer-over-half-space models for mountains with roots. The configurations were like those for the irregular Moho problems discussed in section 5.2. with the addition of variable surface topography. No results are presented here because we find that the surface displacements are unchanged (with the exception of added time delays over the mountains) from those in the problems involving plane free surfaces. We used exaggerated mountain sizes (as much as 5 km high by 50 km wide) and time decays sufficiently long to admit laterally propagating multiples within the mountain. Our conclusion for these SH wave examples, and for P wave cases as well, is that anomalous amplitudes observed on mountains must be the result of inhomogeneities beneath the mountains rather than the mountain relief.

5.2.5. Love waves scattered from surface topography. When the frequency is real, our solutions to the crust-mantle problem involving variable surface topography display oscillatory character such as in the example in Figure 5.15. There, the surface feature is a cosine-shaped valley 1-km deep by 50-km wide. The amplitude oscillations are caused by interference of the vertically incident waves with waves propagating to the left and right just as was observed in real ω problems involving an irregular Moho. But now, these interfering waves are Love wave modes. To see this, first note that the distance between peaks is equal to the apparent wavelength (18.2 km) of the interfering waves. The theoretical dispersion curves for the fundamental and next two higher order Love wave modes are

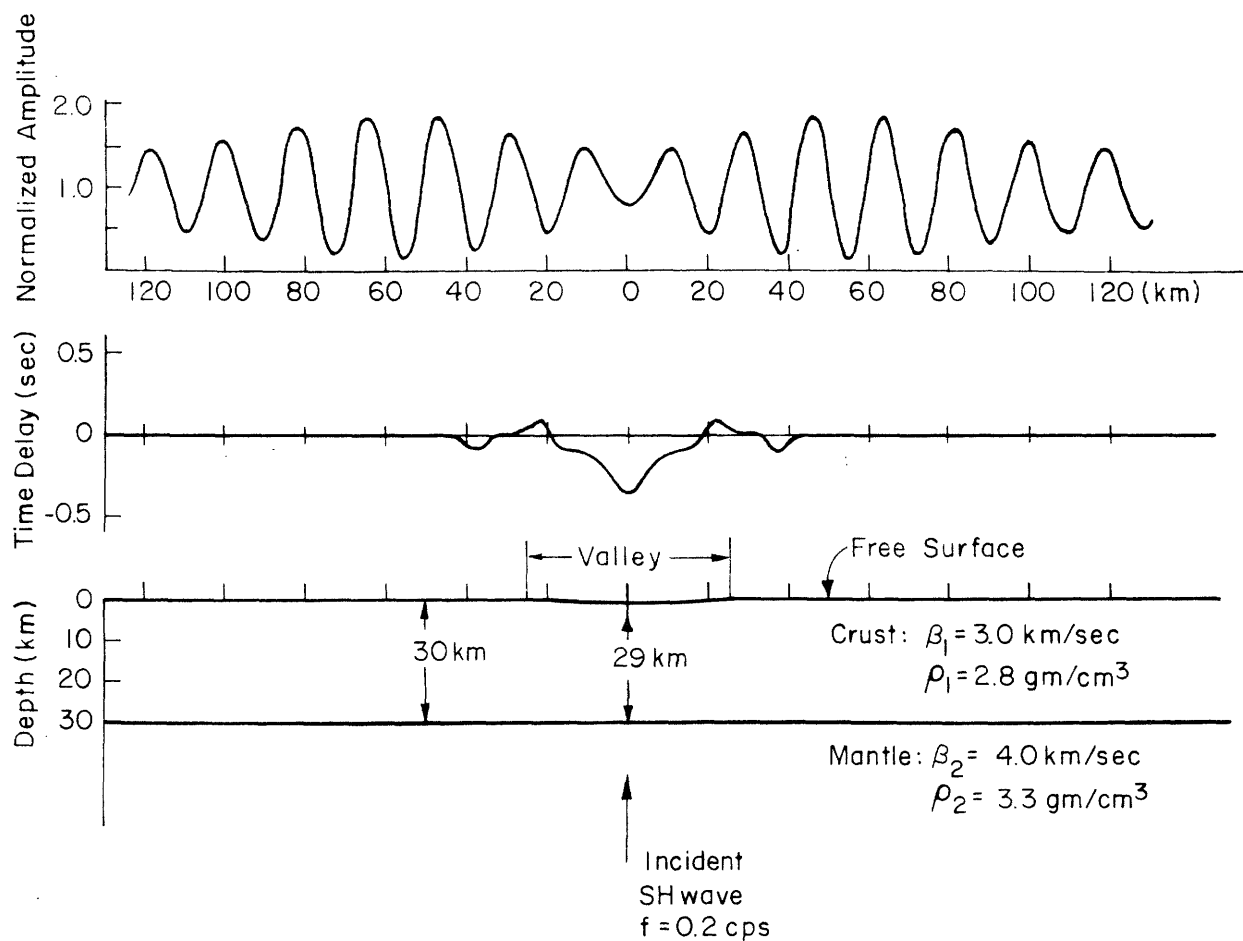


Figure 5.15. Generation of Love waves by the scattering of teleseismic SH waves at a valley. Frequency is real so that surface displacement amplitude displays oscillation caused by the interference of the primary wave with Love waves, propagating in both directions, generated by the repeated valleys spaced every $L=256 \text{ km}$.

shown in Figure 5.16. The seven cases indicated are results from applications of our method to the variable topography problems with problem parameters given in Table 5.2 (W , c , and D are defined by (4.7), and W_s and c_s are similar parameters for the free surface shape). The problem in Figure 5.15 is case 5. In each case, the distance between amplitude oscillation peaks λ_L yields a phase velocity $f\lambda_L$ that implies that one of the Love wave modes is dominant.

We note several interesting features. Valleys (cases 5, 6, 7) generate the highest mode allowed ($M=2$ in these cases). The fundamental mode predominates only when no other modes are allowed (case 3). The hills whose amplitude c_s is not small compared with D (cases 1 and 2) generate the first Love mode whereas the low profile hill (case 4) generates the $M=2$ mode. The wave number spectra for the seven cases are shown in Figure 5.17. In all cases, the amplitude of the dominant mode is larger than the neighboring amplitudes. Comparing the spectra, we note that amplitudes generally decrease at first with increasing n (the initial rate of decrease for case 6 is small because diffraction, i.e. wave number coupling, is relatively most important for the smallest surface feature). The amplitudes vary smoothly until $n=13$ where amplitude drops abruptly in each case. $n=13$ denotes the first inhomogeneous scatter order in the half-space. Beyond $n=13$, amplitudes decrease rapidly except for those of the trapped Love wave modes. Note that the dominant mode amplitudes are larger for problems involving valleys than for those involving hills. This is reflected by larger amplitude oscillations such as those in Figure 5.15 for the scattering from valleys.

Based upon the wave number spectra, we interpret the tendency to

TABLE 5.2

Free Surface and Interface Shape Parameters for the Cases in
Figures 5.16 and 5.17

Case	Feature	D (km)	W_s (km)	c_s (km)	W (km)	c (km)
1	Hill	30	50	-2.5	50	2.5
2	"	17	"	-2.5	"	"
3	"	10	"	-5.0	—	0
4	"	30	"	-1.0	—	"
5	Valley	"	"	1.0	—	"
6	"	"	25	0.5	—	"
7	"	"	50	5.0	—	"

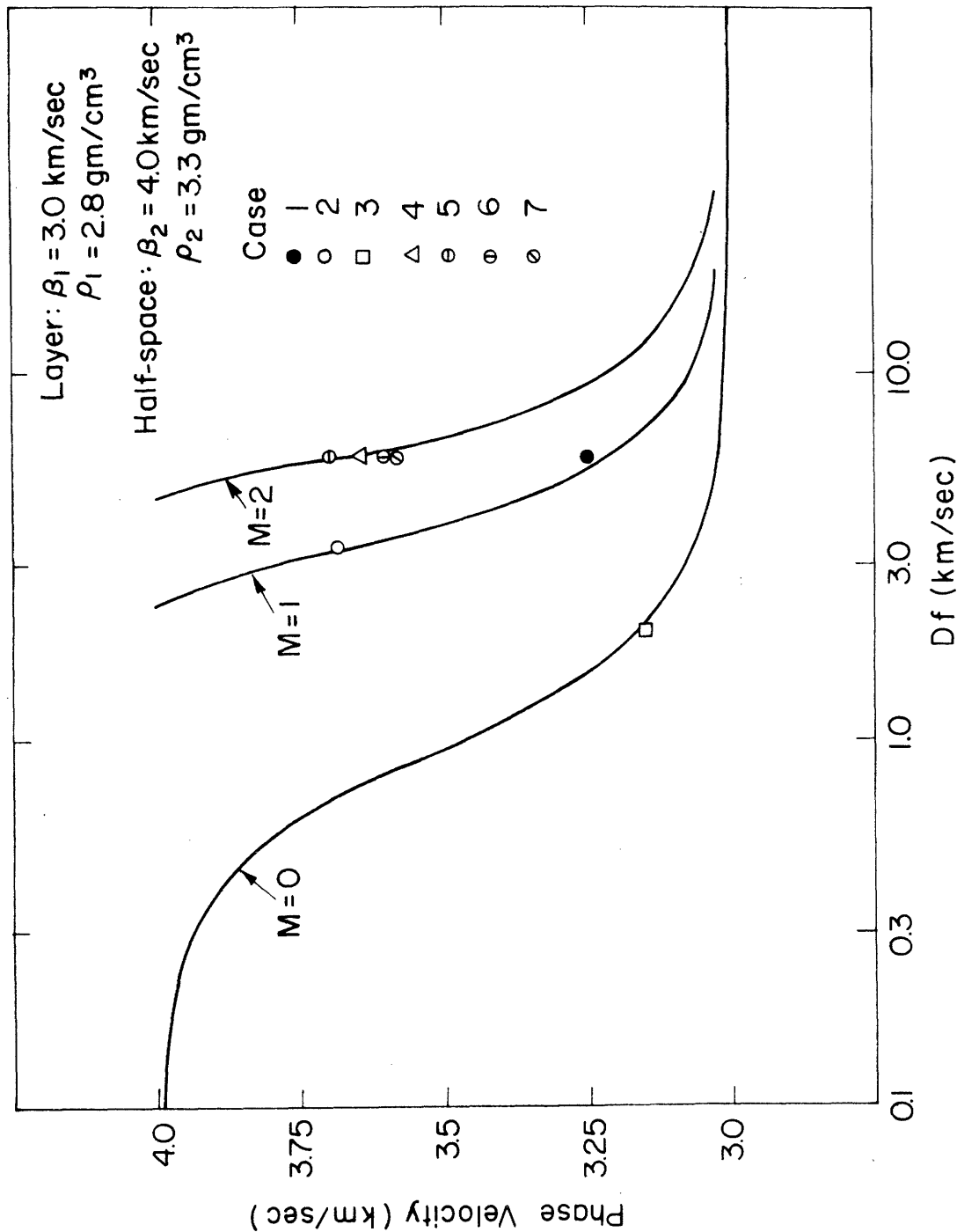


Figure 5.16. Love wave dispersion curves for a single layer over a half-space. The topographic and interface shape parameters for the seven wave scattering cases are given in Table 5.2. M=0 denotes the fundamental Love wave mode; M=1 and M=2 are the first and second higher order modes.

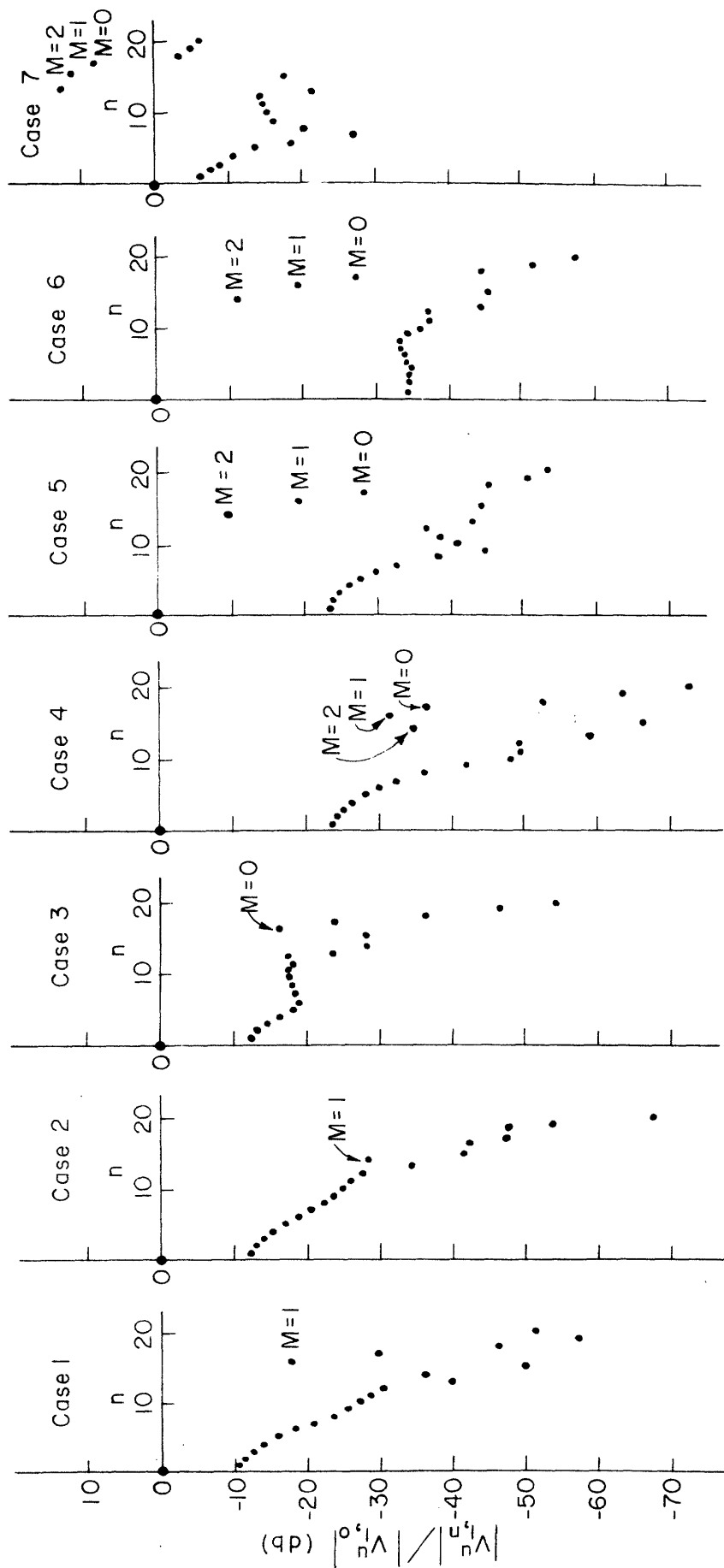


Figure 5.17. Wave number spectra for the seven SH wave scattering cases listed in Table 5.2. The dots labeled with an M number are amplitudes of the indicated Love wave modes.

generate the higher modes rather than the fundamental as caused by larger source excitation functions for waves having the larger phase velocities. This is clearly true for scattering from valleys but the scattering from hills is probably less straightforward.

Of course these Love wave manifestations were artificially enhanced in our solutions by the periodic surface shape every $L=256$ km. Therefore we do not interpret the displacement amplitudes as having reality. Rather we suggest that the results may be useful from a relative viewpoint, i.e. valleys are relatively more efficient generators of scattered Love wave modes and the higher modes are preferred over the fundamental.

We made no comparable study of Rayleigh wave generation by the scattering of teleseismic P waves. We note that in his theoretical study, McIvor (1969) found that vertically incident plane P waves generated larger amplitude Rayleigh waves from a sinusoidal surface irregularity having valleys than from a parabolic-shaped hill.

5.3. P-SV Wave Scattering Problems.

5.3.1. Comparison with a laboratory refraction model study. Here, we shall compare our solutions for grazing incidence P waves with results from a refraction model study by Laster, Backus, and Schell (1967). Their model consisted of a strip of brass plate (layer) over a stainless steel plate representing a half-space. The interface had a localized circular dome-shaped irregularity as in Figure 5.18. A barium titanate crystal, placed on top of the brass layer, provided a transient elastic wave signal having a peak frequency of 180 cps. The vertical component of motion was

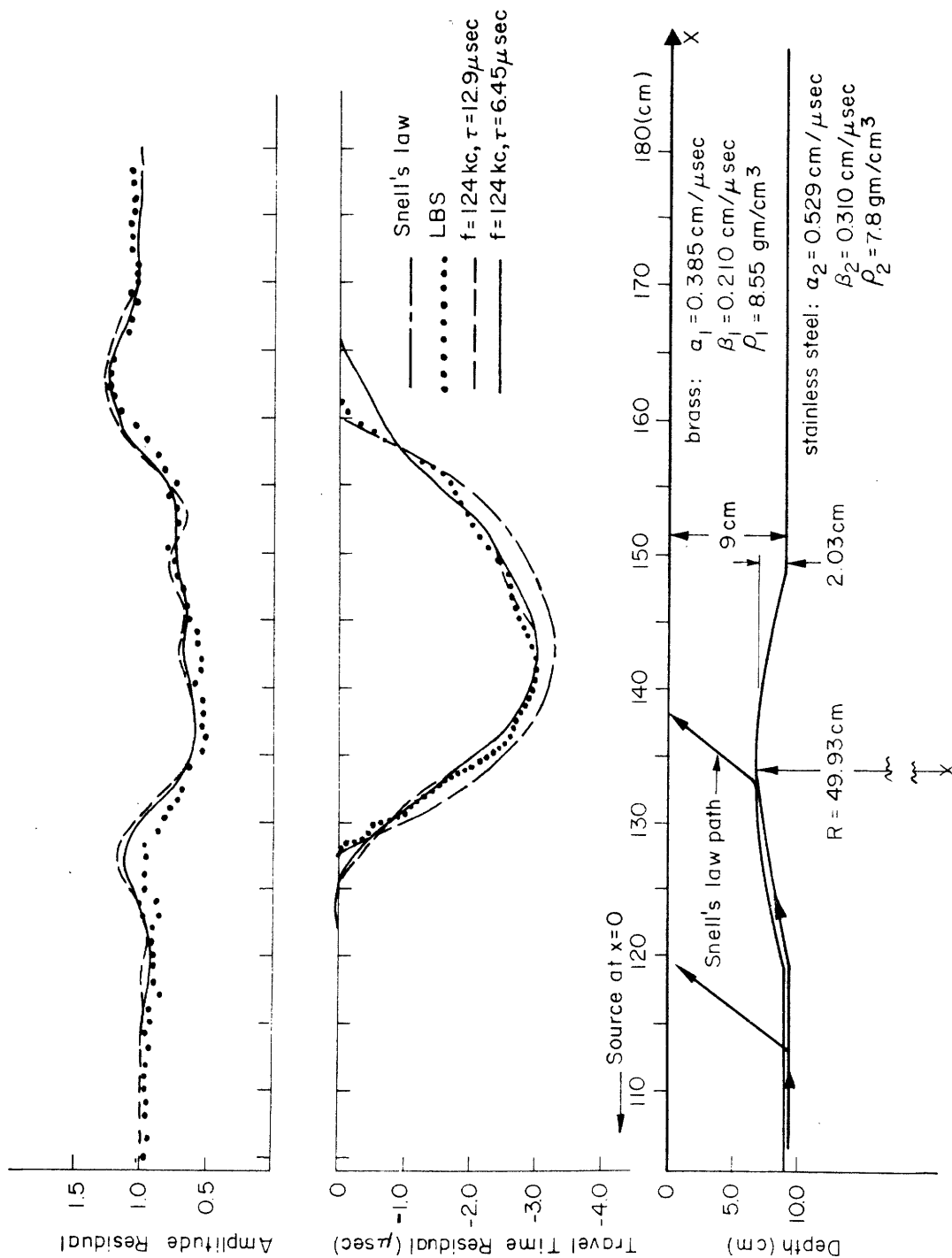


Figure 5.18. Comparison of two theoretical solutions with the results of a laboratory refraction model study by Laster, Backus, and Schell (LBS). The amplitude and travel time residuals pertain to the vertical component of motion along the free surface.

detected along a profile on the top edge of the model.

In our method, we cannot isolate the various arriving phases. Indeed, since our solutions are source free, most later phases do not enter our solutions. Through the use of complex frequency we can, in effect, isolate the P-wave arrivals from the trailing S waves. Since our solutions for the two values of decay time are similar, we conclude that τ is sufficiently short so that the contribution from S waves is small. Therefore our solutions can be compared with the LBS measurements for the first refraction arrival. The LBS amplitudes are departures from $x^{-3/2}$ dependence where x is the distance from the source. Our amplitudes have the factor $e^{\Delta t/\tau}$ restored as in the discussion of Figure 5.6. The amplitudes compare well considering that ours is a single frequency solution and the LBS solution is for a 60 to 300 kc pass-band signal. The travel time residuals also agree well. Laster, et. al. pointed out that the departures from the Snell's law curve would result in erroneous estimates of the shape of the irregularity. We also recognize these departures as being related to the phase dispersion noted in the SH wave examples.

This example demonstrates the applicability of our technique as an interpretive tool in refraction seismology.

5.3.2. Irregular Moho problems. The seven cases presented in Figures 5.19 and 5.20 are selected to demonstrate effects of wavelength, decay time, interface shape, and layer thickness upon the spatial distributions of amplitude and phase delay for the vertical component of displacement. The width W of the Moho depression is 40 km in each case. As in the SH-wave cases, the widths of the amplitude anomalies increase with wavelength

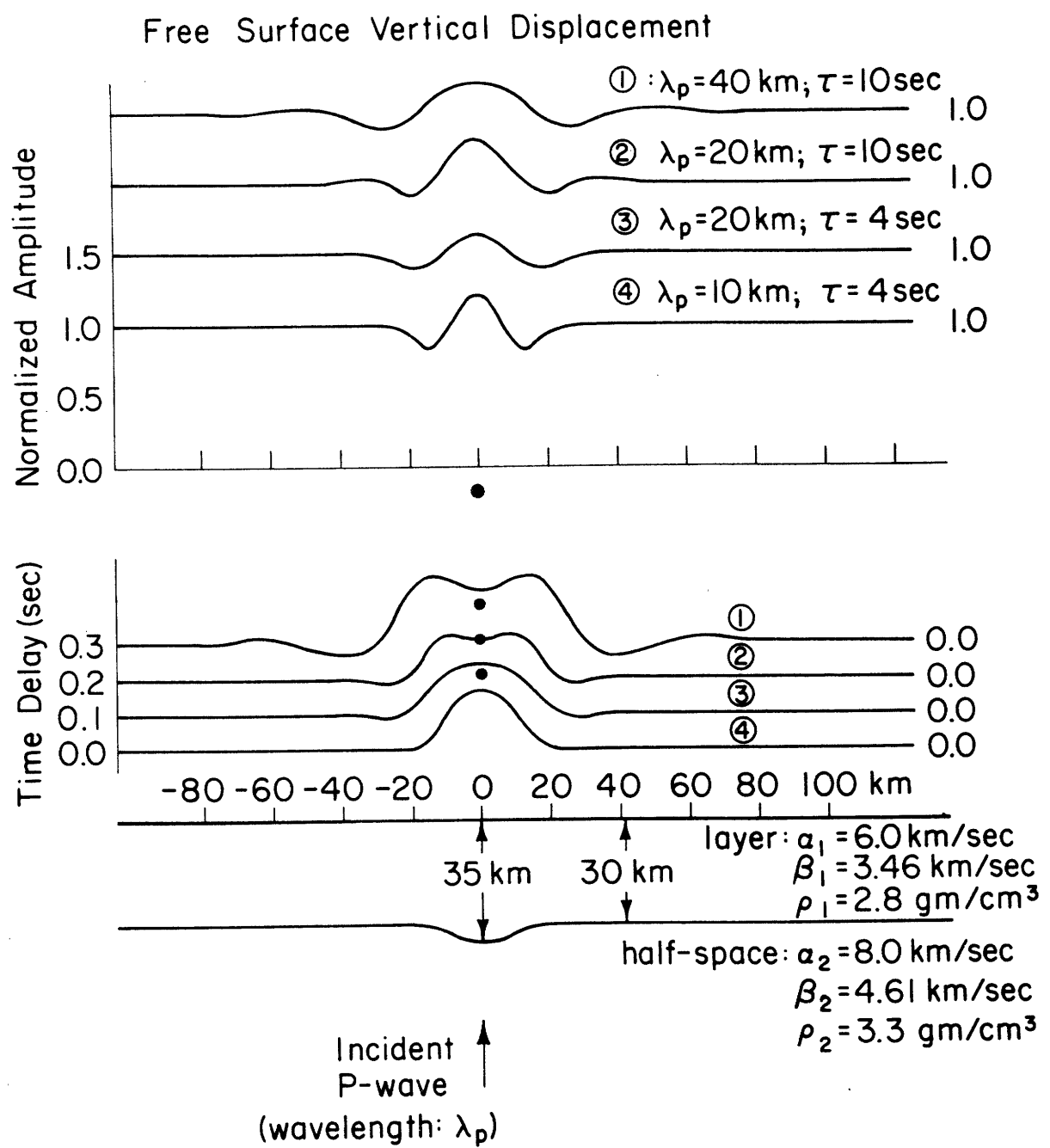


Figure 5.19. Vertical component of free surface motion for teleseismic P waves scattered at a depression in the Moho, displaying wavelength and complex frequency effects. The depth to the center of the depression should read 40 km for case 1. The dots denote the ray theoretical time delays at 0 km. The common scales are shown for the lower curves only.

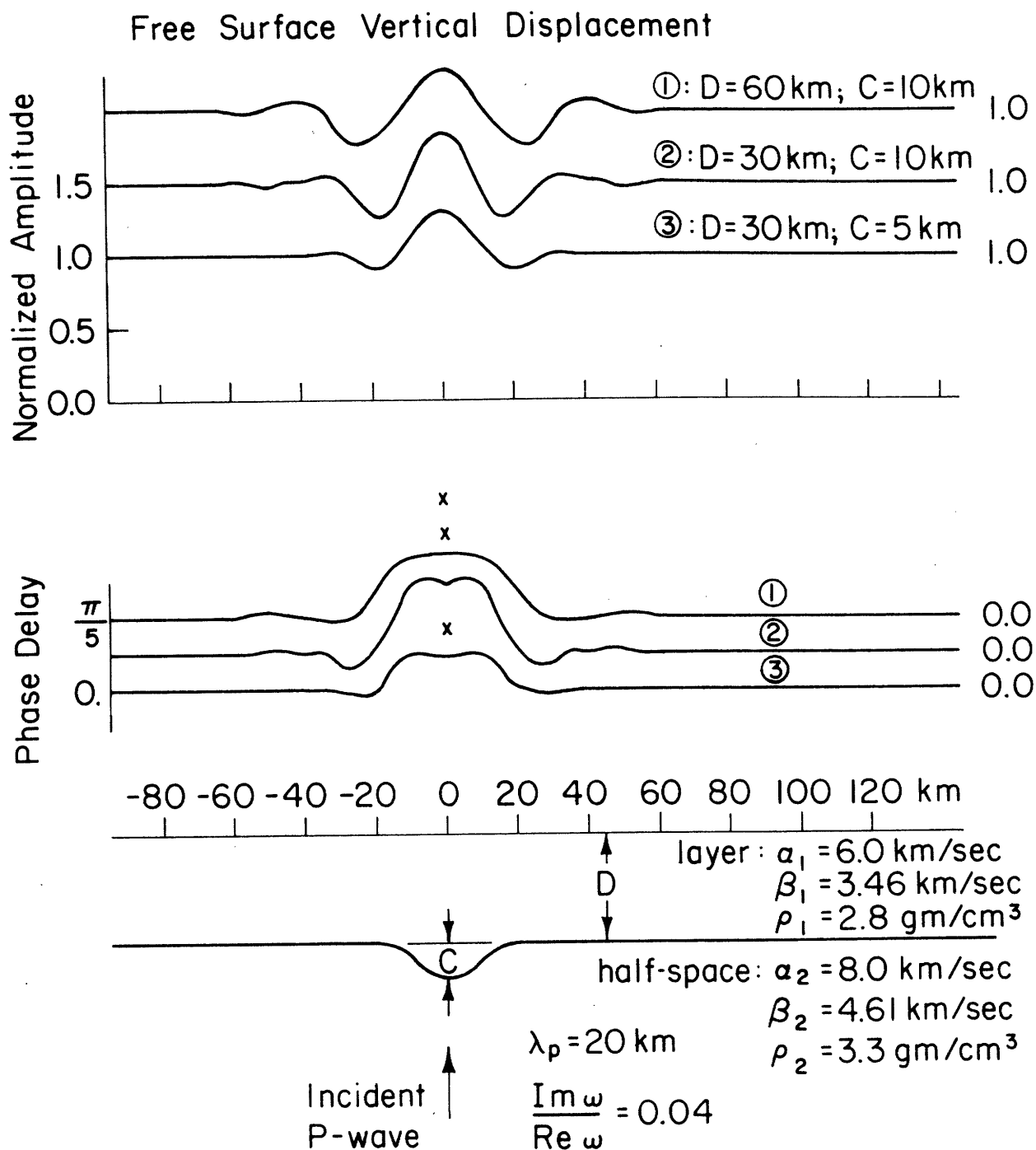


Figure 5.20. Vertical component of free surface displacement for teleseismic P waves scattered at a depression in the Moho, displaying effects of layer thickness D and interface depression amplitude c . The X's denote ray theoretical time delays at 0 km. In these problems, $f=0.4$ cps and $\tau=9.95$ sec. The common scales are shown for the lower curves only.

and with layer thickness. The peak-to-trough variations in the amplitude anomalies for cases 2 and 3 in Figure 5.20 are in the approximate ratio 1.5 whereas the amplitudes of the Moho depression c differ by the factor 2. Considering the further effect of layer thickness on the amplitude variations, we judge that the quality of observed data must be very good in order to use the actual amplitudes in the determination of subsurface structure. The locations of the peak amplitudes or the ratios of various components of motion may be more useful as interpretive tools. The actual amplitudes may also be of use in making amplitude corrections in areas where the subsurface structure is known.

Phase dispersion - the departures from the dots and x's - is evident in each case. The flat, phase-delay anomalies and the dips over the center of the Moho depression are typical of long wavelength solutions.

Figure 5.21 demonstrates the generation of a vertical component of motion by the scattering of a vertically incident teleseismic S wave. The slopes of the spatial distribution of phase delay for the vertical component imply that the apparent velocity of the scattered wave approaches the P-wave velocity in the half-space. The dot is the ray theoretical phase delay for the horizontal component.

Scattering of obliquely incident, teleseismic P waves is shown in Figure 5.22. The vertical component amplitude peaks between the ray theoretical caustics for the P-wave arrival and displays an indication of sensitivity to the converted S-wave arrival as well. The horizontal component appears to be more sensitive to the flat layer wave interference effects. The ratio of vertical to horizontal amplitude (V/H) is compared with the usual Haskell flat-layer theory solution. A question arises as to

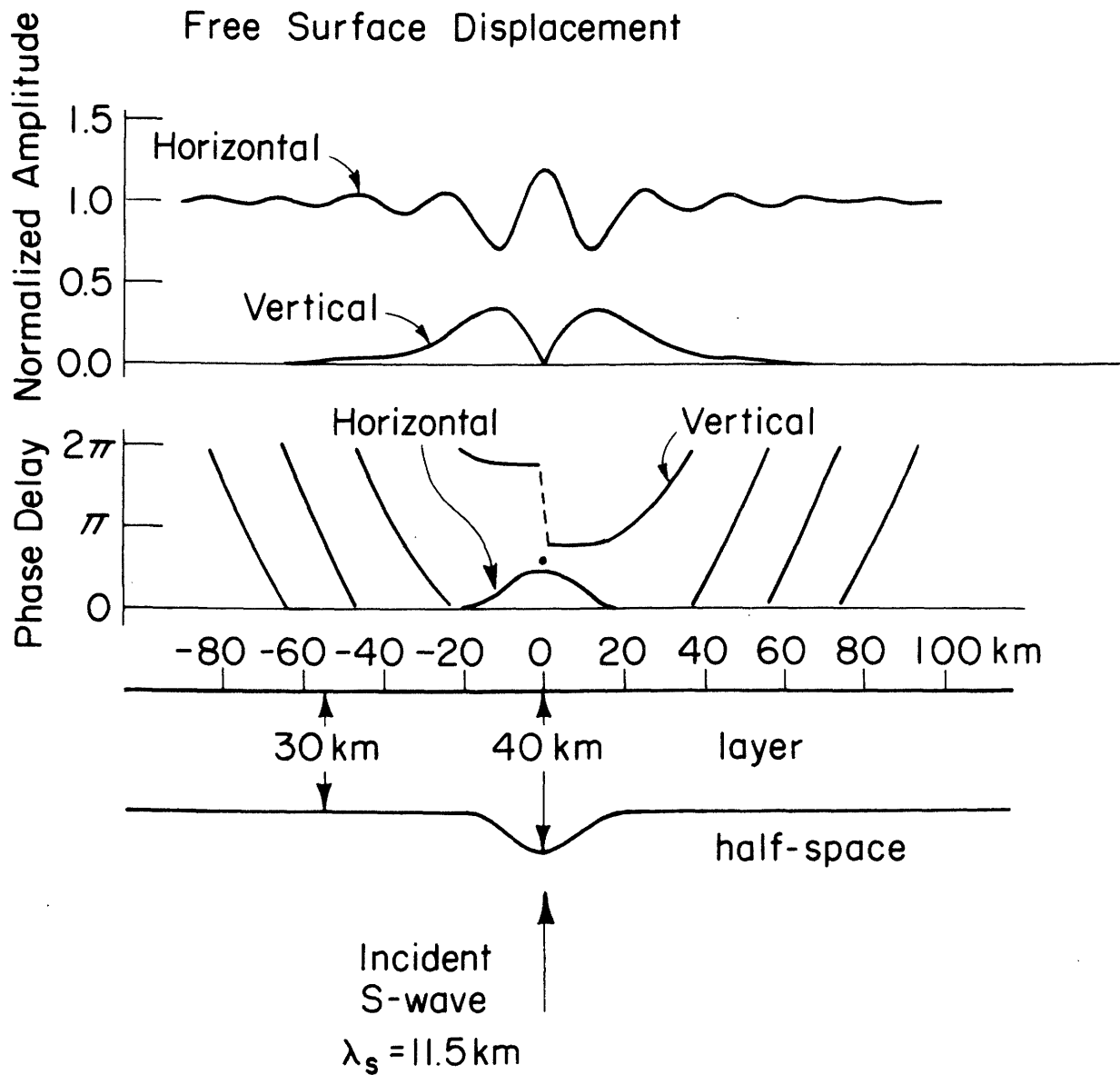


Figure 5.21. Displacements resulting from the scattering of vertically incident teleseismic S waves (particle motion in the plane of the figure) at a depression in the Moho. The layer parameters are the same as those in Figure 5.20. Here, $f=0.4$ cps and $\tau=9.95$ sec.

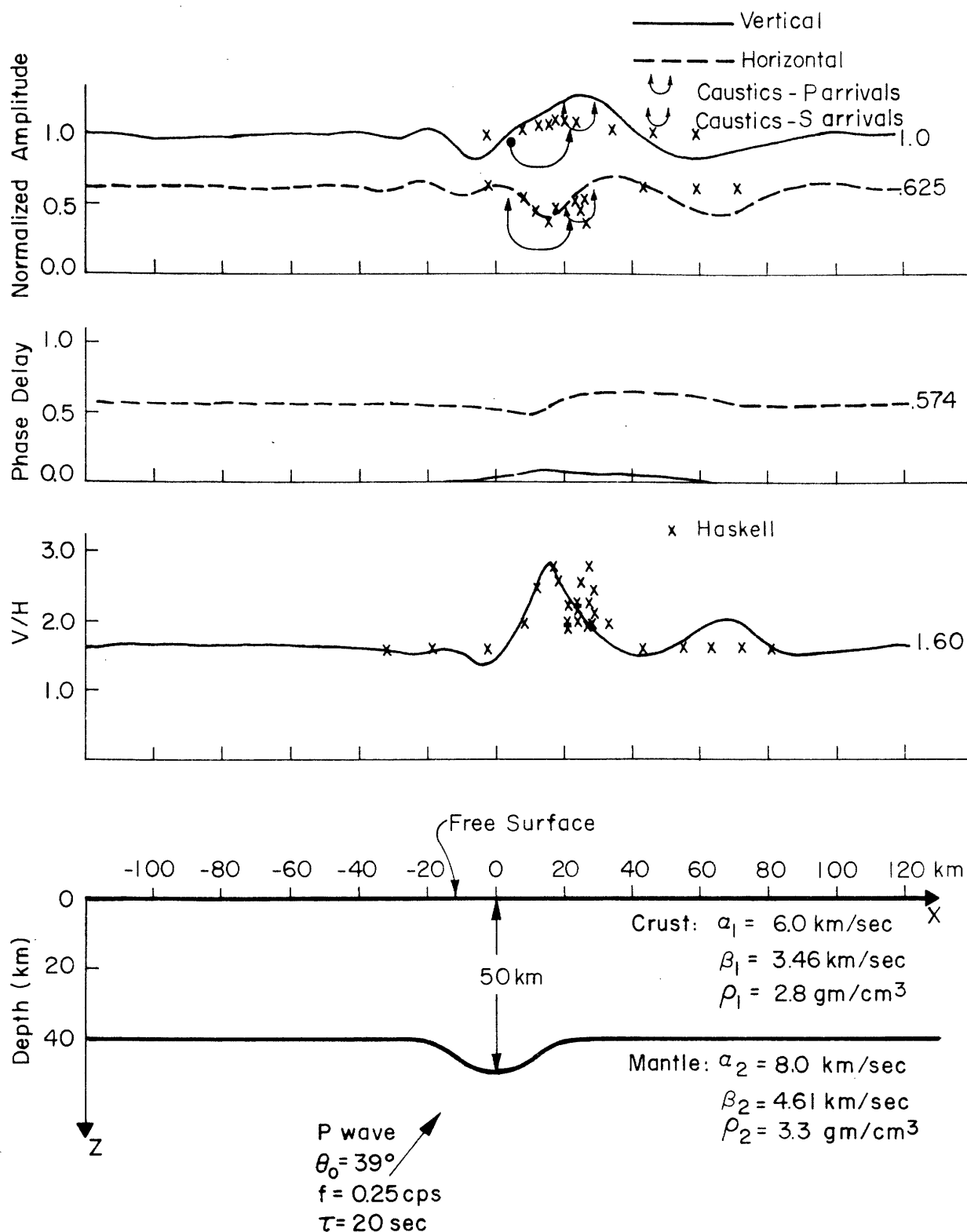


Figure 5.22. Two components of displacement caused by scattering of teleseismic P waves at a depression in the Moho. The locations of the caustics are determined by ray theory. The numbers to the right of the curves are theoretical values over the flat layer portion. V/H is the (spectral) ratio of the vertical to horizontal amplitude. The x's are Haskell flat-layer solutions assuming a layer thickness equal to the depth of the interface at the position projected back from the observation point along the geometric ray.

what layer thickness to use in the Haskell solution at a particular observation position x . We used a mixture with ray theory by assigning the depth of the interface at the projection of the observation position backward along the geometric ray path. The comparison with the Haskell solutions is not bad for this rather severe irregularity. However the comparison most likely is fortuitous as discussed in the next section. Our solutions indicate that wave focusing tends to predominate as θ_0 increases.

5.3.3. Spectral amplitude ratios. In the Phinney method for the estimation of crustal structure, observed values of the ratio of the vertical to horizontal component of spectral amplitude $V(f)/H(f)$ are plotted as a function of frequency and compared by trial-and-error matching with theoretical V/H curves for assumed flat layer models. The V/H curve in Figure 5.23 is a typical example. It was computed for waves having an apparent velocity of 17.8 km/sec incident upon a single layer over a half-space with medium parameters given in Figure 5.22. The locations and amplitudes of the peaks in the curves are diagnostic of layer thicknesses and velocity contrasts. We show the horizontal and vertical components separately in Figure 5.23 to demonstrate that the V/H curve is most sensitive to variations in the horizontal component amplitude. For reasons described by Phinney (1964), the observed data is truncated and windowed prior to spectral analysis. For appropriate comparison, the theoretical V/H curve should be similarly smoothed. Various authors have different choices for smoothing windows (Phinney, 1964; Fernandez and Careaga, 1968; Utsu, 1966). Consistent with the philosophy of our method, we would use the exponential time window. Thus, the V/H curve in Figure 5.23 was computed directly by the Haskell method using complex frequency.

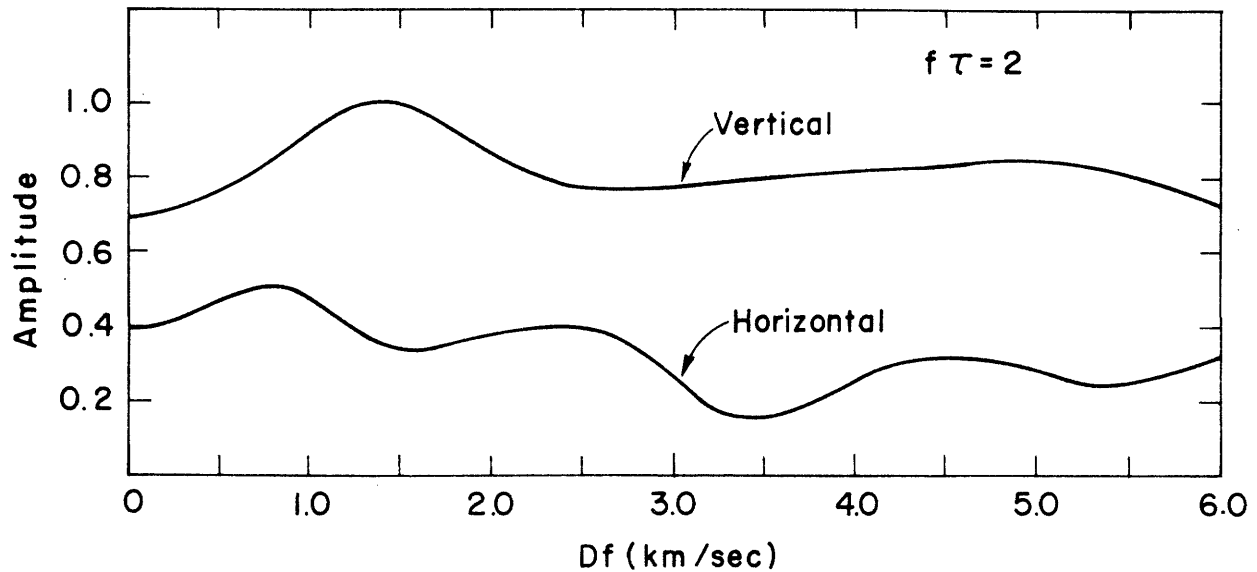
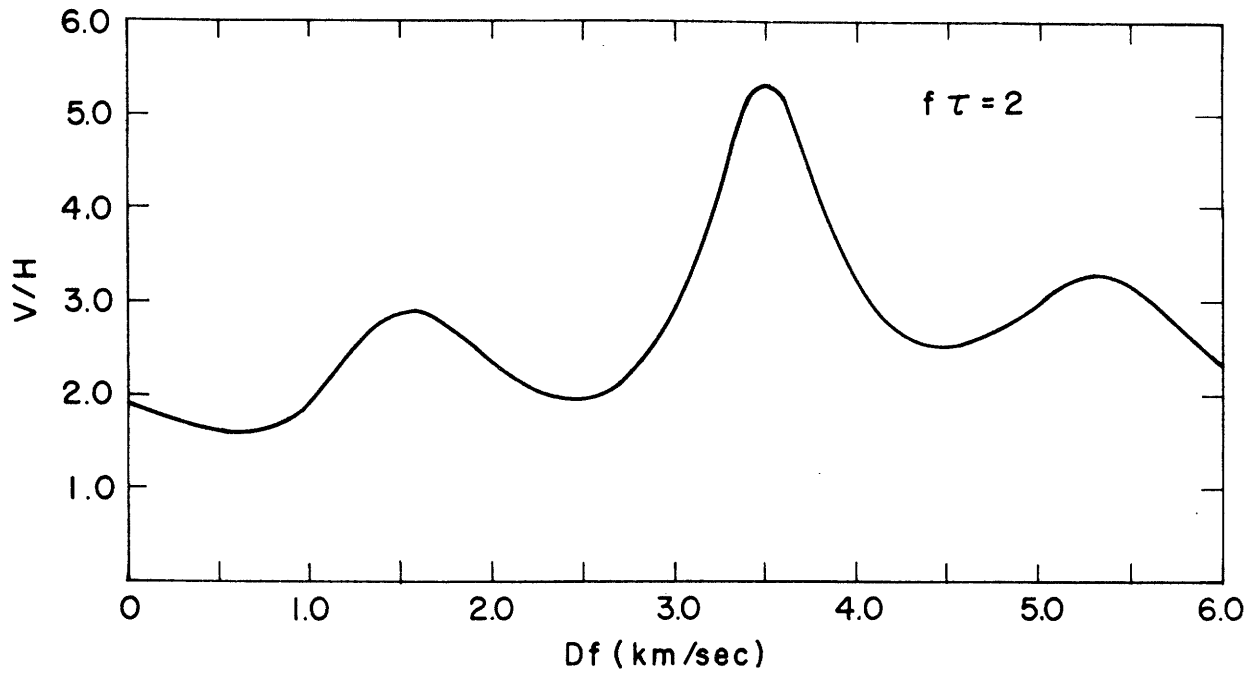


Figure 5.23. (Upper portion). Theoretical spectral ratio of vertical to horizontal amplitude versus the product of layer thickness and frequency for a single flat layer over a half-space. The medium parameters are given in Figure 5.22. Apparent velocity is 17.8 km/sec.

(Lower portion). Amplitudes (arbitrary units) of the two components of motion. In this Haskell solution, frequency ω is complex such that $f\tau = 2$.

The question that we investigate in the next three figures is that of validity of the Phinney technique when the layers are not uniformly thick. In each figure the Haskell solutions use the layer thicknesses directly beneath the observation positions. This choice is arbitrary and was made for simplicity; yet it appears surprisingly appropriate in Figures 5.24 and 5.25. The two frequencies selected for study in these figures are such that the large V/H peak occurs at $D=35$ km and 45 km, the shallowest and deepest Moho depths in the problem. The departures from the Haskell solutions are caused both by wave focusing and by smearing of the apparent velocity and constant depth requirements for the flat-layer solutions. Nevertheless, these results suggest that at most positions x the large peak in the V/H vs. frequency curve will still be observed. The height of the peak will be reduced much the same as a) when more severe frequency smoothing is used, b) when the solutions for several incident wave directions are averaged, or c) when the single crustal layer is replaced by several layers and velocity contrasts are reduced. In Phinney's actual use of the method, the observational data is so smoothed that the smearing introduced by these mild undulations in the Moho should not be deleterious.

In the two examples shown in Figure 5.26, the Moho undulations are more severe. The Phinney method appears to break down over the irregularity and, surprisingly, may even be vitiated as far away as at positions $x=-90$ km and +100 km. The oscillations in our computed V/H distributions are caused primarily by focusing effects in the vertical component.

By scaling the dimensions and times in these examples, the results are apropos of the use of the Phinney technique by Ellis and Basham (1968) for study of shallow crustal structure using short-period waves.

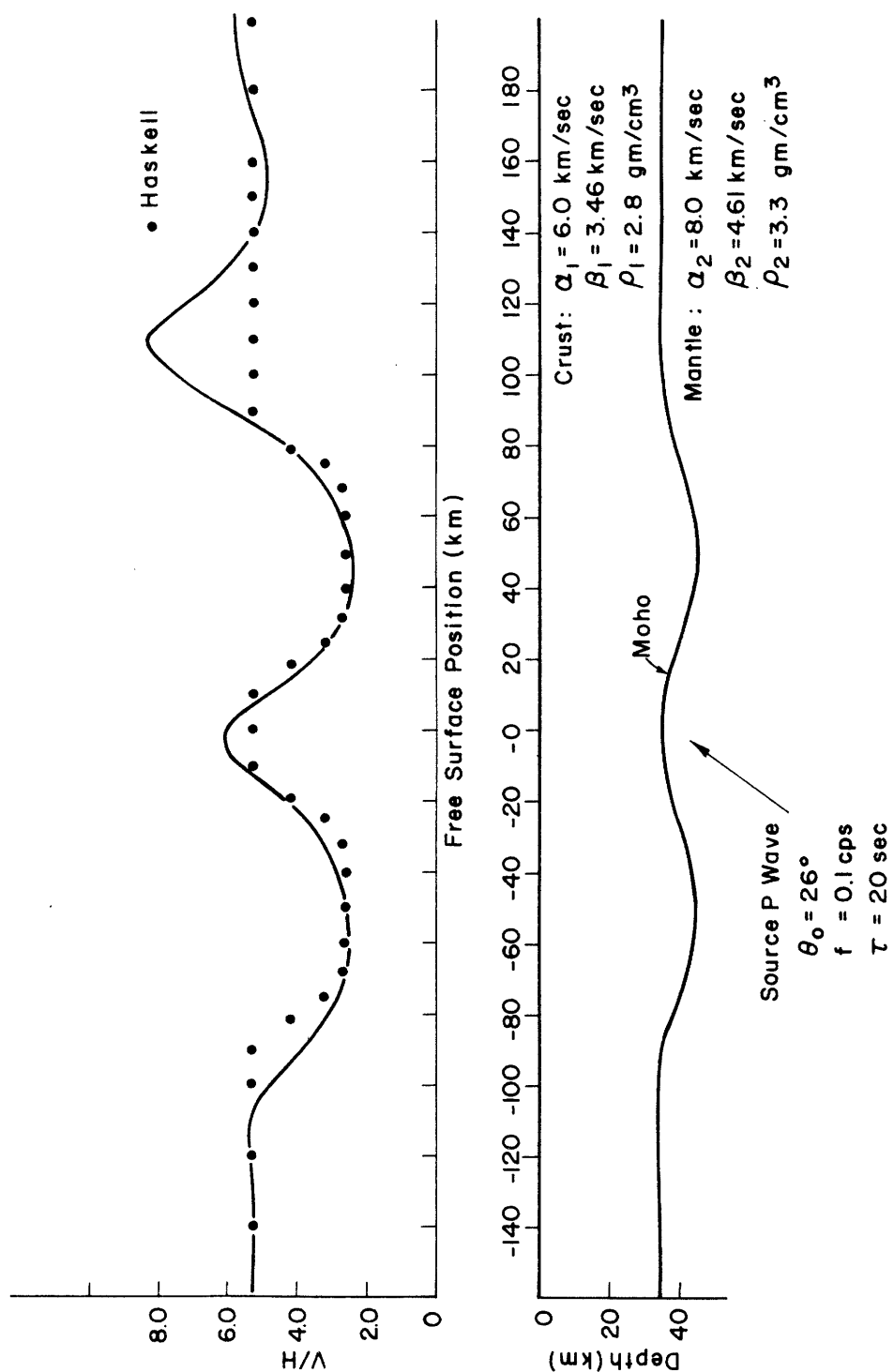


Figure 5.24. Spatial distributions of the spectral amplitude ratio V/H for scattering of teleseismic P waves at a mildly undulating Moho. The Haskell solutions are computed using the layer thickness directly beneath the observation point. Frequency is 0.1 cps.

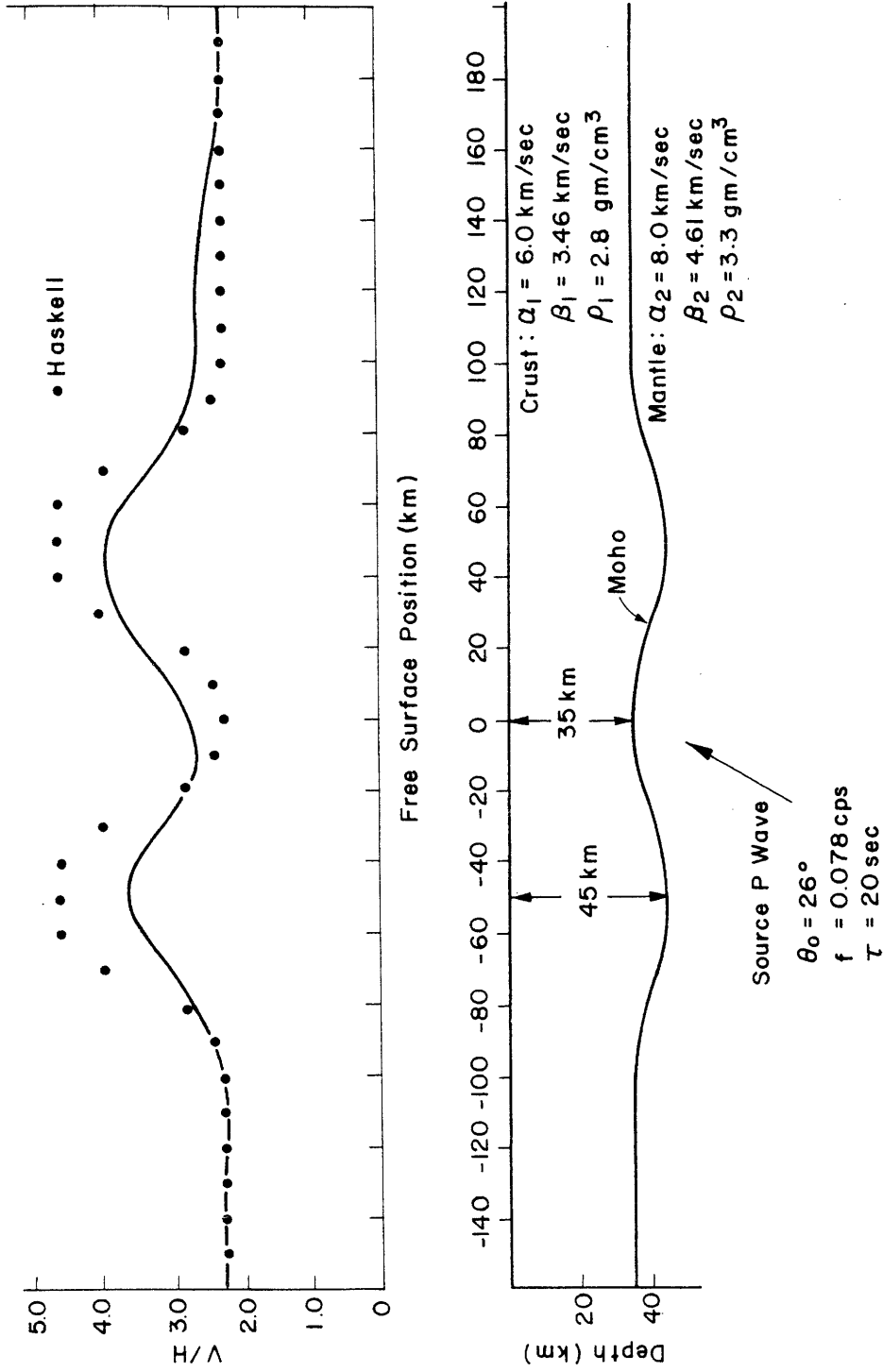


Figure 5.25. Spatial distributions of the spectral amplitude ratio V/H for scattering of teleseismic P waves at a mildly undulating Moho. The Haskell solutions use the layer thickness directly beneath the observation point.

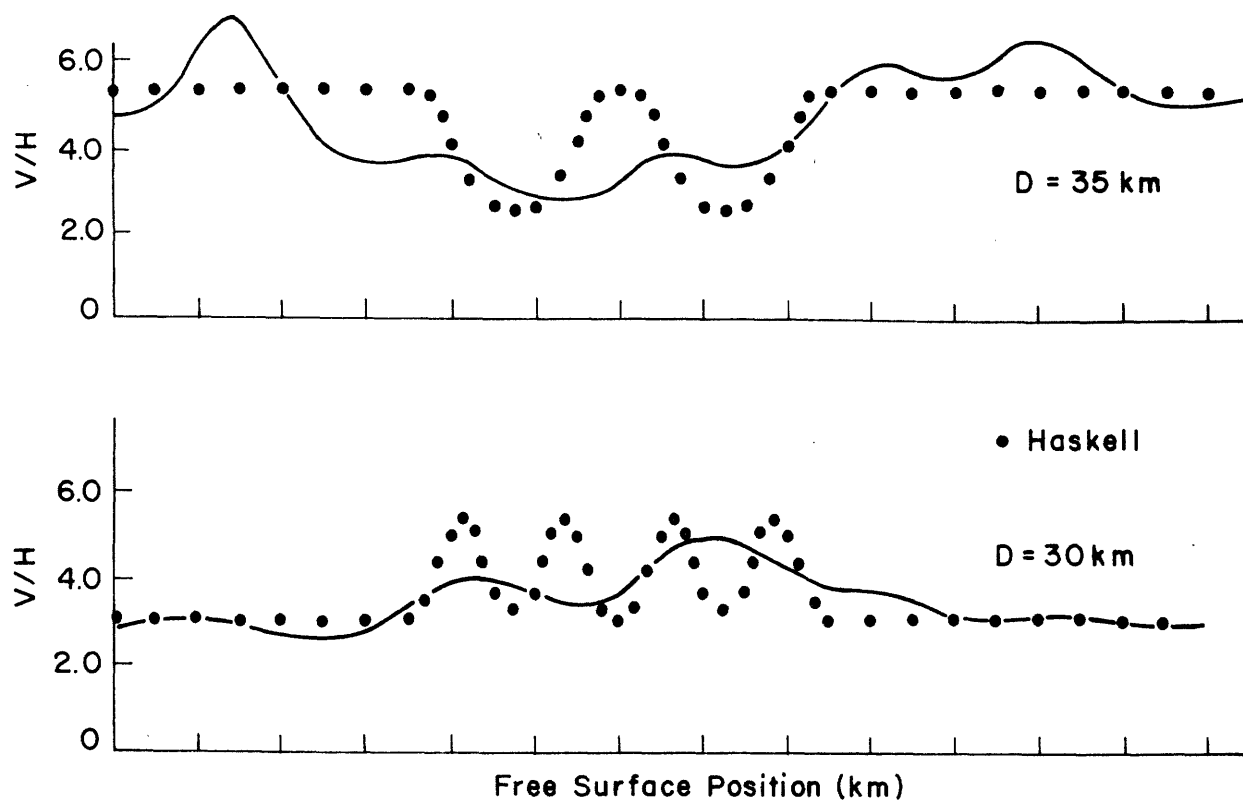


Figure 5.26. Spatial distributions of the spectral amplitude ratio V/H for scattering of teleseismic P waves at a severely undulating Moho. The Haskell solutions use the layer thickness directly beneath the observation point.

5.4. Arbitrary-Azimuth Incidence Problems.

In the examples considered in this section, the incident wave need not propagate parallel to the plane of the figure. The interaction of P, SV, and SH waves at the irregular Moho gives rise to three components of motion at the surface. Since the amplitude and phase delay anomalies are still independent of the strike direction we continue to plot the spatial distributions along the x-direction. In other words, the horizontal direction normal to the strike is the only appropriate direction for plotting spatial distributions of displacement caused by scattering at one-dimensionally irregular interfaces.

The transverse component of motion arising from the scattering of teleseismic P waves is demonstrated in Figure 5.27. Ellis and Basham (1968) and Basham and Ellis (1968) present observations of significant transverse-component motion that usually builds up a short time after the P-wave arrival. They use this data as evidence for lateral inhomogeneities in the crust, and find an interpretation in terms for uniformly dipping layers. In our example, we observe the sizeable transverse components (T motion), at $x=+30$ km, which is beyond the x interval over which **single travel path ray** theory would predict such motion. We find that the generation of T motion for teleseismic P waves is more significant a) as the arrival azimuth Ω_0 relative to the x-direction increases to 90° , b) as the slope of the interface irregularity increases, c) as wavelength decreases, and d) as the incidence angle Θ_0 increases. For an example of the latter effect, compare Figures 5.27 and 5.31.

Note, in Figure 5.27, that incident SV waves generate insignificant T

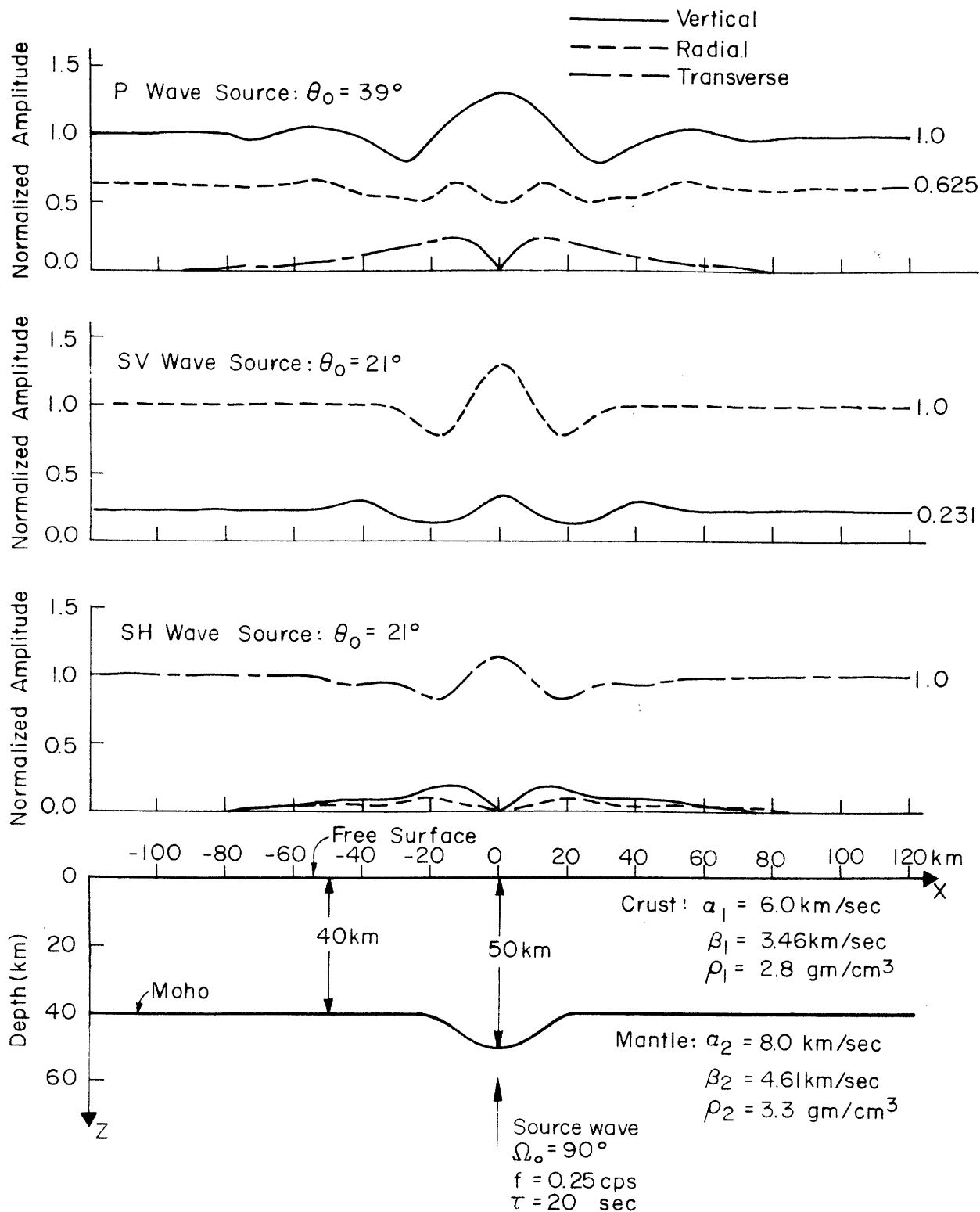


Figure 5.27. Spatial distributions of the three components of displacement for teleseismic waves incoming at azimuth $\Omega_0 = 90^\circ$ (parallel to the strike of the Moho depression). The apparent velocity of the source waves is 12.6 km/sec in each problem. Radial and transverse denote those horizontal components referenced to the source-wave azimuth. The numbers at the right are Haskell solutions where the Moho is flat.

motion and similarly the SH-wave source generates little radial component (R) motion. Such coupling is small for all azimuths Ω_0 but seems largest for $\Omega_0 = 45^\circ$. Finally, we note that the vertical-component (V) motion arising from SH source waves and the T motion due to P waves bear a somewhat reciprocal relationship.

In their arguments for lateral heterogeneity in the crust, Ellis and Basham presented horizontal particle motion orbits which often had elliptical shapes or were linear, but askew to the source-wave azimuth direction. Our solutions yield the counterpart representations shown in Figure 5.28. Solutions for teleseismic P waves arriving from three azimuths are compared. In all cases, the apparent velocity is 12.6 km/sec. To the right of the dashed line are plan views of horizontal motion ellipses at various positions x . The elliptical orbits are computed from the parametric equations

$$R = |R| \cos \omega(t - \epsilon_R)$$

$$T = |T| \cos \omega(t - \epsilon_T)$$

where $|R|$ is the amplitude of radial component at position x and ϵ_R is the time delay, and $|T|$ and ϵ_T are similar quantities for the transverse motion. The case $\Omega_0 = 0^\circ$ is a P-SV problem. Motion is linear and parallel to x . For other source azimuths the eccentricities of the ellipses vary with x as does the apparent arrival azimuth.

Such theoretical solutions might make it possible to use three-component motion at a single station to study local crustal structure. The observational data would consist of horizontal components of motion for P waves from earthquakes at all azimuths and teleseismic distances Δ .

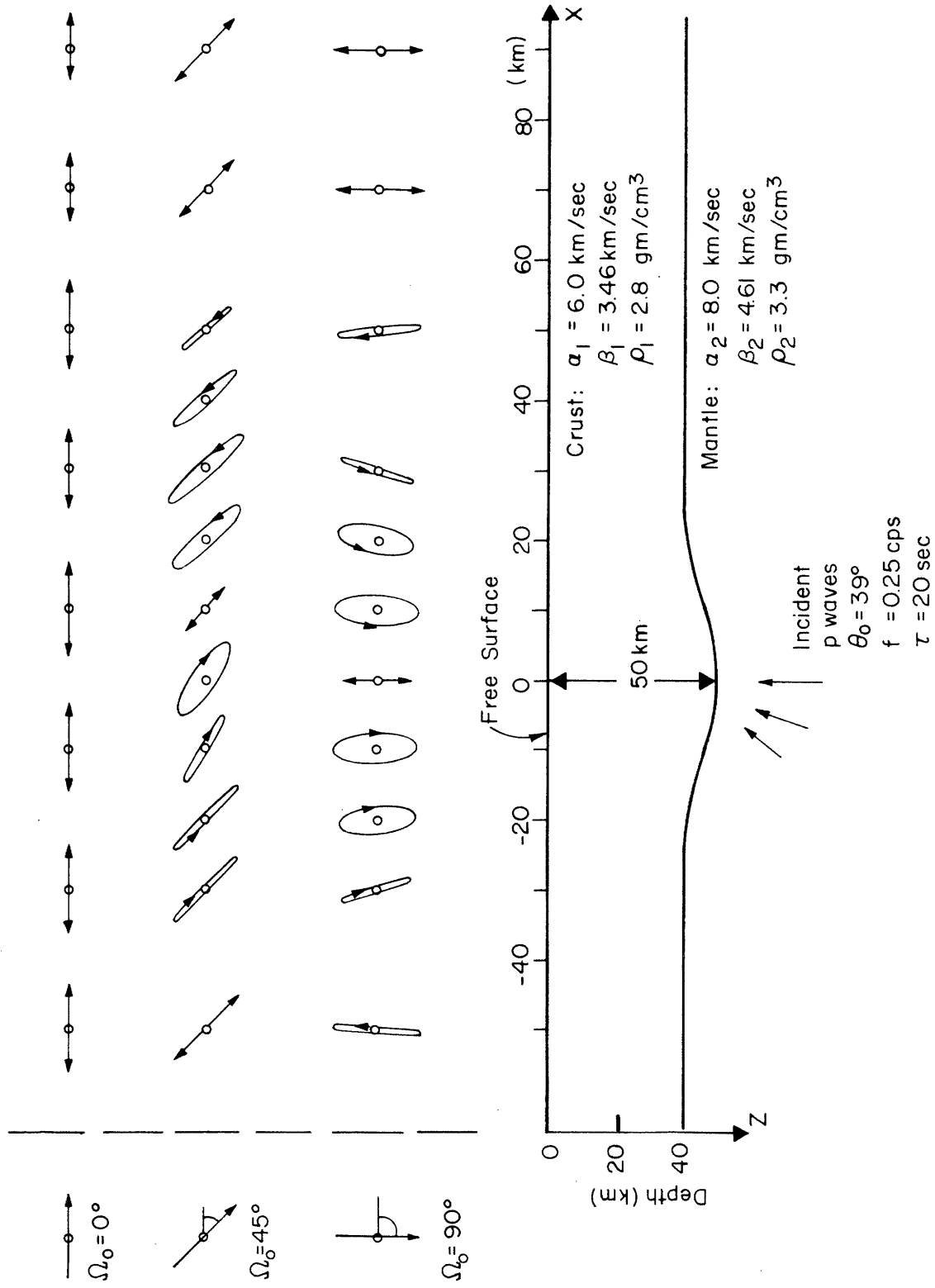


Figure 5.28. Plan view showing horizontal particle motion ellipses at positions x along the free surface for three teleseismic P wave problems: azimuth angles $\Omega_0 = 0^\circ$, 45° , and 90° (normal to the strike, 45° to the strike, and parallel to the strike). The apparent velocity of the source waves is 12.6 km/sec in each case.

Often the horizontal-component data is absent as is the case for the short-period (SP) seismic stations in Montana LASA. In a detailed analysis of early motion at LASA, Mack (1969) computed apparent azimuths across subarrays consisting of 25 vertical-component seismometers. He found that the apparent azimuths varied by as much as 50° across portions of LASA. He concluded from the curved wavefronts that the motion was dominated by scattering from small-scale, two-dimensionally irregular features. However, the presence of curved wave fronts does not preclude an interpretation of the structure as having a dominant strike direction. Figure 5.29 is another presentation of apparent azimuth directions as functions of x for the three cases treated in Figure 5.28. These azimuth directions were computed using the observed phase delays for the vertical component of displacement. That is

$$\tan \Omega_a = \eta_o / [k_o + 2\pi \frac{d\Delta\phi}{dx}]$$

where Ω_a is the apparent azimuth, k_o and η_o are the x - and y -components of source wave number, and $\Delta\phi$ is the computed phase delay, in circles. The apparent azimuths behave much as those in Figure 5.28. The largest difference in this example is 37° between the values at ± 25 km for the case $\Omega_o = 90^\circ$.

It is of interest to know whether the solutions for V motion obtained in P-SV problems ($\Omega_o = 0^\circ$) can suffice for interpretations of observed data from earthquakes at arbitrary azimuths relative to the strike. In Figure 5.30 solutions to P-SV and arbitrary azimuth problems are compared for source P waves having the same x -components of apparent velocity c_x . The solutions are comparable when $c_x = 17.8$ km/sec, whereas the amplitude anomalies differ when $c_x = \infty$. However, we observe that the x -coordinate of

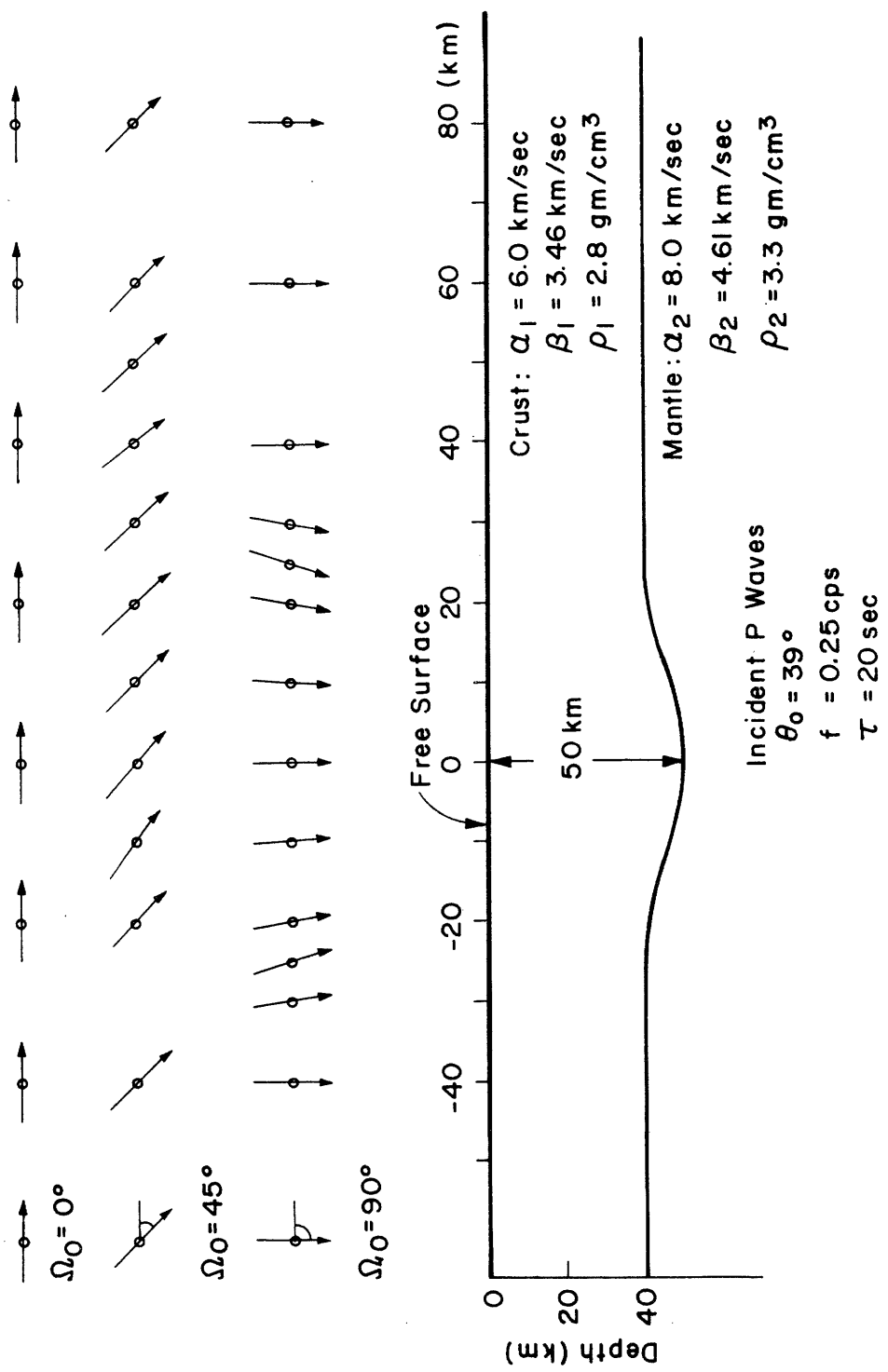


Figure 5.29. Plan view showing the apparent arrival azimuth at positions x along the free surface for the three teleseismic P wave problems considered in Figure 5.28. The apparent azimuth is based upon the directions of the wavefronts for the vertical component of motion.

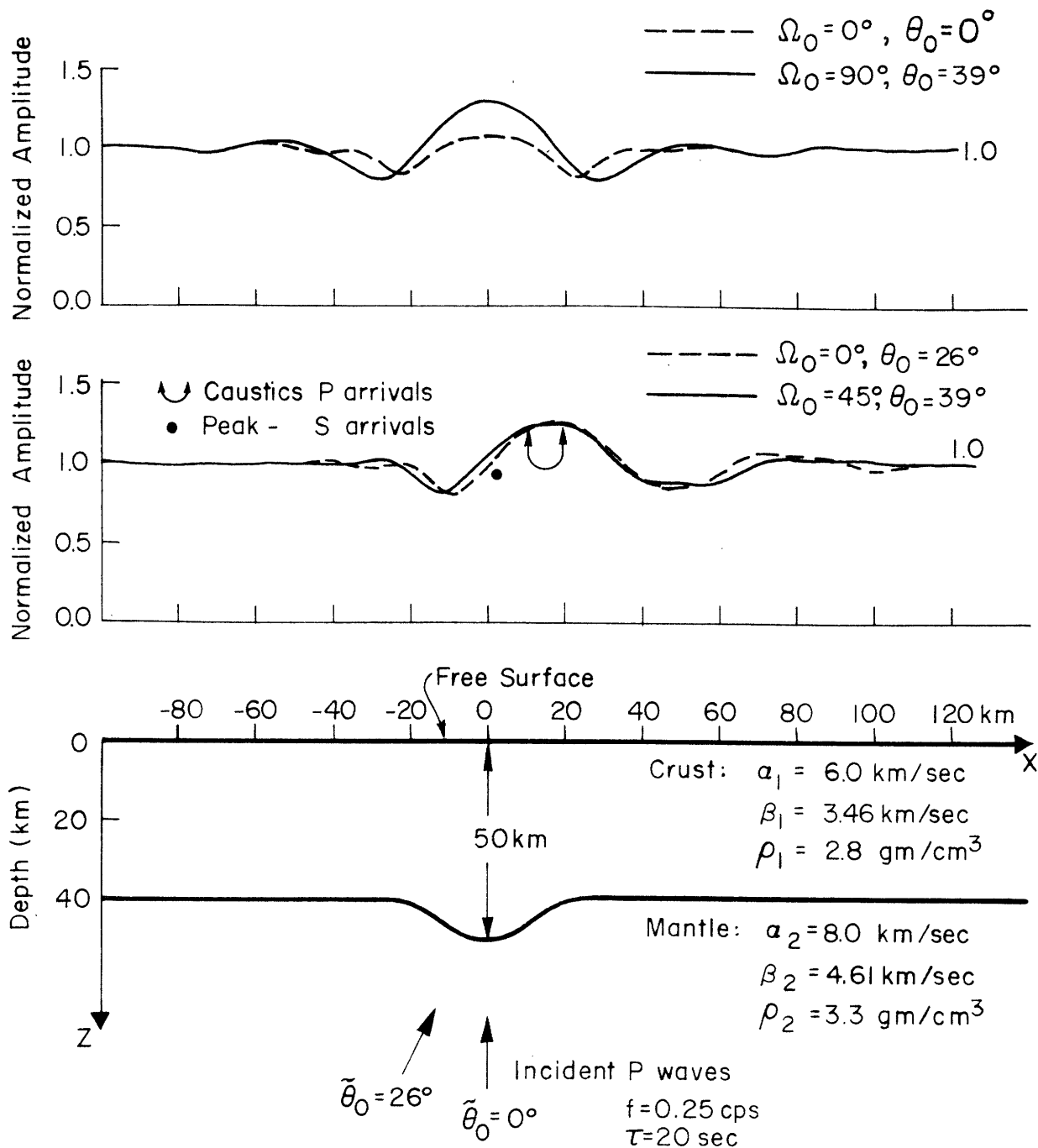


Figure 5.30. Vertical displacement amplitudes for four cases involving the scattering of teleseismic P waves at a depression in the Moho. In the top pair, the x-component of apparent velocity is infinite, and the incidence angles are $\theta_0 = 0^\circ$ and $\theta_0 = 39^\circ$. In the second pair, the x-component of apparent velocity is 17.8 km/sec and $\theta_0 = 26^\circ$ and 39° . The caustics and peak positions are ray theoretical.

the amplitude peak is the same for a given c_x , independent of Ω_0 .

The next example, shown in Figure 5.31, involves a P wave propagating at grazing incidence along the strike of a depression in the Moho. The amplitude anomalies are large just as were the anomalies for grazing incidence in the SH-wave examples. The T motion actually exceeds the R motion at $x=+35$ km. Note the flat phase delay anomaly for the vertical component and the departure from the ray theoretical value (the X).

All the problems considered thus far, involved a single-layer crust. If the crust were multi-layered and had several irregular interfaces (with a common strike) we would anticipate more complex spatial variations of surface displacement. And, of course, we recognize that any proposed irregular interface model in an inverse problem must be nonunique. The last example in this section demonstrates dependence of the solutions on variations in crustal layering even when only one interface (the Moho) is irregular. The three models are shown in Figure 5.32a. In case 1, layer c might represent a simple model of a localized velocity transition zone, or it could be a laccolith or other isolated lens. Layer a is a thin sedimentary layer. In case 2 the transition zone is removed and in case 3 the surface layer is removed. The solutions are shown in Figure 5.32b.

The apparent affect of the transition zone is to diminish the amplitude anomalies. Extrapolating this result, it appears that wherever the Moho is a velocity transition zone several km thick, we expect the displacement anomalies to have smaller variations than do those in most of the examples considered in this thesis. Comparison of cases 2 and 3 reveals the profound influence that the sedimentary layer has upon the horizontal components of motion. The decay time in this example is long enough to allow many

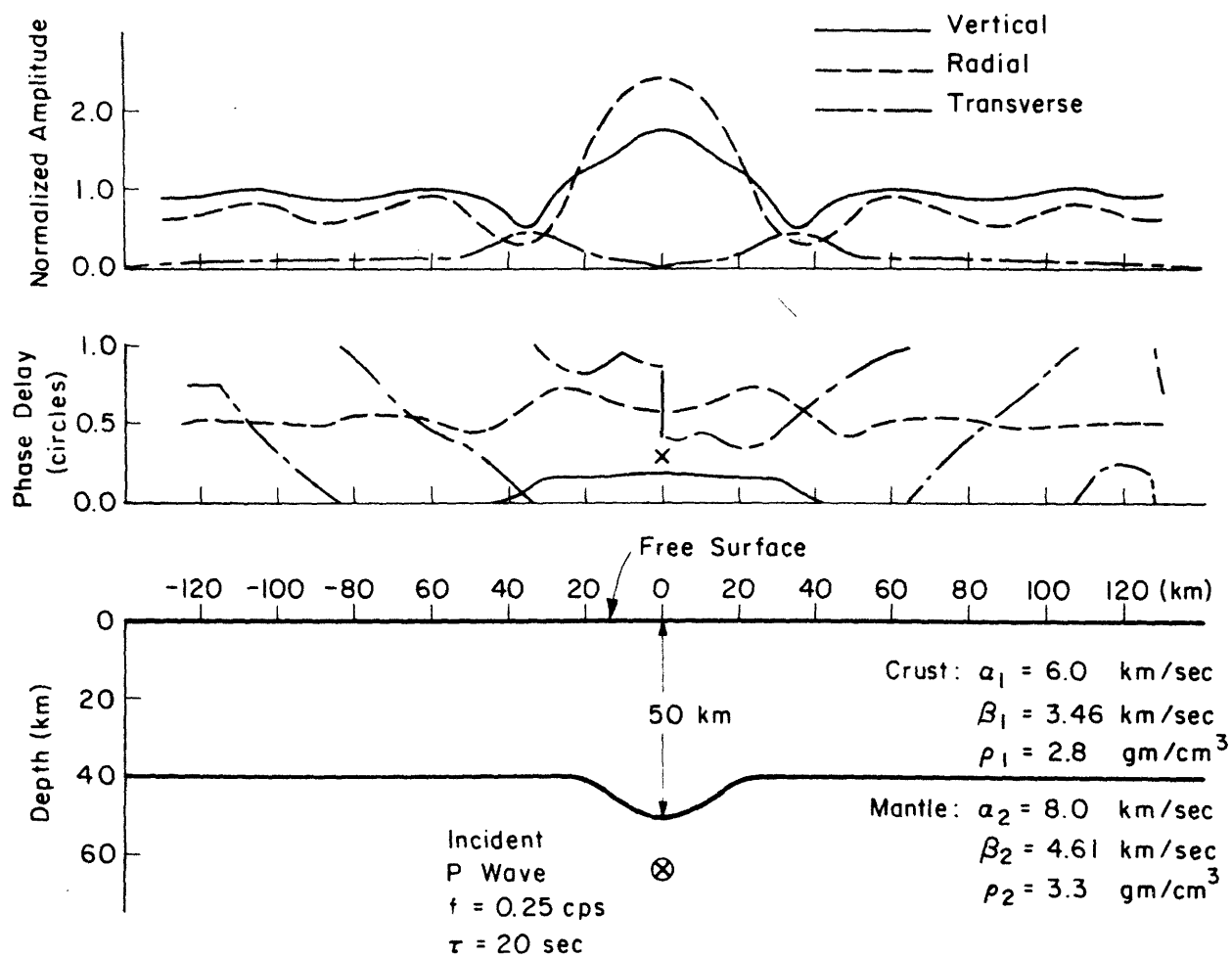


Figure 5.31. Three components of displacement due to scattering of plane P waves grazing ($\Omega_0 = 90^\circ$) along the strike of a depression in the Moho. The radial component denotes horizontal motion parallel to the strike.

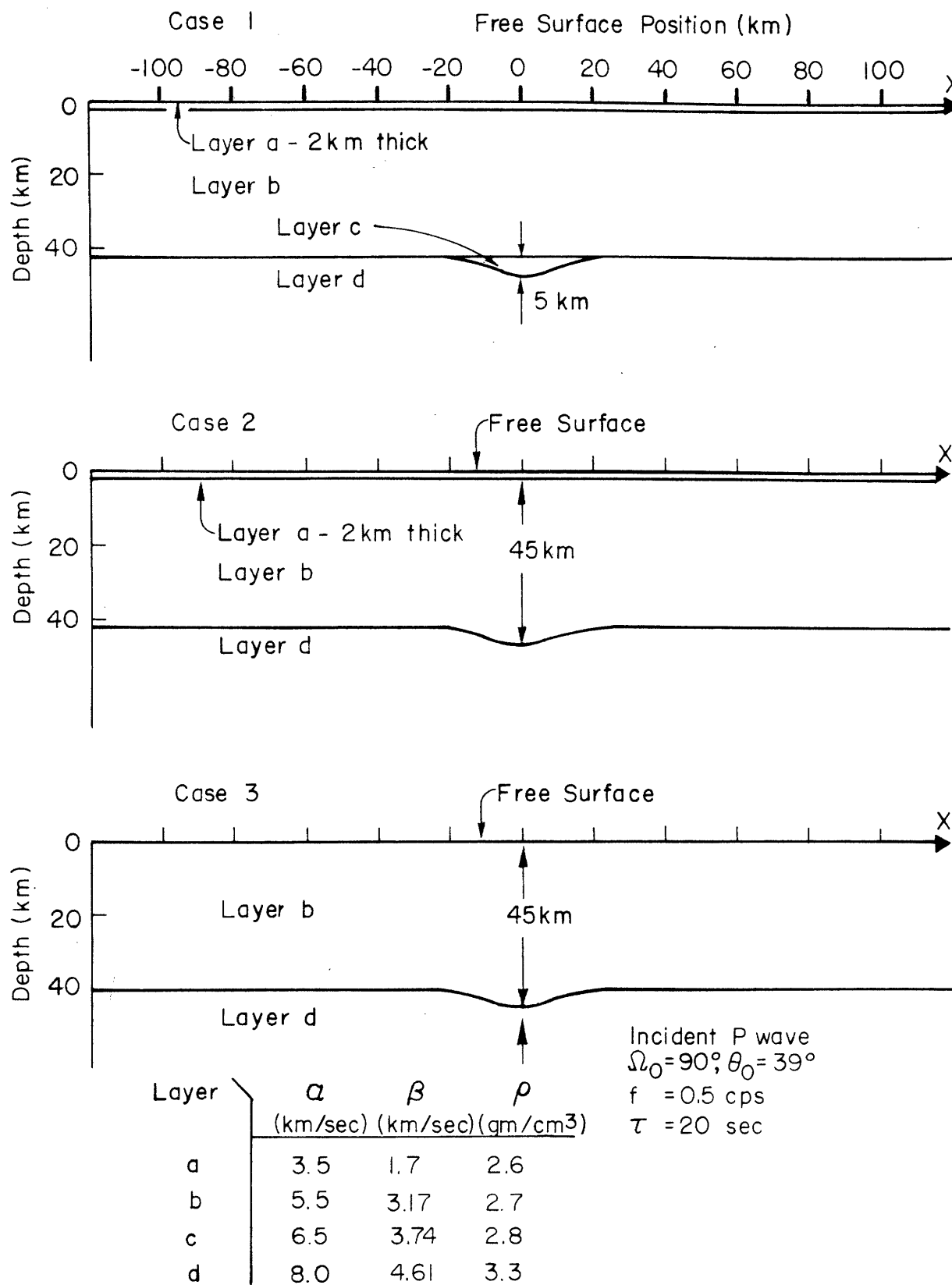


Figure 5.32a. Three multi-layered crust models having a depression in the Moho.

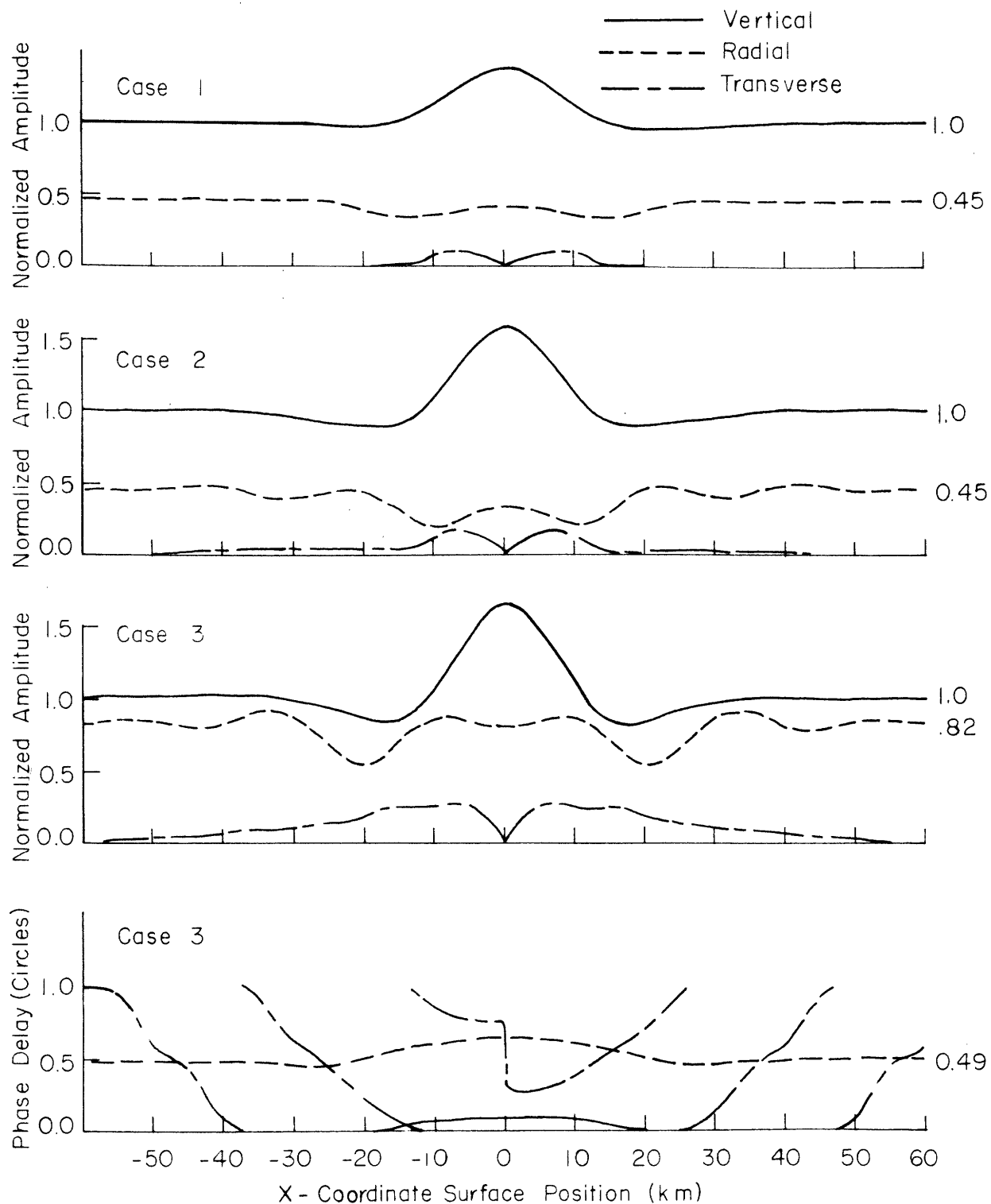


Figure 5.32b. Three components of motion for scattering of teleseismic P waves in the multi-layered models shown in Figure 5.32a. The waves are incident with apparent velocity 12.6 km/sec at an azimuth parallel to the strike of the depression. The numbers at the right are Haskell theoretical values where the Moho is flat.

reverberations within the layer. Such a surface layer effect might vitiate attempts to use horizontal motion at a single station to infer subsurface structure. The surface layer has a strong effect on the time delays as well. At $x=0$, the computed time delays for the three cases are 0.16 sec, 0.29 sec, and 0.20 sec. All are considerably less than the ray theoretical time delays 0.22 sec, 0.37 sec, and 0.37 sec because of the usual phase dispersion. The discrepancy in the computed time delays for cases 2 and 3 cannot be explained in simple ray theoretical terms.

We mention one last example not illustrated in a figure. The problem involved the scattering of teleseismic P waves at an irregularity in the upper boundary of the low-velocity layer in the upper mantle. The frequency was 0.5 cps, $\Omega_0 = 45^\circ$, $\Theta_0 = 39^\circ$, and the boundary depth varied 10 km as a single cycle cosine rise over a distance of 100 km. We used Gutenberg's velocities and found no significant anomalies in surface motion. The primary reason is the small velocity contrast and a secondary reason may be the large depth. The conclusion is that such a feature does not substantially distort arriving plane waves.

5.5. Application to Montana LASA Crustal Structure.

5.5.1. Determination of strike direction. Greenfield and Sheppard (1969) proposed a single-layer model for the LASA crustal structure. The Moho depth varied in the direction $N30^\circ W$ only. A cross-section of their model in that direction is shown in Figure 5.41 (A0 is the central station at LASA) and the indicated parameters are listed in Table 5.6. Questions have been raised concerning the large depth of Moho (Boore and Toksoz,

1969), the one-dimensionality of the irregularity (Mack, 1969), and the direction of the strike (Glover and Alexander, 1969). We shall use observed spectral amplitude and phase data together with our wave scattering solutions to check their model.

In order to apply our method, we must first determine whether the structure at LASA is indeed one-dimensionally irregular. The basic data used in the study are short-period, vertical-component records of the 17 earthquake events listed in Table 5.3. Records (on LASA tapes) at the 84 stations shown in plan view in Figure 5.33 were Fourier spectrum analyzed in the following manner. First, the arrival times at the centers of 21 LASA subarrays were used in a least-squares procedure to determine the mean apparent velocity c_a and apparent back azimuth Ω_B . Next, a signal length t (usually about 4 sec) starting at time t_0 was determined for the central station A0. A cosine shaped data window starting at $t_0 - 0.4t$ and ending $t_0 + 1.35t$ was applied to the data after digitized at 20 samples/sec. The windowed signal was then Fourier analyzed. A similar procedure was applied at the remaining 83 stations, where the starting time was taken as $t_0 - \underline{s} \cdot \underline{r}$. Here, \underline{r} is the station location vector relative to A0 and \underline{s} is the mean apparent wave-slowness vector. The cosine data window was an expedient choice over the exponential window appropriate to our theoretical solutions because of the large number of records Fourier analyzed. The difference in smoothing effects should be small for so short a window length.

Rather than constructing contour maps of spectral amplitudes and phases for each event over the LASA array, we use the following more

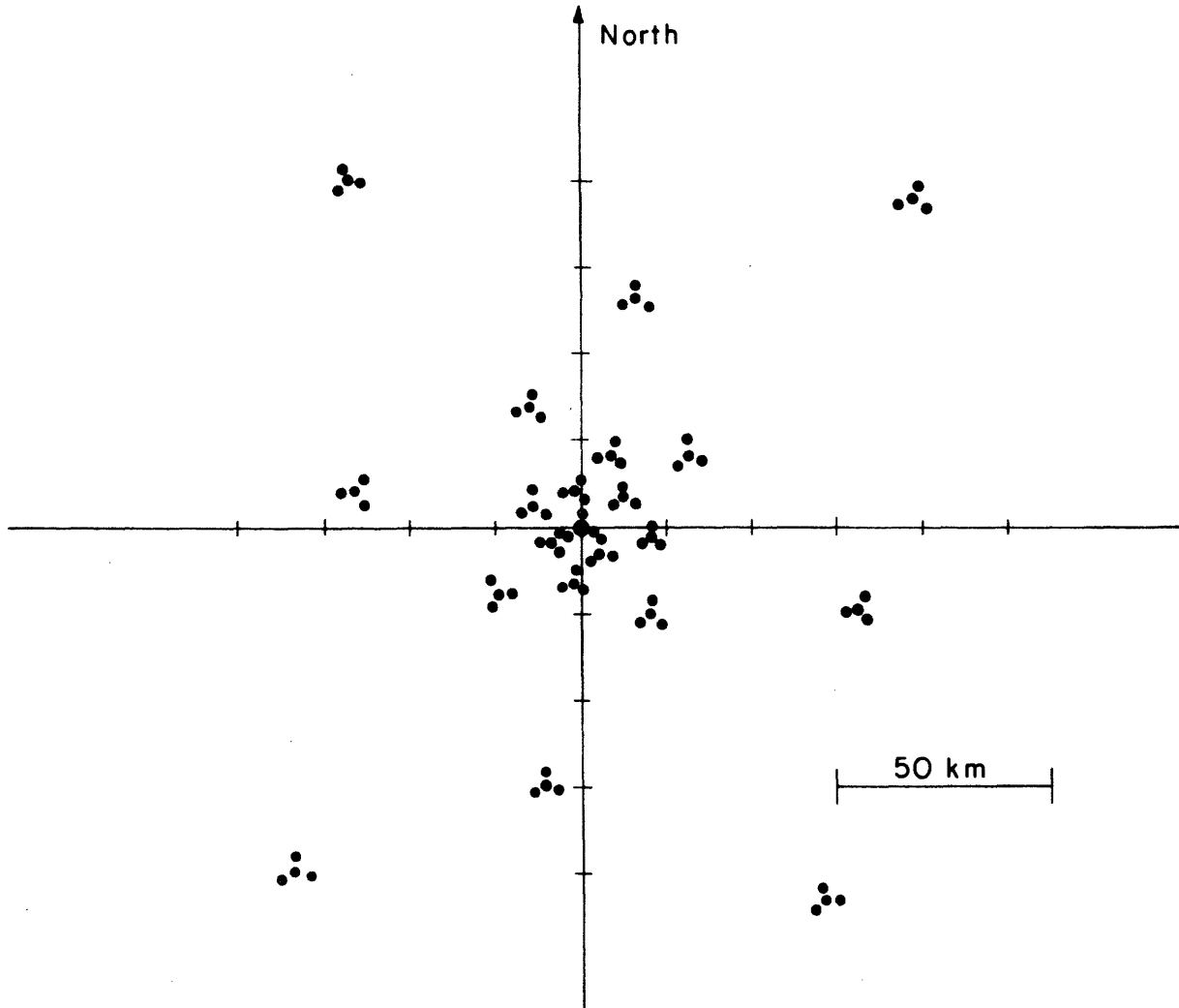


Figure 5.33. Plan view showing relative locations of the 84 SP stations of Montana LASA used in this study. The station located at the origin is denoted AO.

TABLE 5.3

Earthquake Event Data

Event No.	Region	Phase	Date M D Y	Arrival Time at Station AO (GMT)	Apparent Back Azimuth Ω_B (deg)	c (km/sec)	c_x (km/sec)	Ω_0 (deg)
1	N. Celebes	PKKP	6- 2-66	7:36:42	*128.8	†22.2	‡23.8	④21.2
2	Caribbean Sea	P	11- 8-67	3:17:00	143.6	12.3	12.4	6.4
3	S. of Panama	P	6-15-68	7:16:55	147.1	13.5	13.5	2.9
4	Costa Rica	PCP	10- 4-67	6:09:09	147.5	31.3	31.3	2.5
5	Chile- Argentina	P	11- 2-67	3:44:04	148.8	20.4	20.4	1.2
6	Coast of Costa Rica	P	10- 4-67	6:09:09	150.3	12.8	12.8	0.3
7	Coast of C.Chile	P	11-27-67	5:25:10	151.2	20.7	20.7	1.2
8	Samoa	P	11- 7-67	4:01:18	-118.5	22.7	-714	-88.5
9	Fiji	P	10-12-67	6:46:44	-117.6	24.4	-582	-87.6
10	Fiji	P	11-24-67	5:54:00	-114.0	23.4	-224	-84.0
11	Banda Sea	PKIKP	11- 9-67	2:36:08	- 77.8	61.8	- 92	-47.8
12	Andreasnof Is.	PCP	9-16-67	8:41:39	- 61.5	29.1	-34.2	-31.5
13	Andreasnof Is.	P	12- 5-67	9:12:32	- 59.6	13.6	-15.7	-29.6
14	Andreasnof Is.	P	9-16-67	8:39:27	- 57.3	13.8	-15.5	-27.3
15	E. Coast of Honshu	P	5-16-67	2:39:10	- 56.1	20.1	-22.4	-26.1
16	S. of Honshu	P	11-28-67	2:48:48	- 48.0	21.9	-23.0	-18.0
17	E. Kazakh	P	5-28-67	4:20:06	- 7.2	23.9	-25.9	-22.8

See following page for notes.

NOTES FOR TABLE 5.3

- * Determined by least-mean-square analysis of arrival times across Montana LASA.
- † Apparent velocity determined along with apparent back azimuth.
- Apparent velocity along the line $S30^{\circ}E-N30^{\circ}W$; positive from SE.
- Azimuthal angle between arriving wave direction and $N30^{\circ}W$; positive if angle is acute.

quantitative approach to determine the trend direction and, indeed, whether one exists. Trial trend directions (indexed n) are taken at equal azimuth increments from 0° to 180° clockwise from north. For each direction, the 84 stations are projected along that trend to a common line. The station coordinates along that line are labeled \bar{x}_i , $i=1,84$ where indexing is such that \bar{x}_i is a monotonic function of i . Let the spectral data be d_i , according to the same indexing. We define a 'trend measure' $M_n(\Omega_n)$

$$M_n^2(\Omega_n) = \frac{\sum_{i=2}^{84} w_i (d_i - d_{i-1})^2}{\sum_{i=2}^{84} w_i} \quad (5.1)$$

where Ω_n is the trial azimuth direction and

$$w_i = \begin{cases} 1 - (\bar{x}_i - \bar{x}_{i-1})/\lambda & ; \text{ for } (\bar{x}_i - \bar{x}_{i-1}) < \lambda \\ 0 & ; \text{ for } (\bar{x}_i - \bar{x}_{i-1}) \geq \lambda \end{cases} \quad (5.2)$$

λ is some specified length

The meaning of M_n is simply this. It is like a standard deviation of the projected data, and should attain its minimum when $\Omega_n = \Omega_c$, the correct strike azimuth. Along that direction the station positions are projected along the strike and the data is plotted just as in one of our theoretical scattering problems. Any scatter is caused by 'inherent noise', i.e. instrument noise, seismic background noise, departure from plane incident wave fronts, and the effects of crustal structure departures from the ideal one-dimensional irregularities. When the data is projected along some direction other than the strike, M_n receives added contributions from 'jumbling noise', the mixing of proper relative station positions. The weighting function w_i weights the most closely spaced data the most.

The results of six trend measure analyses are shown in Figure 5.34. All cases are for $f=0.9$ cps. The merit of this approach is that all trend measure analyses should indicate the same strike direction, independent of the earthquake locations. The redundancy is necessary since M_n is, itself, a statistical quantity. In Figure 5.34, we see a tendency toward small values of M_n for trial trend directions in the range 40° to 80° . Also note that the phase measures have more pronounced minima and that the quality of the measure M_n varies with different events.

To estimate the minimum, a least-squares cosine fit is made to each curve,

$$M_L = B_1 + B_2 \cos \frac{\pi}{90} (\Omega - \epsilon) \quad (5.3)$$

Here Ω is a trial trend azimuth, and B_1 , B_2 , and ϵ are determined constants. Finally, we take as the determined trend, the simple average of the azimuths at the minimum of M_L and at the minimum of the M_n . Such trial trend analyses were made individually for amplitude and phase data at the frequencies $f=0.5$ and 0.9 cps for the 9 events listed in Table 5.4. The columns labeled 'strike' are the results of such analyses. The quantity $B_1 - B_2$, in units of normalized amplitude and fractions of a circle, is a measure of the jumbling noise.

To determine our best estimates of the strike direction for various combinations of data we computed weighted averages of the strikes in Table 5.4. The weights were based on the quality of trend measure curves such as those in Figure 5.34. These weights are the ratios B_2^2 / \mathcal{S}^2 listed in Table 5.4. \mathcal{S} is the computed variance for the departures of the M_n values from the M_L curves. The following equations were used in the final analysis of mean trend directions.

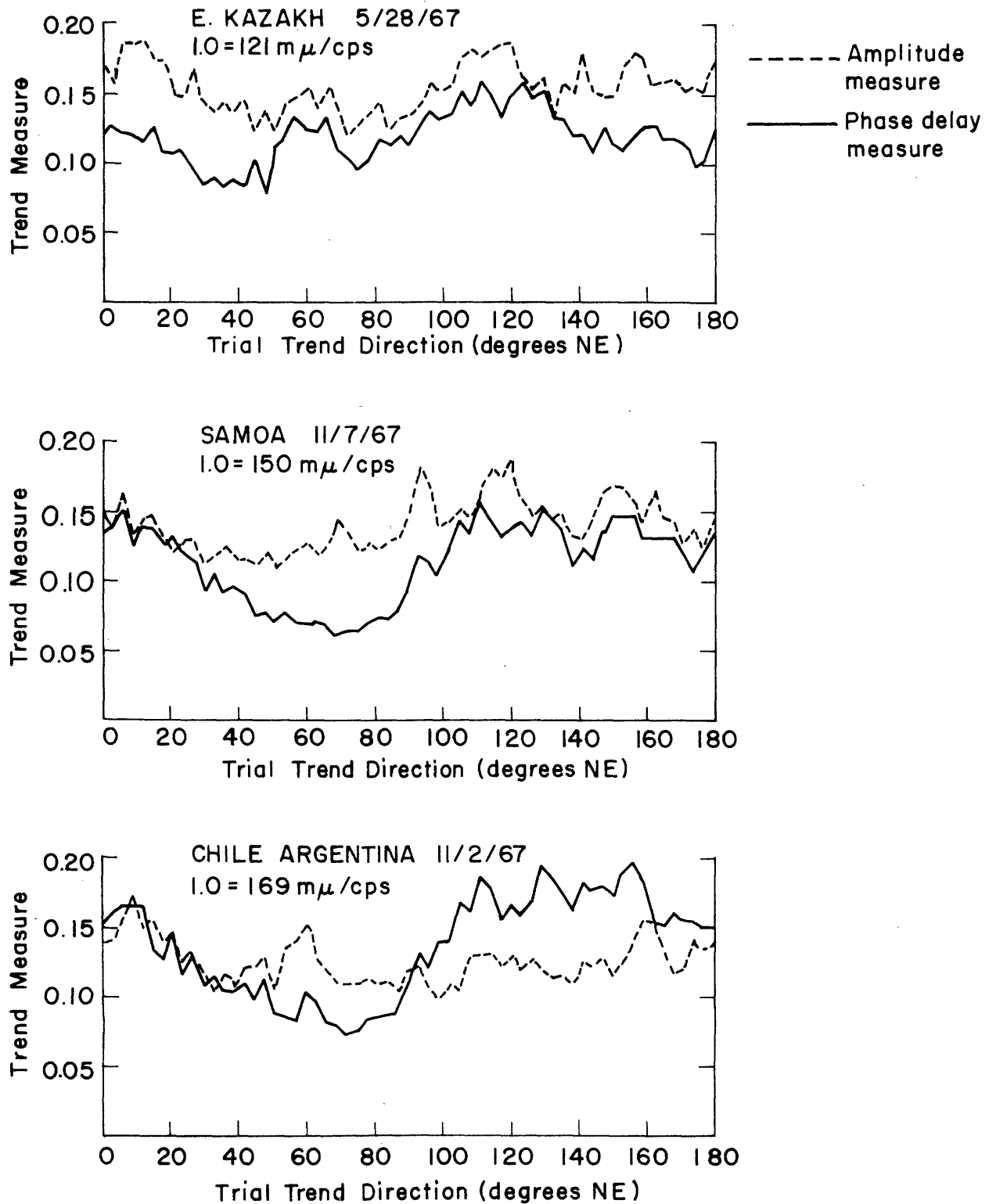


Figure 5.34. Representative plots of the trend measure versus the trial trend direction (degrees clockwise from north). The trend measures were computed using the Fourier spectral data at 0.9 cps in each case.

TABLE 5.4
Data Used in Determination of Trend Direction at Montana LASA

Event No.	Group	Region	Date M D Y	Frequency (cps)	Amplitude		Phase			
					B ₁ -B ₂	Weight	B ₁ -B ₂	Weight	Strike (deg)	Strike (deg)
2	SE	Carribbean	11- 8-67	0.5	.16	1.52	.05	1.84	98	79
5	SE	Chile- Argentina Coast of	11- 2-67	0.9	.12	4.26	.08	0.52	51	38
6	SE	Costa Rica Samoa	10- 4-67	0.5	.12	0.19	.07	11.6	143	57
8	SW	Fiji	11- 7-67	0.9	.14	1.10	.09	10.6	95	65
9	SW	Fiji	10-12-67	0.5	.11	0.04	.07	2.08	98	72
10	SW	Fiji	11-24-67	0.9	.11	0.31	.10	0.61	52	49
13	NW	Andreanof Is.	12-5-67	0.5	.13	0.63	.05	4.48	134	70
16	NW	S. of Honshu	11-28-67	0.9	.11	2.35	.08	4.51	50	65
17	NW	E. Kazakh	5-28-67	0.9	.11	2.38	.05	4.70	56	70
					.15	2.59	.10	2.89	55	68
					.12	0.22	.06	2.21	25	66
					.13	1.47	.10	2.38	60	63
					.15	0.63	.07	1.62	78	41
					.14	0.03	.08	2.00	133	47
					.13	0.61	.04	3.62	83	68
					.15	2.95	.07	1.00	69	82
					.14	0.02	.08	0.28	49	129
					.14	0.85	.10	2.04	67	54

$$\bar{n} = \frac{\sum_{i=1}^K \omega_i S_i}{\sum_{i=1}^K \omega_i} = \text{mean trend,}$$

$$\omega_i = B_{2,i}^2 / S_i^2 = \text{weight for data type } i \text{ in Table 5.4,}$$

$$S_i = \text{strike determined from data type } i,$$

$$K = \text{number of data types used in the averaging,}$$

$$s^2 = \frac{N}{N-1} \frac{\sum_{i=1}^K \omega_i (S_i - \bar{n})^2}{\sum_{i=1}^K \omega_i} = \text{estimate of variance of}$$

population from which S_i are samples,

$$N = \frac{(\sum_{i=1}^K \omega_i)^2}{\sum_{i=1}^K \omega_i^2},$$

$$N-1 = \text{number of degrees of freedom, and}$$

$$\bar{\omega} = \frac{\sum_{i=1}^K \omega_i}{K} = \text{average weight.}$$

The results for the estimated mean trend directions are listed in Table 5.5 for 10 combinations of data, and histograms are plotted in Figure 5.35 for 5 of the combinations. The \pm values in Table 5.5 indicate 95% confidence intervals based upon Student t tests of the data. The mean trend determination based upon all the data is $N64^{\circ} \pm 6^{\circ} E$. The mean trends computed for every subgroup, except for the 0.5 cps, amplitude group are within these confidence limits. The data for the exceptional case is least significant (smallest average weight). Based upon this table we conclude

- a) time delay data is more reliable, but amplitude data is sufficiently good to support the conclusions.
- b) teleseismic waves from different azimuths 'see' the same trend.
- c) the data from the SW group of events is excellent; that from the NW group shows the largest scatter.
- d) different frequencies 'see' the same trend.

TABLE 5.5

Results of Trend Determination

Data	Frequency (cps)	Type *	Mean Trend	Degrees of Freedom	Average Weight
9 Events	0.5 & 0.9	A & P	$N64^{\circ} \pm 6^{\circ} E$	14.5	2.58
"	"	A	63 ± 13	7.5	1.62
"	"	P	64 ± 7	8.6	3.28
"	0.5	A	75 ± 52	2.1	1.04
"	0.9	"	60 ± 14	4.8	1.99
"	0.5	P	65 ± 13	4.1	3.60
"	0.9	"	63 ± 12	3.5	2.95
SE Events	0.5 & 0.9	"	62 ± 24	1.9	4.58
SW Events	"	"	67 ± 3	4.5	3.53
NW Events	"	"	60 ± 26	3.5	1.76

*A=Amplitude
P=Phase

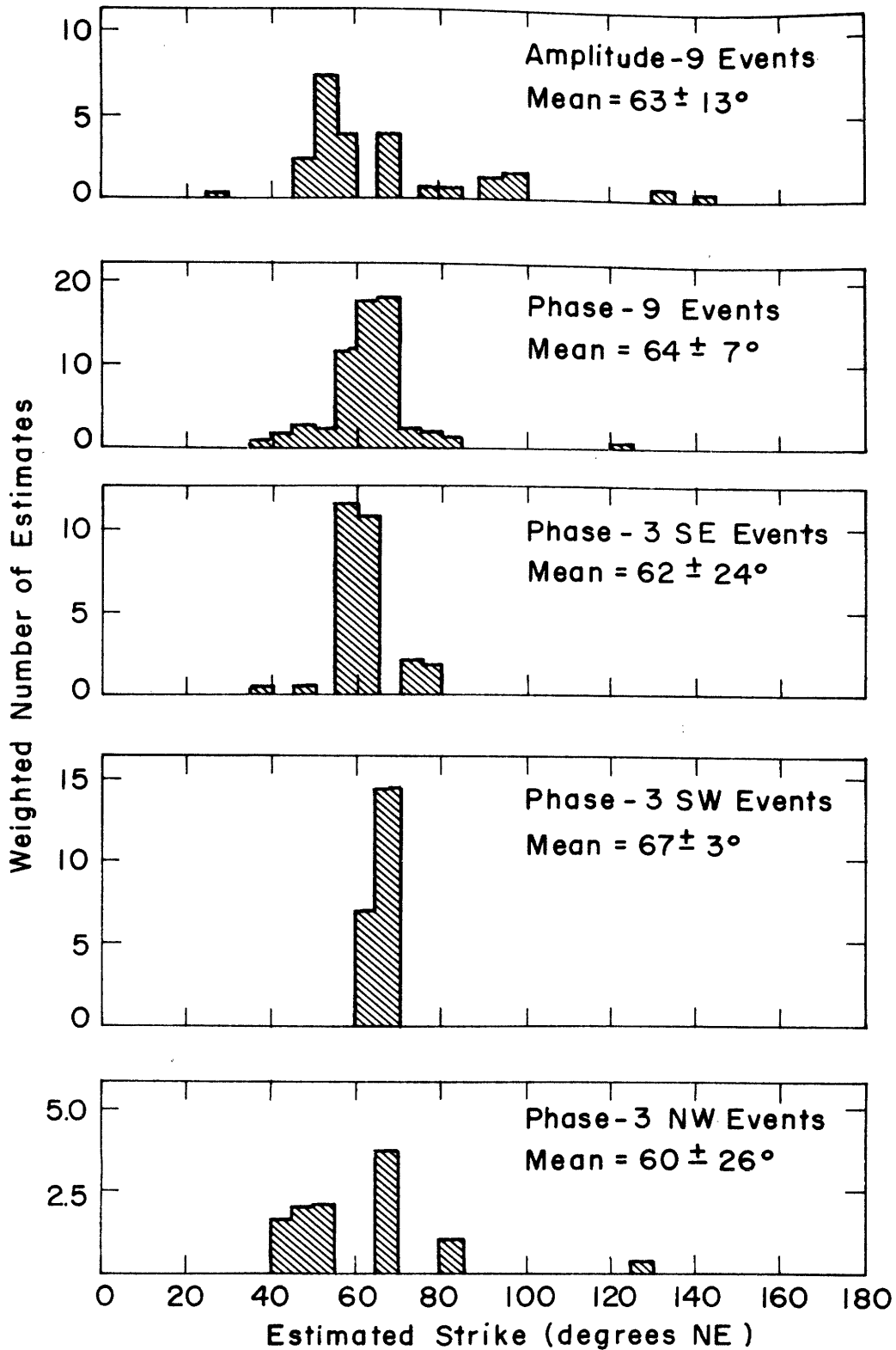


Figure 5.35. Histograms for estimating the Moho strike at Montana LASA. The number of estimates (in 5° blocks) is weighted as described in the text. The labels 'amplitude' and 'phase' indicate that the histograms are based upon amplitude and phase determinations of trend respectively. In each case, both 0.5 cps and 0.9 cps spectral data were used. The events are listed in Table 5.4.

e) there is a significant underlying one-dimensionally irregular structure at LASA.

The larger scatter from directions other than to the SW may be caused by non-planar source wavefronts or by relatively larger departures of the interfaces from one-dimensionality.

5.5.2. Depth and shape of Moho. Our determination of the trend direction supports the trend estimate in the Greenfield and Sheppard (GS) model. We shall now consider other parameters in their model. We have said that there is only one appropriate line of projection of the data for all source-wave-azimuth events. That is along the line normal to the strike. In Figure 5.36 we present observed amplitude and phase delay spatial distributions along the x-direction $S30^{\circ}E-N30^{\circ}W$ (this is close enough to the optimum direction) for events from each of the three groups. SAMOA, one of the excellent SW group, displays the least scatter with time delays showing less scatter than do the amplitudes. These data are for 0.9 cps. Typical amplitude behavior with frequency is shown in the hand-smoothed curves in Figure 5.37. The anomalies become more narrow and increase in peak-to-trough ratio as frequency increases, just as we observed in the theoretical solutions. No new features develop as frequency increases. Apparently, all frequencies considered in this study are sensitive to the same subsurface features. The shift in peak position toward the SE as frequency increases may indicate some exceptional behavior. We leave it for future study.

Let us return to a discussion of Figure 5.36. The peaks in time delay tend to lie to the NW of the amplitude peaks, independent of azimuth of

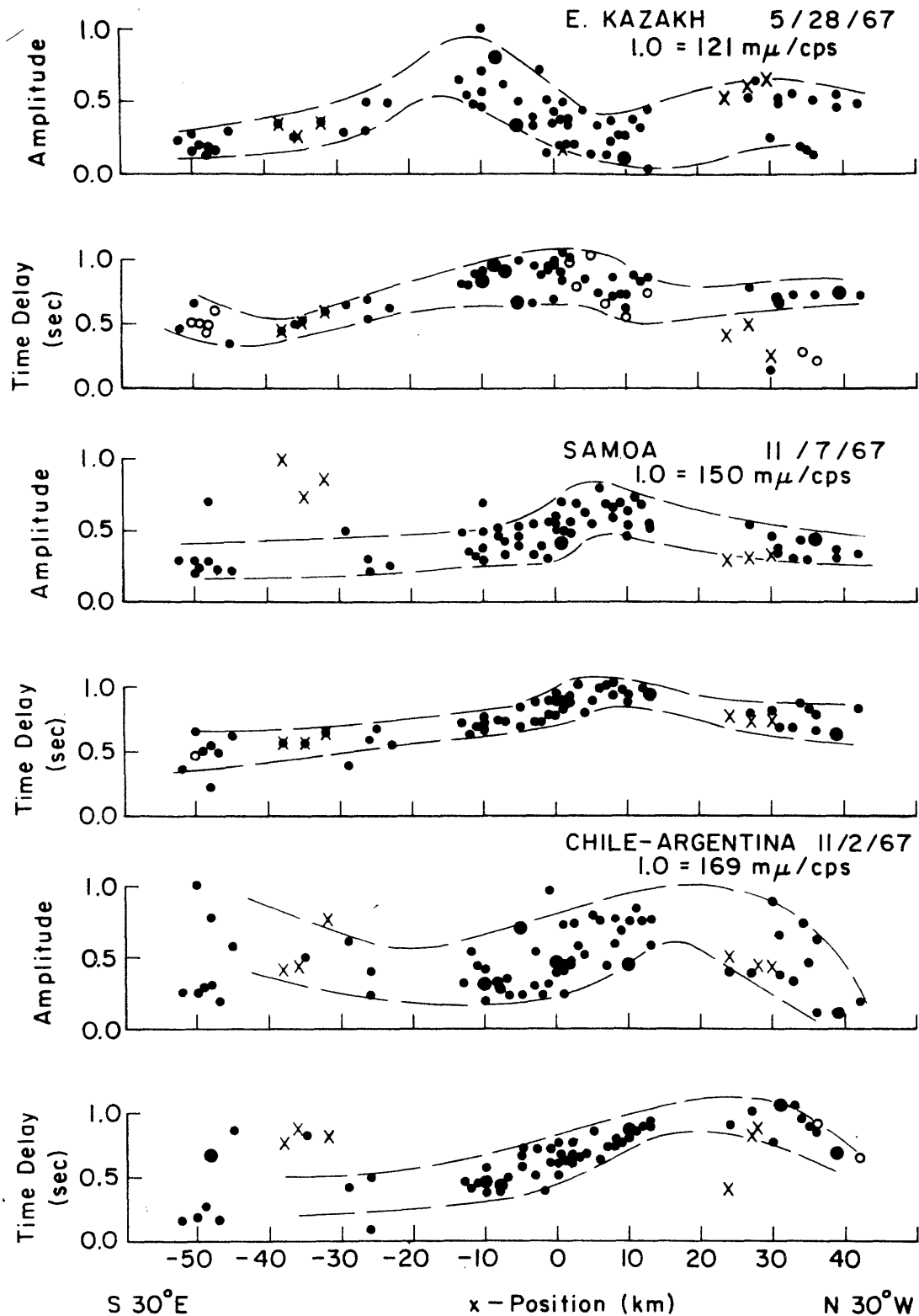


Figure 5.36. Observed spatial distributions of vertical displacement amplitude and time delay, at 0.9 cps, projected along the direction S30°E-N30°W. Open circles are time delays associated with normalized amplitudes less than 0.2. The x's denote stations more than 90 km removed from the line through station A0.

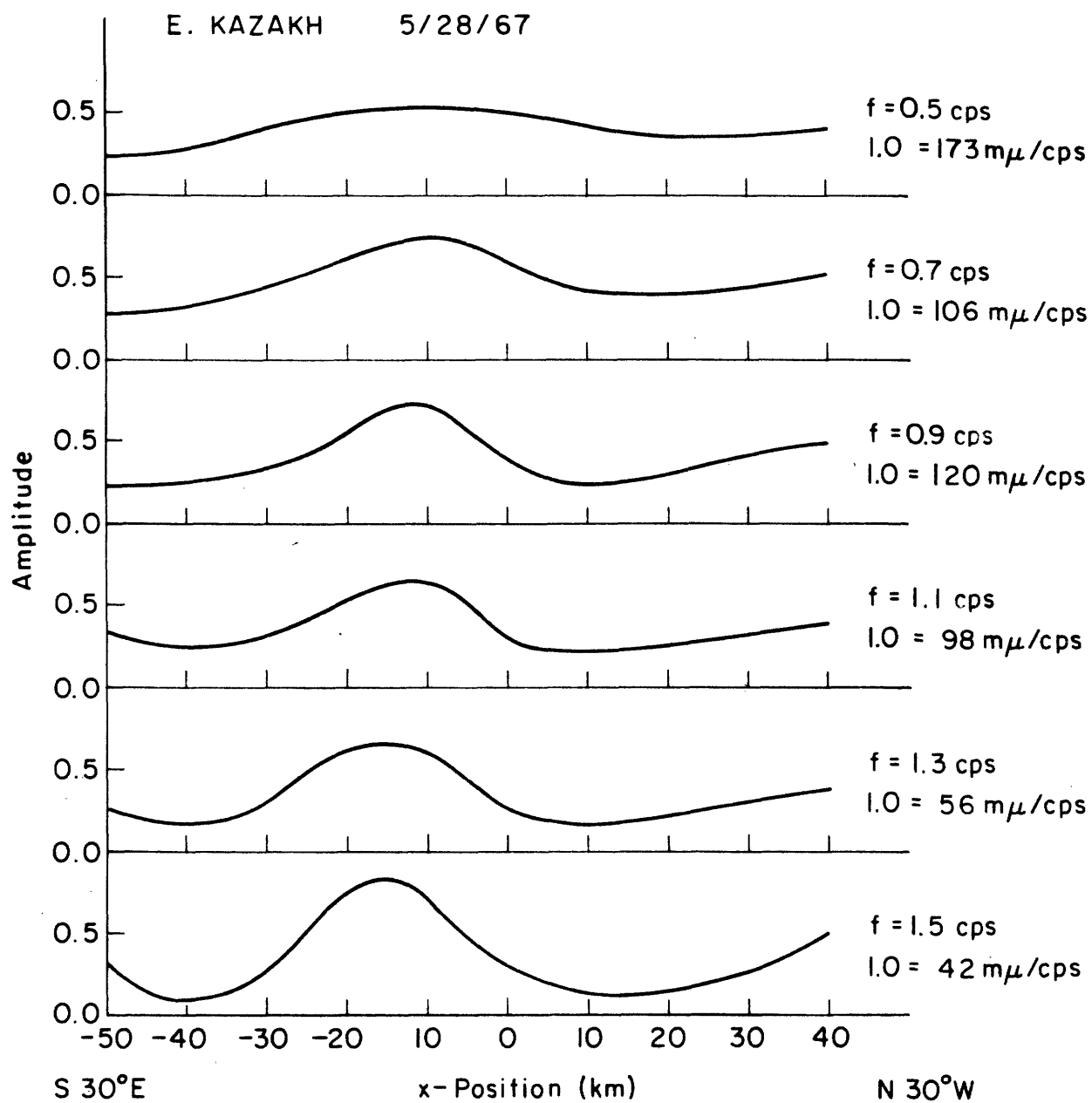


Figure 5.37. Hand smoothed spatial distributions of vertical displacement amplitude for the E. KAZAKH event at several values of frequency.

wave approach. The time delay distributions are unsymmetric with the more rapid changes toward the SE. SAMOA is the most unbiased example since the incident direction is nearly along the strike ($\Omega_0 = -88.5^\circ$ in Table 5.3). Finally, analysis of similar curves at different frequencies reveals no evident phase dispersion as in our solutions for a depression in the Moho. This evidence supports the GS model of an asymmetric step-like feature.

Figure 5.38 displays a theoretical solution for scattering of P waves at a step change in the Moho. The frequency is 0.5 cps and the decay time is comparable with the length of cosine window used for the LASA data. We are assuming the behavior observed in Figure 5.30, i.e. that the P-SV wave problem solution is adequate for study of the migration of the x-coordinates of features in the displacement anomalies for the general azimuth problem so long as the x-components of apparent velocity c_x are the same. Note, in Figure 5.38, that the time delays decrease toward the thin crust direction.

In Figure 5.39 we plot the x-coordinates of the peaks and troughs in amplitude against $\tan \Theta_1$, where Θ_1 is the incident angle of the primary P waves at the surface

$$\sin \Theta_1 = (\alpha_1 / \alpha_2) \sin \Theta_0 = \alpha_1 / c_x \quad (5.4)$$

The positions labeled as time delay peaks are the locations where the time delay curves flatten. All the curves are concave toward the thicker crust side. Also, the time delay peaks are displaced, relative to the amplitude peaks, toward the thicker crust independent of the azimuth of wave approach. This is readily understood with reference to Figure 5.38.

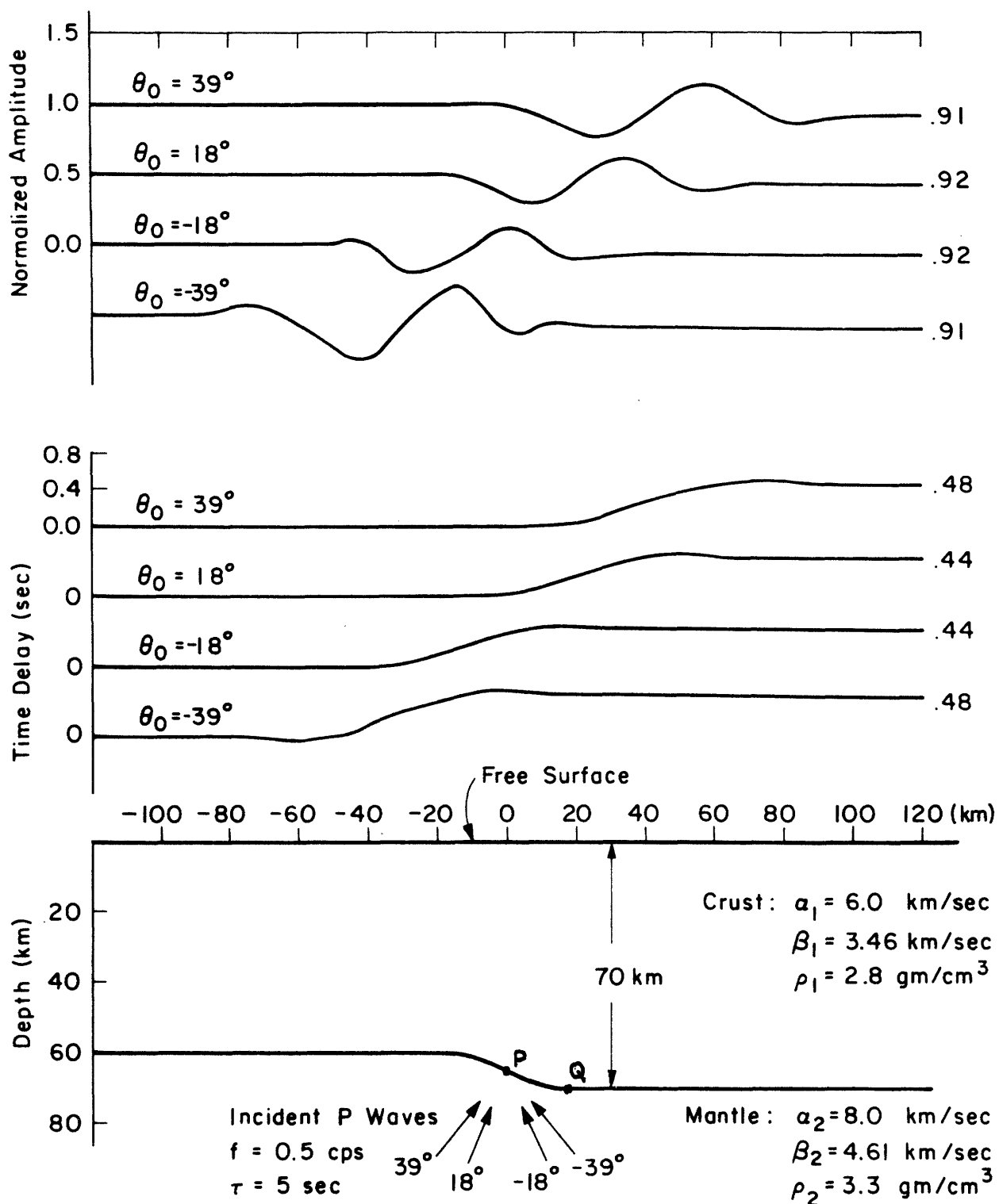


Figure 5.38. Theoretical normalized amplitudes and time delays for the vertical component of motion due to the scattering of teleseismic P waves at a step in the Moho.

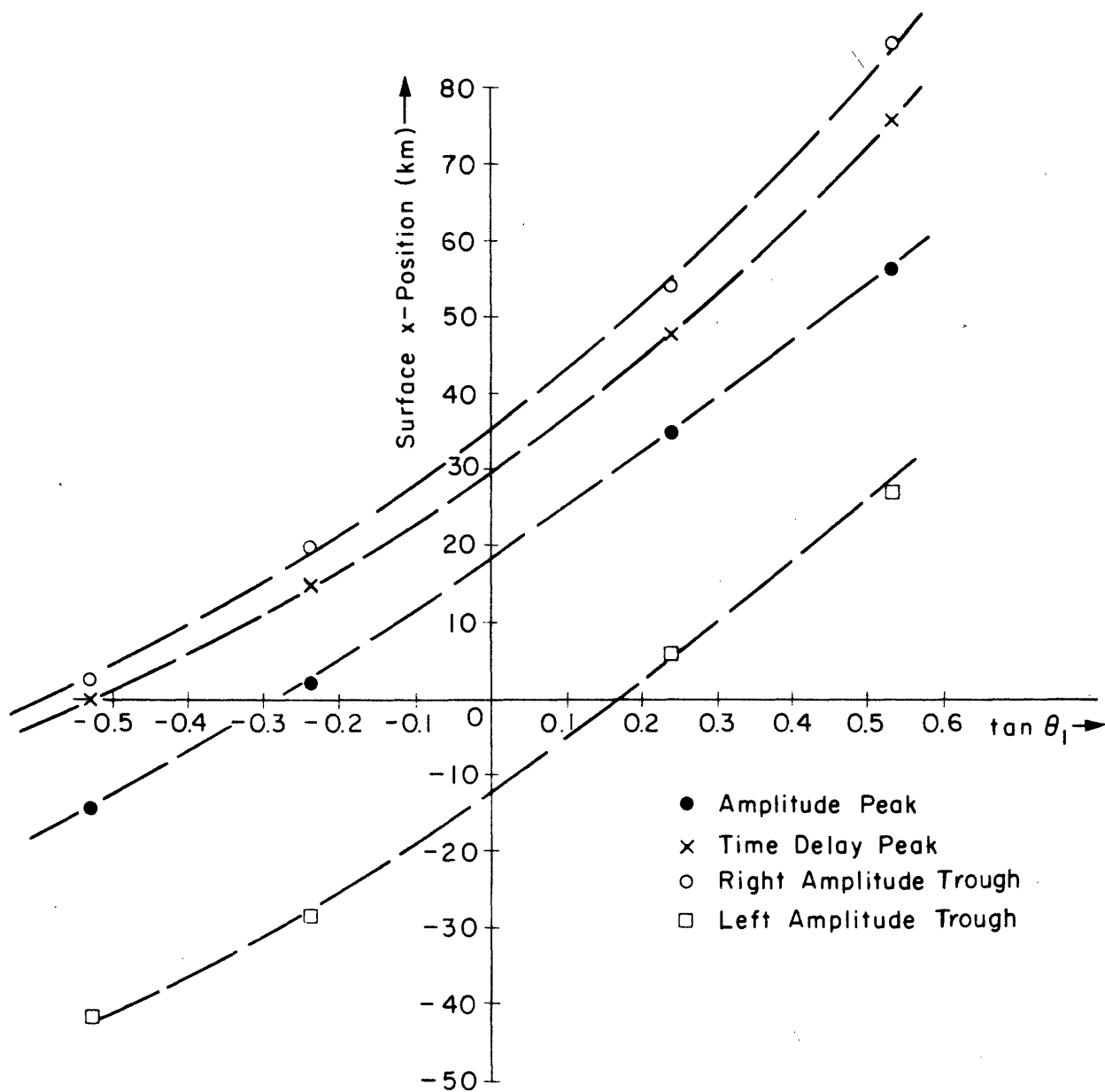


Figure 5.39. Plots showing the migrations of the x-coordinates of features in the theoretical solutions shown in Figure 5.38, as a function of $\tan \theta_1$. θ_1 is the angle from vertical of the primary scattered waves in the crust.

According to a simplified ray theory, the projections of the points P and Q along geometric ray paths onto the free surface should yield the positions of peak amplitude and time delay respectively. At longer wavelengths the time delay peak will shift somewhat further toward the right. Also in a simplified ray theory, the slope of the amplitude peak curve in Figure 5.39 would be equal to the depth to the Moho. This behavior is confirmed in this theoretical solution, i.e. the mean slope of the curve in Figure 5.39 between $\tan \Theta_1 = \pm 0.5$ is 65 km.

In Figure 5.40, the LASA-observed peak positions along the S30°E-N30°W line (x-coordinate) are plotted against $\tan \tilde{\Theta}_1$. $\tilde{\Theta}_1$ is the angle from vertical of the projection onto the x-z plane of the incident primary P-wave vector at the surface.

$$\sin \tilde{\Theta}_1 = \frac{\alpha_1}{c_x} [1 - \gamma_0^2 / k_{\alpha_1}^2]^{-1/2} \quad (5.5)$$

where γ_0 is the y-component of wave number, α_1 is the P wave velocity in the layer (6.0 km/sec in this model), and $k_{\alpha_1} = \omega / \alpha_1$. The data consists of average positions over the frequency range 0.5 to 1.1 cps, measured on curves like those in Figure 5.36, for all events listed in Table 5.3. The apparent velocities in the x-direction are also listed in Table 5.3.

The slope of the least-square fit to the amplitude peak curve is 48+5 km. The time-delay peak curve is displaced toward the NW, not so much as in the theoretical solution, yet the shift is apparent for all values $\tilde{\Theta}_1$. If the interface irregularity were a symmetrical depression we should expect the amplitude peak and time-delay peak curves to cross at $\tilde{\Theta}_1 = 0$ and we should have observed phase dispersion. We interpret the shift of the time-delay curve in Figure 5.40 to be significant so that the

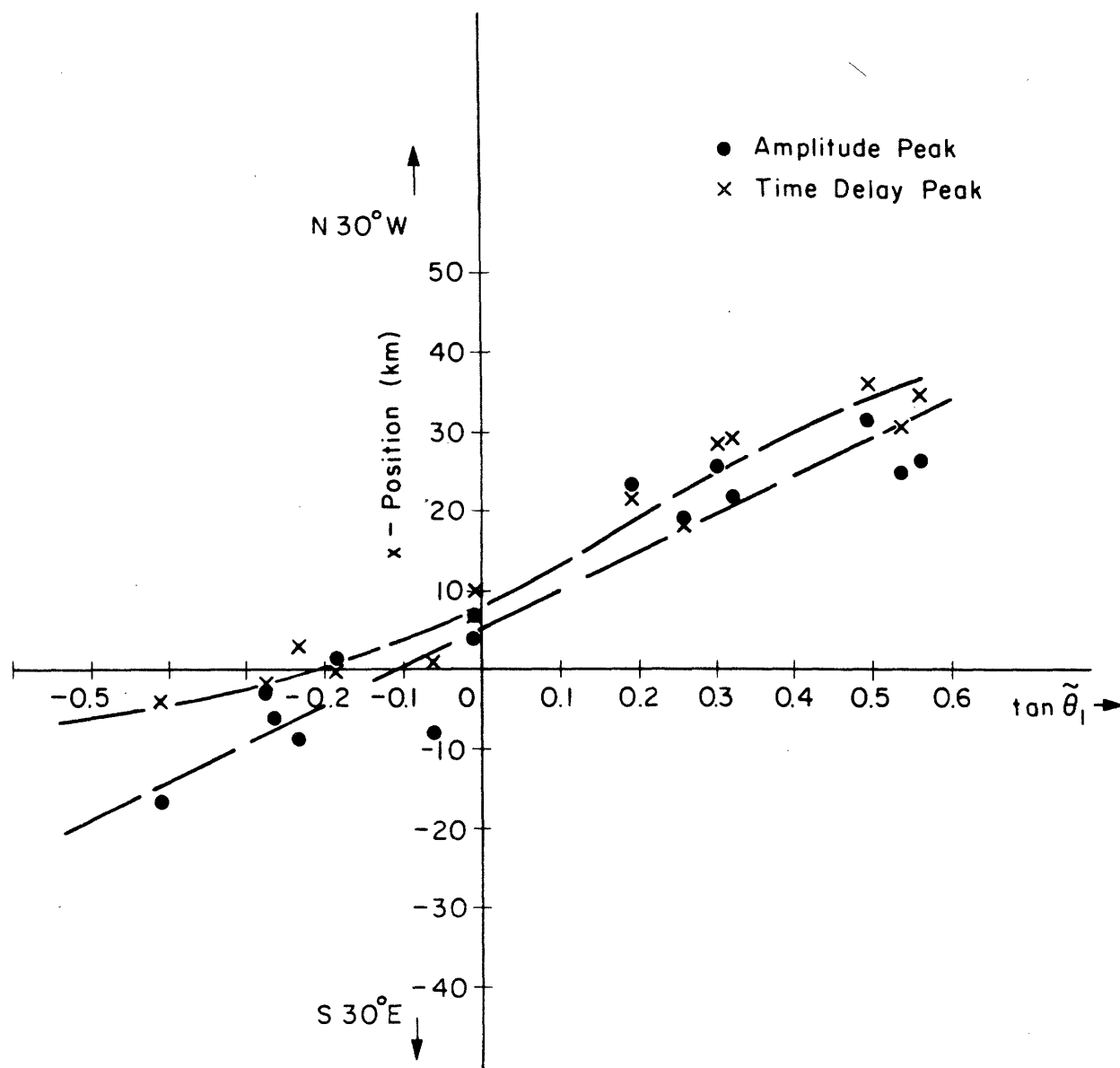


Figure 5.40. Plots of the migrations of the x-coordinates of the observed amplitude and time delay peaks along the S30°E-N30°W line for the seventeen events listed in Table 5.3. The positions are mean values for spectral data in the interval 0.5-1.1 cps. $\tilde{\theta}_1$ is the computed projection of θ_1 onto the x-z plane (vertical plane containing S30°E-N30°W). In the computation α_1 is assumed, and the apparent velocity and azimuth are mean values across LASA.

Moho varies as a step. This point is crucial to the following estimation of the size of the irregularity. Using the observed typical time-delay anomalies (0.40 to 0.45 sec) and the theoretical picture in Figure 5.38, we estimate a step amplitude of 11 ± 3 km with the step centered 2 km SE of A0. Again, using the argument of the ray-geometric projection of points P and Q in Figure 5.38, the close spacing of the amplitude and time-delay curves implies a large step gradient. The estimated width is 20 ± 5 km; thus, the feature is quite localized. We made no estimates of the angles γ_1 and γ_2 in Figure 5.41 but the time delay anomalies indicate that the Moho thins on either side away from the feature. These results are summarized in Table 5.6.

Although our model has only a single crustal layer, we can draw several significant conclusions. Our estimate of Moho depth is significantly less than that in the GS model. However, it is comparable with the Boore and Toksöz (1969) depth of 52 km based upon surface wave data and with the U.S.G.S. refraction-profile-determined depth of 47 to 52 km (Borcherdt and Roller, 1967). The crustal models used in both those studies are multi-layered and the mean crustal P-wave velocities (based on total travel time through the layers) are larger than our 6.0 km/sec. Our computed Moho depth is determined by the value that we assume for the mean P-wave velocity above the irregular interface. The solutions are such that an increase in P wave velocity would yield more shallow estimates of depth and a decrease would yield the opposite. Therefore, if we used the Boore and Toksöz velocities our estimated Moho depth would be reduced. Of course we may not alter α_1 to get the GS depth of 64 km because we already are using their value of α_1 .

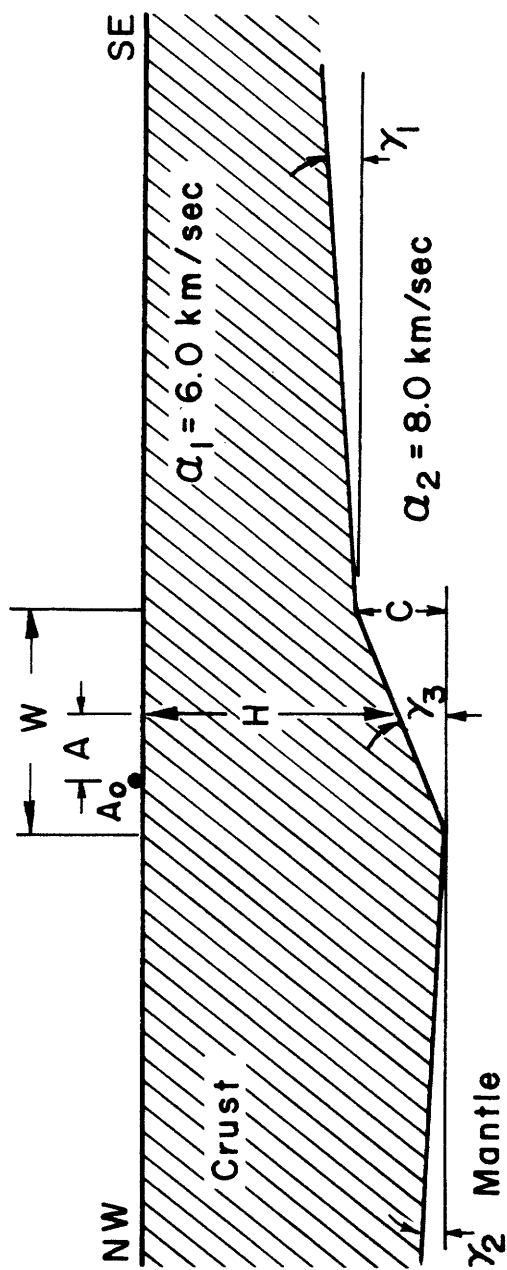


Figure 5.41. Schematic diagram showing the crustal structure parameters investigated in the Greenfield and Sheppard model. The numerical values are given in Table 5.6.

TABLE 5.6

Parameters for Single Layer Models of Montana LASA Structure

Parameter	Model	
	Greenfield & Sheppard	Ours
H(km)	64	48 \pm 5
c(km)	12	11 \pm 3
W(km)	35	20 \pm 5
A(km)	12	2 \pm 3
γ_1 (deg)	3	--
γ_2 (deg)	5	--
γ_3 (deg)	19	29 \pm 8
Strike	N60 $^\circ$ E	N64 $^\circ$ \pm 6 $^\circ$ E

Based on this same reasoning, we conclude that the irregular interface that is the scattering source of both the amplitude and time delay anomalies near the center of LASA must be deep-seated. Glover and Alexander (1969) have suggested that the anomalies are attributable to variations in basement topography that has a NW-SE trend. The observed large migrations of amplitude and time delay peaks with incidence direction cannot support such an interpretation either for so shallow a depth to irregular interface or for the trend direction. Using the low mean velocity of the sediments in our method would yield estimates of depth that are much larger than 48 km. Also, the large amplitude anomalies observed cannot be the result of focusing of waves scattered from the basement irregularity, as suggested by Glover and Alexander. According to our theoretical solutions, their basement depths and relief would result in only small focusing effects. Undoubtedly, however, the more complicated two-dimensionally irregular interfaces shapes likely at the shallower depths do contribute to the observed scatter in the data.

VI CONCLUSION

6.1. General Comments.

Our method provides a practical means for the study of aspects of the wave fields peculiar to the two-dimensional models discussed. The amplitudes and slopes of the interface irregularities that we study are larger than those allowed in the iterative approximation method of Rayleigh or in the various approximation methods (Gilbert and Knopoff, 1960; Herrera, 1964; and McIvor, 1969). With good accuracy, our method affords study of scattering for a range of reasonable, laterally heterogeneous crustal structures. The method adds to the stock of theoretical tools available to the seismologist. Besides having value for the inverse problem of interpretation of subsurface structure, the method should be of as much use to seismologists desiring quantitative estimates of the amplitude and time-delay anomalies expected in typical scattering problems. For example, in an attenuation (Q) study based upon spectral amplitudes, one could determine the extent to which the Q estimates may be biased by anomalous amplitudes associated with the scattering from anticipated interface irregularities.

The study of the Moho structure beneath Montana LASA demonstrates the potentiality of using spectral amplitudes as well as time delays to formulate a more unique picture of deep-seated structure. Our method is particularly well suited for investigating Moho or basement shape irregularities of the size found at LASA. The technique may bridge a gap that has existed previously because of the difficulties in obtaining

seismic reflections from the Moho and in interpreting the effects of rapid lateral changes in structure in the conventional seismic refraction method. Until recently the existence of deep-seated irregularities of the size suggested for LASA was not given much consideration. However, interpretations of the PROJECT EARLY RISE refraction experiment (Mereu and Hunter, 1969) indicate such irregularities in Moho depth in the Lake Superior region. Moreover, the large regional anomalies in spatially smoothed data from aeromagnetic surveys across wide belts of the United States also suggest deep-seated lateral variations in structure having linear trends that extend over large distances (Zietz, 1969). The steep dip in the Moho at LASA may be interpreted as evidence of a dip slip fault or localized intrusions.

6.2. Computational Time.

The method was programmed for the IBM 360-65 at the M.I.T. computation center. The computation time is controlled by the total number of complex wave amplitudes representing our solution (the matrix size number K in Table 3.1). For a given problem configuration and frequency, we economize by solving problems involving various source wave directions and source wave types concurrently. For the SH wave problems, typical computer time for problems involving the maximum number of scattering orders is 4 minutes for the first incident wave direction and 20 sec for each additional direction. Of that time approximately a minute is required to synthesize the interface displacements and stresses. The computation times are considerably shorter when fewer scattered waves are used. For the multi-layered general-azimuth problems, the computation times for the largest

number of scattered wave orders are 5 minutes for the first wave type and 30 sec for each additional type with 90 sec required for the synthesis of all interface quantities. We could handle larger problems with the present computer storage capacity; however, at considerably increased cost in time.

6.3. Recommendations for Future Work.

The use of SP spectral amplitudes and time delays in a systematic study of the depth and shape of irregularities in the Moho as described here, may provide a new interpretive tool in seismology. Because the method uses observational data from earthquakes at all azimuths and teleseismic distances, we might consider the deployment of mobile arrays of seismometer stations for use in such passive experiments. Two to four months occupation of a given site might be sufficient to gather the required data. Three-component stations within such an array could provide further diagnostic information as indicated in our theoretical solutions. It would be of value, for example, to learn whether the steeply dipping anomaly in the Moho persists for some distance along the indicated strike. Furthered knowledge of the existence of such features and interpretation of their meaning may yield new understanding of the regional characteristics of the upper mantle.

The theoretical solutions to grazing incidence problems may be used to aid in the interpretation of the amplitudes and time delays observed in the large seismic refraction experiments such as PROJECT EARLY RISE. Mereu (1969) has attempted analysis of amplitude variations in that experiment using ray theory.

Regarding application of our approximate method in its present form, the work performed for this thesis is preliminary. The problems investigated in Chapter V were intended to be representative of the range of applications in which the method may be of value, and further systematic investigation of some of the applications is warranted. One example is a closer study of the dependences of solutions to problems in multi-layered crust models on changes in relative layer thicknesses and on wavelength. The variety of interface shapes investigated can be enlarged so as to determine the sensitivity of the computed spatial distributions of amplitude and phase delay to the details in shape. One interesting experiment, for example, might be to let the interface take the shape of a sample from an ensemble of smoothed, random shapes. We may use the solutions to plane wave source problems to estimate the variances in the spatial distributions of free surface displacement amplitude and phase delay as functions of the statistical properties of the interface shape. The shapes must, of course, repeat every distance L in the x -direction.

Improved understanding of the relationship between our grazing incidence problems and the scattering of head waves may prove useful in refraction seismology. We particularly desire further comparisons with results for laboratory models having interface depressions and step changes. Also, by comparing solutions with those of the finite difference technique we may extend our confidence in using both techniques for treatment of the stepped interface problems.

The computer programs have not yet been written to include the case of variable surface topography in P-wave scattering problems. Possibly further study of details in the surface wave generation by scattering

from surface features might yield estimates of the actual amplitudes of the scattered waves. Preliminary results, not shown in this thesis, suggest that the technique may work for the problem of the scattering of incident surface waves at changes in layer thickness. The case of two or more internal irregular interfaces, also has not been programmed. Because the coefficient matrix for the simultaneous system of equations has many zero elements, special techniques may enable practical solution of these problems. With no new conceptual difficulties, the class of propagation mediums can also be expanded to include fluid layers.

In considering the future usage of the method, probably no aspect deserves more attention than that of increasing the computational speed. Many efficiencies are incorporated into the present programs, yet the author would be surprised if significant further increases in speed cannot be attained.

APPENDIX A

RELATIONSHIPS BETWEEN UPGOING AND DOWNGOING WAVES

A1. Review of Flat-Layer Theory.

Consider the sequence of layers bounded by planes at constant z' as shown in Figure A1. The layers are specified in terms of the parameters ρ_m , density; α_m , P wave velocity; β_m , S wave velocity; and z_m , z' coordinate of the interface at the bottom of the layer. Layers \tilde{n} and p need not be half-spaces; that is, there may be layers above and below those shown in the figure.

Consider source waves (waves incoming from above in layer p or from below in layer \tilde{n}) that are propagating parallel to the $x'-z'$ plane with the x' -component of wavenumber given by \mathcal{K} . To satisfy stress and displacement continuity conditions at all the interfaces for all x' and y' , all waves must propagate parallel to the $x'-z'$ plane (called the propagation plane in sections 2.3 through 2.5) and have the same wavenumber \mathcal{K} . Moreover, as we found in (2.37), the P-SV wave motion is uncoupled from the SH wave motion. In section 2.3, we derived relationships (2.44) and (2.45) for the displacements and stresses, acting on planes of constant z , in terms of upgoing and downgoing P, SV, and SH wave amplitudes. In all that follows, we suppress the factor $e^{i(\mathcal{K}x' - \omega t)}$ that is common to all the wave amplitude vectors by supposing that all quantities are evaluated at $x'=0$ and $t=0$. Repeating (2.47), we have, for layer m

$$\underline{M}_m(z) = \underline{E}_m(z) \underline{\sigma}_m \quad (2.47)$$

$$\underline{m}_m(z) = \underline{\epsilon}_m(z) \underline{\alpha}_m$$

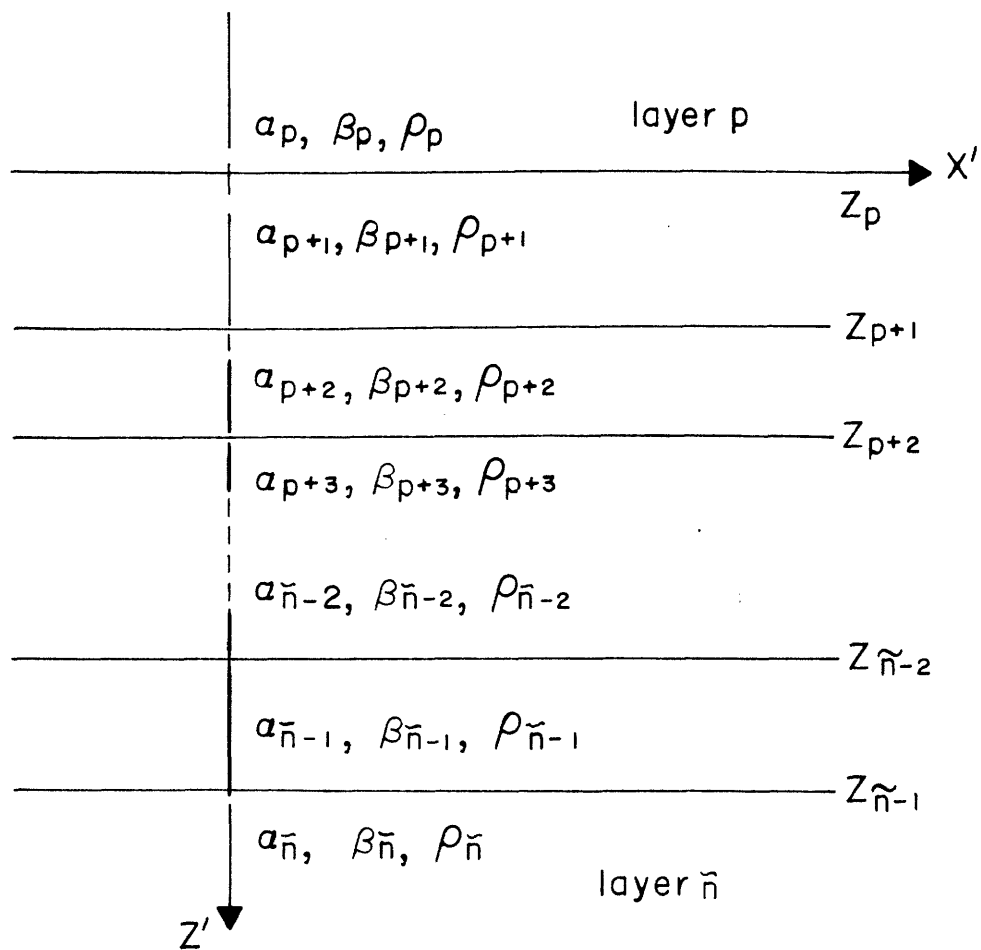


Figure A1. Sequence of flat, homogeneous, isotropic layers.

where the motion-stress vectors, \underline{M}_m and \underline{m}_m , and the wave amplitude vectors, \underline{Q}_m and \underline{q}_m , are defined by (2.48) and (2.49). By (2.44) and (2.45), the \underline{E}_m and \underline{E}_m matrices are

$$\underline{E}_m(z) = \begin{pmatrix} ix e^{ip_m} & -i\gamma'_m e^{iq_m} & ix e^{-ip_m} & i\gamma'_m e^{-iq_m} \\ i\gamma_m e^{ip_m} & ix e^{iq_m} & -i\gamma_m e^{-ip_m} & ix e^{-iq_m} \\ \mu_m f_m e^{ip_m} & -2\mu_m \kappa \gamma'_m e^{iq_m} & \mu_m f_m e^{-ip_m} & 2\mu_m \kappa \gamma'_m e^{-iq_m} \\ -2\mu_m \kappa \gamma_m e^{ip_m} & -\mu_m f_m e^{iq_m} & 2\mu_m \kappa \gamma_m e^{-ip_m} & -\mu_m f_m e^{-iq_m} \end{pmatrix} \quad (A1)$$

and

$$\underline{E}_m = \begin{pmatrix} e^{iq_m} & e^{-iq_m} \\ i\mu_m \gamma'_m e^{iq_m} & -i\mu_m \gamma'_m e^{-iq_m} \end{pmatrix} \quad (A2)$$

where γ_m and γ'_m are the vertical components of wave-number defined by (2.40) and

$$p_m \equiv \gamma_m (z' - z_{m-1})$$

$$q_m \equiv \gamma'_m (z' - z_{m-1})$$

$$f_m \equiv 2\kappa^2 - k_{\beta m}^2$$

We now follow the layer matrix method of **Thomson(1950)** and Haskell (1953). Consider the P-SV problem first. The motion-stress vector at the bottom and top of layer m are

$$\underline{M}_m(z_m) = \underline{E}_m(z_m) \underline{Q}_m$$

and

$$\underline{M}_m(z_{m-1}) = \underline{E}_m(z_{m-1}) \underline{Q}_m \quad (A3)$$

Assuming, for the present, that $\underline{E}_m(z_{m-1})$ is nonsingular, we can eliminate the vector \underline{Q}_m from this pair of equations to arrive at

$$\underline{M}_m(z_m) = \underline{E}_m(z_m) \underline{E}_m^{-1}(z_{m-1}) \underline{M}_m(z_{m-1}) \quad (\text{A4})$$

According to the continuity requirements, each element of \underline{M}_m is continuous across an interface at constant z' so that

$$\underline{M}_m(z_{m-1}) = \underline{M}_{m-1}(z_{m-1})$$

Thus (A4) becomes

$$\underline{M}_m(z_m) = \underline{A}_m \underline{M}_{m-1}(z_{m-1}) \quad (\text{A5})$$

where

$$\underline{A}_m = \underline{E}_m(z_m) \underline{E}_m^{-1}(z_{m-1}) \quad (\text{A6})$$

Using (A5), we can express the motion and stress at the bottom of layer m in terms of the motion and stress at the bottom of layer $m-1$. Matrix \underline{A}_m is called the layer matrix; its elements are functions of ω , κ , $z'-z_{m-1}$, and the layer parameters ρ_m , α_m , β_m . Similarly, provided that $\underline{E}_m(z_{m-1})$ is nonsingular, we can relate SH motion and stress in adjacent layers by

$$\underline{m}_m(z_m) = \underline{Q}_m \underline{m}_{m-1}(z_{m-1}) \quad (\text{A7})$$

$$\underline{Q}_m = \underline{E}_m(z_m) \underline{E}_m^{-1}(z_{m-1})$$

By simple iteration, we can express the motion-stress vector at the bottom of a layer m in terms of the motion-stress vector at the corresponding position of a layer p above. We have

$$\underline{M}_m(z_m) = [\underline{A}_m \cdot \underline{A}_{m-1} \cdots \underline{A}_{p+2} \cdot \underline{A}_{p+1}] \cdot \underline{M}_p(z_p)$$

and

$$\underline{m}_m(z_m) = [\underline{a}_m \cdot \underline{a}_{m-1} \cdots \underline{a}_{p+2} \cdot \underline{a}_{p+1}] \cdot \underline{m}_p(z_p)$$

(A8)

Comparable expressions could be written, say, between \underline{D}_m and \underline{D}_p or between $\underline{M}_m(z_m)$ and \underline{D}_p .

The matrix \underline{E}_m given by (A1) is singular when $\nu_m = 0$ or when $\nu'_m = 0$, and the matrix $\underline{\xi}_m$ given by (A2) is singular when $\nu'_m = 0$. In those special cases \underline{E}_m and $\underline{\xi}_m$ may be redefined so as to be nonsingular.

We will now use (A3) through (A8) in problems involving irregular interfaces.

A2. Sequence of Flat Layers With One Irregular Interface.

As shown in Figure 2.5, we consider $\tilde{n}-1$ layers, between two half-spaces, with one irregular interface bounding layer s from below. A plane source wave is incident from below in the half-space \tilde{n} , and no waves are incident from above in the half-space 0.

We consider three distinct cases.

Case (A2.1): $1 \leq s \leq \tilde{n}-2$; the general case.

Case (A2.2): $s = \tilde{n}-1$; bottom interface is irregular.

Case (A2.3): $s = 0$; top interface is irregular.

Case (A2.1). First, consider the layers below the interface. By (A3) and (A8), we have

$$\underline{D}_{\tilde{n}} = \underline{E}_{\tilde{n}}^{-1}(z_{\tilde{n}-1}) \cdot \underline{M}_{\tilde{n}}(z_{\tilde{n}-1}) = \underline{L} \cdot \underline{D}_{s+1} \quad (A9)$$

and

$$\underline{d}_n = \underline{P} \cdot \underline{d}_{s+1} \quad (\text{A10})$$

where

$$\underline{L} = \underline{E}_n^{-1}(z_{n-1}) \cdot \underline{A}_{n-1} \cdot \underline{A}_{n-2} \cdots \cdots \underline{A}_{s+2} \cdot \underline{E}_{s+1}(z_{s+1}) \quad (\text{A11})$$

$$\underline{P} = \underline{E}_n^{-1}(z_{n-1}) \cdot \underline{Q}_{n-1} \cdot \underline{Q}_{n-2} \cdots \cdots \underline{Q}_{s+2} \cdot \underline{E}_{s+1}(z_{s+1}) \quad (\text{A12})$$

\underline{L} is a 4×4 matrix whose elements are \underline{l}_{ij} and \underline{P} is a 2×2 matrix whose elements are p_{ij} (i is the row index; j , the column index). We can also write \underline{L} in block form as

$$\underline{L} = \begin{pmatrix} \underline{L}_{11} & | & \underline{L}_{12} \\ \hline \underline{L}_{21} & | & \underline{L}_{22} \end{pmatrix}$$

where the \underline{L}_{ij} are 2×2 matrices. Equations (A9) are 4 linear equations

from which we can solve for ϕ_{s+1}^u , ψ_{s+1}^u , ϕ_n^d , and ψ_n^d in terms of

ϕ_{s+1}^d , ψ_{s+1}^d , and the known source terms $\phi_n^u = \phi^*$ and $\psi_n^u = \psi^*$ (see equation 2.41). We find

$$\begin{pmatrix} \phi_{s+1}^u \\ \psi_{s+1}^u \end{pmatrix} = \underline{L}_{22}^{-1} \begin{pmatrix} \phi^* \\ \psi^* \end{pmatrix} - \underline{L}_{22}^{-1} \underline{L}_{21} \begin{pmatrix} \phi_{s+1}^d \\ \psi_{s+1}^d \end{pmatrix} \quad (\text{A13})$$

and

$$\begin{pmatrix} \phi_n^d \\ \psi_n^d \end{pmatrix} = \underline{L}_{12} \underline{L}_{22}^{-1} \begin{pmatrix} \phi^* \\ \psi^* \end{pmatrix} + \left[\underline{L}_{11} - \underline{L}_{12} \underline{L}_{22}^{-1} \underline{L}_{21} \right] \begin{pmatrix} \phi_{s+1}^d \\ \psi_{s+1}^d \end{pmatrix} \quad (\text{A14})$$

provided that the submatrix $\underline{\mathcal{L}}_{22}$ is nonsingular. Actually, this matrix can be singular for certain values of \mathcal{K} (for given frequency ω). We discuss such singular cases in Appendix B.

Similarly, for the SH motion, we can solve (A10) for V_{s+1}^u and $V_{\tilde{n}}^d$ in terms of V_{s+1}^d and the source amplitude V^* .

$$V_{s+1}^u = (1/p_{22}) V^* - (p_{21}/p_{22}) V_{s+1}^d \quad (\text{A15})$$

$$V_{\tilde{n}}^d = (p_{12}/p_{22}) V^* + (p_{11} - p_{12}p_{21}/p_{22}) V_{s+1}^d \quad (\text{A16})$$

The singular case, $p_{22}=0$, is discussed in Appendix B. For use elsewhere, we write the three solutions as

$$\begin{aligned} \phi_{s+1}^u &= A_1 \delta(k-k_0) + B_1 \phi_{s+1}^d + C_2 \psi_{s+1}^d \\ \psi_{s+1}^u &= A_2 \delta(k-k_0) + C_1 \phi_{s+1}^d + B_2 \psi_{s+1}^d \\ V_{s+1}^u &= A_3 \delta(k-k_0) + B_3 V_{s+1}^d \end{aligned} \quad (\text{A17})$$

where the various coefficients are

$$\begin{aligned} B_1 &= \mathcal{L} \begin{pmatrix} 3 & 4 \\ 4 & 1 \end{pmatrix} / \mathcal{L} \begin{pmatrix} 3 & 3 \\ 4 & 4 \end{pmatrix} \\ B_2 &= \mathcal{L} \begin{pmatrix} 3 & 2 \\ 4 & 3 \end{pmatrix} / \mathcal{L} \begin{pmatrix} 3 & 3 \\ 4 & 4 \end{pmatrix} \\ B_3 &= -p_{21}/p_{22} \\ C_1 &= \mathcal{L} \begin{pmatrix} 3 & 1 \\ 4 & 3 \end{pmatrix} / \mathcal{L} \begin{pmatrix} 3 & 3 \\ 4 & 4 \end{pmatrix} \\ C_2 &= \mathcal{L} \begin{pmatrix} 3 & 4 \\ 4 & 2 \end{pmatrix} / \mathcal{L} \begin{pmatrix} 3 & 3 \\ 4 & 4 \end{pmatrix} \end{aligned} \quad (\text{A18})$$

We have used the symbol $\mathcal{L} \begin{pmatrix} ij \\ km \end{pmatrix} \equiv l_{ij} l_{km} - l_{im} l_{kj}$. For example, $\mathcal{L} \begin{pmatrix} 33 \\ 44 \end{pmatrix}$ is the determinant of $\underline{\underline{\mathcal{L}}}_{22}$.

Now consider the layers above the irregular interface. We relate the wave amplitudes in layer s and in the half-space 0 by again using (A3) and (A8)

$$\underline{\underline{d}}_s = \underline{\underline{\eta}} \cdot \underline{\underline{d}}_0 \quad (\text{A19})$$

$$\underline{\underline{d}}_s = \underline{\underline{Q}} \cdot \underline{\underline{d}}_0 \quad (\text{A20})$$

where

$$\underline{\underline{\eta}} = \underline{\underline{E}}_s^{-1}(z_{s-1}) \cdot \underline{\underline{A}}_{s-1} \cdots \cdots \underline{\underline{A}}_1 \cdot \underline{\underline{E}}_0(z_0) \quad (\text{A21})$$

$$\underline{\underline{Q}} = \underline{\underline{E}}_s^{-1}(z_{s-1}) \cdot \underline{\underline{a}}_{s-1} \cdots \cdots \underline{\underline{a}}_1 \cdot \underline{\underline{E}}_0(z_0) \quad (\text{A22})$$

Let n_{ij} and q_{ij} be the elements of the 4×4 matrix $\underline{\underline{\eta}}$ and the 2×2 matrix $\underline{\underline{Q}}$, respectively. Since we postulate no downgoing waves in the upper half-space, we have $\phi_0^d = \psi_0^d = v_0^d = 0$. Using the 2×2 block matrix notation, (A2.13) can be written as

$$\begin{pmatrix} \phi_s^d \\ \psi_s^d \\ \phi_s^u \\ \psi_s^u \end{pmatrix} = \begin{pmatrix} \underline{\underline{\eta}}_{11} & | & \underline{\underline{\eta}}_{12} \\ \underline{\underline{\eta}}_{21} & | & \underline{\underline{\eta}}_{22} \end{pmatrix} = \begin{pmatrix} 0 \\ 0 \\ \phi_0^u \\ \psi_0^u \end{pmatrix}$$

from which we obtain

$$\begin{pmatrix} \phi_0^u \\ \psi_0^u \end{pmatrix} = \underline{\underline{\eta}}_{22}^{-1} \begin{pmatrix} \phi_s^u \\ \psi_s^u \end{pmatrix} \quad (\text{A23})$$

and

$$\begin{pmatrix} \phi_s^d \\ \psi_s^d \end{pmatrix} = \underline{\underline{\eta}}_{12} \underline{\underline{\eta}}_{22}^{-1} \begin{pmatrix} \phi_s^u \\ \psi_s^u \end{pmatrix} \quad (\text{A24})$$

provided that $\underline{\eta}_{22}$ is nonsingular. Similarly, for the SH motion, we have

$$V_s^d = q_{12} V_0^d \quad (A25)$$

$$V_0^u = V_s^u / q_{22}$$

when $q_{22} \neq 0$. See Appendix B for the cases $q_{22} = 0$ and $\det(\underline{\eta}_{22}) = 0$.

For reference elsewhere, we write these equations as

$$\begin{aligned} \phi_s^d &= \bar{B}_1 \phi_s^u + \bar{C}_2 \psi_s^u \\ \psi_s^d &= \bar{C}_1 \phi_s^u + \bar{B}_2 \psi_s^u \\ V_s^d &= \bar{B}_3 V_s^u \end{aligned} \quad (A26)$$

where

$$\begin{aligned} \bar{B}_1 &= \eta \begin{pmatrix} 1 & 3 \\ 4 & 4 \end{pmatrix} / \eta \begin{pmatrix} 3 & 3 \\ 4 & 4 \end{pmatrix} \\ \bar{B}_2 &= \eta \begin{pmatrix} 3 & 3 \\ 2 & 4 \end{pmatrix} / \eta \begin{pmatrix} 3 & 3 \\ 4 & 4 \end{pmatrix} \\ \bar{B}_3 &= q_{12} / q_{22} \\ \bar{C}_1 &= \eta \begin{pmatrix} 2 & 3 \\ 4 & 4 \end{pmatrix} / \eta \begin{pmatrix} 3 & 3 \\ 4 & 4 \end{pmatrix} \\ \bar{C}_2 &= \eta \begin{pmatrix} 3 & 3 \\ 1 & 4 \end{pmatrix} / \eta \begin{pmatrix} 3 & 3 \\ 4 & 4 \end{pmatrix} \end{aligned} \quad (A27)$$

and $\eta \begin{pmatrix} ij \\ km \end{pmatrix} = \eta_{ij} \eta_{km} - \eta_{im} \eta_{kj}$.

The wave amplitudes ϕ_{s+1}^d , ψ_{s+1}^d , V_{s+1}^d , and ϕ_s^u , ψ_s^u , V_s^u are determined by matching boundary conditions at the irregular interface as described in Chapter II. Then we can use (A14), (A16), (A23), and (A25) to determine $\phi_{\bar{n}}^d$, $\psi_{\bar{n}}^d$, $V_{\bar{n}}^d$ and ϕ_0^u , ψ_0^u , V_0^u . With these quantities, we can determine, say, the motion-stress vector at any height z in the upper half-space by using (A3). That is,

$$\underline{M}_0(z) = \underline{E}_0(z) \cdot \underline{D}_0$$

Also, in Appendix E, we shall use these quantities to evaluate a conservation of energy flux check on the accuracy of our solutions.

The method used here is analogous to the method used by Harkrider(1964) to express the field of elastic wave sources in a layered half-space. The waves ϕ_{s+1}^d , ϕ_s^u , etc. that leave the irregular interface are considered as source waves just as are the true sources ϕ^* , ψ^* , and v^* . That is, since the primary field waves with wavenumber \mathcal{K}_0 are scattered at the irregular interface into waves having all values of \mathcal{K} , we consider the region near the irregular interface to be a source region for the scattered field.

Note that, if $s=1$, we delete the layer matrices \underline{A}_m and \underline{a}_m in defining the \underline{N} and \underline{Q} matrices by (A21) and (A22). Similarly, when $s=\tilde{n}-2$, we delete the layer matrices in defining $\underline{\mathcal{L}}$ and $\underline{\mathcal{P}}$ by (A11) and (A12).

Case (A2.2). When $s=\tilde{n}-1$, the bottom interface is irregular, and we have, simply $\underline{\mathcal{L}} = \underline{1}_4$ and $\underline{\mathcal{P}} = \underline{1}_2$ the 4x4 and 2x2 identity matrices, respectively. Obviously, the coefficients in (A17) are $B_1=B_2=B_3=C_1=C_2=0$, $A_1 = \phi^*$, $A_2 = \psi^*$, $A_3 = v^*$ so that

$$\begin{array}{ll} \phi_{s+1}^u = \phi^* & \phi_{\tilde{n}}^d = \phi_{s+1}^d \\ \psi_{s+1}^u = \psi^* & \psi_{\tilde{n}}^d = \psi_{s+1}^d \\ v_{s+1}^u = v^* & v_{\tilde{n}}^d = v_{s+1}^d \end{array} \quad (\text{A28})$$

Case (A2.3). When $s=0$, the top interface is irregular, and $\underline{N} = \underline{1}_4$ and $\underline{Q} = \underline{1}_2$. That is, trivially,

$$\phi_s^d = \psi_s^d = v_s^d = 0$$

and

$$\phi_o^u = \phi_s^u$$

$$\psi_o^u = \psi_s^u$$

$$V_o^u = V_s^u$$

(A29)

A3. Layered Half-Space Having One Irregular Interface.

The medium is changed in that the upper half-space 0 is replaced by free space. Equations (A9) through (A18), relating the wave amplitudes below the irregular interface s , are unchanged. Above interface s , we shall express the three components of motion at the free surface and the amplitudes of waves that approach the interface in terms of the amplitudes of the waves that leave. We consider two cases.

Case (A3.1): $s \neq 0$, the general case involving a plane free surface.

Case (A3.2): $s = 0$, variable topography.

Case (A3.1). Making use of (A3) and (A8), we have

$$\underline{D}_s = \underline{\tilde{N}} \cdot \underline{M}_o(z_o) \quad (A30)$$

$$\underline{d}_s = \underline{\tilde{Q}} \cdot \underline{m}_o(z_o) \quad (A31)$$

where

$$\underline{\tilde{N}} = \underline{E}_s^{-1}(z_{s-1}) \cdot \underline{A}_{s-1} \cdots \underline{A}_1 \quad (A32)$$

$$\underline{\tilde{Q}} = \underline{E}_s^{-1}(z_{s-1}) \cdot \underline{a}_{s-1} \cdots \underline{a}_1 \quad (A33)$$

Let \tilde{n}_{ij} be the elements of the 4x4 matrix $\tilde{\mathbf{n}}$ and \tilde{q}_{ij} be those of the 2x2 matrix $\tilde{\mathbf{Q}}$. Since stress must vanish at the free surface, (A30) may be written, using 2x2 block matrix notation, as

$$\begin{pmatrix} \phi_s^d \\ \psi_s^d \\ \phi_s^u \\ \psi_s^u \end{pmatrix} = \begin{pmatrix} \tilde{n}_{11} & \tilde{n}_{12} \\ \tilde{n}_{21} & \tilde{n}_{22} \end{pmatrix} \begin{pmatrix} u_o' \\ w_o' \\ 0 \\ 0 \end{pmatrix}$$

where u_o' and w_o' are the radial and vertical components of displacement at the free surface. Solving, we obtain

$$\begin{pmatrix} u_o' \\ w_o' \end{pmatrix} = \tilde{n}_{21}^{-1} \begin{pmatrix} \phi_s^u \\ \psi_s^u \end{pmatrix} \quad (\text{A34})$$

and

$$\begin{pmatrix} \phi_s^d \\ \psi_s^d \end{pmatrix} = \tilde{n}_{11} \tilde{n}_{21}^{-1} \begin{pmatrix} \phi_s^u \\ \psi_s^u \end{pmatrix} \quad (\text{A35})$$

provided that \tilde{n}_{21} is nonsingular. Similarly, for the SH motion,

$$\begin{aligned} v_o' &= v_s^u / \tilde{q}_{21} \\ v_s^d &= (\tilde{q}_{11} / \tilde{q}_{21}) v_s^u \end{aligned} \quad (\text{A36})$$

so long as $\tilde{q}_{21} \neq 0$.

ϕ_s^d , ψ_s^d , and v_s^d still satisfy (A26), but now

$$\begin{aligned} \bar{B}_1 &= \tilde{n} \begin{pmatrix} 1 \\ 4 \end{pmatrix} / \tilde{n} \begin{pmatrix} 3 \\ 4 \end{pmatrix} \\ \bar{B}_2 &= \tilde{n} \begin{pmatrix} 2 \\ 2 \end{pmatrix} / \tilde{n} \begin{pmatrix} 3 \\ 4 \end{pmatrix} \\ \bar{B}_3 &= \tilde{q}_{11} / \tilde{q}_{21} \\ \bar{C}_1 &= \tilde{n} \begin{pmatrix} 2 \\ 4 \end{pmatrix} / \tilde{n} \begin{pmatrix} 3 \\ 4 \end{pmatrix} \\ \bar{C}_2 &= \tilde{n} \begin{pmatrix} 1 \\ 2 \end{pmatrix} / \tilde{n} \begin{pmatrix} 3 \\ 4 \end{pmatrix} \end{aligned} \quad (\text{A37})$$

Case (A3.2). When $s=0$, the free surface is irregular, and since no waves exist above this surface, ϕ_s^d , ϕ_s^u , etc. no longer enter the problem. There are but three boundary conditions at the free surface, the vanishing of the three components of stress; and, correspondingly, there are but three wave amplitudes ϕ_{s+1}^d , ψ_{s+1}^d , and V_{s+1}^d to determine by the method discussed in Chapter II.

A4. More Than One Irregular Interface in the Layer Sequence.

The layers below the lowest irregular interface and those above the uppermost irregular interface are treated as in the cases already discussed. The final cases to consider involve the region between irregular interfaces r and s where, say, $s > r$. In the general case, $s > r+2$. Using (A3) and (A8), we have

$$\underline{\underline{D}}_s = \underline{\underline{J}} \underline{\underline{D}}_{r+1} \quad (\text{A38})$$

$$\underline{\underline{d}}_s = \underline{\underline{K}} \underline{\underline{d}}_{r+1} \quad (\text{A39})$$

where

$$\underline{\underline{J}} = \underline{\underline{E}}_s^{-1}(z_{s-1}) \underline{\underline{A}}_{s-1} \cdots \underline{\underline{A}}_{r+2} \underline{\underline{E}}_{r+1}(z_{r+1}) \quad (\text{A40})$$

$$\underline{\underline{K}} = \underline{\underline{E}}_s^{-1}(z_{s-1}) \underline{\underline{a}}_{s-1} \cdots \underline{\underline{a}}_{r+2} \underline{\underline{E}}_{r+1}(z_{r+1}) \quad (\text{A41})$$

We can express (A38) in block matrix notation as follows.

$$\begin{pmatrix} \phi_s^d \\ \psi_s^d \\ \phi_s^u \\ \psi_s^u \end{pmatrix} = \begin{pmatrix} \underline{\underline{J}}_{11} & \underline{\underline{J}}_{12} \\ \underline{\underline{J}}_{21} & \underline{\underline{J}}_{22} \end{pmatrix} \begin{pmatrix} \phi_{r+1}^d \\ \psi_{r+1}^d \\ \phi_{r+1}^u \\ \psi_{r+1}^u \end{pmatrix}$$

from which we write

$$\begin{pmatrix} \phi_{r+1}^u \\ \psi_{r+1}^u \end{pmatrix} = \underline{\underline{J}}_{22}^{-1} \begin{pmatrix} \phi_s^u \\ \psi_s^u \end{pmatrix} - \underline{\underline{J}}_{22}^{-1} \underline{\underline{J}}_{21} \begin{pmatrix} \phi_{r+1}^d \\ \psi_{r+1}^d \end{pmatrix} \quad (\text{A42})$$

and

$$\begin{pmatrix} \phi_s^d \\ \psi_s^d \end{pmatrix} = \underline{\underline{J}}_{12} \underline{\underline{J}}_{22}^{-1} \begin{pmatrix} \phi_s^u \\ \psi_s^u \end{pmatrix} + [\underline{\underline{J}}_{11} - \underline{\underline{J}}_{12} \underline{\underline{J}}_{22}^{-1} \underline{\underline{J}}_{21}] \begin{pmatrix} \phi_{r+1}^d \\ \psi_{r+1}^d \end{pmatrix}$$

provided that the 2x2 submatrix $\underline{\underline{J}}_{22}$ is nonsingular. Similarly, if k_{ij} are the elements of the 2x2 matrix $\underline{\underline{K}}$, we can express V_s^d and V_{r+1}^u in terms of V_s^u and V_{r+1}^d .

$$\begin{aligned} V_{r+1}^u &= (1/k_{22}) V_s^u - (k_{21}/k_{22}) V_{r+1}^d \\ V_s^d &= (k_{12}/k_{22}) V_s^u + (k_{11} - k_{12}k_{21}/k_{22}) V_{r+1}^d \end{aligned} \quad (\text{A43})$$

so long as $k_{22} \neq 0$.

When $s=r+2$, simply delete the $\underline{\underline{A}}_{\underline{\underline{m}}}$ and $\underline{\underline{a}}_{\underline{\underline{m}}}$ matrices from (A40) and (A41).

When $s=r+1$, the irregular interfaces are adjacent, and

$$\underline{\underline{J}} = \underline{\underline{1}}_4 \quad \underline{\underline{K}} = \underline{\underline{1}}_2$$

so that we have, immediately, $\phi_s^d = \phi_{r+1}^d$, $\phi_{r+1}^u = \phi_s^u$, etc.

Using the relations derived in this appendix, we can express the boundary conditions at any irregular interface in terms of the amplitudes of the three outgoing waves in each adjoining solid plus three more amplitudes for each of the nearest additional irregular interfaces. The integral equations for the general case involving more than one irregular interface are formulated in section 2.5.

APPENDIX B

SINGULARITIES OF THE INTEGRAL EQUATIONS

In Appendix A, we found that the complex amplitudes of waves leaving an irregular interface could be expressed in terms of the amplitudes of incoming waves and source terms except when certain 2x2 matrices were singular or when certain scalars vanished. For example, in equations (A34) and (A35), we expressed the free surface displacements $v'_0(\mathcal{K})$, $w'_0(\mathcal{K})$ and amplitudes of downgoing waves toward the uppermost irregular interface $\phi_s^d(\mathcal{K})$, $\psi_s^d(\mathcal{K})$ in terms of the upgoing wave amplitudes $\phi_s^u(\mathcal{K})$, $\psi_s^u(\mathcal{K})$ provided that the submatrix $\tilde{\mathcal{N}}_{21}$ was nonsingular; that is provided that the determinant $\det \tilde{\mathcal{N}}_{21} \neq 0$. Similarly, for SH motion $v'_0(\mathcal{K})$ and $v_s^d(\mathcal{K})$ were expressed in terms of $v_s^u(\mathcal{K})$ so long as $\tilde{\mathcal{Q}}_{21} \neq 0$.

Quantities such as $\det \tilde{\mathcal{N}}_{21}$ and $\tilde{\mathcal{Q}}_{21}$ enter into the denominators of the integrands of our basic integral equations (2.52), hence their vanishing along an integration path renders the integral equations singular. For example, if ω is real, the integrals are performed over real values of the x-component of wave number k . We are then concerned with the real roots of equations like

$$\begin{aligned} \det \tilde{\mathcal{N}}_{21}(\mathcal{K}, \omega) &= 0 \\ \tilde{\mathcal{Q}}_{21}(\mathcal{K}, \omega) &= 0 \end{aligned} \tag{B1}$$

($\mathcal{K} = (k^2 + \gamma_s^2)^{1/2}$ is the horizontal component of wave number).

According to (A34), (A35), and (A36), at these roots, we would observe free surface motion and downward attenuating waves in layers in the absence

of any upgoing driving waves in the layer. Evidently, (B1) are the period equations (dispersion relations) for locked or normal modes of P-SV and SH wave motion in the upper plane layers. The waves ϕ_s^d , ψ_s^d , and V_s^d are attenuating rather than propagating, in these cases, because otherwise energy would be propagating downward away from the surface layers in the absence of sources in the layers.

The medium for which either of equations (B1) applies consists of the plane layers above the irregular interface s overlying a half-space whose parameters are those of layer s , i.e., α_s , β_s , ρ_s . (The layers below interface s are replaced by a half-space.) For example, consider the problem involving a single layer $s=1$ over a half-space where the free surface is plane and the interface is irregular. By (A32) and (A33), $\tilde{\underline{\underline{\eta}}} = \underline{\underline{\epsilon}}_1^{-1}(z_0)$ and $\tilde{\underline{\underline{q}}} = \underline{\underline{\epsilon}}_1^{-1}(z_0)$. Using (A1) and (A2), we find

$$\tilde{\underline{\underline{\eta}}}_{21} = \frac{1}{2k_{\beta,1}^2} \begin{pmatrix} -2i\kappa & -i(2\kappa^2 - k_{\beta,1}^2)/\nu_1 \\ i(2\kappa^2 - k_{\beta,1}^2)/\nu_1' & -2i\kappa \end{pmatrix} \quad (\text{B2})$$

$$\tilde{\underline{\underline{q}}}_{21} = 1/2$$

Thus the zeros of $\det \tilde{\underline{\underline{\eta}}}_{21}$ are given by the roots of

$$F(\omega, \kappa) = 4\kappa^2 \nu_1 \nu_1' + (2\kappa^2 - k_{\beta,1}^2)^2$$

the familiar Rayleigh function (Ewing, Jardetsky, and Press, 1957), corresponding to Rayleigh waves in medium 1. Also, we note that $\tilde{\underline{\underline{q}}}_{21}$ does not vanish; that is, for the single layer over a half-space, no

singularities arise from expressing V_s^d in terms of V_s^u . There are no trapped SH modes (surface waves) at a single interface.

We interpret, similarly, the singular cases (equations (A18))

$$\det \underline{\underline{L}}_{22}(\kappa, \omega) = 0$$

$$p_{22}(\kappa, \omega) = 0$$
(B3)

which arise in relating incoming and outgoing waves below the lowest irregular interface. Equations (B3) are period equations for trapped modes in an infinite medium consisting of the plane layers $m=s+2, \dots, \tilde{n}-1$ bounded by the half-space \tilde{n} below and a half-space with the parameters of layer $s+1$ above. The singular cases (equations (A27))

$$\det \underline{\underline{N}}_{22}(\kappa, \omega) = 0$$

$$q_{22}(\kappa, \omega) = 0$$
(B4)

are the period equations for trapped modes in the infinite medium consisting of half-spaces, 0 and s , above and below the system of plane layers 1 through $s-1$. Finally, consider the singular cases (equations (A42) and (A43))

$$\det \underline{\underline{J}}_{22}(\kappa, \omega) = 0$$

$$k_{22}(\kappa, \omega) = 0$$
(B5)

that arise in relating up and downgoing waves between irregular interfaces r and s . These are period equations for trapped modes in an infinite medium consisting of plane layers $r+s, r+3, \dots, s-1$ bounded by a half-space $r+1$ above and a half-space s below.

We note that, in all of the above cases, at least two adjacent plane interfaces are required for there to arise singularities in SH wave motion problems. There are no normal modes associated with adjacent irregular interfaces and, in fact, the integral equations would have no singularities if all interfaces were irregular. Physically, this is because normal modes are constructive interference phenomena that require plane boundaries.

APPENDIX C

DETAILS IN THE DERIVATION OF INTEGRAL EQUATION (2.52)

Equations (2.44), (2.45), and (2.46) are expressions for the components (in the propagation coordinates basis) of the k-spectrum decomposed displacement and stress in medium m , in terms of the amplitudes of upgoing and downgoing P, SV, and SH waves. We first substitute (2.50) and (2.51) into the equations for layer s and layer $s+1$ to express the field at the irregular interface s in terms of outgoing wave amplitudes and source terms. For the equations that follow we define

$$\begin{aligned}
 p_s(x) &= \nu_s (z_s(x) - z_{s-1}) = \nu_s \zeta_s(x) \\
 q_s(x) &= \nu_s' \zeta_s(x) \\
 p_{s+1}(x) &= \nu_{s+1} \zeta_s(x) \\
 q_{s+1}(x) &= \nu_{s+1}' \zeta_s(x) \\
 f_m &= 2\kappa^2 - k_{\beta_m}^2 \quad m = s, s+1
 \end{aligned} \tag{C1}$$

The coefficients $A_1, A_2, \dots, \bar{C}_1, \bar{C}_2$ are given in Appendix A. At the upper side of the interface (layer s), we have the displacements

$$\begin{aligned}
 u_s' &= \bar{a}_1 \phi_s^u + \bar{a}_2 \psi_s^u \\
 v_s' &= \bar{a}_3 \psi_s^u \\
 w_s' &= \bar{a}_4 \phi_s^u + \bar{a}_5 \psi_s^u
 \end{aligned} \tag{C2.1}$$

and the stresses

$$\begin{aligned}
 S_{z'z'}^{(s)} &= \bar{b}_1 \phi_s^u + \bar{b}_2 \psi_s^u \\
 S_{x'z'}^{(s)} &= \bar{b}_3 \phi_s^u + \bar{b}_4 \psi_s^u \\
 S_{y'z'}^{(s)} &= \bar{b}_5 V_s^u \\
 S_{x'x'}^{(s)} &= \bar{b}_6 \phi_s^u + \bar{b}_7 \psi_s^u \\
 S_{x'y'}^{(s)} &= \bar{b}_8 V_s^u \\
 S_{y'y'}^{(s)} &= \bar{b}_9 \phi_s^u + \bar{b}_{10} \psi_s^u
 \end{aligned} \tag{C2.2}$$

where

$$\begin{aligned}
 \bar{a}_1 &= i\kappa (\bar{B}_1 e^{i\rho_s} + e^{-i\rho_s}) - i\gamma_s' \bar{C}_1 e^{i\vartheta_s} \\
 \bar{a}_2 &= i\kappa \bar{C}_2 e^{i\rho_s} - i\gamma_s' (\bar{B}_2 e^{i\vartheta_s} - e^{-i\vartheta_s}) \\
 \bar{a}_3 &= \bar{B}_3 e^{i\vartheta_s} + e^{-i\vartheta_s} \\
 \bar{a}_4 &= i\gamma_s' (\bar{B}_1 e^{i\rho_s} - e^{-i\rho_s}) + i\kappa \bar{C}_1 e^{i\vartheta_s} \\
 \bar{a}_5 &= i\gamma_s' \bar{C}_2 e^{i\rho_s} + i\kappa (\bar{B}_2 e^{i\vartheta_s} + e^{-i\vartheta_s})
 \end{aligned} \tag{C3.1}$$

and

$$\begin{aligned}
 \bar{b}_1 &= \mu_s [f_s (\bar{B}_1 e^{i\rho_s} + e^{-i\rho_s}) - 2\kappa\gamma_s' \bar{C}_1 e^{i\vartheta_s}] \\
 \bar{b}_2 &= \mu_s [f_s \bar{C}_2 e^{i\rho_s} - 2\kappa\gamma_s' (\bar{B}_2 e^{i\vartheta_s} - e^{-i\vartheta_s})] \\
 \bar{b}_3 &= -\mu_s [2\kappa\gamma_s' (\bar{B}_1 e^{i\rho_s} - e^{-i\rho_s}) + f_s \bar{C}_1 e^{i\vartheta_s}] \\
 \bar{b}_4 &= -\mu_s [2\kappa\gamma_s' \bar{C}_2 e^{i\rho_s} + f_s (\bar{B}_2 e^{i\vartheta_s} + e^{-i\vartheta_s})] \\
 \bar{b}_5 &= \mu_s i\gamma_s' (\bar{B}_3 e^{i\vartheta_s} - e^{-i\vartheta_s}) \\
 \bar{b}_6 &= \mu_s [(2k_{\alpha_s}^2 - k_{\beta_s}^2 - 2\kappa^2) (\bar{B}_1 e^{i\rho_s} + e^{-i\rho_s}) + 2\kappa\gamma_s' \bar{C}_1 e^{i\vartheta_s}] \\
 \bar{b}_7 &= \mu_s [(2k_{\alpha_s}^2 - k_{\beta_s}^2 - 2\kappa^2) \bar{C}_2 e^{i\rho_s} + 2\kappa\gamma_s' (\bar{B}_2 e^{i\vartheta_s} - e^{-i\vartheta_s})] \\
 \bar{b}_8 &= \mu_s i\kappa (\bar{B}_3 e^{i\vartheta_s} + e^{-i\vartheta_s}) \\
 \bar{b}_9 &= \mu_s (2k_{\alpha_s}^2 - k_{\beta_s}^2) (\bar{B}_1 e^{i\rho_s} + e^{-i\rho_s}) \\
 \bar{b}_{10} &= \mu_s (2k_{\alpha_s}^2 - k_{\beta_s}^2) \bar{C}_2 e^{i\rho_s}
 \end{aligned} \tag{C3.2}$$

At the lower side of the interface, in layer $s+1$, we have

$$\begin{aligned} u'_{s+1} &= u'^* \delta(k-k_0) + a_1 \phi_{s+1}^d + a_2 \psi_{s+1}^d \\ v'_{s+1} &= v'^* \delta(k-k_0) + a_3 \psi_{s+1}^d \\ w'_{s+1} &= w'^* \delta(k-k_0) + a_4 \phi_{s+1}^d + a_5 \psi_{s+1}^d \end{aligned} \quad (C4.1)$$

and

$$\begin{aligned} S_{z'z'}^{(s+1)} &= S_{z'z'}^* \delta(k-k_0) + b_1 \phi_{s+1}^d + b_2 \psi_{s+1}^d \\ S_{x'z'}^{(s+1)} &= S_{x'z'}^* \delta(k-k_0) + b_3 \phi_{s+1}^d + b_4 \psi_{s+1}^d \\ S_{y'z'}^{(s+1)} &= S_{y'z'}^* \delta(k-k_0) + b_5 \psi_{s+1}^d \\ S_{x'x'}^{(s+1)} &= S_{x'x'}^* \delta(k-k_0) + b_6 \phi_{s+1}^d + b_7 \psi_{s+1}^d \\ S_{x'y'}^{(s+1)} &= S_{x'y'}^* \delta(k-k_0) + b_8 \psi_{s+1}^d \\ S_{y'y'}^{(s+1)} &= S_{y'y'}^* \delta(k-k_0) + b_9 \phi_{s+1}^d + b_{10} \psi_{s+1}^d \end{aligned} \quad (C4.2)$$

where

$$\begin{aligned} a_1 &= i\kappa (e^{ip_{s+1}} + B_1 e^{-ip_{s+1}}) + i\gamma'_{s+1} C_1 e^{-iq_{s+1}} \\ a_2 &= i\kappa C_2 e^{-ip_{s+1}} - i\gamma'_{s+1} (e^{iq_{s+1}} - B_2 e^{-iq_{s+1}}) \\ a_3 &= e^{iq_{s+1}} + B_3 e^{-iq_{s+1}} \\ a_4 &= i\gamma'_{s+1} (e^{ip_{s+1}} - B_1 e^{-ip_{s+1}}) + i\kappa C_1 e^{-iq_{s+1}} \\ a_5 &= -i\gamma'_{s+1} C_2 e^{-ip_{s+1}} + i\kappa (e^{iq_{s+1}} + B_2 e^{-iq_{s+1}}) \end{aligned} \quad (C5.1)$$

and

$$\begin{aligned} b_1 &= \mu_{s+1} [f_{s+1} (e^{ip_{s+1}} + B_1 e^{-ip_{s+1}}) + 2\kappa \gamma'_{s+1} C_1 e^{-iq_{s+1}}] \\ b_2 &= \mu_{s+1} [f_{s+1} C_2 e^{-ip_{s+1}} - 2\kappa \gamma'_{s+1} (e^{iq_{s+1}} - B_2 e^{-iq_{s+1}})] \\ b_3 &= -\mu_{s+1} [2\kappa \gamma'_{s+1} (e^{ip_{s+1}} - B_1 e^{-ip_{s+1}}) + f_{s+1} C_1 e^{-iq_{s+1}}] \\ b_4 &= \mu_{s+1} [2\kappa \gamma'_{s+1} C_2 e^{-ip_{s+1}} - f_{s+1} (e^{iq_{s+1}} + B_2 e^{-iq_{s+1}})] \\ b_5 &= \mu_{s+1} i\gamma'_{s+1} (e^{iq_{s+1}} - B_3 e^{-iq_{s+1}}) \end{aligned} \quad (C5.2)$$

$$\begin{aligned}
b_6 &= \mu_{s+1} [(2k_{\alpha_{s+1}}^2 - k_{\beta_{s+1}}^2 - 2\kappa^2)(e^{i\rho_{s+1}} + B_1 e^{-i\rho_{s+1}}) - 2\kappa\gamma'_{s+1} C_1 e^{-i\vartheta_{s+1}}] \\
b_7 &= \mu_{s+1} [(2k_{\alpha_{s+1}}^2 - k_{\beta_{s+1}}^2 - 2\kappa^2) C_2 e^{-i\rho_{s+1}} + 2\kappa\gamma'_{s+1} (e^{i\vartheta_{s+1}} - B_2 e^{-i\vartheta_{s+1}})] \\
b_8 &= \mu_{s+1} i\kappa (e^{i\vartheta_{s+1}} + B_3 e^{-i\vartheta_{s+1}}) \\
b_9 &= \mu_{s+1} (2k_{\alpha_{s+1}}^2 - k_{\beta_{s+1}}^2) (e^{i\rho_{s+1}} + B_1 e^{-i\rho_{s+1}}) \\
b_{10} &= \mu_{s+1} (2k_{\alpha_{s+1}}^2 - k_{\beta_{s+1}}^2) C_2 e^{-i\rho_{s+1}}
\end{aligned} \tag{C5.2}$$

The source terms in (C4.1) and C4.2) are

$$\begin{aligned}
u^{*\prime} &= i\kappa A_1 e^{-i\rho_{s+1}} + i\gamma'_{s+1} A_2 e^{-i\vartheta_{s+1}} \\
v^{*\prime} &= A_3 e^{-i\vartheta_{s+1}} \\
w^{*\prime} &= -i\gamma'_{s+1} A_1 e^{-i\rho_{s+1}} + i\kappa A_2 e^{-i\vartheta_{s+1}}
\end{aligned} \tag{C6}$$

and

$$\begin{aligned}
S_{z'z'}^* &= \mu_{s+1} [f_{s+1} A_1 e^{-i\rho_{s+1}} + 2\kappa\gamma'_{s+1} A_2 e^{-i\vartheta_{s+1}}] \\
S_{x'z'}^* &= \mu_{s+1} [2\kappa\gamma'_{s+1} A_1 e^{-i\rho_{s+1}} - f_{s+1} A_2 e^{-i\vartheta_{s+1}}] \\
S_{y'z'}^* &= -\mu_{s+1} i\gamma'_{s+1} A_3 e^{-i\vartheta_{s+1}} \\
S_{x'x'}^* &= \mu_{s+1} [(2k_{\alpha_{s+1}}^2 - k_{\beta_{s+1}}^2 - 2\kappa^2) A_1 e^{-i\rho_{s+1}} - 2\kappa\gamma'_{s+1} A_2 e^{-i\vartheta_{s+1}}] \\
S_{x'y'}^* &= \mu_{s+1} i\kappa A_3 e^{-i\vartheta_{s+1}} \\
S_{y'y'}^* &= \mu_{s+1} (2k_{\alpha_{s+1}}^2 - k_{\beta_{s+1}}^2) A_1 e^{-i\rho_{s+1}}
\end{aligned} \tag{C7}$$

Next, we make the transformation from the propagation coordinates (x', y', z') basis to the standard coordinates (x, y, z) basis. Using (2.31), (2.32), and (2.33), we have

$$\begin{aligned}
u &= u' \cos \Omega - v' \sin \Omega \\
v &= u' \sin \Omega + v' \cos \Omega \\
w &= w'
\end{aligned} \tag{C8}$$

and

$$\begin{aligned}
S_{zz} &= S_{z'z'} \\
S_{xz} &= S_{x'z'} \cos \Omega - S_{y'z'} \sin \Omega \\
S_{yz} &= S_{x'z'} \sin \Omega + S_{y'z'} \cos \Omega \\
S_{xx} &= S_{x'x'} \cos^2 \Omega - S_{x'y'} \sin 2\Omega + S_{y'y'} \sin^2 \Omega \\
S_{xy} &= \frac{1}{2} S_{x'x'} \sin 2\Omega + S_{x'y'} \cos 2\Omega - \frac{1}{2} S_{y'y'} \sin 2\Omega \\
S_{yy} &= S_{x'x'} \sin^2 \Omega + S_{x'y'} \sin 2\Omega + S_{y'y'} \cos^2 \Omega
\end{aligned} \tag{C9}$$

The layer index has been suppressed in these equations. These expressions apply separately to the components of stress and displacement in each medium and to the source terms. Also, we note that

$$\begin{aligned}
\cos \Omega &= k / \kappa \\
\sin \Omega &= \eta_0 / \kappa \\
\kappa &= (k^2 + \eta_0^2)^{1/2}
\end{aligned} \tag{C10}$$

Now, we postmultiply the stress tensors $\underline{S}_s(\underline{r}_s, \omega, k)$ and $\underline{S}_{s+1}(\underline{r}_s, \omega, k)$ by \underline{n}_s to obtain the stress vectors $\underline{T}_s(\underline{r}_s, \omega, k)$ and $\underline{T}_{s+1}(\underline{r}_s, \omega, k)$ acting on the interface s (equation (2.35)). The three components of stress on the interface are

$$\begin{aligned}
t_z &= -S_{xz} \sin \gamma + S_{zz} \cos \gamma \\
t_x &= -S_{xx} \sin \gamma + S_{xz} \cos \gamma \\
t_y &= -S_{xy} \sin \gamma + S_{yz} \cos \gamma
\end{aligned} \tag{C11}$$

where (C11) holds separately for stresses in either layer and for the source term stresses. In (C11), γ is the local interface dip angle; that is

$$\tan \gamma = \frac{d \xi_s'(x)}{dx} = \xi_s'(x)$$

so that

$$\begin{aligned} \sin \gamma &= \xi_s'(x) [1 + (\xi_s'(x))^2]^{-1/2} \\ \cos \gamma &= [1 + (\xi_s'(x))^2]^{-1/2} \end{aligned} \quad (C12)$$

Equations (C2) through (C11) provide the details required for writing the integral equation boundary conditions implied in (2.34). For example, consider the requirement of continuity of the x-component of displacement

$$\hat{u}_s(r_s, \omega) - \hat{u}_{s+1}(r_s, \omega) = 0$$

By (2.32), (C2), and (C4), this is

$$\begin{aligned} \int_{-\infty}^{\infty} [(u_s' - u_{s+1}') \cos \Omega - (v_s' - v_{s+1}') \sin \Omega] dk &= \int_{-\infty}^{\infty} [\bar{a}_1 \cos \Omega \phi_s^u + \bar{a}_2 \cos \Omega \psi_s^u \\ &- a_1 \cos \Omega \phi_{s+1}^d - a_2 \cos \Omega \psi_{s+1}^d - \bar{a}_3 \sin \Omega v_s^u + a_3 \sin \Omega v_{s+1}^d \\ &- (u^* \cos \Omega - v^* \sin \Omega) \delta(k - k_0)] e^{ikx + i\eta_0 y} dk = 0 \end{aligned} \quad (C13)$$

In (C13), we have restored the factor $e^{ikx + i\eta_0 y}$. Using the sifting property of the Dirac delta function, we can integrate the source contribution integral. Finally, we write the equation with source terms on the right

$$\begin{aligned} \int_{-\infty}^{\infty} [f_{11}(\kappa, x) \phi_s^u + f_{12}(\kappa, x) \phi_{s+1}^d + f_{13}(\kappa, x) \psi_s^u + f_{14}(\kappa, x) \psi_{s+1}^d \\ + f_{15}(\kappa, x) v_s^u + f_{16}(\kappa, x) v_{s+1}^d] e^{ikx} dk = h_1(\kappa_0, x) e^{ik_0 x} \end{aligned} \quad (C14)$$

The $f_{ij}(\kappa, x)$ and $h_i(\kappa_0, x)$ are given later in (C17) and (C18). We see that one boundary condition requirement (C13) at the irregular interface yields a single integral equation for the six wave amplitudes ϕ_s^u , ϕ_{s+1}^d , ψ_s^u , ψ_{s+1}^d , v_s^u , and v_{s+1}^d . Imposing the five other interface conditions yields five more coupled integral equations of this form. We write these equations as the single matrix integral equation

$$\int_{-\infty}^{\infty} \underline{\underline{F}}(\kappa, x) \underline{C}_s(\kappa) e^{ikx} dk = \underline{H}(\kappa_0, x) e^{ik_0 x} \quad (C15)$$

where $\underline{\underline{F}}$ is a 6x6 matrix whose elements are $f_{ij}(\kappa, x)$. $\underline{C}_s(\kappa)$ is 6x1 matrix of the amplitudes of the waves leaving the interface

$$\underline{C}_s = \begin{pmatrix} \phi_s^u \\ \phi_{s+1}^d \\ \psi_s^u \\ \psi_{s+1}^d \\ v_s^u \\ v_{s+1}^d \end{pmatrix} \quad (C16)$$

and $\underline{H}(\kappa_0, x)$ is the 6x1 matrix of source terms $h_i(\kappa_0, x)$ given by

$$h_1 = u'^* \cos \Omega_0 - v'^* \sin \Omega_0$$

$$h_2 = w'^*$$

$$h_3 = -(S_{x'z'}^* \cos \Omega_0 - S_{y'z'}^* \sin \Omega_0) \sin \gamma + S_{z'z'}^* \cos \gamma \quad (C17)$$

$$h_4 = -(S_{x'y'}^* \cos^2 \Omega_0 - S_{x'y'}^* \sin^2 \Omega_0 + S_{y'y'}^* \sin^2 \Omega_0) \sin \gamma + (S_{x'z'}^* \cos \Omega_0 - S_{y'z'}^* \sin \Omega_0) \cos \gamma$$

$$h_5 = u'^* \sin \Omega_0 + v'^* \cos \Omega_0$$

$$h_6 = \left(\frac{1}{2} S_{x'x'}^* \sin 2\Omega_0 + S_{x'y'}^* \cos 2\Omega_0 - \frac{1}{2} S_{y'y'}^* \sin 2\Omega_0\right) \sin \gamma + (S_{x'z'}^* \sin \Omega_0 + S_{y'z'}^* \cos \Omega_0) \cos \gamma$$

The six equations in (C15) correspond, in order, to continuity of the x- and z-components of displacement, the z- and x-components of stress across the interface, and the y-components of displacement and stress. The 36 elements of the $\underline{\underline{J}}$ matrix are expressed here in terms of the coefficients a_j , \bar{a}_j , b_j , and \bar{b}_j given in equations (C3.1), (C3.2), (C5.1), and (C5.2).

$$\begin{array}{ll}
 f_{11} = \bar{a}_1 \cos \Omega & f_{21} = \bar{a}_4 \\
 f_{12} = -a_1 \cos \Omega & f_{22} = -a_4 \\
 f_{13} = \bar{a}_2 \cos \Omega & f_{23} = \bar{a}_5 \\
 f_{14} = -a_2 \cos \Omega & f_{24} = a_5 \\
 f_{15} = -\bar{a}_3 \sin \Omega & f_{25} = 0 \\
 f_{16} = a_3 \sin \Omega & f_{26} = 0
 \end{array}$$

$$\begin{array}{l}
 f_{31} = -\bar{b}_3 \cos \Omega \sin \Upsilon + \bar{b}_1 \cos \Upsilon \\
 f_{32} = b_3 \cos \Omega \sin \Upsilon - b_1 \cos \Upsilon \\
 f_{33} = -\bar{b}_4 \cos \Omega \sin \Upsilon + \bar{b}_2 \cos \Upsilon \\
 f_{34} = b_4 \cos \Omega \sin \Upsilon - b_2 \cos \Upsilon \\
 f_{35} = \bar{b}_5 \sin \Omega \sin \Upsilon \\
 f_{36} = -b_5 \sin \Omega \sin \Upsilon
 \end{array}$$

(C18)

$$f_{41} = -(\bar{b}_6 \cos^2 \Omega + \bar{b}_9 \sin^2 \Omega) \sin \Upsilon + \bar{b}_3 \cos \Omega \cos \Upsilon$$

$$f_{42} = (b_6 \cos^2 \Omega + b_9 \sin^2 \Omega) \sin \Upsilon - b_3 \cos \Omega \cos \Upsilon$$

$$f_{43} = -(\bar{b}_7 \cos^2 \Omega + \bar{b}_{10} \sin^2 \Omega) \sin \Upsilon + \bar{b}_4 \cos \Omega \cos \Upsilon$$

$$f_{44} = (b_7 \cos^2 \Omega + b_{10} \sin^2 \Omega) \sin \Upsilon - b_4 \cos \Omega \cos \Upsilon$$

$$f_{45} = 2 \bar{b}_8 \sin \Omega \cos \Omega \sin \Upsilon - \bar{b}_5 \sin \Omega \cos \Upsilon$$

$$f_{46} = -2 b_8 \sin \Omega \cos \Omega \sin \Upsilon + b_5 \sin \Omega \cos \Upsilon$$

$$f_{51} = \bar{a}_1 \sin \Omega$$

$$f_{52} = -a_1 \sin \Omega$$

$$f_{53} = \bar{a}_2 \sin \Omega$$

$$f_{54} = -a_2 \sin \Omega$$

$$f_{55} = \bar{a}_3 \cos \Omega$$

$$f_{56} = -a_3 \cos \Omega$$

(C18)

$$f_{61} = (\bar{b}_9 - \bar{b}_6) \sin \Omega \cos \Omega \sin \Upsilon + \bar{b}_3 \sin \Omega \cos \Upsilon$$

$$f_{62} = -(b_9 - b_6) \sin \Omega \cos \Omega \sin \Upsilon - b_3 \sin \Omega \cos \Upsilon$$

$$f_{63} = -(\bar{b}_7 - \bar{b}_{10}) \sin \Omega \cos \Omega \sin \Upsilon + \bar{b}_4 \sin \Omega \cos \Upsilon$$

$$f_{64} = (b_7 - b_{10}) \sin \Omega \cos \Omega \sin \Upsilon - b_4 \sin \Omega \cos \Upsilon$$

$$f_{65} = -\bar{b}_8 \cos 2\Omega \sin \Upsilon + \bar{b}_5 \cos \Omega \cos \Upsilon$$

$$f_{66} = b_8 \cos 2\Omega \sin \Upsilon - b_5 \cos \Omega \cos \Upsilon$$

APPENDIX D

REPRESENTATION THEOREMS FOR USE IN ERROR ESTIMATES

The residual discontinuities in stress and displacement at the irregular interfaces provide one measure of the accuracy of our technique; however, the errors of most interest are those in the displacements at the observation positions (usually along the free surface). Using an appropriate representation theorem, we should be able to compute the errors exactly in terms of the residuals at the interfaces and thereby correct the approximate solutions to obtain exact solutions. Indeed, in the method of Banaugh (1962) an exact solution is formulated initially in terms of such a representation theorem. However, just as the Banaugh method can be complicated for the type of scattering problems that we consider, the exact use of the representation theorem approach to correct our solutions can be exceedingly more involved than is our approximate method. This will become evident below. In this appendix, we look at the form that the representation theorem takes in the most simple problems in order to understand qualitatively how errors in displacement at the free surface are related to errors in displacement and stress at interfaces.

First consider the two-dimensional scattering problem of harmonic SH wave motion in a layer over a half-space (see Figure 2.3). The exact solution displacement field $V_1(x,z)$ in the layer satisfies the scalar Helmholtz equation, and can be written in terms of the Kirchhoff integral solution

$$v_i(x, z) = \int_S \mu_1 \left[G(x, z; x', z') \frac{\partial v_i(x', z')}{\partial n} - v_i(x', z') \frac{\partial G(x, z; x', z')}{\partial n} \right] dS \quad (D1)$$

The variables x' and z' are coordinates on the line boundary S consisting of the free surface $z=0$, the interface $z = \zeta(x)$, and verticals at $x = \pm \infty$ connecting the free surface and interface; μ_1 is rigidity; and $\frac{\partial}{\partial n}$ is the spatial derivative in the outward normal direction to S . The function G satisfies the inhomogeneous wave equation

$$\mu_1 \nabla^2 G + \rho_1 \omega^2 G = -\delta(x-x') \delta(z-z') \quad (D2)$$

throughout the region \mathcal{R} bounded by S . Here, $\rho_1(x)$ is the mass density and $\delta(x)$ is the Dirac delta function.

Our approximate solution $v_{i,N}$ also satisfies the scalar Helmholtz equation within the layer. Therefore the difference or error, $\Delta v_{i,N} = v_{i,N} - v_i$, must satisfy (D1). By assuming that a small amount of attenuation exists within the layer, we can neglect the contributions to motion from sources along the vertical lines at infinity. We now define the Green's function G to be that solution to (D2) whose normal derivative vanishes along the plane free surface. The stress-free requirement at the free surface was imposed upon both the exact and approximate solutions to our problem and, hence, upon the difference $\Delta v_{i,N}$. With our choice for the Green's function, the free surface contribution to the Kirchhoff integral is zero; therefore, the error in surface motion is expressed in terms of the errors in displacement and stress along the interface as

$$\Delta v_{,n}(x,0) = \int_{z=\xi(x')} [G(x,0;x',\xi) \Delta T_{,n}(x',\xi) - \Delta v_{,n}(x',\xi) \tau_G(x,0;x',\xi)] dS \quad (D3)$$

where $\Delta T_{,n}(x',\xi) = \mu_1 \left[\frac{\partial v_{,n}(x',\xi)}{\partial n} - \frac{\partial v_{,n}(x',\xi)}{\partial n} \right]$ is the error in the y component of stress along the interface and

$$\tau_G(x,0;x',\xi) = \mu_1 \frac{\partial G(x,0;x',\xi)}{\partial n}$$

The Green's function that satisfies (D2), the free surface condition, and the radiation condition consistent with $e^{-i\omega t}$ time dependence is given by

$$G(x,z;x',z') = \frac{i}{4\mu_1} \left[H_0^{(1)}\left(\frac{\omega R}{\beta_1}\right) + H_0^{(1)}\left(\frac{\omega R'}{\beta_1}\right) \right] \quad (D4)$$

where $R = [(x-x')^2 + (z-z')^2]^{1/2}$

$$R' = [(x-x')^2 + (z+z')^2]^{1/2}$$

$H_0^{(1)}$ is the zero order Hankel function of the first kind. Along the free surface, $z=0$, this becomes

$$G(x,0;x',\xi) = \frac{i}{2\mu_1} H_0^{(1)}\left(\frac{\omega r}{\beta_1}\right)$$

where $r = [(x-x')^2 + \xi^2]^{1/2}$.

By using (D3), we could compute the exact free surface motion provided that we knew the errors in stress and displacement at the free surface. However, we do not know these errors; instead, we know only the differences (residuals) between the approximate solutions in the layer and in the half-space. We could use these residuals to obtain the exact solution if, in the representation theorem, we let the enclosed region consist of both the

layer and half-space and treated the correction field as the solution to a saltus problem (Burridge and Knopoff, 1964). However, the Green's function in the saltus problem would be the displacement, in a layer of nonuniform thickness over a half-space, caused by point source along the irregular boundary. The determination of the Green's function (which varies with source position in a complicated way), would be an exceedingly more difficult task than that in our approximate method of solution.

Our goal here is the more modest one of estimating the effects of residuals upon computed motion at the free surface. The residuals are just the differences between the real errors (at the interface) in the layer and in the half-space. That is, at the interface

$$\begin{aligned}\tilde{V} &= V_{1N} - V_{2N} = \Delta V_{1N} - \Delta V_{2N} \\ \tilde{T} &= T_{1N} - T_{2N} = \Delta T_{1N} - \Delta T_{2N}\end{aligned}\tag{D5}$$

where \tilde{V} and \tilde{T} are the displacement and stress residuals, respectively; and ΔV_{2N} and ΔT_{2N} are the real errors in the half-space at the interface. In order to make a low order estimate of the error in free surface motion, we shall assume that the residuals are comparable to the actual errors at the interface. That is, at the interface,

$$\tilde{V} \simeq \Delta V_{1N}$$

$$\tilde{T} \simeq \Delta T_{1N}$$

Using \tilde{V} and \tilde{T} as sources in (D3) yields the estimated error in displacement at the free surface

$$U_{\epsilon}(x, 0) = \frac{i}{2} \int_{z'=\zeta(x')} \left[\left(\frac{\tilde{\tau}}{\mu_1} \right) H_0^{(i)} \left(\frac{\omega r}{\beta_1} \right) + \left(\frac{\omega \tilde{v}}{\beta_1} \right) \cos(\phi - \gamma) H_1^{(i)} \left(\frac{\omega r}{\beta_1} \right) \right] dS \quad (D6)$$

where γ = dip angle at the interface

$$\phi = \tan^{-1} \left(\frac{x - x'}{\zeta(x')} \right)$$

$H_1^{(i)}$ is the first order Hankel function of the first kind. Without actually evaluating (D6), we can now discuss the relative influence of the dimensionless residuals $\tilde{\tau}/\mu_1$ and $\omega \tilde{v}/\beta_1$, upon motion at the free surface. The Hankel functions are decreasing oscillatory functions of their arguments. The rates of decrease are largest for small arguments; moreover, $H_1^{(i)}(x)$ dominates $H_0^{(i)}(x)$ for small values of x . Hence, for example, in the case of a shallow depth of interface ($\omega \zeta/\beta_1 \ll 1$), the surface motion is determined primarily by displacements at positions on the interface nearest to the observation point. The rates of decrease of the Hankel functions with increasing absolute values of their arguments are greater when frequency is complex. Thus, when ω is complex, we expect localized residuals to yield errors that decrease rapidly with distance from the interface.

The quantities μ_1 and ω/β_1 , by which the stress and displacement residuals are normalized in (D6) provide a means for comparing the root-mean-square errors (RMSE-see equations (4.1) through (4.5)) in stress with those in displacement. We multiply the interface stresses by $\beta_1/\mu_1 \omega = 1/\rho_1 \beta_1 \omega$ to obtain their values in terms of 'equivalent displacements'. Although the conversion factor is a crude one with no meaning beyond that implied in (D6), it enables us to obtain, in each practical problem, a single RMSE

by weighting the stress RMSE and displacement RMSE according to the mean amplitudes of stress and displacement at the irregular interface.

For convenience, we use the same conversion factor in more complicated problems. If the medium were multi-layered, the representation theorem integral (D3) would be replaced by integrals along each irregular interface, and the Green's functions would be much more complicated than Hankel functions. An alternative conversion factor might be $1/\rho_s \beta_s \omega$, where ρ_s and β_s are the density and S wave speed in the layer just above irregular interface s . The choice $1/\rho_s \beta_s \omega$ is generally a more conservative one because density and wave speeds are usually lowest in the uppermost layer so that the stress RMSE is weighted more heavily than the (usually smaller) displacement RMSE in computing the single measure of error.

For the single layer over half-space problems involving arbitrary azimuth incidence direction relative to the strike of the irregular interface, the representation theorem analog of the Kirchhoff integral is the Somigliana formula (Ben-Menahem and Singh, 1968)

$$\underline{U}_i(\underline{r}) = \oint_{\Sigma} \left\{ \underline{G}(\underline{r}; \underline{r}') \cdot [\underline{S}_i(\underline{r}') \cdot \underline{e}_n] - [\underline{S}_{iG}(\underline{r}; \underline{r}') \cdot \underline{e}_n] \cdot \underline{U}_i(\underline{r}') \right\} d\underline{r}' \quad (D7)$$

where $\underline{U}_i(\underline{r})$ is the vector displacement field at space position \underline{r} within a volume of medium 1 (the layer) bounded by the surface Σ ; \underline{e}_n is the unit vector outward normal to Σ ; $\underline{G}(\underline{r}; \underline{r}_0)$ is the Somigliani tensor, which satisfies

$$\mu_i \nabla \cdot (\nabla \underline{G}) + (\lambda_i + \mu_i) \nabla (\nabla \cdot \underline{G}) + \rho_i \omega^2 \underline{G} = -\frac{1}{4\pi} \underline{1}_3 \delta(\underline{r} - \underline{r}_0) \quad (D8)$$

where λ_1 is the Lamé constant and $\underline{\underline{1}}_3$ is the idemfactor; $(\underline{\underline{S}}_1(\underline{r}') \cdot \underline{e}_n)$ is the stress acting on Σ ; and $\underline{\underline{S}}_G(\underline{r}; \underline{r}')$ is a triad or tensor of the third rank. Let x, y, z be interchangeable with x_1, x_2, x_3 respectively. Using indicial notation, the elements of $\underline{\underline{G}}$ are $g_k^m(\underline{r}; \underline{r}_0)$, representing the displacement component in the Cartesian direction x_k at position \underline{r} due to a localized displacement in the direction x_m at position \underline{r}_0 . The triad $\underline{\underline{S}}_G(\underline{r}; \underline{r}_0)$ has components

$$S_{kj}^m = \lambda_1 \delta_{kj} \frac{\partial g_n^m}{\partial x_n} + \mu_1 \left(\frac{\partial g_k^m}{\partial x_j} + \frac{\partial g_j^m}{\partial x_k} \right)$$

where the summation convention for the repeated index n is used and δ_{kj} is the Kronecker delta function.

Proceeding as in the SH wave motion example, we define the Somigliani tensor (or Green's function) $\underline{\underline{G}}$ to be that solution to (D8) which satisfies the stress-free condition $\underline{\underline{S}}_G(x, y, 0; \underline{r}_0) \cdot \underline{e}_n = 0$ at the plane free surface. Then, since the stress must vanish at the free surface in the exact solution, the displacement field at the free surface can be written in terms of displacements and stresses at the interface $z = \zeta_s(x)$

$$\underline{U}_1(x, y, 0) = \int_{-\infty}^{\infty} dy' \int_{\zeta' = \zeta_s(x')} \left\{ \underline{\underline{G}} \cdot [\underline{\underline{S}}_1 \cdot \underline{e}_n] - [\underline{\underline{S}}_G \cdot \underline{e}_n] \cdot \underline{U}_1 \right\} d\sigma \quad (D9)$$

where we neglect the surface integral contributions along vertical planes at $y = \pm\infty$ and $x = \pm\infty$. The displacement field $\underline{U}_1(\underline{r})$ and stress field $\underline{\underline{S}}_1(\underline{r})$ both depend on y through the common factor $e^{i\eta_0 y}$ where η_0 is the y -component of source wave number (see section 2.3.2). We can perform the integration over y' to arrive at the line integral

$$\underline{U}'_i(x, 0) = \int_{z'=\xi_s(x')} \left\{ \underline{G}'_i \cdot [\underline{S}'_i \cdot \underline{e}_n] - [\underline{S}'_{G_i} \cdot \underline{e}_n] \cdot \underline{U}'_i \right\} d\sigma \quad (D10)$$

where

$$\underline{U}_i(x, y, z) = \underline{U}'_i(x, z) e^{i\eta_0 y}$$

$$\underline{S}_i(x, y, z) = \underline{S}'_i(x, z) e^{i\eta_0 y}$$

$$\underline{G}'_i(x, z; x', z') e^{i\eta_0 y} = \int_{-\infty}^{\infty} \underline{G}_i(\underline{r}; \underline{r}') e^{i\eta_0 y'} dy'$$

$$\underline{S}'_{G_i}(x, z; x', z') e^{i\eta_0 y} = \int_{-\infty}^{\infty} \underline{S}_{G_i}(\underline{r}; \underline{r}') e^{i\eta_0 y'} dy'$$

Our approximate solution satisfies the Somigliana formula and an equation similar to (D10). Hence, the difference between our solution and the exact solution is found to satisfy

$$\begin{aligned} \Delta \underline{U}'_{iN}(x, 0) = \underline{U}'_{iN} - \underline{U}'_i = \int_{z'=\xi_s(x')} \left\{ \underline{G}'_i(x, 0; x', \xi_s) \cdot [\Delta \underline{S}'_{iN}(x', \xi_s) \cdot \underline{e}_n] \right. \\ \left. - [\underline{S}'_{G_i}(x, 0; x', \xi_s) \cdot \underline{e}_n] \cdot \Delta \underline{U}'_{iN}(x', \xi_s) \right\} d\sigma \end{aligned} \quad (D11)$$

where

$$\Delta \underline{S}'_{iN} = \underline{S}'_{iN}(\underline{U}_{iN}) - \underline{S}'_i(\underline{U}_i)$$

The line integral (D11) is the extension of result (D3) to the problem of arbitrary azimuth incidence. The error in each component of displacement at the free surface is a line integral of the errors in the three components of stress and of displacement at the irregular interface weighted by the appropriate component of the Green's function \underline{G} and of its related function $\underline{S}_{G_i} \cdot \underline{e}_n$. The difficulty in using (D11) to estimate errors is compounded over that in the comparable SH wave motion case not so much by the vector nature of (D11) as by the form of each component of \underline{G} . For even the two-dimensional

case of P-SV wave motion ($\eta_0=0$) the four pertinent components of \underline{G} are the complicated integrals over the x-component of wave number given by Fredericks (1959).

Because the Green's functions are so complicated, any single RMSE measure of error based on interface residuals is necessarily crude, and its use is justified on the basis of expedience. Taking a clue from the SH wave case and the form of the Green's functions given by Fredericks, we chose the conversion factor $1/\rho, (\alpha, \beta)^{1/2} \omega$ for converting stresses to equivalent displacements. With all interface values in units of displacement, we then weight the six different RMSE at an irregular interface by the mean value of each 'displacement' to obtain the single RMSE measure of accuracy.

APPENDIX E
CONSERVATION OF ENERGY

In this appendix, we derive a relationship among the computed complex wave amplitudes in the lower half-space that can be interpreted in terms of a conservation of energy flux requirement for the exact solution plus a small error term. The error term is shown to be a weighted integral of the residuals at interfaces.

For problems having $e^{-i\omega t}$ time dependence, the particle displacements in each isotropic layer m satisfy the Navier homogeneous equation

$$(\mathcal{L} + \rho\omega^2) \underline{U}(\underline{r}, \omega) = 0 \quad (\text{E1})$$

where $\mathcal{L} = \mu \operatorname{div} \operatorname{grad} + (\lambda + \mu) \operatorname{grad} \operatorname{div}$, the Navier operator; ρ is density; ω is real frequency; \underline{U} is the particle displacement vector with components (u_1, u_2, u_3) ; and \underline{r} is the space position vector with components (x, y, z) . Equation (E1) is the same as (2.20) except that we have deleted the symbol \wedge over the displacement vector and temporarily deleted the layer index m . Let \underline{V} and \underline{W} be two vector fields which satisfy (E1) throughout the volume τ bounded by the surface Σ . These solutions satisfy the Betti identity (Ben-Menahem and Singh, 1968)

$$\oint_{\Sigma} \{ \underline{S}(\underline{V}) \cdot \underline{W} - \underline{S}(\underline{W}) \cdot \underline{V} \} \cdot \underline{e}_n \, d\Sigma = \oint_{\tau} \{ \mathcal{L}(\underline{V}) \cdot \underline{W} - \mathcal{L}(\underline{W}) \cdot \underline{V} \} \, d\tau \quad (\text{E2})$$

where

$$\underline{S}(\underline{V}) = \lambda \underline{1}_3 (\nabla \cdot \underline{V}) + \mu (\nabla \underline{V} + \underline{V} \nabla)$$

is the stress dyad field associated with the displacement field \underline{V} (see equation (2.21)), dots denote single dot products, and \underline{e}_n is the unit outward normal vector to Σ . The right side of (E2) vanishes by virtue of (E1) so that

$$\oint_{\Sigma} \{ \underline{\underline{S}}(\underline{V}) \cdot \underline{W} - \underline{\underline{S}}(\underline{W}) \cdot \underline{V} \} \cdot \underline{e}_n d\Sigma = 0 \quad (\text{E3})$$

Our solution field \underline{U} is a complex quantity. When frequency ω is real, the real and imaginary parts of \underline{U} satisfy (E1) individually. By letting $\underline{U} = \underline{U}' + i \underline{U}''$ where \underline{U}' and \underline{U}'' are real, and choosing $\underline{V} = \underline{U}'$ and $\underline{W} = \underline{U}''$ in (E3) we get

$$\text{Im} \oint_{\Sigma} \{ \underline{\underline{S}}(\underline{U}) \cdot \underline{U}^* \} \cdot \underline{e}_n d\Sigma = 0 \quad (\text{E4})$$

where Im denotes 'imaginary part of' and the asterisk denotes complex conjugate. Using indicial notation with the summation convention for repeated subscripts j , we rewrite (E4) as

$$\text{Im} \oint_{\Sigma} S_{\gamma j} \cdot u_j^* d\Sigma = 0 \quad j = 1, 2, 3 \quad (\text{E5})$$

where $S_{\gamma j}$ is the j component of the stress vector acting on the outside of Σ .

Equation (E5) is the analytic statement of the fact that the time averaged net flux across a surface enclosing a volume containing no sources is zero in this steady-state problem.

Now apply (E5) to each isotropic layer m in the layered half-space problem. We have

$$\begin{aligned} \oint_{\Sigma_m} S_{\nu j}^{(m)} u_j^{(m)*} d\Sigma &= 0 & m=1, 2, \dots, \tilde{n}-1 \\ \oint_{\Sigma_{\tilde{n}}} S_{\nu j}^{(\tilde{n})} u_j^{(\tilde{n})*} d\Sigma &= 0 \end{aligned} \quad (E6)$$

where the surface Σ_m bounds the volume τ_m along the interface $m-1$ above, interface m below, and vertical planes at $x=0$, $x=L$, $y=0$, $y=1$; the surface $\Sigma_{\tilde{n}}$ consists of the interface $\tilde{n}-1$ above, $x=0$, $x=L$, $y=0$, $y=1$ on the sides, and a plane at large depth $z=H$ below. Because the $u_j^{(m)}$ all have the common y -dependence $e^{i\eta_0 y}$, the integrands in (E6) are independent of y . Hence the integrations over the vertical planes $y=0$ and $y=1$ cancel and we may replace the surface integrals in (E6) by line integrals in the x - z planes.

For convenience, let the plane source wave direction be such that L is an integral number of wavelengths in the x -direction. This choice simplifies the integrations while not affecting the results. With this choice, the integrations over the lines $x=0$ and $x=L$ cancel, leaving only line integrals along the interfaces and along the plane at $z=H$. Now redefine $S_{\nu j}^{(m)}$ be the stress acting on the bottom of each bounding interface. Summing the line integral equivalents of (E6) yields

$$\begin{aligned} \int_0^L S_{3j}^{(\tilde{n})} u_j^{(\tilde{n})*} dx + \sum_{m=1}^{\tilde{n}-1} \oint_{\sigma_m} [S_{\nu j}^{(m)} u_j^{(m)*} - S_{\nu j}^{(m+1)} u_j^{(m+1)*}] d\sigma \\ = \oint_{\sigma_0} S_{\nu j}^{(1)} u_j^{(1)*} d\sigma \quad j=1, 2, 3 \end{aligned} \quad (E7)$$

where σ_m denotes interface m , σ_0 is the free surface, and $S_{3j}^{(\tilde{n})}$ are the components of stress acting on a plane $z=\text{constant}$.

In problems involving plane free surfaces we require $S_{\nu j}^{(i)} = 0$ identically, and therefore the right side of (E7) vanishes. When the free surface is irregular, $S_{\nu j}^{(i)}$ are residual errors arising from inexact matching of the stress-free condition along the free surface. Similarly, at all plane interfaces σ_p we require $S_{\nu j}^{(\rho)} = S_{\nu j}^{(\rho+1)}$ and $u_j^{(\rho)} = u_j^{(\rho+1)}$ so that the integrals over plane interfaces vanish in (E7). Thus we may write (E7) as

$$\int_m \int_0^L S_{3j}^{(\tilde{n})} u_j^{(\tilde{n})*} dx = \eta \quad (E8)$$

$z=H$

where

$$\eta = \sum_i \int_{\sigma_i} [S_{\nu j}^{(i+1)} u_j^{(i+1)*} - S_{\nu j}^{(i)} u_j^{(i)*}] d\sigma \quad (E9)$$

In (E9), the summation is over the irregular interfaces only, and $S_{\nu j}^{(0)} = 0$, $u_j^{(0)} = 0$ for the half-space problems.

Equation (E8) is an analytic statement of the conservation of energy requirement in our solutions. The left side integration can be readily evaluated, as we show below. It is the time averaged net flow of energy across the plane at large depth $z=H$. Now let

$$\begin{aligned} \tilde{u}_j^{(i)} &= u_j^{(i+1)} - u_j^{(i)} \\ \tilde{S}_{\nu j}^{(i)} &= S_{\nu j}^{(i+1)} - S_{\nu j}^{(i)} \end{aligned} \quad (E10)$$

be the displacement and stress residuals at interface i . Then (E9) becomes

$$\eta = \sum_i \int_{\sigma_i} \{ S_{\nu j}^{(i)} \tilde{u}_j^{(i)*} + \tilde{S}_{\nu j}^{(i)} u_j^{(i)*} + \tilde{S}_{\nu j}^{(i)} \tilde{u}_j^{(i)*} \} d\sigma \quad (E11)$$

$j=1,2,3$

Thus, η is a sum of integrals of interface stress and displacement residuals weighted by the computed solutions at the irregular interfaces. If our computed solutions were exact the residuals, and hence η , would vanish. Then, by (E8), the conservation of energy requirement for the exact solution is that the time averaged net energy flow across a plane $z=H$ in the lower half-space is zero. Interpreting the residuals as sources and sinks of energy, we conclude that η is the net time averaged energy flow into the medium from artificial sources along the interfaces.

If the interface O were not free but rather bounded an upper half-space O , we would simply include an additional surface integral in that medium. Equation (E8) would be replaced by

$$\int_{z=H}^L S_{3j}^{(\tilde{n})} u_j^{(\tilde{n})*} dx = \int_{z=h}^L S_{3j}^{(o)} u_j^{(o)*} dx + \eta \quad (E12)$$

$j=1,2,3$

where $z=h$ is some large constant height in half-space O .

Let us now evaluate the integral on the left side of (E8). Recall that in our solutions the components of displacement $u_j^{(\tilde{n})}$, $j=1,2,3$ are expressed as superpositions of plane wave displacements each characterized by an x -component of wavenumber k_n . (The notation in Chapter II was $(\hat{u}_n, \hat{v}_n, \hat{w}_n)$ for the displacement components.) Those plane wave contributions are written in terms of P, SV, and SH wave functions (see equation (2.39)). Likewise, the stresses $S_{\nu j}^{(\tilde{n})}$ can be written as superpositions of stresses in plane P, SV, and SH waves. Inserting these

plane wave representations into the integrand of (E8) yields a large complicated quadratic form that includes double summations over the wave number indices m and n . The terms involving regular waves only, have the form

$$(\phi_{\tilde{n},n}^d)^* (\psi_{\tilde{n},m}^d) e^{2\pi i(m-n)x/L + i(\nu_{\tilde{n},m}' - \nu_{\tilde{n},n})z} \quad (\text{E13})$$

where $\phi_{\tilde{n},n}^d$ and $\psi_{\tilde{n},m}^d$ are the complex wave amplitudes of the n th scatter order P waves and m th scatter order SV waves, respectively, downgoing in half-space \tilde{n} ; $\nu_{\tilde{n},m}'$ is the vertical component of wavenumber of the m th scatter order SV wave; and $\nu_{\tilde{n},n}$ is that of the n th scatter order P wave. Other like terms in the quadratic expression involve the SH wave amplitudes $v_{\tilde{n},n}^d$ and source wave amplitudes. Terms involving inhomogeneous waves have factors like $e^{-\Im_m(\nu_{\tilde{n},n})z}$. By taking the depth H to be very large, the inhomogeneous waves are insensible, so that we need sum over regular wave contributions only. The integrand in (E8) is greatly simplified by the orthogonality condition

$$\int_0^L e^{2\pi i(m-n)x/L} dx = \begin{cases} L, & m=n \\ 0, & m \neq n \end{cases}$$

Therefore, of the terms like (E13), the only ones remaining after integration look like

$$(\phi_{\tilde{n},n}^d)^* (\psi_{\tilde{n},n}^d) e^{i(\nu_{\tilde{n},n}' - \nu_{\tilde{n},n})z}$$

But we next find that such cross-product terms appear in complex conjugate pairs. The sums of the conjugate pairs are real quantities which make no contribution to equation (E8). The terms that remain after integrating and

taking the imaginary part involve no cross-products of wave amplitudes.

After these reductions we find that

$$\begin{aligned} \eta = \mu_{\tilde{n}} L \sum_{\tilde{n}} \{ & k_{\beta_{\tilde{n}}}^2 (\nu_{\tilde{n},n} |\phi_{\tilde{n},n}^d|^2 + \nu'_{\tilde{n},n} |\psi_{\tilde{n},n}^d|^2) + \nu'_{\tilde{n},n} |v_{\tilde{n},n}^d|^2 \} \\ & - \mu_{\tilde{n}} L \{ k_{\beta_{\tilde{n}}}^2 (\nu_0 |\phi^*|^2 + \nu'_0 |\psi^*|^2) + \nu'_0 |v^*|^2 \} \end{aligned} \quad (E14)$$

where ϕ^* , ψ^* , v^* are the source wave amplitudes (equation (2.41)), only one of which is nonzero in a given problem; ν_0 , ν'_0 are the vertical components of the source wavenumber; and $k_{\beta_{\tilde{n}}} = \omega/\beta_{\tilde{n}}$. The first term on the right is a summation of the contributions to downward energy flow in each regular plane wave, and the second term is the upward energy flow in the source wave.

Equation (E14) can be rewritten as

$$\frac{\sum_{\tilde{n}} \{ k_{\beta_{\tilde{n}}}^2 (\nu_{\tilde{n},n} |\phi_{\tilde{n},n}^d|^2 + \nu'_{\tilde{n},n} |\psi_{\tilde{n},n}^d|^2) + \nu'_{\tilde{n},n} |v_{\tilde{n},n}^d|^2 \}}{k_{\beta_{\tilde{n}}}^2 (\nu_0 |\phi^*|^2 + \nu'_0 |\psi^*|^2) + \nu'_0 |v^*|^2} = 1 + \delta \quad (E15)$$

with

$$\delta = \frac{\eta}{\mu_{\tilde{n}} L [k_{\beta_{\tilde{n}}}^2 (\nu_0 |\phi^*|^2 + \nu'_0 |\psi^*|^2) + \nu'_0 |v^*|^2]} \quad (E16)$$

In problems involving a solid upper half-space 0, we add to the numerator of (E15) the summation over regular waves in the upper half-space

$$\sum_{\tilde{n}} \{ k_{\beta_0}^2 (\nu_{0,n} |\phi_{0,n}^u|^2 + \nu'_{0,n} |\psi_{0,n}^u|^2) + \nu'_{0,n} |v_{0,n}^u|^2 \}$$

The small quantity δ is the conservation of energy error measure that we list in Table F1 for the problems involving real ω . Whereas small RMS errors in the residuals infer that the integral equations were solved

reasonably accurately, it does not follow that the equations of motion were correctly programmed for computation. Small values of the δ error indicate both that the boundary conditions were well approximated and that the equations of motion were probably written correctly. The δ errors listed in Table F1 are small and, in most instances, sizeable contributions to the energy flux were made by the higher order scattered waves. Thus the δ error measure is not dominated by the energy flux in the primary scattered waves.

We cannot use this error measure when ω is complex. In that case, the real and imaginary parts of \underline{V} do not individually satisfy (E1). Because the source wave is nonstationary, the upward energy flux through the plane $z=H$ is greater than the energy flux returned.

APPENDIX F

TABLE OF ERRORS AND CRITICAL PARAMETERS

The errors for every example presented in Chapters IV and V are listed in Table F1. Each example is tabulated according to the number of the figure (column 1) in which it appeared in the text. Where more than one case is presented in a single figure, the values in the other columns distinguish the cases. The symbol † appearing in column 2 indicates that the errors are presented for a case that was investigated but not plotted in the figure. The symbols in the table have the meanings

$2N+1$ = number of scattered wave orders,

Θ_0 = incidence angle from vertical (positive from lower left),

f = frequency = $\omega_R/2\pi$,

τ = decay time = $1/\omega_I$,

ω_R, ω_I = real and imaginary parts of radial frequency,

c = amplitude of irregularity = $\zeta_{\max} - \zeta_{\min}$,

λ = shortest wavelength in a medium bounded by an irregular interface,

S_M = $\left| \frac{d\zeta}{dx} \right|_{\max}$ = maximum gradient along the interface,

L = basic periodicity length (usually 256 km),

W = typical width of anomaly (see equation 4.7); in the case of a step, W is twice the width of the step,

RMSE = relative root-mean-square error (equations (4.4) and (4.5)); a weighted average of the errors in each type

of interface residual,

δ = conservation-of-energy-flux error measure (equation (4.6)).

TABLE F1

Figure	2N+1	θ_0 (deg)	f (cps)	τ (sec)	c/ λ (km/km)	S_M	L/W	RMSE	δ	Additional Description
4.1	45 53 [†] 79	0 " "	0.07 " "	22.7 " "	5/10 " "	0.31 " "	5.1 " "	0.22 0.12 0.0082	— — —	
4.3	41 17	0 "	0.40 "	9.95 "	5/8.65 "	0.39 "	6.4 "	0.0055 0.068	— —	
4.4	79 61 41 25	40 " " "	0.40 " " "	3.98 " " "	5/7.5 " " "	1.96 " " "	32 " " "	0.039 0.045 0.054 0.071	— — — —	
4.5	65 "	0 "	0.40 "	∞ 39.8	5/7.5 "	0.31 "	5.1 "	0.0019 0.0004	2 10 ⁻⁵ —	
4.6	65 [†] 41 65	55 " "	0.40 " "	∞ 3.98 ∞	5/7.5 " "	0.31 " "	5.1 " "	0.0003 0.011	3 10 ⁻⁶ —	layer over half-space "
4.7	41 41 "	0 " "	0.40 " "	3.98 ∞ 3.98	5/8.65 " "	0.39 " "	6.4 " "	0.0029 0.0084	— 10 ⁻⁶ —	two half-spaces "
4.8	65	0	0.0585	9.95	5/13	0.31	5.1	0.0043	— 10 ⁻⁵ —	
5.1	79 65 41	55 " "	0.8 0.4 0.2	13.32 ∞ "	5/3.75 5/7.5 5/15	0.31 " "	5.1 " "	0.0081 0.0084 0.0034	2 10 ⁻⁶ 2 10 ⁻⁶ 10 ⁻⁶	
5.3	41 53 "	89.9 78 64	0.4 " "	3.98 " "	5/7.5 " "	0.31 " "	5.1 " "	0.021 0.023 0.0075	— — —	

TABLE F1 (cont.)

Figure	2N+1	θ_0 (deg)	f (cps)	τ (sec)	c/ λ (km/km)	S_M	L/W	RMSE	δ	Additional Description
5.3	53	55	0.4	3.98	5/7.5	0.31	5.1	0.0041	—	
	"	48	"	"	"	"	"	0.0031	—	
	"	42	"	"	"	"	"	0.0040	—	
5.4	41	89.9	0.4	3.98	5/7.5	0.31	5.1	0.0061	—	
	53	78	"	"	"	"	"	0.0092	—	
	"	64	"	"	"	"	"	0.0078	—	
	"	55	"	"	"	"	"	0.0053	—	
	"	48	"	"	"	"	"	0.0091	—	
5.5	"	42	"	"	"	"	"	0.0185	—	
	53	89.7	0.2	3.98	5/15	0.31	5.1	0.028	—	58° unambiguous
	"	58	"	"	"	"	"	0.0046	—	"
	"	43	"	"	"	"	"	0.0009	—	"
	"	32	"	"	"	"	"	0.0009	—	"
5.6	45	89.7	"	"	"	"	"	0.0053	—	89.7° unambiguous
	"	58	"	"	"	"	"	0.0017	—	"
	53	55	0.4	3.98	5/7.5	0.31	5.1	0.0041	—	a
	"	"	"	"	10/7.5	"	2.6	0.0033	—	b
	41	"	"	"	"	"	"	0.0107	—	c
5.7	53	"	"	"	"	0.62	5.1	0.023	—	d
	"	"	"	"	"	"	"	0.057	—	e
	79	50	0.4	3.98	5/7.5	1.96	32	0.048	—	
	"	40	"	"	"	"	"	0.038	—	
	"	32	"	"	"	"	"	0.027	—	
5.7	"	18	"	"	"	"	"	0.012	—	
	"	9	"	"	"	"	"	0.019	—	
	"	0	"	"	"	"	"	0.027	—	
	"	-9	"	"	"	"	"	0.032	—	
	"	-18	"	"	"	"	"	0.035	—	
	"	-32	"	"	"	"	"	0.052	—	

TABLE F1 (cont.)

Figure	2N+1	θ_0 (deg)	f (cps)	τ (sec)	c/ λ (km/km)	S_M	L/W	RMSE	δ	Additional Description
5.7	79	-40	0.4	3.98	5/7.5	1.96	32	0.049	—	
	"	-50	"	"	"	"	"	0.075	—	
5.8	61	55	0.4	3.98	5/7.5	1.0	16	0.074	—	gentle
	79	"	"	"	"	3.9	64	0.067	—	steep
5.10	65	0	0.14	9.39	1/5	0.06	5.1	0.012	—	
5.11	65	0	0.175	9.09	2/4	0.06	2.6	0.062	—	
5.12	79	0	0.175	9.09	1/4	0.15	13	0.013	—	
5.13	79	0	0.175	9.09	1/4	0.15	13	0.017	—	
5.14	65	0	0.035	∞	5/20	0.31	5.1	0.0006	7×10^{-6}	motion in y-direction
	41	"	"	"	"	"	"	0.0097	2×10^{-4}	motion in x-z plane
	65	51	"	"	"	"	"	0.0013	3×10^{-5}	motion in y-direction
	41	"	"	"	"	"	"	0.0082	10^{-4}	motion in x-z plane
5.15	41	0	0.2	∞	1/15	0.06	5.1	0.0015	3×10^{-6}	Case 5
5.17	41	0	0.2	∞	2.5/15	0.16	5.1	0.0037	2×10^{-5}	Case 1
	"	"	"	"	"	"	"	0.0014	10^{-5}	Case 2
	"	"	"	"	5/15	0.31	"	0.0038	2×10^{-5}	Case 3
	"	"	"	"	1/15	0.06	"	0.0008	4×10^{-6}	Case 4
	"	"	"	"	1/15	"	"	0.0015	3×10^{-6}	Case 5
	"	"	"	"	0.5/15	"	10.2	0.0006	4×10^{-6}	Case 6
	"	"	"	"	5/15	0.31	"	0.032	5×10^{-3}	Case 7
5.18	41	90	124 kc	12.9 μ s	2/1.7	0.29	4.6	0.115	—	
	"	"	"	6.45 μ s	2/1.7	"	"	0.089	—	
5.19	41	0	0.2	9.95	10/17.3	0.78	6.4	0.023	—	Case 1
	"	"	0.4	"	5/8.65	0.39	"	0.0055	—	Case 2
	"	"	"	3.98	"	"	"	0.0057	—	Case 3

TABLE F1 (cont.)

Figure	2N+1	θ_0 (deg)	f (cps)	τ (sec)	c/ λ (km/km)	S_M	L/W	RMSE	δ	Additional Description
5.19	41	0	0.4	3.98	5/8.65	0.39	6.4	0.0057	—	Case 3
	"	"	0.8	"	5/4.33	"	"	0.077	—	Case 4
5.20	41	0	0.4	9.95	10/17.3	0.78	6.4	0.042	—	Case 1
	"	"	"	"	"	"	"	0.066	—	Case 2
	"	"	"	"	5/17.3	0.39	"	0.0055	—	Case 3
5.21	41	0	0.4	3.98	10/8.65	0.78	6.4	0.057	—	
5.22	27	39	0.25	20	10/13.9	0.63	5.1	0.065	—	
5.24	21	26	0.1	20	10/34.6	0.31	5.1	0.022	—	
5.25	21	26	0.087	20	10/34.6	0.31	5.1	0.020	—	
5.26	41	26	0.1	20	10/34.6	0.62	10.2	0.031	—	D=35 km
	21	"	"	"	"	"	5.1	0.063	—	D=30 km
5.27	27	39	0.25	20	10/13.8	0.62	5.1	0.029	—	Incident P wave
	"	21	"	"	"	"	"	0.043	—	Incident SV wave
	"	"	"	"	"	"	"	0.089	—	Incident SH wave
5.28	27	39	0.25	20	10/13.8	0.62	5.1	0.029	—	$\Omega_0=90^\circ$
	"	"	"	"	"	"	"	0.049	—	$\Omega_0=45^\circ$
5.29	"	"	"	"	"	"	"	0.065	—	$\Omega_0=0^\circ$
	"	"	"	"	"	"	"	0.029	—	$\Omega_0=90^\circ$, $\theta_0=39^\circ$
5.30	27	39	0.25	20	10/13.8	0.62	5.1	0.038	—	$\Omega_0=0^\circ$, $\theta_0=0^\circ$
	"	0	"	"	"	"	"	0.049	—	$\Omega_0=45^\circ$, $\theta_0=39^\circ$
	"	26	"	"	"	"	"	0.042	—	$\Omega_0=0^\circ$, $\theta_0=26^\circ$
5.31	27	89.9	0.25	20	10/13.8	0.62	5.1	0.059	—	Case 1
5.32	27	39	0.5	20	5/6.9	0.31	5.1	0.025	—	Case 2
	"	"	"	"	"	"	"	0.041	—	Case 3
	"	"	"	"	"	"	"	0.063	—	
5.38	41	± 39	0.5	5	10/7	0.52	3.7	0.090	—	
	"	± 18	"	"	"	"	"	0.135	—	

APPENDIX G

RAY THEORETICAL METHOD

The ray theoretical solutions with which our solutions are compared in Chapter V are obtained by the simple ray tracing method described here. We shall consider only cases involving a single layer over a half-space as shown in Figure G1. Both media are homogeneous and isotropic, hence ray paths are straight line segments joined at the irregular interface $z = \zeta(x)$. The medium is uniform in the y -direction and, for convenience, we consider only plane source waves that propagate parallel to the x - z plane. For now, we restrict the source wave type to be SH (particle motion confined to the y -direction). The case of coupled P and SV wave motion will follow directly. We further limit the complexity of the method by ignoring multiple reflections within the layer. The determination of ray paths for multiple reflected waves in problems involving irregular interfaces can be exceedingly tedious. Thus these solutions differ from those involving scattering at the interface connecting two half-spaces only by the effect of the free surface. For SH wave cases, the free surface introduces a factor of 2 in amplitude at all values of x along $z=0$.

We wish to determine the amplitude ratio $\bar{v}_s(x_s) = v_s(x_s)/v_D$ and time delay $\Delta t_s(x_s) = t_s(x_s) - t_D(x_s)$ at positions $x=x_s$ along the plane free surface. Here v_D and $t_D(x_s)$ are the amplitude and arrival time that would be obtained if the layer were uniform with thickness D ; $v_s(x_s)$ and $t_s(x_s)$ are the amplitude and arrival time in the case of the nonuniform layer. Obviously $\bar{v}_s(x_s) = 1$ and $\Delta t_s(x_s) = 0$ at positions x_s far removed from the isolated irregularity.

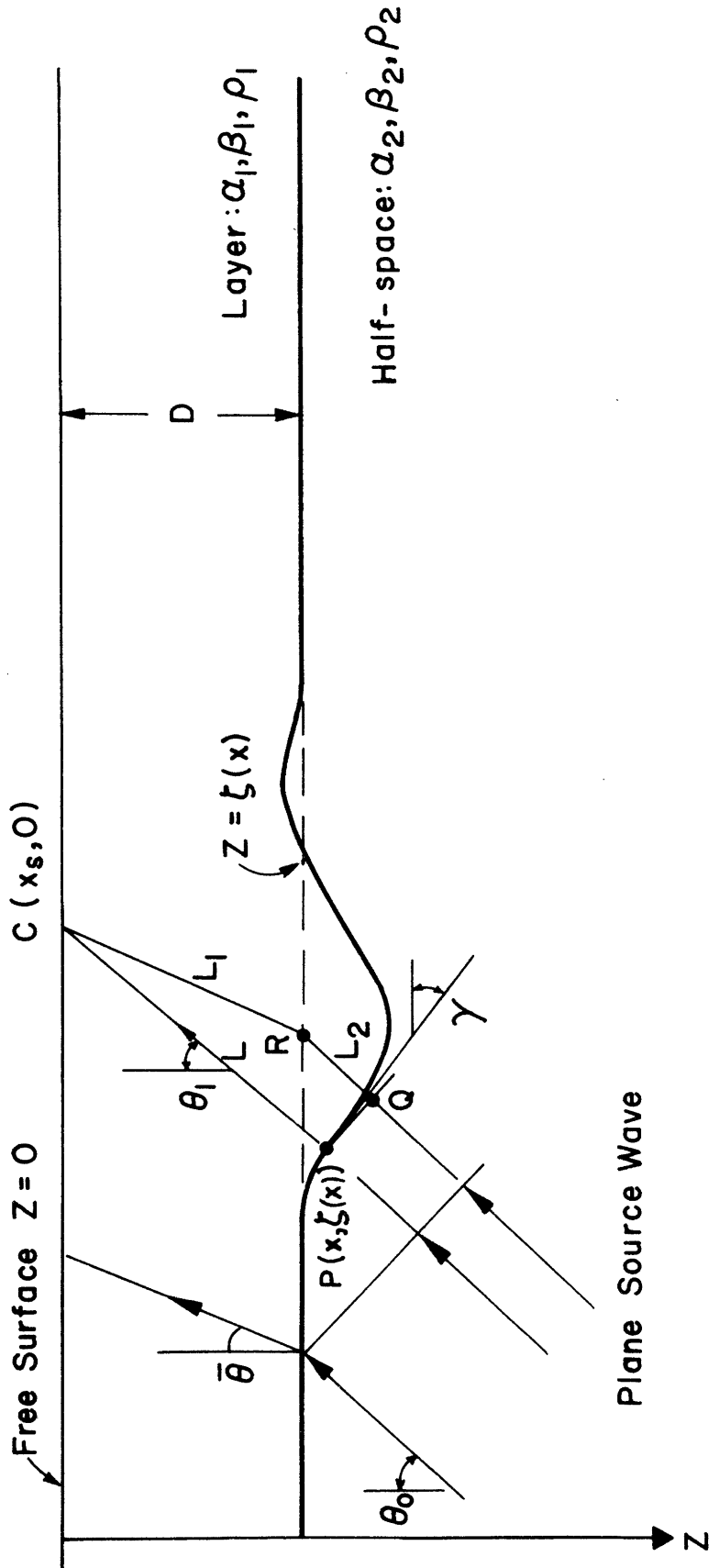


Figure G1. Problem configuration used in the discussion of the ray theoretical method.

Consider the time delay first. Our approach is to compute the time delay $\Delta t_s(x_s)$ and position $C(x_s, 0)$ along the surface parametrically in terms of the x-coordinate of the position P, $(x, \zeta(x))$, along the interface, through which the ray passes. Let the incident ray direction make the angle θ_0 with vertical. The ray is refracted at the interface $z = \zeta(x)$ according to Snell's law

$$\sin(\theta_1 - \gamma) = (\beta_1/\beta_2) \sin(\theta_0 - \gamma) \quad (G1)$$

where θ_1 is the angle from vertical of the refracted ray in the layer,

β_1 and β_2 are the transverse wave velocities in the layer and half-space respectively, and $\gamma(x)$ is the local interface dip angle given by

$$\gamma(x) = \tan^{-1} \frac{d\zeta(x)}{dx} \quad (G2)$$

Where the interface is flat, we have $\theta_1(x) = \bar{\theta}$ with

$$\bar{\theta} = \sin^{-1} [(\beta_1/\beta_2) \sin \theta_0] \quad (G3)$$

The coordinate x_s is then given by

$$x_s(x) = x + \zeta(x) \tan \theta_1(x) \quad (G4)$$

Referring to Figure G1, let L denote the distance from P to the surface position $(x_s, 0)$. If the layer were uniform, the ray arriving at x_s would have been refracted at position R and L_1 would be the distance traveled through the layer. The position Q is the point of intersection of the source ray through R and the source wave front through P. If L_2 denotes the distance from Q to R, the time delay is

$$\Delta t_s [X_s(x)] = \frac{L}{\beta_1} - \left(\frac{L_1}{\beta_1} + \frac{L_2}{\beta_2} \right) \quad (G5)$$

After some trigonometry, we get

$$\begin{aligned} L &= \zeta(x) \sec \theta_1 \\ L_1 &= D \sec \bar{\theta} \\ L_2 &= (\zeta - D) \sec \theta_0 + [\zeta(\tan \theta_1 - \tan \theta_0) - D(\tan \bar{\theta} - \tan \theta_0)] \sin \theta_0 \end{aligned} \quad (G6)$$

To compute the amplitude anomalies, we start with Rayleigh's result for plane harmonic waves that the mean energy density is

$$E = \frac{1}{2} \rho \omega^2 A^2 \quad (G7)$$

where ρ is density, ω is frequency, and A is wave amplitude. The energy density in the incident plane waves in medium 2 is independent of position. For waves in the layer, E is variable owing to reflection losses at the irregular interface and geometric spreading (and converging) of the waves.

Let v^* denote the displacement amplitude associated with source waves in the half-space; $v_1(x)$, the amplitude for waves transmitted across the interface at P ; and $v_s(x_s)$, that for waves at the free surface position $(x_s, 0)$. Using (G7), we have

$$\frac{v_s(x_s)}{v^*} = \frac{v_s(x_s)}{v_1(x)} \frac{v_1(x)}{v^*} = 2 \sqrt{\frac{E_s}{E_1}} T \quad (G8)$$

where T is the amplitude transmission coefficient at interface position P , E_1 is the energy density of waves upgoing from position P , and E_s is the energy density of waves arriving at $(x_s, 0)$. The factor 2 accounts for the reflection of the SH waves at the free surface. For the transmission coefficient, we use the value appropriate for plane waves incident at a

plane interface, i.e. we neglect interface curvature. The familiar expression for T is

$$T = 2 Z_2 / (Z_1 + Z_2) \quad (G9)$$

where $Z_j = \rho_j \beta_j \cos \delta_j$ is the characteristic impedance for waves in medium j , $\delta_2 = \Theta_0 - \gamma$ is the incidence angle at P, $\delta_1 = \Theta_1 - \gamma$ is the angle of refraction of waves leaving P.

To obtain the ratio E_s/E_1 in (G8) we require conservation of energy flow along tubes bounded by rays in the layer. With no energy sources or sinks in the layer, we require

$$E_1 \beta_1 (da_1) = E_s \beta_s (da_s) \quad (G10)$$

where da_1 and da_s are cross-sectional areas of a single elemental tube at P(x, $\zeta(x)$) and at C(x_s, 0). For our two-dimensional problems, (G10) reduces to

$$E_s / E_1 = |dl_1 / dl_s| \quad (G11)$$

where $dl_1 = da_1 \Delta y$ and $dl_s = da_s \Delta y$ with Δy some fixed length in the y-direction. Figure G2 illustrates the geometry for the computation of E_s/E_1 . Absolute values are used in (G11) to cover the situation in which C lies beyond a focus (point of zero cross-sectional area of the elemental tube of rays). In this approximation, amplitudes artificially become infinite at such focal points or caustics. Let ds be a line element along $z = \zeta(x)$. We have

$$E_s / E_1 = \frac{|ds| \cos(\Theta_1 - \gamma)}{|dx_s| \cos \Theta_1} \quad (G12)$$

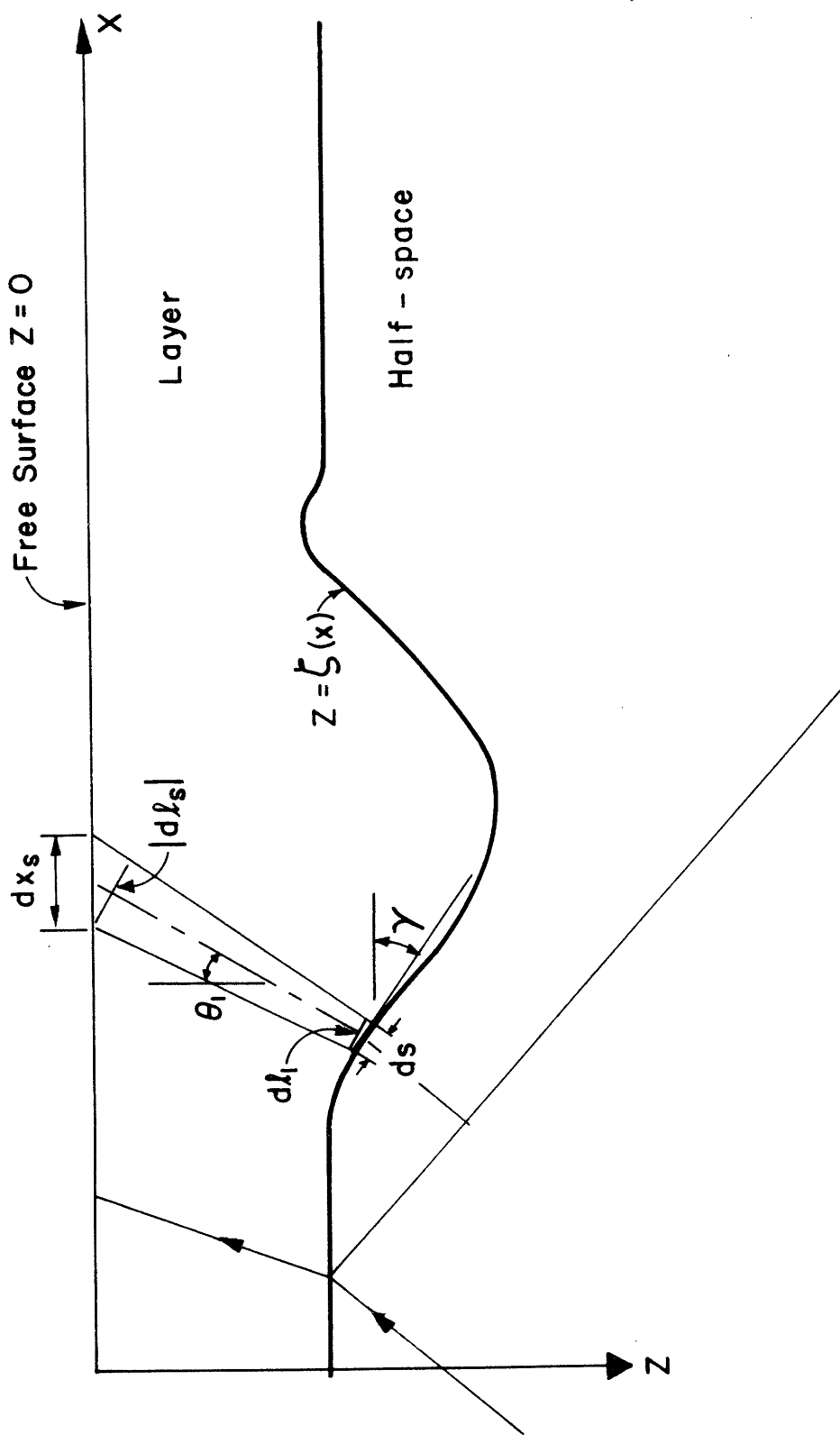


Figure G2. Schematic diagram showing a tube of rays leaving area (ds) (Δy) on the interface and arriving at area (dx_s) (Δy) at the free surface.

and

$$ds = \sec \gamma dx \quad (G13)$$

Differentiating (G4) yields

$$dx_s = \left[1 + \bar{s} \tan \theta_1 + \zeta \frac{d \tan \theta_1}{dx} \right] dx \quad (G14)$$

where we have let $\bar{s} = \frac{d\zeta}{dx}$, the local slope at the interface. Now,

$$\frac{d \tan \theta_1}{dx} = \sec^2 \theta_1 \frac{d\theta_1}{dx} \quad \text{and} \quad \frac{d\theta_1}{dx} \quad \text{can be obtained from (G1). Putting}$$

(G13) and (G14) into (G12), we find

$$E_s / E_1 = \left| \frac{\cos \theta_1 \cos \gamma}{\cos(\theta_1 - \gamma)} \left\{ 1 + \bar{s} \tan \theta_1 + \zeta \sec^2 \theta_1 \cos^2 \gamma \frac{d^2 \zeta}{dx^2} \left[1 - \frac{\beta_1 \cos(\theta_0 - \gamma)}{\beta_2 \cos(\theta_1 - \gamma)} \right] \right\} \right|^{-1} \quad (G15)$$

It is readily seen that $E_s/E_1 = 1$ at large distances from the interface anomaly. Therefore, by (G8), the normalized amplitude $\bar{v}_s(x_s)$ is

$$\bar{v}_s(x_s) = \frac{v_s(x_s)/V^*}{v_0/V^*} = \frac{T}{T_0} \sqrt{E_s/E_1} \quad (G16)$$

where $T = 2 \left[1 + \frac{\beta_1 \beta_2 \cos \bar{\theta}}{\beta_2 \beta_2 \cos \theta_0} \right]^{-1}$ is the transmission coefficient at the flat portions of the interface.

It is the amplitude anomaly $\bar{v}_s(x_s)$ with which our solutions are compared. We have mentioned the artificially large amplitudes that would be computed at caustics. Also note in (G15) that the amplitudes are dependent upon $\frac{d^2 \zeta}{dx^2}$ and, consequently, are sensitive to small-scale details in interface shape. This accounts for the discontinuities in the ray theoretical solution, for example, in Figure 5.1. The ray theoretical time delays (equation (G5)) are less sensitive to small details in interface shape. Our wave theoretical solutions are also not sensitive to small features, and therefore the time delays compare more favorably than do the amplitudes.

The extension of this ray theoretical approach to the case of incident plane P or SV waves is straightforward. P or SV waves incident upon the interface give rise to transmitted P and SV waves in the layer. The arrival of either of these wave types results in two components of displacement at the free surface. Let us consider the example of P-type source waves directed at the angle $\Theta_{o,p}$ from vertical. According to Snell's law, the transmitted P and SV waves depart from interface position $P(x, \zeta(x))$ at the angles $\Theta_{1,pp}$ and $\Theta_{1,ps}$ from vertical, given by

$$\sin(\Theta_{1,pp} - \gamma) = (\alpha_1/\alpha_2) \sin(\Theta_{o,p} - \gamma)$$

$$\sin(\Theta_{1,ps} - \gamma) = (\beta_1/\alpha_2) \sin(\Theta_{o,p} - \gamma)$$

These refracted waves propagate independently, arriving at surface positions $x_{s,pp}$ and $x_{s,ps}$ with delay times $\Delta t_{s,pp} = t_{s,pp} - t_{D,pp}$ and $\Delta t_{s,ps} = t_{s,ps} - t_{D,pp}$ respectively. ($t_{D,pp}$ is the arrival time of the refracted P wave if the layer thickness were uniform.) These quantities are computed using equations analogous to (G4) and (G5).

In the computation of the amplitude anomalies for the vertical and horizontal components of displacement at the free surface, we again consider reflection losses at the interface (neglecting curvature) and follow tubes bounded by rays in the layer. The vertical component $W_{pp}(x_{s,pp})$ of displacement amplitude associated with the refracted P wave (P wave source) is computed from

$$\frac{W_{pp}(x_{s,pp})}{\phi^*} = F_{pw} \frac{\phi_s}{\phi_i} T_{pp} \quad (G17)$$

In (G17), ϕ^* , ϕ_s , and ϕ_1 are P-wave amplitudes analogous to the displacement amplitudes v , v_1 , and v_s in (G8); T_{pp} is the transmission coefficient for P waves incident to and transmitted across the irregular interface; and $F_{pw} = W_{pp}(x_{s,pp})/\phi_s(x_{s,pp})$ is the coefficient expressing the vertical displacement at the free surface in terms of the amplitude of the arriving P waves. The ratio ϕ_s/ϕ_1 is again determined by conservation of energy flow in a tube of rays, that is

$$\phi_s / \phi_1 = \sqrt{E_{s,p} / E_{1,p}}$$

The energy ratio $E_{s,p} / E_{1,p}$ is given by an expression like (G15) where the quantities θ_1 , θ_0 , β_1 , and β_2 are replaced by those appropriate to the P-type source and transmitted waves.

When the source wave is SV-type (amplitude ψ^*) or the refracted wave is SV-type (amplitudes ψ_1 and ψ_2), the transmission coefficient T_{pp} is replaced by T_{ps} , T_{sp} , or T_{ss} (the first subscript refers to source wave type and the second to the transmitted wave type). These transmission coefficients are analogous to those in Knott's equations (Knott, 1899; Muskat and Meres, 1940). They were rederived for this study using the Haskell matrix technique; that is, by equating the motion-stress vectors in each medium at the interface. Using matrix notation, we have

$$\underline{T} = \begin{bmatrix} T_{pp} & T_{ps} \\ T_{sp} & T_{ss} \end{bmatrix} = \frac{1}{\Delta} \begin{bmatrix} l_{22} & -l_{12} \\ -l_{21} & l_{11} \end{bmatrix} \quad (G18)$$

where

$$\Delta = l_{11} l_{22} - l_{12} l_{21}$$

$$l_{11} = \frac{1}{2k\beta_2} \left[2k^2 \left(1 + \frac{\mu_1 \nu_1}{\mu_2 \nu_2} \right) - \frac{\nu_1}{\nu_2} f_2 - \frac{\mu_1}{\mu_2} f_1 \right]$$

$$\begin{aligned}
 l_{22} &= \frac{1}{2k_{\beta_2}^2} \left[2k^2 \left(1 + \frac{\mu_1 \nu_1'}{\mu_2 \nu_2'} \right) - \frac{\nu_1'}{\nu_2'} f_2 - \frac{\mu_1}{\mu_2} f_1 \right] \\
 l_{12} &= \frac{1}{2k_{\beta_2}^2} \left[2k \nu_1' \left(1 - \frac{\mu_1}{\mu_2} \right) - \frac{k}{\nu_2'} \left(\frac{\mu_1 f_1}{\mu_2} - f_2 \right) \right] \\
 l_{21} &= \frac{1}{2k_{\beta_2}^2} \left[-2k \nu_1 \left(1 - \frac{\mu_1}{\mu_2} \right) + \frac{k}{\nu_2'} \left(\frac{\mu_1 f_1}{\mu_2} - f_2 \right) \right]
 \end{aligned} \tag{G19}$$

In these expressions,

μ_j is the rigidity in medium j ; ($j=1,2$)

$$k_{\beta_j} = \omega / \beta_j$$

$$k_{\alpha_j} = \omega / \alpha_j$$

$$\nu_j = k_{\alpha_j} \cos \delta_{\alpha_j}$$

$$\nu_j' = k_{\beta_j} \cos \delta_{\beta_j}$$

(G20)

δ_{α_j} is the angle of reflection (or refraction) for P waves

δ_{β_j} is the angle of reflection (or refraction) for S waves

$$k = k_{\beta_2} \sin \delta_{\beta_2}$$

$$f_j = 2k^2 - k_{\beta_j}^2$$

The frequency ω is a dummy quantity here, i.e. the elements of T are independent of ω so long as no critical angle is exceeded (all waves are regular).

The ratio F_{PW} is one of four similar quantities - $F_{PW}, F_{PU}, F_{SW}, F_{SU}$ - where the first subscript refers to the arriving wave type and the second refers to the component of motion (W for vertical and U for horizontal). These are derived by writing the motion-stress vector at the free surface in terms of the arriving and reflected wave amplitude vector and requiring the vanishing of stress. We find

$$\begin{aligned}
 F_{SW} &= F_{PU} = 4ik k_{\beta}^2 \nu_i \nu'_i / F \\
 F_{SU} &= -2ik_{\beta}^2 \nu'_i f_i / F \\
 F_{PW} &= 2ik_{\beta}^2 \nu_i f_i / F
 \end{aligned}
 \tag{G21}$$

where $F = f_i^2 + 4k^2 \nu_i \nu'_i$ is the Rayleigh wave denominator and the angles $\delta\alpha_i$ and $\delta\beta_i$ in (G20) are angles of reflection at the free surface.

Finally, the displacement amplitudes computed by equations like (G17) are normalized to similarly computed amplitudes obtained for the uniform layer problem normalization is to the vertical component for incident P waves and to the horizontal component for incident SV waves.

According to this ray theoretical description, motion at a surface position x_s has contributions from both P and SV wave arrivals. If x_s lies between caustics, there will also be multiple arrivals. When comparing with the wave theoretical solutions, we may include the effects of all arrivals by convolving this spike time series with a harmonic wave. When a large imaginary part of ω is used in the wave theoretical solution, so as to simulate the effects of early arrivals, it is appropriate to consider only the P wave arrivals in the ray theoretical solutions.

We remark, finally, on the extension to the case of an incident wave at

arbitrary azimuth angle relative to the strike (y-direction). An incident wave of any type gives rise to transmitted P and linearly polarized S waves at the interface. The two-dimensionality of the problem is maintained in that the y-component of wave slowness of all scattered waves is unchanged from that of the source wave. Thus, again the cross-sectional area of a tube of rays varies only with the change in width parallel to the x-z plane. The transmission coefficients are again given by (G9) and (G18) once the S-wave particle motion is resolved into components in the plane of incidence and normal to it. The same is true of the free surface factors F_{pw} , etc. The ray theory was not used for the arbitrary azimuth incidence problems in this thesis.

REFERENCES

- Abubakar, I., Reflection and refraction of plane SH waves at irregular interfaces, I, J. Phys. Earth, 10, 1, 1962a.
- Abubakar, I., Reflection and refraction of plane SH waves at irregular interfaces, II, J. Phys. Earth, 10, 15, 1962b.
- Abubakar, I., Buried compressional line source in a half-space with an irregular boundary, J. Phys. Earth, 10, 21, 1962c.
- Aki, K. and K.L. Larner, Surface motion of a layered medium having an irregular interface due to incident plane SH waves, J. Geophys. Res., in press, 1970.
- Asano, S., Reflection and refraction of elastic waves at a corrugated boundary surface. Part I. The case of incidence of SH wave, Bull. Earthquake Res. Inst., 38, 177, 1960.
- Asano, S., Reflection and refraction of elastic waves at a corrugated boundary surface. Part II, Bull. Earthquake Res. Inst., 39, 367, 1961.
- Asano, S., Reflection and refraction of elastic waves at a corrugated boundary surface, Part II, Bull. Seism. Soc. Am., 56, 210, 1966.
- Banaugh, R.P., Scattering of acoustic and elastic waves by surfaces of arbitrary shape, Univ. Calif. Radiation Lab., report UCRL 6779, 174 pp., 1962.
- Basham, P.W. and R.M. Ellis, The composition of P codas using magnetic tape seismograms, Bull. Seism. Soc. Am., 59, 473, 1969.
- Ban-Menahem, A. and S.J. Singh, Multipolar elastic fields in a layered half space, Bull. Seism. Soc. Am., 58, 1519, 1968.
- Boore, D.M., Finite difference solutions to the equations of elastic wave-propagation, with application to Love waves over dipping interfaces, Ph.D. thesis, Massachusetts Institute of Technology, Cambridge, 1969.
- Boore, D.M., K.L. Larner, and K. Aki, A comparison of two independent methods for the solution of wave scattering problems: theoretical response of a sedimentary basin to vertically incident SH waves; (in preparation, to be submitted to the J. Geophys. Res.).
- Boore, D.M. and M.N. Toksoz, Rayleigh wave particle motion and crustal structure, Bull. Seism. Soc. Am., 59, 331, 1969.

- Borcherdt, C.A. and J.C. Roller, Preliminary interpretation of a seismic-refraction profile across the Large Aperture Seismic Array, Montana, USGS Tech-Letter No. NCER-2, U.S. Geological Survey, Menlo Park, 1967.
- Brekhovskikh, L.M., Waves in layered media, Academic Press, New York, 516 p., 1960.
- Burridge, R. and L. Knopoff, Body force equivalents for seismic dislocations, Bull. Seism. Soc. Am., 54, 1875, 1964.
- Cooley, J.W. and J.W. Tukey, An algorithm for the machine computation of complex Fourier series, Math. Computation, 19, 297, 1965.
- Dunkin, J.W. and A. Eringen, The reflection of elastic waves from the wavy boundary of a half-space, Proc. 4th U.S. Nat. Congress on Appl. Mech. (Berkeley), 143, 1962.
- Ellis, R.M. and P.W. Basham, Crustal characteristics from short-period P waves, Bull. Seism. Soc. Am., 58, 1681, 1968.
- Ewing, W.M., W.S. Jardetsky, and F. Press, Elastic waves in layered media, McGraw-Hill, New York, 380 p., 1957.
- Fernandez, L.M. and J. Careaga, The thickness of the crust in Central United States and La Paz, Bolivia, from the spectrum of longitudinal seismic waves, Bull. Seism. Soc. Am., 58, 711, 1968.
- Fredericks, R.W., Scattering of elastic pulses by obstacles of infinite impedance and semi-infinite dimensions on the surface of a half-space, Ph.D. thesis, Univ. of California, Los Angeles, 1969.
- Gilbert, F., Propagation of transient leaking modes in a stratified elastic waveguide, Rev. Geophys., 2, 123, 1964.
- Gilbert, F. and L. Knopoff, Seismic scattering from topographic irregularities, J. Geophys. Res., 65, 3437, 1960.
- Glover, P. and S.S. Alexander, Lateral variations in crustal structure beneath the Montana LASA, J. Geophys. Res., 74, 505, 1969.
- Greenfield, R.J. and R.M. Sheppard, The Mohorovicic depth variations under the LASA and their effect on $dT/d\Delta$ measurements, Bull. Seism. Soc. Am., 59, 409, 1969.
- Harkrider, D.G., Surface waves in multilayered elastic media, 1, Rayleigh and Love waves from buried sources in a multilayered elastic half-space, Bull. Seism. Soc. Am., 54, 627, 1964.
- Haskell, N.A., The dispersion of surface waves in multi-layered media, Bull. Seism. Soc. Am., 43, 17, 1953.

- Haskell, N.A., Crustal reflection of plane SH waves, J. Geophys. Res., 65, 4147, 1960.
- Haskell, N.A., Crustal reflection of plane P and SV waves, J. Geophys. Res., 67, 4751, 1962.
- Heaps, H.S., Reflection of plane waves of sound from a sinusoidal surface, J. Appl. Phys., 28, 815, 1957.
- Herrera, I., A perturbation method for elastic wave propagation, 1. Nonparallel boundaries, J. Geophys. Res., 69, 3845, 1964.
- Isaacson, E. and H.B. Keller, Analysis of numerical methods, John Wiley & Sons, New York, 541 p., 1966.
- Jardetsky, W.S., Period equation for an n-layered half-space and some related questions, Columbia Univ. Lamont Geol. Obs. Tech. Rept. Seismology, 29, 1953.
- Kanai, K., Relation between the nature of surface layer and the amplitude of earthquake motions, Bull. Earthquake Res. Inst., 30, 31, 1952.
- Kanai, K., T. Tanaka, and S. Yoshizawa, Comparative studies of earthquake motions on the ground and underground, Bull. Earthquake Res. Inst., 37, 53, 1959.
- Knott, C.G., On the reflexion and refraction of elastic waves, with seismological applications, Phil. Mag., 5th ser., 48, 64, 1899.
- Lapwood, E.R., The disturbance due to a line source in a semi-infinite elastic medium, Phil. Trans. Roy. Soc. London, A, 242, 63, 1949.
- Laster, S.J., M.M. Backus, and R. Schell, Analog model studies of the simple refraction problem, Seismic refraction prospecting, A.W. Musgrave, ed., Soc of Exploration Geophysicists; Tulsa, Oklahoma, 604 p, 1967.
- Levy, A. and H. Deresiewicz, Reflection and transmission of elastic waves in a system of corrugated layers, Bull. Seism. Soc. Am., 57, 393, 1967.
- Lippmann, B.A., J. Opt. Soc. Amer., 43, 408, 1954.
- Mack, H., Nature of short-period P-wave signal variations at LASA, J. Geophys. Res., 74, 3161, 1969.
- McIvor, I.K., Two-dimensional scattering of a plane compressional wave by surface imperfections, Bull. Seism. Soc. Am., 59, 1349, 1969.
- Mechler, P. and Y. Rocard, Geologic limitations of the use of an array of seismometers (abstract), Abstracts of Papers, International Association of Seismology and Physics of the Earth's Interior, 123, 1967.

- Meecham, W.C., Variational method for the calculation of the distribution of energy reflected from a periodic surface, I, J. Appl. Phys., 27, 361, 1956.
- Mereu, R.F., Effect of Mohorovicic topography on the amplitudes of seismic P waves, J. Geophys. Res., 74, 4371, 1969.
- Mereu, R.F. and J.A. Hunter, Crustal and upper mantle structure under the Canadian Shield from Project Early Rise data, Bull. Seism. Soc. Am., 59, 147, 1969.
- Mikhlin, S.G., Integral equations, Pergamon Press, New York, 338 p., 1957.
- Mikumo, T., Crustal structure in Central California in relation to the Sierra Nevada, Bull. Seism. Soc. Am., 55, 65, 1965.
- Muskat, M. and M.W. Meres, Reflection and transmission coefficients for plane waves in elastic media, Geophysics, 5, 115, 1940.
- Nadeau, G., Introduction to elasticity, Holt, Rinehart, and Winston, New York, 285 p., 1964.
- Papoulis, A., The Fourier integral and its applications, McGraw-Hill Book Co., New York, 318 p., 1962.
- Phinney, R.A., Structure of the earth's crust from spectral behavior of long-period body waves, J. Geophys. Res., 69, 2997, 1964.
- Phinney, R.A., Theoretical calculations of the spectrum of first arrivals in layered elastic mediums, J. Geophys. Res., 70, 5107, 1965.
- Poceski, A., The ground effect of the Skopje July 26, 1963 earthquake, Bull. Seism. Soc. Am., 59, 1, 1969.
- Rayleigh, J.W.S., On the dynamical theory of gratings, Proc. Roy. Soc. London, A, 79, 399, 1907.
- Rayleigh, J.W.S., The theory of sound, II, 504 pp., Dover, New York, 1945.
- Ricker, N., The computation of output disturbances from amplifiers for true wavelet inputs, Geophysics, 10, 207, 1945.
- Saito, M., Excitation of free oscillations and surface waves by a point source in a vertically heterogeneous Earth, J. Geophys. Res., 72, 3689, 1967.
- Sharma, D.I., Scattering of steady elastic waves by surfaces of arbitrary shape, Bull. Seism. Soc. Am., 57, 795, 1967.
- Thomson, W.T., Transmission of elastic waves through a stratified medium, J. Appl. Phys., 21, 89, 1950.
- Uretzky, J.L., The scattering of plane waves from periodic surfaces, Annals of Physics, 33, 400, 1965.

Utsu, T., Variations in spectra of P waves recorded at Canadian Arctic Seismograph Stations, Can. J. of Earth Sci., 3, 597, 1966.

Zietz, I., Aeromagnetic investigations of the Earth's crust in the United States, The Earth's crust and upper mantle, P.J. Hart, ed., Amer. Geophys. Union, Washington, D.C., 735 p., 1969.

BIOGRAPHICAL NOTE

The author was born in Chicago, Illinois on November 1, 1938, and moved to Miami, Florida during high school. After graduation from Miami Edison Sr. High School he entered the Colorado School of Mines. There he was elected to Tau Beta Pi, the engineering honor society and received the Outstanding Junior Award by the American Society of Mechanical Engineers. During the senior year, he served as president of his social fraternity, and was awarded a Socony-Mobil Scholarship. He graduated with highest honors, receiving a Geophysical Engineering degree, in June, 1960 and entered the Massachusetts Institute of Technology on a Whitney Fellowship. The following year he received a National Science Foundation Fellowship. He worked as a research geophysicist with the Atlantic Refining Company during the summers of 1960 and 1961 and with Texas Instruments, Science Services Division, during the next summer. In the fall of 1964, he entered the U.S. Army with an R.O.T.C. commission. He served in the Corps of Engineers Nuclear Cratering Group at the Lawrence Radiation Laboratory for one year, then in Vietnam until the completion of his tour of duty. After being discharged in November, 1966, he worked for E.G. & G. in Boston as a senior research scientist until returning to M.I.T. in the fall of 1968. His publications include

D. Eckhardt, K. Larner, and T. Madden, Long period magnetic fluctuations and mantle conductivity estimates, J. Geophys. Res. 68, 1963, p. 6279-86.

Schneider, W. A., K. L. Larner, J. P. Burg, Milo M. Backus, A new data processing technique for the elimination of ghost arrivals on reflection seismograms, Geophysics, v 29, 1964, p. 783-805.